

---

# The Chemical Evolution of Galaxies in Semi-Analytic Models and Observations

Robert M. Yates

---



München 2014



---

# **The Chemical Evolution of Galaxies in Semi-Analytic Models and Observations**

**Robert M. Yates**

---

Dissertation  
an der Fakultät für Physik  
der Ludwig–Maximilians–Universität  
München

vorgelegt von  
Robert M. Yates  
aus London

München, den 28.02.2014

Erstgutachter: Prof. Simon D. M. White

Zweitgutachter: Dr. Klaus Dolag

Tag der mündlichen Prüfung: 07.05.2014

*“What can be asserted without proof can be dismissed without proof.”*

**Christopher Hitchens**



# Contents

<b>Zusammenfassung</b>	<b>xvii</b>
<b>Summary</b>	<b>xix</b>
<b>1 Introduction</b>	<b>1</b>
1.1 Metallicities in galaxies . . . . .	2
1.1.1 Total metallicity . . . . .	2
1.1.2 Oxygen abundance . . . . .	2
1.1.3 Iron abundance . . . . .	3
1.1.4 Alpha enhancement . . . . .	4
1.2 Measuring the gas-phase oxygen abundance . . . . .	5
1.2.1 The $T_e$ method . . . . .	5
1.2.2 The Empirical method . . . . .	7
1.2.3 The Theoretical method . . . . .	12
1.2.4 Implications for the mass-metallicity relation . . . . .	13
1.3 GCE modelling . . . . .	14
1.3.1 The closed box . . . . .	14
1.3.2 The leaky box . . . . .	16
1.3.3 The accreting box . . . . .	18
1.4 N-body simulations of dark matter structure formation . . . . .	20
1.4.1 Millennium and Millennium-II . . . . .	21
1.4.2 Output snapshots and subhalo merger trees . . . . .	22
1.5 Semi-analytic modelling . . . . .	25
1.5.1 L-Galaxies . . . . .	26
1.5.2 A defense of SAMs . . . . .	38
<b>2 The relation between <math>Z_g</math>, <math>M_*</math>, and SFR in galaxies</b>	<b>41</b>
2.1 Introduction . . . . .	41
2.2 The Observational Sample . . . . .	44

2.3	Estimation of Stellar Mass, Star Formation Rate and Metallicity . . .	45
2.4	Observational Results . . . . .	48
2.4.1	The $M_*$ - $Z_g$ relation . . . . .	48
2.4.2	The $M_*$ - $Z_g$ relation, as a function of SFR . . . . .	50
2.4.3	The SFR- $Z_g$ and sSFR- $Z_g$ relations, as a function of $M_*$ . . .	55
2.4.4	Projection of least scatter . . . . .	57
2.5	Gas-phase metallicity diagnostics . . . . .	58
2.5.1	An additional set of massive galaxies . . . . .	60
2.6	Model Sample . . . . .	60
2.7	Model Results . . . . .	64
2.7.1	The relation between $M_*$ , SFR and $Z_{\text{cold}}$ at $z = 0$ . . . . .	64
2.7.2	Metallicity evolution in model galaxies . . . . .	66
2.7.3	Bulge and black hole masses . . . . .	73
2.7.4	Evolution of the $M_*$ - $Z_{\text{cold}}$ relation out to $z \sim 3$ . . . . .	74
2.8	Discussion . . . . .	79
2.9	Conclusions . . . . .	81
<b>3</b>	<b>Dilution in elliptical galaxies</b>	<b>83</b>
3.1	Introduction . . . . .	83
3.2	The model sample . . . . .	86
3.3	Model Results . . . . .	87
3.3.1	Two classes of massive galaxy . . . . .	87
3.3.2	Dilution in elliptical galaxies . . . . .	92
3.4	The observational samples . . . . .	98
3.4.1	Main sample . . . . .	98
3.4.2	HI-detected sample . . . . .	98
3.4.3	$Z_*$ sample . . . . .	101
3.4.4	NUV-r sample . . . . .	101
3.4.5	HI scaling relations . . . . .	102
3.5	Observational Results . . . . .	104
3.5.1	Two classes of massive galaxy in the SDSS . . . . .	106
3.6	Comparisons to other works . . . . .	115
3.6.1	Accretion onto elliptical galaxies . . . . .	115
3.6.2	Interacting galaxies . . . . .	117
3.6.3	The relation between $M_*$ , $Z_g$ , and $M_{\text{HI}}$ . . . . .	118
3.6.4	The FMR at $z=0$ . . . . .	120
3.7	Conclusions . . . . .	121

<b>4</b>	<b>GCE modelling</b>	<b>123</b>
4.1	Introduction . . . . .	123
4.2	The semi-analytic model . . . . .	125
4.3	GCE Ingredients . . . . .	126
4.3.1	The IMF . . . . .	126
4.3.2	Stellar lifetimes . . . . .	129
4.3.3	AGB wind yields . . . . .	129
4.3.4	SN-Ia yields . . . . .	131
4.3.5	SN-II yields . . . . .	131
4.4	The GCE Equation . . . . .	134
4.4.1	SN-Ia delay-time distribution . . . . .	138
4.5	Implementation . . . . .	140
4.5.1	SFH, ZH and EH arrays . . . . .	140
4.5.2	Implementing the GCE equation . . . . .	142
4.5.3	SN feedback . . . . .	143
4.5.4	Default set-ups . . . . .	144
4.6	Conclusions . . . . .	145
<b>5</b>	<b>The chemical properties of local galaxies</b>	<b>147</b>
5.1	Introduction . . . . .	147
5.2	The mass-metallicity relations . . . . .	148
5.3	The Milky Way disc . . . . .	152
5.3.1	MW-type model galaxies . . . . .	154
5.3.2	An individual MW-type model galaxy . . . . .	158
5.4	Elliptical galaxies . . . . .	160
5.4.1	The mass-age relation . . . . .	162
5.4.2	$[\alpha/\text{Fe}]$ relations . . . . .	162
5.4.3	Galactic winds . . . . .	168
5.4.4	Carbon and Nitrogen . . . . .	170
5.5	Conclusions . . . . .	172
	<b>Acknowledgements</b>	<b>192</b>



# List of Figures

1.1	Analytic GCE models . . . . .	17
1.2	Snapshot and timestep widths . . . . .	24
1.3	Semi-analytic galaxy types . . . . .	28
1.4	Mass and energy transfer . . . . .	29
1.5	Semi-analytic galaxy mergers . . . . .	35
2.1	The $M_*$ - $Z_g$ relation . . . . .	49
2.2	The $M_*$ - $Z_g$ relation residuals . . . . .	49
2.3	The $M_*$ -SFR- $Z_g$ relation . . . . .	51
2.4	The dependence of SFR on the estimation method . . . . .	52
2.5	Comparison of metallicity diagnostics . . . . .	53
2.6	Relations with metallicity . . . . .	54
2.7	The optimal FMR projection . . . . .	56
2.8	Errors in $M_*$ and $Z_g$ estimates . . . . .	61
2.9	The $M_*$ - $Z$ relation with additional galaxies . . . . .	62
2.10	Model $M_*$ - $Z_{\text{cold}}$ relation . . . . .	63
2.11	Model relations with metallicity . . . . .	65
2.12	The sSFR- $(M_{\text{cold}}/M_*)$ relation . . . . .	66
2.13	Enriching galaxies' evolution . . . . .	68
2.14	Diluting galaxies' evolution . . . . .	69
2.15	The $M_{\text{bulge}}$ - $M_{\text{BH}}$ relation . . . . .	70
2.16	Black hole masses . . . . .	72
2.17	Black hole mass distribution . . . . .	74
2.18	Evolution of the $M_*$ -SFR relation . . . . .	75
2.19	Evolution of the $M_*$ - $Z_{\text{cold}}$ relation . . . . .	76
2.20	Galaxies' metallicity evolution . . . . .	78
3.1	Model sample distributions . . . . .	85
3.2	Sample distribution in the sSFR- $Z_{\text{cold}}$ plane . . . . .	86

3.3	Model galaxy properties . . . . .	88
3.4	Model mass distribution . . . . .	89
3.5	Enriching & diluting galaxies' properties . . . . .	90
3.6	The age – $Z_{\text{cold}} - Z_*$ relation . . . . .	91
3.7	Gas clumps and merging satellites . . . . .	93
3.8	Diluting galaxies' progenitor properties . . . . .	94
3.9	The evolution of dilution . . . . .	96
3.10	Cooling versus cold accretion . . . . .	97
3.11	Local galaxies' distributions . . . . .	99
3.12	Local galaxies' distribution in the sSFR- $Z_g$ plane . . . . .	99
3.13	Direct versus estimated $M_{\text{HI}}$ measurements . . . . .	103
3.14	Local galaxy properties . . . . .	105
3.15	Mass distribution of local enriching & diluting galaxies . . . . .	107
3.16	Properties of local enriching & diluting galaxies . . . . .	110
3.17	The $D_n4000 - Z_g - Z_*$ relation . . . . .	111
3.18	Higher-sSFR galaxies . . . . .	112
3.19	Images & spectra of potentially diluting local galaxies . . . . .	113
3.20	Higher-sSFR galaxies . . . . .	118
3.21	Model $M_*-M_{\text{cold}}/(M_* + M_{\text{cold}})$ relation . . . . .	119
4.1	Stellar lifetimes . . . . .	127
4.2	AGB wind yields . . . . .	128
4.3	SN-Ia yields . . . . .	130
4.4	SN-II yields . . . . .	132
4.5	The secondary mass fraction distribution function . . . . .	137
4.6	SN-Ia DTDs . . . . .	138
4.7	Higher-resolution SFHs in post-processing . . . . .	141
5.1	The new model $M_*-Z_{\text{cold}}$ relation . . . . .	149
5.2	The new model $M_*-Z_*$ relation . . . . .	150
5.3	Example model Milky Way SFHs . . . . .	152
5.4	The $[\text{Fe}/\text{H}]-[\text{O}/\text{Fe}]$ relation for three DTDs . . . . .	153
5.5	$[\text{Fe}/\text{H}]$ and $[\text{O}/\text{Fe}]$ distributions . . . . .	155
5.6	$[\text{Fe}/\text{H}]$ and $[\text{O}/\text{Fe}]$ distributions by age . . . . .	155
5.7	The evolution of a Milky-Way-type model galaxy . . . . .	157
5.8	Example model elliptical SFHs . . . . .	160
5.9	The $M_*$ -age relation . . . . .	161
5.10	The $M_*-[\text{O}/\text{Fe}]$ relation for model ellipticals . . . . .	163
5.11	The age- $[\text{O}/\text{Fe}]$ relation . . . . .	164

---

5.12	Model $M_*$ - $[\alpha/\text{Fe}]$ relations . . . . .	166
5.13	The $M_*$ - $[\text{O}/\text{Fe}]$ relation including galactic winds . . . . .	169
5.14	The $[\text{Fe}/\text{H}]$ and $[\text{O}/\text{Fe}]$ distributions including galactic winds . . . . .	169
5.15	The model elliptical $M_*$ - $[\text{N}/\text{O}]$ relation . . . . .	171



# List of Tables

1.1	Simulation properties . . . . .	23
1.2	Semi-analytic model parameters . . . . .	32
2.1	Selection criteria and sample cuts . . . . .	44
2.2	Sample properties . . . . .	46
3.1	The properties of enriching & diluting galaxies . . . . .	109



# Zusammenfassung

In den entscheidenden Entstehungsprozessen von Galaxien spielt die chemische Zusammensetzung von Sternen und Gas eine bedeutende Rolle: Von der Gaskühlung über die Sternentstehung bis hin zur Produktion neuer schwerer Elemente, die ins Gas zurückgegeben werden, wenn Sterne in Supernovae-Explosionen sterben. Eine theoretische Erklärung der Produktion von schwerer Elementen in Sternen sowie deren Verteilung in Galaxien wurde seit der ersten Erklärung der stellaren Nukleosynthese in den 1920ern entwickelt. Dennoch gibt es immer noch eine Reihe offener Fragen auf dem Gebiet der chemischen Galaxienentwicklung (galactic chemical evolution - GCE). Zum Beispiel: Was ist die genaueste Methode um die Metallizität von Galaxien zu messen? Welches sind die verhältnismäßigen Anteile der GCE bei unterschiedlichen Sternarten? Wie ist das metallreiche Material innerhalb der verschiedenen Teile einer Galaxie verteilt? Wie können wir die scheinbar inkompatiblen chemischen Eigenschaften erklären, die in verschiedenen Galaxien der kosmischen Nachbarschaft beobachtet werden? Diese Doktorarbeit untersucht die chemische Anreicherung von Galaxien in zweierlei Hinsicht: Es werden sowohl Beobachtungen naher Galaxien, als auch differenzierte GCE-Modelle im Rahmen eines semi-analytischen Galaxienentwicklungsmodells verwendet. Folgende Ziele hat die Arbeit: a) Sie soll die chemischen Eigenschaften von Galaxien mit niedriger Rotverschiebung quantifizierbar machen und mögliche Ursachen erklären. b) Es soll ein verbessertes GCE-Modell entwickelt werden, das die verschiedenen chemischen Eigenschaften abbildet, die in den Galaxien der kosmischen Nachbarschaft beobachtet werden können.

Aufbauend auf dieser Zielsetzung wird in Kapitel 1 das nötige Hintergrundwissen erläutert, das für das Verständnis der Untersuchung wichtig ist. Dabei geht es um die verschiedenen Messmethoden zur Feststellung der Metallizität echter Galaxien sowie deren Schwächen. Neben einfachen analytischen GCE-Modellen werden auch die semi-analytischen Modelle, L-GALAXIES beschrieben. In den Kapiteln 2 und 3 erläutere ich den Zusammenhang von stellar mass ( $M_*$ ), star formation rate (SFR) und der gas-phase metallicity ( $Z_g$ ) in Galaxien. Es zeigt sich, dass das L-GALAXIES-Modell den positiven Zusammenhang zwischen SFR und  $Z_g$  in

massiven Galaxien abbildet. Dieser wird auch deutlich, wenn theoretische Metalizitätsdiagnosen zur Anwendung kommen statt einfacherer Diagnosen. Außerdem wird gezeigt, dass im semi-analytischen Modell die Wechselwirkung von SFR- $Z_g$  auf eine allmähliche Verdünnung des Gas in elliptischen Galaxien zurückzuführen ist, die nach dem Verschmelzen zweier gas-reicher Galaxien SFR-arm sind. Einige Merkmale dieser besonderen Entstehung, wie beispielsweise eine niedrige Gasfraktion und niedrige  $Z_g-Z_*$ , können auch in den besagten Modellgalaxien gesehen werden. Entscheidend ist außerdem, dass all diese Eigenschaften auch im Rahmen der Sloan Digital Sky Survey (SDSS) in nahe gelegenen elliptischen Galaxien beobachtet werden. Das ist ein indirekter Beweis dafür, dass es diese Art von evolutionärem Entstehungsprozess tatsächlich in den elliptischen Galaxien unseres Universums gibt.

In Kapitel 4 stelle ich ein neues, differenziertes GCE-Modell vor, das in L-GALAXIES implementiert wurde. Es ist besser als sein Vorgänger, da es die durch Sternenwinde und Supernoven verzögerte Anreicherung vieler chemischer Elemente von verschiedenen Sternen berücksichtigt. Das neue Modell erlaubt also zum einen eine detailliertere Betrachtung der chemischen Entstehung von Galaxien und zum anderen macht es den Vergleich einer größeren Bandbreite von Beobachtungsdaten möglich. In Kapitel 5 erläutere ich schließlich, dass das neue Modell gleichzeitig die chemischen Eigenschaften reproduzieren kann, die an folgenden Stellen beobachtet werden: a) im Gas lokaler, sternbildender Galaxien. b) in den Photosphären von G-Zwergen auf der Milchstraßen . c) den integrierten Sternpopulationen elliptischer Galaxien in der Nachbarschaft. Hinzu kommt, dass es das Modell ermöglicht, all dies zu tun, ohne dabei vom Standardrahmen abzuweichen, den unser kanonisches Verständnis der Galaxienentwicklung bildet. Diese bedeutende Errungenschaft macht es uns jetzt möglich, GCE in einem wesentlich umfassenderen Rahmen zu betrachten.

# Summary

The chemical compositions of the stars and gas in galaxies play a significant role in all their key evolutionary processes, from gas cooling, through star formation, to the production of new heavy elements that are released back into the gas as stars die in supernova explosions. A theoretical explanation of the production of elements heavier than helium (known simply as ‘metals’ in astrophysics) in stars and its distribution throughout galaxies has been developing since the first postulation of stellar nucleosynthesis in the 1920s. However, there are still a number of unanswered questions in the field of galactic chemical evolution (GCE). For example, what is the most accurate way to measure the metallicities in galaxies? What are the relative contributions to GCE from different types of stars? How is this metal-rich material circulated throughout the various components of a galaxy? And how can we explain the seemingly incompatible chemical properties observed in different galaxies in the local Universe? This thesis provides an investigation into the chemical enrichment of galaxies, by utilising both observations of nearby galaxies and sophisticated GCE models within a semi-analytic model of galaxy evolution. Its core aims are a) to better quantify the chemical properties seen in low-redshift galaxies and explain their likely causes, and b) to develop an improved GCE model that can simultaneously reproduce the diverse chemical properties seen in different types of galaxies in the local Universe.

With these aims in mind, Chapter 1 outlines the key background knowledge required for such an investigation. It discusses the different methods used for measuring the metallicity of real galaxies, and their various shortcomings. It also describes simple, analytic GCE models, and the sophisticated semi-analytic model, L-GALAXIES, that is used to simulate galaxy evolution in detail. In Chapters 2 and 3, I provide an investigation into the relation between stellar mass ( $M_*$ ), star formation rate (SFR), and gas-phase metallicity ( $Z_g$ ) in galaxies. It is shown that the L-GALAXIES model reproduces the *positive* correlation between SFR and  $Z_g$  in massive galaxies that is seen when using sophisticated, theoretical metallicity diagnostics. This lends support to the use of such diagnostics over simpler, emission-line ratios. It is further

shown that, in the semi-analytic model, this SFR- $Z_g$  correlation is due to the gradual dilution of the gas in low-SFR, elliptical galaxies, after a gas-rich merger event. A number of signatures of this particular evolution can be seen in these model galaxies at redshift zero, including low gas fractions and low values of  $Z_g-Z_*$ . Crucially, all of these properties are also seen in nearby elliptical galaxies in the Sloan Digital Sky Survey (SDSS), providing indirect evidence that such an evolutionary process is also occurring in the elliptical galaxy population in the real Universe.

In Chapter 4, I present a new, sophisticated GCE model implemented into L-GALAXIES, that significantly improves on the previous scheme. It does this by accounting for the delayed enrichment of many chemical elements from stars, of various initial masses and metallicities, via stellar winds and supernovae. This new scheme enables a much more detailed study of the chemical evolution of galaxies, and enables a comparison with a larger range of observational data. In Chapter 5, I demonstrate that this new model is able to simultaneously reproduce the chemical properties observed in a) the gas of local, star-forming galaxies, b) the photospheres of G dwarfs in the Milky Way disc, and c) the integrated stellar populations of nearby elliptical galaxies. Furthermore, the model is able to do this without any significant deviation from the standard framework of galaxy formation in the canonical paradigm of hierarchical structure formation. This can be seen as a significant achievement, which has allowed us to form a much more comprehensive view of GCE than was possible before.

**To Charlie, and in memory of Cyril Hutchins**



# Chapter 1

## Introduction

*“... there are those youthful and enthusiastic, but totally irresponsible cosmologists and theoretical physicists who build imaginary universes which are neither of any scientific nor of any artistic value.”*

**Fritz Zwicky**

Fritz Zwicky’s quotation, from the introduction of his book, ‘Morphological Astronomy’, is a stark reminder of the narrow path that theoretical astrophysicists have to tread between radical new ideas and physical reality. His comment was likely directed to contemporary cosmologists who were developing models of the large-scale structure of the Universe in conflict with the observational evidence of the time. However, his sentiment is no less important for the galaxy formation modellers of today, not least those interested in galactic chemical evolution. Although we have a good, general understanding of how all elements heavier than helium (known as ‘metals’ in astrophysics) are forged in the furnaces of stars and during supernova explosions, we are less certain of the details of these processes and their consequences on the evolution of galaxies. In this thesis, I hope to further that understanding, by offering a study of the chemical properties of galaxies in the local Universe, as seen in both observations and semi-analytic models. In so doing, I hope to tread on the right side of Prof. Zwicky’s criticism, while also taking the conclusions drawn as far as possible.

## 1.1 Metallicities in galaxies

I begin by describing the various observables that are commonly used as synonyms for ‘metallicity’,  $Z$ , in the literature. These can be quite different from each other; for example, oxygen abundance measured from emission lines is often used when studying ionised-hydrogen (HII) regions in the ISM of galaxies, whereas iron abundance from absorption lines is commonly chosen when analysing the spectra of stars or stellar populations. Also, some metrics assume a normalisation to the solar metallicity, whereas others do not, with the former being very dependent of the particular solar data chosen. It is therefore important to first decipher what actually constitutes metallicity in any given study, before comparisons can be made.

### 1.1.1 Total metallicity

The most straightforward way to quantify the metallicity of an astrophysical object is to simply write the ratio of the mass in metals to its total baryonic mass:

$$Z = \frac{M_Z}{M_b} \equiv \frac{\sum_{i=2}^N M_i}{\sum_{i=0}^N M_i} , \quad (1.1)$$

where  $i$  iterates over the complete set of  $N$  chemical element species, from hydrogen ( $i = 0$ ) onward. This is often the scale used in galaxy formation models, where the total mass of metals is known by construction. However, such a quantity is much more difficult to obtain from observations, as not all of the heavy elements present in the region of interest can be (simultaneously) observed. Therefore, a single *element abundance* is often used as a proxy for the total metallicity.

### 1.1.2 Oxygen abundance

The most common proxy for metallicity in studies of the gaseous regions within galaxies is the oxygen abundance,  $\log(\epsilon_O)$ . This is given by the ratio of the number density of oxygen atoms ( $n_O$ ) to the number density of hydrogen atoms ( $n_H$ ), and is usually scaled to a hydrogen abundance of  $\log(\epsilon_H) = 12.0$  as follows:

$$\log(\epsilon_O) = 12 + \log(\text{O}/\text{H}) \equiv 12 + \log(n_O/n_H) . \quad (1.2)$$

If required, a conversion to a mass ratio can be made by multiplying the argument of the logarithm by the ratio of the atomic weights,  $A_O/A_H \sim 15.87$ . As oxygen is the most abundant heavy element in the cosmos (accounting for almost half the total

metallicity in the Sun, by mass), it is normally a close approximation to the total metallicity, or at least to  $Z/X$ , where  $X$  is the mass fraction of hydrogen.

There are many different ways in which the oxygen abundance in the gas of galaxies can be measured, and estimations from different diagnostics can differ from each other substantially (e.g. Kewley & Ellison 2008). This is often due to a) probing different ionisation zones within the HII region(s) observed, b) intrinsic biases in different diagnostics, or c) outright misuse of certain indicators. In Section 1.2, I discuss the principle methods used to determine  $\log(\epsilon_{\text{O}})$ , along with an analysis of their particular strengths and weaknesses.

It is worthwhile noting here that the abundance of oxygen in the solar photosphere has undergone many revisions over the last three decades. In that time, the best estimate has dropped significantly from  $\log(\epsilon_{\text{O},\odot}) = 8.93$  (Anders & Grevesse, 1989) to 8.69 (Asplund et al., 2009). Unsurprisingly, this has coincided with a significant decrease in the estimated total solar metallicity, from  $Z_{\odot} = 0.020$  (Anders & Grevesse, 1989) to 0.0134 (Asplund et al., 2009). The main causes for these revisions have been a) improvements to the atmospheric modelling that allows abundances to be inferred from observed absorption line spectra, b) the incorporation of additional lines into the analysis, and c) more precise de-blending of overlapping lines, such as the [OI] and Ni I lines around 630 nm (Allende Prieto et al., 2001). However, there is still no clear consensus among the solar-abundance community as to the true value of the solar oxygen abundance. For a recent, concise review, see section 2.1.2 of Stasińska et al. 2012. Although this uncertainty should not affect oxygen abundances measured using non-solar-normalised metrics such as that given by Eqn. 1.2, it is important to bear in mind when comparing the enrichment of extra-galactic regions to that of the Sun, or when calculating solar-normalised metallicities such as those described below.

### 1.1.3 Iron abundance

Although oxygen is the most abundant heavy element in most astrophysical regions, including the atmospheres of stars, stellar astrophysicists tend to prefer the iron abundance as a proxy for the photospheric metallicity. This is because heavier elements, such as iron, play a larger role in the structure and evolution of a star, as they provide the dominant source of opacity to escaping photons. Iron lines are also relatively prominent in the spectra of the Sun, as well as of the integrated stellar populations in other galaxies. Iron also presents the strongest spectral lines in the soft ( $\lambda \gtrsim 0.1$  nm) X-ray regime, so is often used to infer the metallicity in studies of the hot, X-ray-emitting gas in the intracluster medium (ICM) of galaxy clusters.

The iron abundance is commonly quoted in units of the solar iron abundance as

$$[\text{Fe}/\text{H}] = \log \left( \frac{n_{\text{Fe}}}{n_{\text{H}}} \right) - \log \left( \frac{n_{\text{Fe},\odot}}{n_{\text{H},\odot}} \right) . \quad (1.3)$$

This measure is therefore dependent on the solar composition assumed, as indicated by the square brackets. The measured solar iron abundance has not changed as drastically as that of oxygen, with variations from  $\log(\epsilon_{\text{Fe},\odot}) = 7.67$  (Anders & Grevesse, 1989) to 7.47 (Lodders, 2003) over the years.<sup>1</sup> However, this discrepancy still needs to be accounted for when comparing data that assume different solar compositions (see Chapter 5).

#### 1.1.4 Alpha enhancement

Alpha elements are those chemical elements predominantly formed via fusion with a helium nucleus. Their most abundant isotopes therefore have nucleon numbers that are multiples of four (i.e. O, Ne, Mg, Si, S, Ar, Ca, and Ti). Although the  $\alpha$  enhancement,  $[\alpha/\text{Fe}]$ , is *not* a measure of metallicity, it is an important and related quantity. This is because  $[\alpha/\text{Fe}]$  is known to anti-correlate with  $Z$  in the photospheres of stars. In theoretical chemical evolution models, this is interpreted as being caused by the early enrichment of SNe-II, which produce predominantly  $\alpha$  elements, followed by subsequent enrichment by SNe-Ia, which produce predominantly Fe. In the absence of other modifying factors, this implies that  $[\alpha/\text{Fe}]$  can be used as a ‘galactic clock’, telling us how quickly a galaxy grew. Galaxies with high  $\alpha$  enhancement should have formed their stars *rapidly*, before the iron from SNe-Ia could pollute the star-forming gas. Galaxies with low  $\alpha$  enhancement, should have formed their stars over an *extended period*, with the youngest stars containing larger amounts of SNe-Ia-produced iron. The success of this theoretical framework at reproducing the observed chemical compositions of galaxies is discussed in Chapter 5.

Oxygen is often used as a proxy for the full compliment of  $\alpha$  elements in a stellar atmosphere. Therefore, the  $\alpha$  enhancement can be well approximated by

$$[\alpha/\text{Fe}] \approx [\text{O}/\text{Fe}] = \log \left( \frac{n_{\text{O}}}{n_{\text{Fe}}} \right) - \log \left( \frac{n_{\text{O},\odot}}{n_{\text{Fe},\odot}} \right) . \quad (1.4)$$

---

<sup>1</sup>Note that Anders & Grevesse (1989) also found  $\log(\epsilon_{\text{Fe},\odot}) = 7.51$  from meteoritic measurements, closer to present-day values estimated from the solar photosphere

## 1.2 Measuring the gas-phase oxygen abundance

The oxygen abundance in extra-galactic regions is determined via observed quantities that correlate with it in some way. This usually involves measurements of the flux from emission lines produced by excited atoms in the HII regions where star formation occurs. The total abundance of an element is given by the sum of the abundances of each ionisation state present. To a good approximation, this is  $O/H = O^+/H^+ + O^{++}/H^+$  for oxygen, so an indication of only two ionic abundances is needed (Stasińska, Schaerer & Leitherer, 2002). The  $O^{++}/H^+$  abundance is determined by the ratio of the intensities of a collisionally-excited forbidden line, such as  $[OIII]\lambda 5007$ , to that of the hydrogen recombination line  $H\beta$ :

$$O^{++}/H^+ = \frac{[OIII]\lambda 5007/H\beta}{j_{[OIII]}(T_e, n_e)/j_{H\beta}(T_e, n_e)} . \quad (1.5)$$

Note that, for a direct measurement of this ratio, an indication of the electron temperature,  $T_e$ , and electron density,  $n_e$ , are also required, in order to calculate the emission coefficients,  $j_\lambda$  (see Section 1.2.1). The  $O^+/H^+$  abundance can either be similarly determined or inferred via an estimate of its ionisation correction factor (icf) from photoionisation models. Below is a description of the key methods used to infer the gas-phase oxygen abundance, along with some indication of when these methods are, *and are not*, suitable.

### 1.2.1 The $T_e$ method

As mentioned above, one can directly determine the emission coefficients in Eqn. 1.5 via measurements of  $T_e$  and  $n_e$ . The electron temperature in an astrophysical (i.e. low density) gas is rather strongly anti-correlated with its metallicity. This is because a greater number of metal atoms implies a greater opportunity for radiative cooling. Such metal-line cooling occurs through the collisional excitation (and subsequent de-excitation plus photon emission) of metal atoms by photoelectrons, which have previously been ionised by radiation from nearby stars. The emitted photons are able to propagate out of the region, and can be detected by telescopes to infer the physical properties of the ionised gas. The higher the energy of the detected photons, the greater the kinetic energy (temperature) of the electrons that caused the initial excitation. Therefore,  $T_e$  can be measured from the relative strength of a higher excitation line to a lower excitation line of the same ion. For example, a popular choice is

$$T_e(\text{O}^{++}) \propto \frac{[\text{OIII}]\lambda 4363}{[\text{OIII}]\lambda 5007} \quad , \quad (1.6)$$

which uses two doubly-ionised oxygen forbidden lines found in the rest-frame optical part of the spectrum. For a full, empirically-motivated equation linking these oxygen line fluxes to  $T_e$ , see e.g. Aller (1984). This can be combined with a single measurement of the electron density (assuming it is constant across the nebula), via, for example,

$$n_e \propto \frac{[\text{SII}]\lambda 6731}{[\text{SII}]\lambda 6717} \quad , \quad (1.7)$$

to obtain a unique estimate of the emission coefficients for  $[\text{OIII}]$  and  $\text{H}\beta$  (Osterbrock, 1989). If this  $[\text{SII}]$  ratio is not available, a density of  $100 \leq n_e [\text{cm}^{-3}] < 400$  can normally be assumed for low-redshift, star-forming galaxies.

The electron temperature in the  $\text{O}^+$  zone can either be determined directly from  $[\text{OII}]$  lines, such as  $[\text{OII}]\lambda 7320/[\text{OII}]\lambda 3726$ , or inferred from fits to the  $T_e(\text{O}^{++})-T_e(\text{O}^+)$  relation from photoionisation models or empirical studies. However, these relations are at variance with recent electron-temperature measurements in nearby, extragalactic HII regions (e.g. Pilyugin et al. 2010; Andrews & Martini 2012). Once  $T_e(\text{O}^+)$ ,  $T_e(\text{O}^{++})$ ,  $n_e$ ,  $[\text{OIII}]\lambda 5007$ , and  $\text{H}\beta$  are determined, the total oxygen abundance can be estimated.

Although the  $T_e$  method is often considered the most precise way of obtaining  $\log(\epsilon_{\text{O}})$ , it does require measurements of a large number of emission line fluxes. It is also vulnerable to two key problems when applied outside of low-redshift, low-metallicity HII regions:

- *Weak lines:* The preferred  $[\text{OIII}]\lambda 4363$  line is very weak, especially at high-metallicity (due to the presence of fewer photoelectrons energetic enough to excite such upper levels) but also in low-metallicity regions, unless very high signal-to-noise (SNR) spectra are available (e.g. Garnett et al. 2004). Therefore, alternative  $T_e$  indicators, such as  $[\text{NII}]\lambda 5755/[\text{NII}]\lambda 6584$  can be used. However, this ratio probes a different ionisation zone and is further removed from the actual *oxygen* abundance.
- *Temperature fluctuations:* Even if the the  $[\text{OIII}]\lambda 4363$  line is detected in a high- $Z$  region, the  $T_e$  method is likely to underestimate the true oxygen abundance by up to 0.4 dex, if spatial temperature fluctuations are present within the HII regions (e.g. Stasińska 1978a, 2005). This is because the emission from doubly-ionised oxygen ions will be dominated by the hotter parts of the  $\text{O}^{++}$

zone. Therefore, the temperature measured from the line ratio will be greater than the average temperature across the whole zone [i.e.  $T_e([\text{OIII}]) > T_e(\text{O}^{++})$ ], providing a *lower* estimate of the  $\text{O}^{++}$  abundance. Temperature fluctuations can form in high- $Z$  HII regions when far-infrared (IR) oxygen lines begin to dominate the nebula cooling: The cooling rates due to line emission at 52 and  $88\mu\text{m}$  remain high, even at low temperatures, causing  $T_e$  to drop more rapidly than in other zones within the HII region (Stasińska, 2002).

In addition to this, the fraction of oxygen that is in the  $\text{O}^{++}$  state will be lower in high-metallicity (low-temperature) regions, so a smaller amount of the *total* oxygen abundance will be probed by  $T_e(\text{O}^{++})$ .

In dealing with temperature fluctuations, one could incorporate lower-energy oxygen lines from the far-IR regime into the analysis. These are less sensitive to temperature fluctuations than the optical lines (e.g. Croxall et al. 2013). However, in the absence of both optical and far-IR spectroscopy, alternative methods should be used when  $\log(\epsilon_{\text{O}}) \gtrsim 8.6$ .

### 1.2.2 The Empirical method

In the absence of a reliable measure of the electron temperature, the oxygen abundance can be determined indirectly from emission line ratios of different species. These ratios are calibrated to metallicities from galactic HII regions or nearby galaxies for which the  $T_e$  method is possible, or to metallicities derived from synthetic spectra (the theoretical method, see below). Such *strong-line-ratio diagnostics* are famous for providing gas-phase metallicities for galaxies that can differ by up to  $\sim 0.7$  dex for the same object (Kewley & Ellison, 2008), so careful analysis of their advantages and disadvantages needs to be made before a particular diagnostic is chosen.

However, one can seldom freely choose which strong-line-ratio diagnostic to use. Instead, one must rely on the emission lines available given the object's redshift and the spectrograph's wavelength range. Nonetheless, one should also always be confident that the object in question shares similar properties (e.g. ionisation parameter, temperature, and gas density) to the HII regions used for the calibration. This is often not the case when the object differs in metallicity or redshift from the calibration sample (e.g. Yates, Kauffmann & Guo 2012; Cullen et al. 2013).

### The $R_{23}$ diagnostic

With the above in mind, an obvious and popular choice is to use the ratio of collisionally-excited oxygen lines to a hydrogen recombination line, such as

$$R_{23} = ([\text{OII}]\lambda 3727 + [\text{OIII}]\lambda\lambda 4959, 5007)/\text{H}\beta \quad , \quad (1.8)$$

which was first calibrated by (Pagel et al., 1979).<sup>2</sup> However, this common diagnostic suffers from three main drawbacks:

- *Degeneracy*: The  $R_{23}$  diagnostic inevitably provides two possible oxygen abundances for the same value of Eqn. 1.8. At low metallicities (high temperatures),  $R_{23}$  positively correlates with metallicity, because an increase in oxygen abundance leads to a proportional increase in the flux of the [OII] and [OIII] lines. However, above some ionisation-parameter-dependent metallicity [around  $\log(\epsilon_{\text{O}}) = 8.2$ ], the two begin to anti-correlate, as the gas becomes so cool that free electrons don't have enough energy to easily excite these oxygen lines. Cooling still continues at greater oxygen abundances due to emission of IR fine-structure lines, but this is no longer traced by the strength of the optical [OII] and [OIII] lines. Such degeneracies are present for all strong-line diagnostics that use a ratio of forbidden to recombination lines. In this case, a secondary diagnostic is required that is not degenerate, so that an initial guess can be made as to whether an object lies on the upper or lower branch of the  $R_{23}$ - $\log(\epsilon_{\text{O}})$  relation. However, at metallicities close to the turning point around  $\log(\epsilon_{\text{O}}) = 8.2$ , the derived metallicity is always sensitive to errors in the measurement of  $R_{23}$ .
- *Dependence on ionisation parameter*: The ionisation parameter,  $q$ , is the ratio of the hydrogen-ionising flux per unit area to the number density of hydrogen atoms in the HII region,

$$q = \frac{S(\text{H}^0)}{n_{\text{H}}} \text{ cm s}^{-1}. \quad (1.9)$$

This parameter tells us how easily an ionising front can propagate through the gas.  $R_{23}$ , like many strong-line diagnostics, is known to be sensitive to  $q$  because the ion fluxes in the numerator and denominator of Eqn. 1.8 have quite different ionisation energies (e.g. Kewley & Dopita 2002). The ionisation

---

<sup>2</sup>For low SNR spectra, where the [OIII] $\lambda$ 4959 is difficult measure, the factor 3.1[OIII] $\lambda$ 5007 is often used as a proxy for the combined flux of the two doubly-ionised oxygen lines.

parameter can be determined and accounted for by measuring the ratio of emission from two different ionisation states of the same element. A good choice, if available, is

$$q \propto \frac{[\text{SIII}]\lambda\lambda 9069, 9532}{[\text{SII}]\lambda\lambda 6717, 6731} . \quad (1.10)$$

This ratio is relatively insensitive to metallicity, because all the lines used have relatively low energies, meaning they can still be easily excited at high metallicities where  $T_e$  is lower. In the absence of these sulphur lines, a more metallicity-dependent ionisation indicator has to be used, such as  $[\text{OIII}]\lambda 5007 / [\text{OII}]\lambda\lambda 3726, 3729$ .

- *Dust attenuation*: Careful corrections to the line fluxes due to internal dust attenuation need to be made when the the lines in the numerator and denominator are not of similar wavelengths. Dust corrections are usually made assuming an attenuation curve,  $A_\lambda/A_V$ , within the optical regime (e.g. Cardelli et al. 1989; Calzetti 1994).<sup>3</sup> This allows us to determine the optical depth in the line in question. First, the total internal dust attenuation in the optical V-band is calculated from the ratio of the observed  $\text{H}\alpha$  ( $\lambda 6563$ ) flux to  $\text{H}\beta$  ( $\lambda 4861$ ) flux, otherwise known as the Balmer decrement,  $B = S_{\text{obs}}(\text{H}\alpha)/S_{\text{obs}}(\text{H}\beta)$ :

$$A_V = -2.5 \log \left( \frac{B}{B_{\text{in}}} \right) \cdot \frac{k_V}{k_{\text{H}\alpha} - k_{\text{H}\beta}} . \quad (1.11)$$

The  $k$ -values represent the ratio of the extinction at a given wavelength to the intrinsic colour excess in the B-band relative to the V-band,  $k_\lambda = A_\lambda/E(B-V)_i$  (Calzetti, 1994). Calzetti (2001) quote these values as  $k_V = 3.10$ ,  $k_{\text{H}\alpha} = 2.468$ , and  $k_{\text{H}\beta} = 3.631$ .  $B_{\text{in}} \equiv j_{\text{H}\alpha}/j_{\text{H}\beta}$  is the intrinsic Balmer decrement, that would be expected in the absence of any dust attenuation. As with other emission-coefficient ratios, this can be obtained given estimates of both  $T_e$  and  $n_e$ . For large, extra-galactic HII regions, where not all photons can escape the region unabsorbed (i.e. with relatively large optical depths), case B recombination and  $T_e = 10^4\text{K}$  are reasonable assumptions. This implies an intrinsic Balmer

---

<sup>3</sup>We note here that, as pointed out by Calzetti (2001), there is a difference between dust *attenuation* due to absorption and scattering by the dust particles in the HII region containing the ionising sources, and dust *extinction* due to foreground dust particles at a distance from the ionising sources. Internal attenuation can increase the strength of a line, due to an additional contribution from photons scattered *into* the line of sight. This is not the case for foreground extinction.

decrement of between 2.81 and 2.88, depending on the electron density in the gas (Osterbrock, 1989).

The mean attenuation can be independently obtained from a fit to that observed in the Milky Way or nearby starburst galaxies,  $\langle A_\lambda/A_V \rangle = a(\lambda) + b(\lambda)/k_V$ , where, for example,

$$a = 1.0 + 0.17699 y - 0.50447 y^2 - 0.02427 y^3 + 0.72085 y^4 + 0.01979 y^5 - 0.77530 y^6 + 0.32999 y^7 \quad (1.12)$$

$$b = 1.41338 y + 2.28305 y^2 + 1.07233 y^3 - 5.38434 y^4 - 0.62251 y^5 + 5.30260 y^6 - 2.09002 y^7 \quad (1.13)$$

$$y = (1/\lambda) - 1.82 \quad (1.14)$$

are the parameters for the fit from Cardelli et al. (1989). The attenuation at the wavelength of the line can then be straightforwardly calculated from  $A_\lambda = \langle A_\lambda/A_V \rangle \cdot A_V$ , and the optical depth from  $\tau_\lambda = A_\lambda/1.086$ . The line flux can then be corrected to  $S_{\text{cor}}(\lambda) = S_{\text{obs}}(\lambda) e^{+\tau_\lambda}$ .

### The $N2$ diagnostic

A tempting alternative diagnostic to  $R_{23}$  is

$$N2 = [\text{NII}]\lambda 6584/\text{H}\alpha \quad , \quad (1.15)$$

which includes the ratio of two prominent emission lines, is not degenerate below  $\log(\epsilon_O) \sim 9.1$ , and does not require a dust correction as both lines are of similar wavelength.  $N2$  is often used at higher redshifts or higher metallicities, when the  $[\text{OIII}]\lambda 4363$  line is too weak for the  $T_e$  method. However, it too suffers from a number of vulnerabilities:

- *Dependence on ionisation parameter:* Because the ionisation states of  $\text{N}^+$  and  $\text{H I}$  have quite different ionisation energies,  $N2$  is also sensitive to  $q$ . In fact, the  $q$ -dependence of  $N2$  is greater than that of  $R_{23}$ . Kewley & Dopita (2002) estimate a difference in the derived oxygen abundance from  $N2$  of  $\sim 0.9$  dex for a range of ionisation parameters from  $q = 5 \times 10^6 \text{ cm s}^{-1}$  to  $3 \times 10^8 \text{ cm s}^{-1}$ . This dependence needs to be accounted for through a measurement of the ionisation parameter, as explained above.

- *Saturation*: At electron temperatures corresponding to  $\log(\epsilon_O) \sim 8.7$ , nitrogen becomes the dominant coolant in the gas. Therefore, at lower temperatures than this, the  $N2$  diagnostic can saturate, and will not yield a higher value for the metallicity, even if one is present in the region. This intrinsic bias can be clearly seen in the shape of the mass-metallicity relation of galaxies when using the  $N2$  diagnostic, at both low redshift (e.g. Liang et al. 2006; Kewley & Ellison 2008) and even high redshift (e.g. Erb et al. 2006a; Reddy et al. 2010). Therefore,  $N2$  should not be used for objects with  $\log(\epsilon_O) \gtrsim 8.7$  (i.e. a significant fraction of the galaxies in the local Universe).
- *Shock excitation and AGN*: The  $N2$  diagnostic is also particularly sensitive to the presence of shocks in the gas, caused by, for example, supernova blast waves or stellar winds. Such shocks can excite metal atoms in HII regions in addition to the expected collisional excitation. Contamination from bright accretion discs around central, super-massive black holes (SMBHs) in active galactic nuclei (AGN) will also affect  $N2$ . Such additional effects can cause an increase in the  $[NII]/H\alpha$  ratio and consequently an overestimate of the oxygen abundance. Spectra should be tested for contamination by shock excitation by comparing the amplitudes of different strong-line ratios. The  $([NII]/H\beta)$ - $([OIII]/H\beta)$  relation (or BPT diagram, Baldwin, Phillips & Terlevich 1981) is often used to identify such galaxies. These objects should be removed from the sample, or if spatially-resolved spectroscopic data is available, the contribution from shocks should be quantified and removed (e.g. Rich, Kewley & Dopita 2014).
- *N-O discrepancy*: It should be kept in mind that  $[NII]/H\alpha$  is really tracing the *nitrogen* abundance in the gas. Although the nitrogen and oxygen abundances are expected to follow each other in low-metallicity regions, it is by no means a tight correlation (see Liang et al. 2006, fig. 2). This is because the interstellar medium (ISM) is enriched with nitrogen by the stellar winds of long-lived AGB stars, in addition to the SNe-II of short-lived stars. Therefore, the nitrogen abundance is more sensitive to the long-term star formation history of a galaxy than the oxygen abundance. At higher metallicities, the calibration of nitrogen diagnostics to the oxygen abundance also requires careful modelling of the secondary production of nitrogen in stars that already contain an abundance of carbon and oxygen at their birth. Secondary nitrogen production dominates when  $\log(\epsilon_O) \gtrsim 9.0$ , as can be seen by the steady increase in the N/O ratio with increasing O/H (see below).

### The N2O2 diagnostic

Given the problems discussed above for  $R_{23}$  and  $N2$ , a promising strong-line diagnostic to use is

$$N2O2 = [\text{NII}]\lambda 6584 / [\text{OII}]\lambda\lambda 3726, 3729 . \quad (1.16)$$

$N2O2$  is a) not as sensitive to  $q$ , due to the similar ionisation energies of the ions involved, b) does not use lines which require correction for absorption in the photospheres of the ionising stars, and c) shows a strong correlation with oxygen abundance at high metallicity. This last attribute is due to two reasons. Firstly, the higher-excitation oxygen lines become weaker at a higher temperature than the nitrogen line, causing an increase in  $[\text{NII}]/\text{O}[\text{II}]$  above  $\log(\epsilon_{\text{O}}) \sim 8.7$ . Secondly, the dominant secondary nitrogen production in metal-rich stars above  $\log(\epsilon_{\text{O}}) \sim 9.0$  also causes and increase in the ratio. The  $O3N2$  diagnostic is another good choice for the same reasons (Pettini & Pagel, 2004).

However,  $N2O2$  does have to be carefully corrected for dust attenuation, as it comprises lines at opposite ends of the visible spectrum. Kewley & Dopita (2002) have found that assigning a random reddening to the line fluxes causes the scatter in the estimated oxygen abundance to increase, as well as a systematic shift to higher metallicities of  $\sim 0.5$  dex. Therefore, additional measurements of the  $\text{H}\alpha$  and  $\text{H}\beta$  lines are important, in order to derive realistic dust corrections from the Balmer decrement, as described above.

### 1.2.3 The Theoretical method

The state-of-the-art in combined photoionisation and stellar population synthesis (SPS) modelling is improving. This makes it now possible to determine the metallicities in the integrated HII regions of galaxies by comparing their observed spectra to the synthetic spectra provided by such models. An example of this is the Bayesian technique of Brinchmann et al. (2004) and Tremonti et al. (2004), who obtained estimates of the star formation rates (SFRs) and oxygen abundances for a large sample of spectroscopically-observed nearby galaxies from the Sloan Digital Sky Survey data release 7 (SDSS-DR7). Their technique follows Charlot & Longhetti (2001) by combining the CLOUDY photoionisation models of Ferland (1996) and Ferland et al. (1998) with the SPS models of Bruzual & Charlot (2003). This provides synthetic spectra for varying effective metallicity, local ionisation parameter ( $U = q/4\pi R_s^2 c$ , representing the ratio of mean photon density to electron density, where  $R_s$  is the dust-free Strömngren radius), dust attenuation in the V-band, and dust-to-metal ratio

within the HII regions. These spectra can then be compared to a set of observed strong emission lines from nearby galaxies, and a likelihood distribution obtained which provides estimates (and their errors) for key galaxy parameters.

As with the simpler strong-line diagnostics discussed above, one should always be confident that the calibration sample (in this case, the properties and structure of the gas assumed in the theoretical model) is comparable to the actual objects observed, before trusting metallicities provided by the theoretical method. Additionally there have been concerns about the treatment of secondary nitrogen production in the SPS models used (e.g. Liang et al. 2006; Yin et al. 2007). The assumed monotonic trend in nitrogen enrichment with metallicity in the Charlot & Longhetti (2001) model is unlikely to fully represent the complex SFH dependence of N/O in real galaxies. However, it is difficult to determine whether the offsets between theoretically-derived oxygen abundances and those obtained from the  $T_e$  or empirical methods are due to inaccurate spectral modelling (e.g. Kennicutt et al. 2003; Yin et al. 2007), or the numerous biases in the simpler methods mentioned above (or both).

In Chapter 2, we argue that the theoretical method described here currently provides the most precise estimates of the gas-phase oxygen abundance in local, high-metallicity galaxies with good quality spectra. It is likely that future improvements to the modelling of the integrated emission from galaxies will strengthen this claim.

### 1.2.4 Implications for the mass-metallicity relation

The discussion provided above attempts to highlight the current difficulty in obtaining accurate gas-phase metallicities for galaxies. The uncertainties involved lead to discrepant interpretations of the relation between galaxy mass and metallicity (the  $M_*$ - $Z_g$  relation) and its higher-dimensional variations, both at low redshift (e.g. Kewley & Ellison 2008; Yates, Kauffmann & Guo 2012) and its evolution to higher redshift (e.g. Erb et al. 2006a; Zahid, Kewley & Bresolin 2011; Moustakas et al. 2011; Wuyts et al. 2012; Cullen et al. 2013).

At low redshift, conversions are provided by Kewley & Ellison (2008), which allow the metallicities derived from one diagnostic to be converted to the scale of any other. However, such conversions only enable a fair comparison of the *relative* metallicity between objects. *Absolute* abundances may still be inaccurate, as intrinsic biases in the chosen reference diagnostic remain. For example, converting the oxygen abundances of a sample of local, metal-rich galaxies measured with a variety of different indicators to that implied by the  $N2$  diagnostic will allow one to determine which galaxy is the *most* metal rich, but all the individual metallicities obtained are likely to be incorrect.

At high redshift, a clear mass-dependent increase in metallicity with cosmic time at fixed stellar mass (often known as ‘chemical downsizing’) has been reported by Maiolino et al. (2008). However, this is less apparent in other studies which utilise different metallicity diagnostics and selection criteria. For example, Erb et al. (2006a) showed that the saturation of the  $N2$  diagnostic above  $\log(\epsilon_O) \sim 8.7$  causes an artificial flattening of the high-mass-end slope of the  $M_*$ - $Z_g$  relation at low-redshift, which mimics a strong chemical downsizing effect between  $z \sim 2$  and zero. In turn, Cullen et al. (2013) have found that changes in the physical conditions of the star-forming gas (particularly  $q$ ) with redshift mean that locally-calibrated strong-line diagnostics are not accurate at  $z \sim 2$ , and that this affects the evolution of the fundamental metallicity relation (FMR, Mannucci et al. 2010, and see Chapter 2). Moustakas et al. (2011) have also found that a more careful sample selection, by a) properly removing AGN hosts, b) ensuring the sample is flux and volume limited, and c) correcting for aperture effects, removes any clear sign of mass-dependent evolution in the  $M_*$ - $Z_g$  relation below  $z \sim 0.75$ . Wuyts et al. (2012) have even found an *inverse* mass dependence in their small sample of 70 lensed galaxies at  $z = 1 - 2$ .

The uncertainties discussed here provide an opportunity for galactic chemical evolution (GCE) models to play a contributory role, by giving an alternative insight into how galaxies produce and distribute their metals throughout the Universe. The basics of GCE modelling are the topic of the next section.

### 1.3 GCE modelling

In Chapter 4 we discuss in detail the sophisticated GCE model used to obtain the results that form the core of this thesis. However, that model is built on simpler, analytical approximations, which we present in this section. These simpler models have been very successful in helping to interpret observations since their conception in the works of Schmidt (1963) and Talbot & Arnett (1971), and it is important to have a good grasp of their concepts before studying more complex chemical evolution models. In this section, I provide a basic introduction to such models and their key results. For a much more rigorous discussion, the celebrated review of Tinsley (1980) is highly recommended.

#### 1.3.1 The closed box

The ‘closed box’ model is the simplest approximation to an evolving galactic system. By construction, the total mass in the box is conserved, by assuming that no material can enter or leave the system. Hence,

$$\frac{dM_{\text{tot}}}{dt} = 0 \quad . \quad (1.17)$$

This model assumes an initial mass of gas,  $M_g = M_{\text{tot}}$ , that is allowed to form stars at a given rate,  $\psi$ . These newly-formed stars instantaneously return a fraction,  $R$ , of their mass to the gas phase. The differential equation governing the evolution of the gas mass is therefore simply given by

$$\frac{dM_g}{dt} = -\psi + R\psi \quad , \quad (1.18)$$

and  $dM_*/dt = -dM_g/dt$ . A fraction,  $y'_Z$ , of the *total* mass of stars formed at time  $t$  is assumed to be instantaneously returned as metals. In a one-zone model, this material is allowed to fully and instantaneously mix with the homogeneous gas component, giving

$$\frac{dM_{Z,g}}{dt} = -Z_g \psi + y'_Z \psi \quad , \quad (1.19)$$

where  $Z_g$  is the total metallicity of the gas, as defined by Eqn. 1.1. In order to distinguish between metals that pass through stars unprocessed and those that are newly-synthesised, an alternative form of the yield is used,  $y_Z$ , which represents the (rather unphysical) ratio of the mass in metals synthesised and released to the *net* mass that remains locked-up in stars. This quantity is related to  $y'_Z$  by

$$y_Z = \frac{y'_Z - Z_g R}{1 - R} \quad . \quad (1.20)$$

In this case, Eqn. 1.19 becomes

$$\frac{dM_{Z,g}}{dt} = -Z_g \psi + Z_g R \psi + y_Z (1 - R) \psi \quad , \quad (1.21)$$

where the second term is the contribution from unprocessed metals, and the third term represents the *effective yield* of newly-synthesised metals. The evolution of the closed-box model over time, assuming a constant SFR of  $\psi = 1 \text{ M}_\odot/\text{yr}$ ,  $R = 0.43$ ,  $y'_Z = 0.03$ , and  $Z_g(t_0) = 0.0$ , is shown by the red lines in Fig. 1.1.

We note here that the effective yield can be derived from Eqn. 1.21 as follows: Given that  $dM_{Z,g}/dt \equiv d(Z_g M_g)/dt$ , we obtain

$$Z_g \frac{dM_g}{dt} + M_g \frac{dZ_g}{dt} = -Z_g \psi + Z_g R \psi + y_Z (1 - R) \psi \quad . \quad (1.22)$$

Factoring-in Eqn. 1.18 and rearranging gives

$$M_g \frac{dZ_g}{dM_g} = -y_Z . \quad (1.23)$$

Integrating between the limits  $Z_g = [0, Z_g(t)]$  and  $M_g = [M_{\text{tot}}, M_g(t)]$ , and remembering that Eqn. 1.17 holds for a closed box, we obtain

$$y_Z \equiv y_{Z,\text{eff}} = \frac{Z_g}{\ln(1/\mu)} , \quad (1.24)$$

where  $\mu \equiv M_g/M_{\text{tot}}$  is the gas fraction. We therefore see that  $y_{Z,\text{eff}}$  is obtainable observationally from measurements of the gas-phase metallicity and gas fraction. The extent to which a system's measured  $y_{Z,\text{eff}}$  differs from the expected 'true' yield,  $y_{Z,0}$ , gives an indication of the significance of infall or outflows on its chemical evolution (Garnett, 2002). For example, Tremonti et al. (2004) have shown that low-mass, star-forming galaxies in the SDSS have significantly lower effective yields than the maximum yield obtained from the whole sample (assumed analogous to  $y_{Z,0}$ ), suggesting that metal loss through galactic winds is an important process in galaxies residing in small potential wells. However, note that Eqn. 1.24 only holds for *primary element* abundances (such as oxygen), whose yield does not depend on the initial metallicity of the star.

Aside from the over-simplifications of the instantaneous recycling approximation (IRA) and instantaneous mixing approximation (IMA), the closed-box model suffers from another significant weakness, known as the 'G-dwarf problem' (van den Bergh, 1962). This states that the metallicity distribution function (MDF) of the stellar component in a closed-box system contains too many low- $Z_*$  stars compared to the observed MDF of (long-lived) G-dwarf stars in the solar neighbourhood. This is mainly because too high a fraction of stars are formed at very early times when  $Z_g$  is low. The gas fraction rapidly decreases in a closed box, preventing significant star formation at later times, when  $Z_g$  is higher (for more details, see Tinsley 1980, section 4.2). One solution to this problem is to allow infall of fresh gas onto the system after  $t = 0$ , and so extend the length of star formation (see Fig. 1.1). An example of this is the 'accreting box' model described in Section 1.3.3.

### 1.3.2 The leaky box

Before introducing infall, we first examine the consequences of outflows from the simple system described above. Such a case is known as a 'leaky box', where

$$\frac{dM_{\text{tot}}}{dt} = -\alpha\psi . \quad (1.25)$$

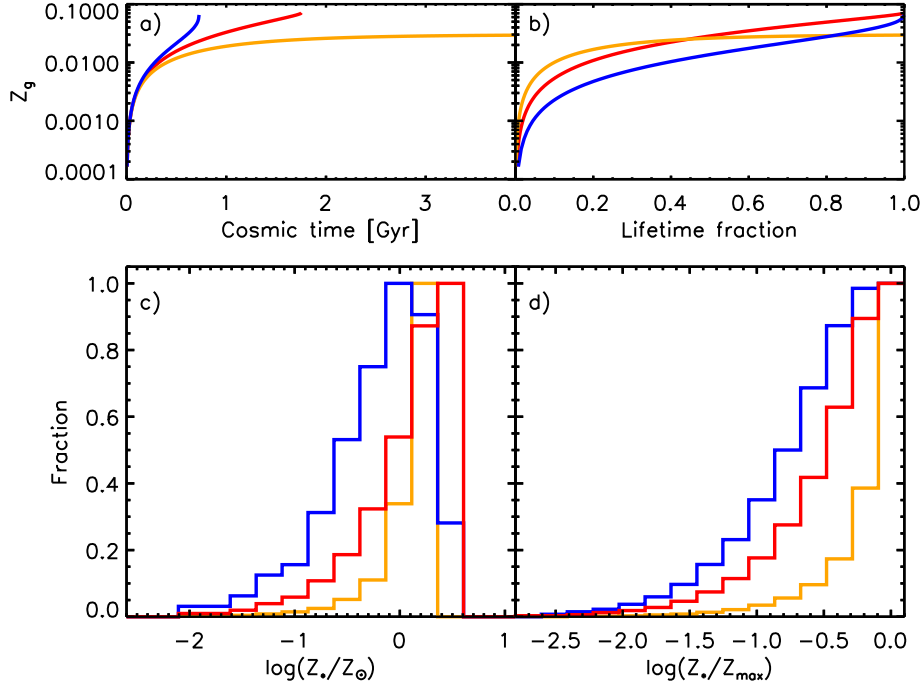


Figure 1.1: Results from a numerical implementation of the closed box (red), leaky box (blue) and accreting box (orange) models described in Section 1.3. For this plot, a constant SFR of  $\psi = 1 M_\odot/\text{yr}$  over 4 Gyr is assumed, with an initial gas mass of  $M_{\text{tot}}(t_0) = 1.0 \times 10^9 M_\odot$ , along with the following parameter values:  $R = 0.43$ ,  $y'_Z = 0.03$ ,  $Z_g(t_0) = 0.0$ ,  $\alpha = 0.8$ ,  $Z_{\text{inf}} = 0.0$ , and  $\beta = (1 - R)\psi$ .

*Panel A:* The evolution of  $Z_g$  with time. *Panel B:* The evolution of  $Z_g$  over the full lifetime of each model, i.e. during the time in which stars are formed (for the accreting box, this is truncated at 4 Gyr). *Panel C:* The MDF for each model after 4 Gyr. Here, the total metallicity is normalised to that measured by Asplund et al. (2009) for the Sun's photosphere,  $Z_\odot = 0.0134$ . *Panel D:* The cumulative MDF for each model, with total metallicity normalised to the maximum metallicity,  $Z_{\max}$ , achieved by each model after 4 Gyr.

The outflow is therefore assumed to be some fraction,  $\alpha$ , of the star formation rate at time  $t$ . Such a model better represents the effect of stellar winds and SN feedback, which are capable of driving gas out of low-mass systems (Larson, 1974). This modifies the key differential equations of the system to the following:

$$\frac{dM_g}{dt} = -\psi + R\psi - \alpha\psi \quad , \quad (1.26)$$

and, when assuming the ejected material has the metallicity of the instantaneously-returned, enriched gas,

$$\frac{dM_{Z,g}}{dt} = -Z_g \psi + y'_Z \psi - \alpha y'_Z \psi \quad (1.27)$$

$$= -Z_g \psi + (1 - \alpha)[Z_g R \psi + y_Z (1 - R) \psi] \quad . \quad (1.28)$$

This approximation is only acceptable when considering metal-rich winds, where the material released by SNe is able to directly escape the galaxy without coupling with the (low-density) ISM. In this case,  $\alpha < R$  must always hold. If we instead assume that the ejecta has the metallicity of the ambient gas, Eqns. 1.27 and 1.28 become

$$\frac{dM_{Z,g}}{dt} = -Z_g \psi + y'_Z \psi - \alpha Z_g \psi \quad (1.29)$$

$$= -(1 + \alpha)Z_g \psi + Z_g R \psi + y_Z (1 - R) \psi \quad . \quad (1.30)$$

The most realistic case is normally somewhere between these two extremes. The evolution of the leaky-box model over time, assuming winds of ambient metallicity and  $\alpha = 0.8$ , is given by the blue lines in Fig. 1.1. We can see that the gas reservoir is used up more quickly than in a closed box model, due to the removal of gas from the system (panel A). This means that there is even less time for more metal-rich stars to form (panel C).

### 1.3.3 The accreting box

Finally, we consider the case where gas is only allowed to flow into the system. This replicates the known accretion of metal-poor gas from the intergalactic medium (IGM) on to galaxies. Here, we have

$$\frac{dM_{\text{tot}}}{dt} = \beta \quad , \quad (1.31)$$

where  $\beta$  is the rate of infall onto the system. Consequently, the evolution of the gas mass is simply described by

$$\frac{dM_g}{dt} = -\psi + R\psi + \beta \quad , \quad (1.32)$$

and the mass of metals by

$$\frac{dM_{Z,g}}{dt} = -Z_g \psi + y'_Z \psi + Z_{\text{inf}} \beta \quad (1.33)$$

$$= -Z_g \psi + Z_g R \psi + y_Z (1 - R) \psi + Z_{\text{inf}} \beta \quad . \quad (1.34)$$

where  $Z_{\text{inf}}$  is the metallicity of the infalling material. The evolution of the accreting-box model over time, assuming  $Z_{\text{inf}} = 0.0$  and the case of ‘extreme infall’, where accretion and mass return are balanced by star formation [i.e.  $\beta = (1 - R)\psi$ ], is given by the orange lines in Fig. 1.1. We can see that the length of star formation is indefinitely extended in this model, because  $M_g$  remains constant, and  $Z_g$  quickly asymptotes towards the value of the yield  $y'_Z = 0.03$  over time (panel A). The accreting-box model therefore contains a much smaller proportion of relatively metal-poor stars than both the closed- and leaky-box models (panel D). More realistic versions of the accreting box, that modify the extreme infall approximation and sometimes include pre-enriched infall, are able to resolve the G-dwarf problem discussed in Section 1.3.1 (see Tinsley 1980, section 4.3).

Analytic models that allow both infall and outflow of gas in the form of a ‘breathing box’ can be easily built, by combining the formalisms described above. Additional considerations can also be included, such as galactic winds of arbitrary metallicity, secondary chemical element production, pre-enrichment, reincorporation of gas in galactic fountains, radially resolved gas and stellar discs (i.e. removing IMA), and mass-dependent stellar lifetimes (i.e. removing IRA). For a recent review, see Matteucci (2012). In the rest of this chapter, I outline a more sophisticated model, that also allows for cosmologically-motivated star formation histories (SFHs); that is, SFHs which depend on the interaction between galaxies and their environments via merging, stripping and stellar disruption. In order to do this self-consistently, a model for the underlying hierarchical structure formation of dark matter (DM) haloes within the canonical  $\Lambda$ CDM cosmology is required. This is the topic of the next section.

## 1.4 N-body simulations of dark matter structure formation

N-body simulations model the collisionless dynamics of a number ( $N$ ) of particles over time. Since dark matter is expected to interact only (or at least predominantly) gravitationally, its formation of non-linear structure offers itself to a numerical treatment in an N-body simulation, where only the gravitational force between each particle needs to be calculated. In practice, this is considerably more difficult than it may seem. Firstly, technological limitations mean that actual DM particles have to be represented by computational point particles or spatial grids with mass resolutions of  $\sim 10^6$  to  $10^9 M_\odot$  (for current cosmological-scale simulations). In the case of point particles, their infinite density means that particle-particle interactions do not behave as they should at close proximities when using the standard Newtonian gravitational force equation, as large-angle scattering events can occur. Therefore, *gravitational softening* is required, so that the gravitational force between two point particles is artificially reduced from the Newtonian approximation by introducing a gravitational softening length,  $l_s$ :

$$\mathbf{F}(\mathbf{r}) = -G \frac{m_i m_j}{(r^2 + l_s^2)^{3/2}} \mathbf{r} \quad , \quad (1.35)$$

where  $m_i$  and  $m_j$  are the masses of the two computational particles in question. The adaptation given by Eqn. 1.35 clearly modifies Newtonian gravity at all length scales. Therefore, an alternative scheme can be used, which assumes an  $l_s$ -dependent density distribution within a kernel. The scale length is often chosen to be between one twentieth and one fiftieth of the mean inter-particle separation (Mo, van den Bosch & White 2010, section C1.1.2), but it can also be made adaptable in both space and time (e.g. Iannuzzi & Dolag 2011).

Secondly, when determining the finite timesteps required in order to numerically integrate the trajectories of computational particles, one has to find a balance between an accurate representation of the dynamics of the system and a realistic computation time, given that such simulations currently include billions of particles, evolved with up to 11,000 timesteps per particle. The very popular GADGET code (Springel et al., 2001b) accounts for this by incorporating distinct timestep widths,  $\Delta t$ , for each particle to vary in time while ensuring that

$$\Delta t = \alpha_{\text{tol}}(\sigma / |\mathbf{a}|) \quad , \quad (1.36)$$

where  $\mathbf{a}$  is the gravitational acceleration, and  $\alpha_{\text{tol}}$  is an assumed tolerance factor, chosen so that the error in the specific kinetic energy of a particle over one timestep

(related to the particle velocity dispersion,  $\sigma$ ) is not too large. This formalism therefore allows for smaller  $\Delta t$  in denser regions. However, this particular method is not fully reversible and still leads to imprecision in the predicted trajectories of particles in the densest regions (Springel, 2005).

Thirdly, the *direct* calculation of the gravitational force exerted by each particle on every other in large cosmological simulations within an acceptable amount of time is also beyond the scope of current computational hardware, as it requires  $N(N + 1)$  calculations per timestep. Therefore, simplifications to this ‘direct summation’ approach are required. For example, in more recent versions of GADGET, a ‘TreePM’ method is implemented, which calculates the short-range and long-range gravitational potential felt by a particle separately (Springel, 2005). For long ranges ( $r \gtrsim 0.5$  per cent of the full simulation box length,  $L$ ), a ‘particle-mesh algorithm’ is used, which calculates the gravitational potential at discrete grid points due to the surrounding mass density using the Poisson equation,

$$\nabla^2 \Phi = 4\pi G \rho \quad . \quad (1.37)$$

The force due to the potential at each grid point is then determined, and the resultant force on a given particle calculated through interpolation. For short ranges ( $r \lesssim 0.005 L$ ), a ‘tree algorithm’ is used, which essentially calculates the residual gravitational force on a particle due to nearby particles grouped into zones whose spatial sizes decrease with decreasing radial distance. Such methods require only  $\mathcal{O}(N \log N)$  calculations per timestep, and so allow reasonable precision at both long and short ranges for less computational cost than the ideal direct-summation method.

Despite these imperfections, N-body simulations still provide the best insight we currently have on the dynamics of dark matter, which we believe constitutes  $\sim 26$  per cent of the energy density in the Universe (Planck Collaboration XVI, 2013). In the next section, we outline the two DM N-body simulations that have been utilised for the work discussed in this thesis.

### 1.4.1 Millennium and Millennium-II

At its release, the MILLENNIUM simulation (Springel et al., 2005) was the largest cosmological N-body solver of its kind, with ten times as many computational particles as the previous biggest simulations. It provided, and still provides, tremendous scope for understanding the formation of cold dark matter (CDM) structures, and interpreting observations of the real Universe across many epochs and spatial scales. The work presented in this thesis forms just a tiny part of the over-600 published papers that have utilised the suite of MILLENNIUM simulations to date.

MILLENNIUM models  $1.0078 \times 10^{10}$  point particles of mass  $1.18 \times 10^9 M_\odot$  within a volume of 685 Mpc on the side.<sup>4</sup> It does this assuming a  $\Lambda$ CDM cosmology with parameters as measured by the first-year WMAP observations (Spergel et al., 2003). A list of the key simulation parameters is given in Table 1.1.

Although the MILLENNIUM is very well suited to the study of relatively large bound DM structures, or ‘haloes’, its mass resolution is too low to accurately investigate lower-mass objects. DM haloes, as determined by the FOF algorithm of Davis et al. (1985) (otherwise known as ‘FOF groups’), are assumed to be resolved if they contain 20 computational particles or more. For MILLENNIUM, this equates to halo masses above  $2.36 \times 10^{10} M_\odot$ . However, in order to reliably represent the internal structure and density profile of a collapsed object,  $\gtrsim 1000$  particles are ideally needed. This implies a minimum halo mass of  $\sim 1.18 \times 10^{12} M_\odot$  for MILLENNIUM, which is around that expected for the DM halo of the Milky Way (McMillan, 2011).

In order to better model DM structures smaller than this, the MILLENNIUM-II simulation was run by Boylan-Kolchin et al. (2009). This simulation contains the same number of computational particles, but placed in a box 5 times smaller and with a particle mass 125 times smaller than used in MILLENNIUM. The increased mass resolution allows MILLENNIUM-II to resolve DM haloes down to  $1.89 \times 10^8 M_\odot$ , with well-resolved haloes having a mass around  $1000 m_p = 9.45 \times 10^9 M_\odot$  and above. This allows us to study galaxies similar to the fainter dwarfs in the Local Group (Guo et al., 2011). In this thesis, the MILLENNIUM-II is utilised for the studies discussed in Chapters 2 and 3, whereas the MILLENNIUM is used for those discussed in Chapters 4 and 5.

### 1.4.2 Output snapshots and subhalo merger trees

Cosmological N-body simulations such as MILLENNIUM and MILLENNIUM-II produce a huge amount of data, which cannot be efficiently output, stored and processed as a whole. Therefore, only certain data from discrete times during the simulation are retained. These discrete times are called output *snapshots*. For the MILLENNIUM and MILLENNIUM-II, such snapshots are chosen to be at redshift intervals given by

$$\log(1 + z_N) = \frac{N(N + 35)}{4200} \quad , \quad (1.38)$$

for  $0 \leq N \leq 63$ . For MILLENNIUM-II, four additional outputs were added at  $z = 31.3, 40, 80,$  and  $127$ , because smaller structures can be resolved, allowing higher-

---

<sup>4</sup>All physical quantities quoted in this section assume the value of the Hubble parameter chosen for MILLENNIUM and MILLENNIUM-II, namely  $H_0 = 73 \text{ km s}^{-1} \text{ Mpc}^{-1}$  (i.e.  $h = 0.73$ ).

	Millennium	Millennium-II
$\Omega_{\text{tot}}$		1.0
$\Omega_{\text{m}}$		0.25
$\Omega_{\text{dm}}$		0.205
$\Omega_{\text{b}}$		0.045
$\Omega_{\Lambda}$		0.75
$\Omega_{\text{curv}}$		0.0
$\sigma_8$		0.9
$n_s$		1.0
$H_0$		$73 \text{ kms}^{-1} \text{ Mpc}^{-1}$
$h$		0.73
$N_{\text{p}}$		$2160^3$
$L$	685 Mpc	137 Mpc
$m_{\text{p}}$	$1.18 \times 10^9 M_{\odot}$	$9.45 \times 10^6 M_{\odot}$
$M_{\text{min}}$	$2.36 \times 10^{10} M_{\odot}$	$1.89 \times 10^8 M_{\odot}$
$M_{\text{FOF,max}}$	$5.16 \times 10^{15} M_{\odot}$	$1.26 \times 10^{15} M_{\odot}$
$N_{\text{FOF},z=0}$	$1.82 \times 10^7$	$1.17 \times 10^7$
$N_{\text{snaps}}$	64	68
$z_{\text{init}}$		127
$l_{\text{s}}$	6.85 kpc	1.37 kpc
$l_{\text{link}}$		$0.2 \bar{r}_{\text{pp}}$
N-body code	Gadget-2	Gadget-3
Halo finder	FOF (Davis et al., 1985)	
Substructures	SUBFIND (Springel et al., 2001a)	
Power spectrum	CMBFast (Seljak & Zaldarriaga, 1996)	
Reference	Springel et al. (2005)	Boylan-Kolchin et al. (2009)

Table 1.1: Key properties of the two N-body simulations utilised in this work, MILLENNIUM and MILLENNIUM-II.

*The top group* shows the cosmological parameters chosen, where energy densities are in units of the critical density for closure,  $\rho_{\text{crit}} = 3H_0^2/(8\pi G)$ .

*The middle group* shows the mass and size specifications for the two simulations. This includes, the number of computational particles ( $N_{\text{p}}$ ), the simulation box side-length ( $L$ ), the particle mass ( $m_{\text{p}}$ ), the minimum resolvable DM (sub)halo mass ( $M_{\text{min}} = 20 m_{\text{p}}$ ), the most massive DM halo (i.e. FOF group) found in the simulation ( $M_{\text{FOF,max}}$ ), the total number of FOF groups resolved at  $z = 0$  ( $N_{\text{FOF},z=0}$ ), the number of output snapshots ( $N_{\text{snaps}}$ ), the starting redshift of the simulation ( $z_{\text{init}}$ ), the gravitational softening length ( $l_{\text{s}}$ ), and the linking length used to associate particles to bound structures ( $l_{\text{link}}$ ), where  $\bar{r}_{\text{pp}}$  is the mean inter-particle separation. All physical quantities assume  $h = 0.73$ .

*The bottom group* cites the various codes used to compute different aspects of the simulation.

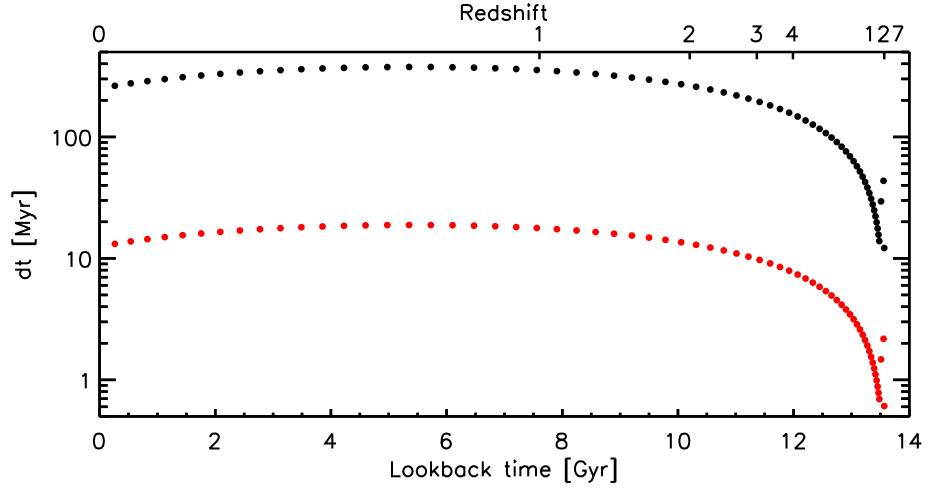


Figure 1.2: The widths of the MILLENNIUM-II simulation output snapshots (black points) and the default L-GALAXIES semi-analytic model timesteps (red points), as a function of snapshot lookback time and redshift. Snapshot lookback times are determined by Eqn. 1.38. There are twenty L-GALAXIES timesteps per simulation snapshot.

redshift objects to be studied. Fig. 1.2 shows the time between snapshots,  $dt$ , in the MILLENNIUM-II (black points).

In addition to the FOF groups mentioned above, ‘subhaloes’ are also identified from the particle data of these simulations, using SUBFIND (Springel et al., 2001a). Subhaloes are over-dense substructures within an FOF group in which galaxies are assumed to reside. They are, in effect, the local environment in which a galaxy can secularly evolve, and their radius (as measured by  $r_{200}$ , the radius within which the mean DM density is 200 times that of the critical density of the Universe) is a good approximation to the virial radius of the collapsed object,  $r_{\text{vir}}$ . As with FOF groups, only those subhaloes containing  $\geq 20$  computational particles are considered.

The subhalo data output by MILLENNIUM and MILLENNIUM-II is used to form ‘merger trees’, which link subhaloes from one output snapshot to their progenitors at higher redshifts, and their descendants at lower redshifts. The change in properties of these linked objects with cosmic time therefore constitutes the evolution of a single DM subhalo. Linking is done by weighting each computational particle by its gravitational binding energy at snapshot  $S_n$ , and then summing these weights for each of the haloes at snapshot  $S_{n+1}$  that contain one or more of its particles. The halo at  $S_{n+1}$  that has the largest weighting is then assigned as the unique descendant.

Trees are thus built from high to low redshift in a way that resembles an inverted tree (see e.g. De Lucia & Blaizot 2007, fig. 1), where the joining of two progenitor ‘branches’ represents the merger of two DM subhaloes.

It is these merger trees on which the semi-analytic model of galaxy formation, L-GALAXIES, is run. This model allows us to track the evolution of galaxies, which unlike their host DM subhaloes, are significantly affected by a number of physical processes in addition to gravity. This is discussed in the next section.

## 1.5 Semi-analytic modelling

Computational modelling has a very important place in modern galaxy evolution research. In the first instance, this is because the majority of physical phenomena we observe *on galaxy scales and above* have such long evolutionary timescales that no significant change can be seen in any given object over the time they are observed.<sup>5</sup> Therefore, in order to understand how they change over time, either an *implied* evolution can be studied by ‘joining the dots’ between galaxies observed at higher redshifts and their likely descendants at lower redshifts (e.g. van Dokkum et al. 2013), or a *direct* evolution of artificial galaxies can be studied using sophisticated computational models. Traditionally, there have been two main types of model used for galaxy evolution in a cosmological context. *Hydrodynamical simulations* solve the equations of hydrodynamics and gravity for a mixture of DM and baryons, represented by either computational particles or spatial grids with a typical baryonic mass of  $10^6$  to  $10^8 M_{\odot}$ .<sup>6</sup> *Semi-analytic models* instead link the growth of dark matter structure, as predicted by N-body simulations (Section 1.4) or the extended Press-Schechter formalism (Press & Schechter, 1974), with the growth of galaxies via analytical descriptions of the key baryonic processes that transfer mass and energy between the main components of a galaxy (e.g. White & Frenk 1991). These two methods are, essentially, complimentary. Simulations provide unique insights into the dynamical and morphological evolution of galaxies, and semi-analytic models efficiently provide insights into their statistical properties.

Indeed, a key aim of semi-analytic models is to efficiently and self-consistently represent the evolution of the galaxy population in a cosmological context. Modifications to the baryonic physics can be made relatively quickly, in order to learn about the significance and interplay between various evolutionary processes. Some simula-

<sup>5</sup>A notable exception to this is the variability in the spectra of AGN.

<sup>6</sup>‘Zoom-in’ re-simulations of particular environments, such as the haloes of dwarf galaxies, can currently have mass resolutions as low as  $\sim 10^3 M_{\odot}$ .

tion suites are now also able to systematically test the influence of varying the input physics (e.g. OWLS, Schaye et al. 2010, and more recently, *Illustris*, Vogelsberger et al. 2013, and EAGLE, Crain et al, in prep.), which has led some to question the further necessity of semi-analytic models. However, there is still a significant difference in the computational time required to re-run models with different physical prescriptions. For example, the typical amount of time it takes to compute one full cosmological run of the very recent EAGLE, with  $6.8 \times 10^9$  particles in a  $50 \text{ Mpc}^3$  box, is  $\sim 40$  million CPU hours.<sup>7</sup> Similarly, a full run of the new *Illustris* simulation, run using the moving-mesh code AREPO (Springel, 2010) with  $1.2 \times 10^{10}$  particles in a  $73 \text{ Mpc}^3$  box with various input-physics prescriptions, requires  $\sim 46$  million CPU hours. In contrast, a run of the Guo et al. (2011) version of the L-GALAXIES semi-analytic model on a complete set of MILLENNIUM merger trees takes only  $\sim 1000$  CPU minutes.

There are also other well-known limitations affecting hydrodynamical simulations in particular. For example, energy is radiated overly-efficiently from SNe when implementing thermal feedback (e.g. Dalla Vecchia & Schaye 2008). Smoothed-particle hydrodynamical (SPH) simulations have also had difficulties resolving shock fronts and fluid instabilities (e.g. Springel 2010). And even the highest-resolution cosmological simulations of today rely on ‘sub-grid’ models to represent key physical processes, such as star formation, that still cannot be adequately resolved. Therefore, at least currently, semi-analytic models still have an important role to play in our theoretical study of galaxy formation and evolution, despite having clear limitations of their own. This is discussed further in Section 1.5.2.

### 1.5.1 L-Galaxies

As mentioned above, semi-analytic galaxies evolve by the transfer of mass and energy among various, homogeneous galaxy components, according to physical laws motivated by observations and simulations. The components usually considered are a stellar disc, stellar bulge, ISM, circumgalactic medium (CGM), ejecta reservoir, and central supermassive black hole (SMBH). The physical laws are modelled as differential equations, which describe physical processes such as gas cooling, star formation, and feedback, in a similar way to the sub-grid models in simulations, but in a global sense. Here, I discuss some of the key physical processes that are modelled in the Munich semi-analytic model, L-GALAXIES.

L-GALAXIES (Springel et al., 2001a; De Lucia et al., 2004; Springel et al., 2005; Croton et al., 2006; De Lucia & Blaizot, 2007; Guo et al., 2011, 2013; Henriques

<sup>7</sup>Info from <http://home.strw.leidenuniv.nl/~crain/index.php/research-projects/eagle-home/>

et al., 2013; Fu et al., 2013; Yates et al., 2013) is a semi-analytic model of galaxy evolution, that has been developed for over a decade at the Max Planck Institute of Astrophysics (MPA) in Garching, and is the focus of much of the work in this thesis. It extends the semi-analytic methods set out in White & Rees (1978); White & Frenk (1991); Kauffmann, White & Guideroni (1993); and Kauffmann et al. (1999a), so that the model can be run on subhalo trees built from the output snapshots of DM N-body simulations such as the MILLENNIUM and MILLENNIUM-II. L-GALAXIES is currently able to reproduce the abundance of galaxies as a function of stellar mass and optical luminosity at  $z \sim 0$  (and also at higher redshifts, Henriques et al. 2013), as well as the relation between r-band luminosity and rotational velocity in disc galaxies (the Tully-Fisher relation), and the large-scale clustering of galaxies (see Guo et al. 2011). In this thesis, I will discuss a number of further achievements of the model related to the chemical properties observed in galaxies.

L-GALAXIES considers three ‘types’ of model galaxy: those whose DM subhalo is at the centre of its FOF group (type 0 galaxies), those at the centre of their own DM subhalo but not of their associated FOF group (type 1 galaxies), and those galaxies that have lost their DM subhalo through tidal disruption but have not yet merged with a central galaxy or been tidally disrupted themselves (type 2 galaxies). These three types are illustrated in Fig. 1.3. The prescriptions for the physical processes included in the model are then applied to galaxies according to their type (see below). For example, infall of pristine gas is only allowed to occur for type 0 galaxies, whereas stripping of hot gas can only occur for type 1 galaxies (once they are within the virial radius of the central type 0).

By default, the model runs with a time resolution of twenty timesteps per output snapshot (see Fig. 1.2). This value is chosen to balance accuracy in calculating properties such as star formation histories and stellar population parameters with efficiency in running the code. At each timestep, newly-formed DM subhaloes are seeded with hot gas, which is assumed to be accreted from the IGM until the cosmic baryon fraction of 0.17, minus any reduction due to the UV background radiation, is met (but see Yates, Thomas & Henriques, in prep.). This gas is then allowed to cool and form stars (with an intermediate step of H<sub>2</sub> formation since implemented by Fu et al. 2013). These stars can then recycle material enriched with newly-synthesised metals back into the ISM and CGM. This recycling is also accompanied by energetic feedback, which is allowed to reheat cold gas in the ISM and eject gas from the CGM to beyond the virial radius of the system. Some of this material is allowed to ‘reincorporate’ onto the halo as pre-enriched infall over a mass- and redshift-dependent timescale (Guo et al. 2011, but see Henriques et al. 2013). Other crucial baryonic processes, such as mass transfer through disc instabilities, hot gas stripping,

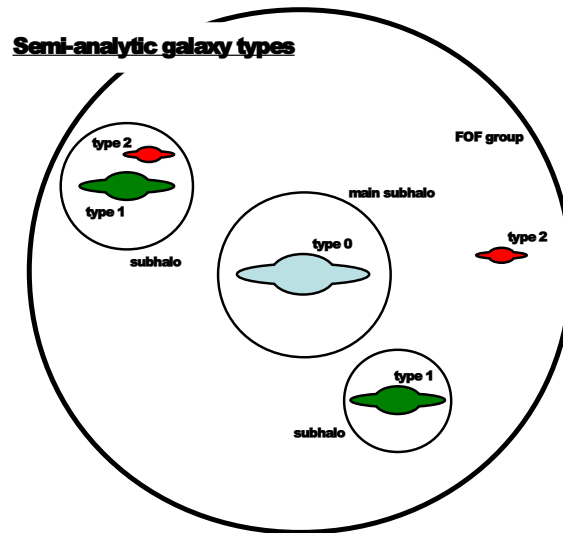


Figure 1.3: An illustration of the different ‘types’ of galaxy considered in L-GALAXIES (see text). The DM haloes (i.e. FOF group, main subhalo, and other subhaloes) are also shown.

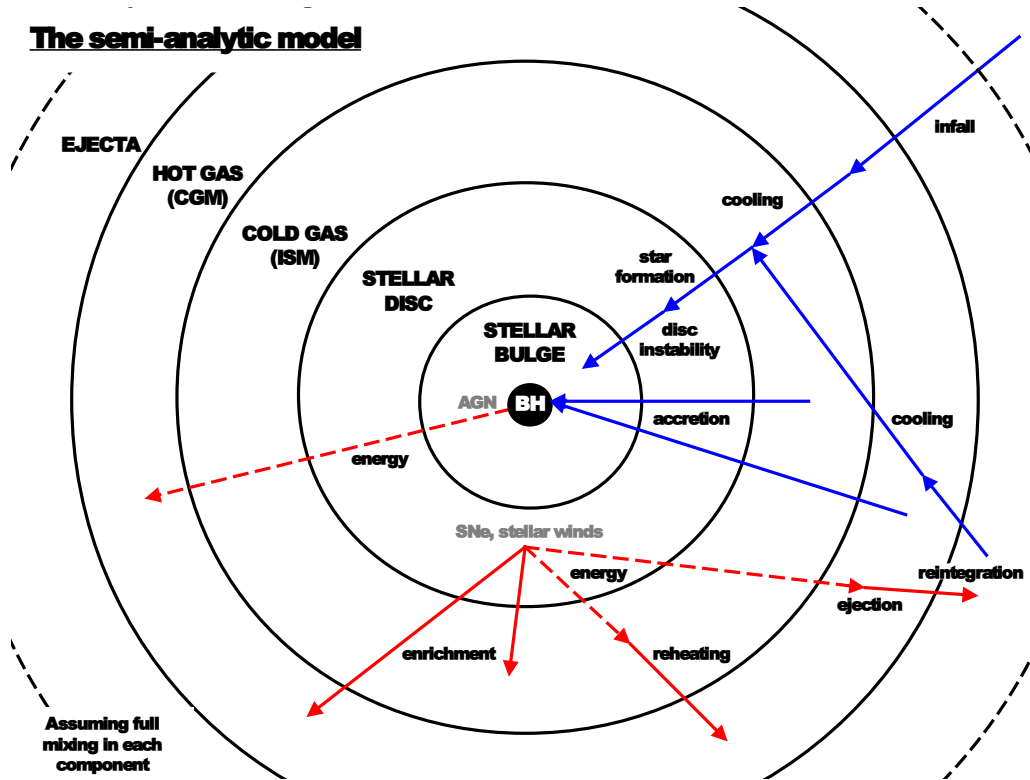


Figure 1.4: An illustration of the mass and energy transfer routes for an isolated model galaxy in L-GALAXIES. The various components of a galaxy are shown (rings), with routes for mass transfer in (blue), mass transfer out (solid red), and energy out (dashed red) given by the arrows.

tidal disruption, galaxy mergers, bulge and central BH growth, dust extinction, and radio-mode AGN feedback are also modelled. Fig. 1.4 shows a schematic illustration of how mass and energy are transferred among galaxy components in L-GALAXIES. All these prescriptions are described in detail in Guo et al. (2011) and references therein. Below, we outline those that are of most importance to the work discussed here.

### Infall

The mass of pristine gas infalling onto the DM halo of a type 0 galaxy is simply determined by the difference between the assumed baryon fraction  $f_b$  and the actual baryon fraction  $M_b/M_{\text{DM}}$  in the DM halo. The assumed baryon fraction is reduced

from the cosmic baryon fraction  $f_{b,\text{cos}}$  (assumed to be 0.17, as given by WMAP1) due to reionisation, and is parameterised following Gnedin (2000) as

$$f_b(z, M_{\text{vir}}) = f_{b,\text{cos}} \left[ 1 + (2^{2/3} - 1) \left( \frac{M_{\text{vir}}}{M_c(z)} \right)^{-2} \right]^{-3/2}, \quad (1.39)$$

where  $M_{\text{vir}}$  is assumed to be the mass within the radius at which the DM halo is 200 times denser than the critical density of the simulation (hereafter, the virial radius,  $R_{\text{vir}}$ ), and  $M_c(z)$  is the chosen characteristic halo mass, whose dependence on redshift has been calculated by Okamoto, Gao & Theuns (2008). In this formalism,  $f_b$  tends towards  $f_{b,\text{cos}}$  as  $M_{\text{vir}}$  increases. Pre-enriched gas can also be re-accreted onto the DM haloes of central galaxies, in addition to this pristine infall, as described along with SN feedback below.

### Cooling

Following White & Frenk (1991), the cooling of gas from the CGM onto the disc of a type 0 or 1 galaxy is considered to fall into two regimes; at early times and in low-mass DM haloes, gas is able to cool rapidly in less than the free-fall time, with the cold-flow accretion onto the central galaxy modelled as

$$\dot{M}_{\text{cool}} = \frac{M_{\text{acc}}}{t_{\text{dyn,h}}}, \quad (1.40)$$

where  $M_{\text{acc}}$  is the mass of gas accreted onto the DM halo, the dynamical time of the DM halo is  $t_{\text{dyn,h}} = R_{\text{vir}}/V_{\text{vir}} = 0.1H(z)^{-1}$ , and  $V_{\text{vir}} = (G \cdot M_{\text{vir}}/R_{\text{vir}})^{1/2}$ . At late times and in massive DM haloes, the accretion shock radius is large, leading to the formation of a hot gas atmosphere. In this case, the accretion rate onto the central galaxy is reduced to a cooling flow, given by

$$\dot{M}_{\text{cool}} = \frac{r_{\text{cool}}}{R_{\text{vir}}} \frac{M_{\text{hot}}}{t_{\text{dyn,h}}}. \quad (1.41)$$

Here, the cooling radius  $r_{\text{cool}}$  is set by the cooling function of Sutherland & Dopita (1993), and  $M_{\text{hot}}$  is the mass of shocked gas in the hot gas reservoir (see Guo et al. 2011, Section 3.2). Strictly speaking, in the model, galaxies fall into the cold-flow or cooling-flow regime when  $r_{\text{cool}}/R_{\text{vir}}$  is greater than or less than 1.0, respectively.

### Star formation

Star formation from dense, cold gas is governed in L-GALAXIES by a simplified form of the Kennicutt-Schmidt law (Schmidt, 1959; Kennicutt, 1998b). This law was

originally based on measurements within the solar neighbourhood, and extended by Kennicutt (1998b) to local galaxies. It parameterises the observed relation between the surface density of hydrogen,  $\Sigma_{\text{H}}$ , and the surface density of star formation,  $\Sigma_{\text{SFR}}$ , and is given by

$$\Sigma_{\text{SFR}} = 2.5 \times 10^{-4} \left( \frac{\Sigma_{\text{H}}}{1 \text{ M}_{\odot} \text{ pc}^{-2}} \right)^{1.4} \text{ M}_{\odot} \text{ yr}^{-1} \text{ kpc}^{-2} . \quad (1.42)$$

The positive correlation between these two properties suggests that galaxies with denser ISM gas form stars more efficiently. A sharp drop-off in SFR for gas surface densities below a critical threshold is also seen (Kennicutt, 1989). Further insights into the conditions required for star formation have been gained by considering the surface density of HI and H<sub>2</sub> gas separately (e.g. Wong & Blitz 2002; Bigiel, Leroy & Walter 2011).

Based on these observational findings, the following parameterisation for the global SFR is used in L-GALAXIES:

$$\dot{M}_{*} = \epsilon_{\text{SFR}}(M_{\text{cold}} - M_{\text{crit}})/t_{\text{dyn,d}} , \quad (1.43)$$

where  $\epsilon_{\text{SFR}}$  is the star-formation efficiency (assumed to be 0.02),  $t_{\text{dyn,d}} = 3r_{\text{gas,d}}/V_{\text{max}}$  is the dynamical time at the edge of the gas disc (assumed to be three times the gas scale length,  $r_{\text{gas,d}}$ ), and  $V_{\text{max}}$  is the maximum circular velocity of the DM subhalo.  $M_{\text{crit}}$  is the gas mass threshold below which no secular star formation is allowed to take place. It is related to the critical surface density required for rotationally-supported disc stability (Toomre, 1964), and is expressed as

$$M_{\text{crit}} = 11.5 \times 10^9 \left( \frac{V_{\text{max}}}{200 \text{ km/s}} \frac{r_{\text{gas,d}}}{10 \text{ kpc}} \right) . \quad (1.44)$$

$M_{\text{crit}}$  plays an important role in the star formation histories of galaxies, as will be shown for a certain class of objects in Chapters 2 and 3. Star formation can also occur in the form of a burst during a merger event. This mode is described along with mergers below.

The efficiency parameters used in semi-analytic models, such as  $\epsilon_{\text{SFR}}$  and the others discussed in this section (see Table 1.2), are tuned so that the model can reproduce certain observables, such as the  $z = 0$  galaxy stellar mass function and the gas fractions seen in galaxies. Such parameters are left ‘free’, as their true value and dependence on various other properties are not well constrained from either observations or high-resolution simulations. However, the physical significance and range of realistic values of such efficiencies have to be kept in mind at all times. The issue of free parameters is discussed further in Section 1.5.2.

Parameter	Fiducial value	Description
$f_{\text{b,cos}}$	0.17	Cosmic baryon fraction
$\epsilon_{\text{SFR}}$	0.02	Star formation efficiency
$^{a,b} \epsilon_{\text{h}}$	$\propto V_{\text{max}}^{-3.5}$	SN energy efficiency
$V_{\text{SN}}$	$630 \text{ km s}^{-1}$	SN ejecta speed
$^a \epsilon_{\text{disc}}$	$\propto V_{\text{max}}^{-3.5}$	Reheating efficiency
$R$	0.43	Mass recycling fraction
$y'_{\text{Z}}$	0.03	Metal yield
$\epsilon_{\text{BH}}$	0.03	BH cold accretion efficiency
$\epsilon_{\text{AGN}}$	0.1	AGN energy efficiency
$\kappa$	$1.5 \times 10^{-3} M_{\odot}/\text{yr}$	BH hot accretion efficiency

Table 1.2: The key parameter values chosen for the version of L-GALAXIES used in this thesis.

<sup>a</sup> See Henriques et al. (2013, fig. 3) for plots of the dependence of  $\epsilon_{\text{h}}$  and  $\epsilon_{\text{disc}}$  on  $V_{\text{max}}$  (the maximum circular velocity of the DM subhalo).

<sup>b</sup> The SN energy efficiency is doubled for the work described in Chapters 4 and 5, to account for changes to the metal yield and recycle fraction when implementing the delayed chemical enrichment scheme.

### SN feedback

SNe explosions can reheat gas and also eject it from a galaxy’s DM halo. Such feedback on a global scale can help galaxy formation models reproduce the number density of lower-mass galaxies observed in the real Universe (e.g. White & Rees 1978). However, the high efficiency of SN feedback required can lead to an unrealistically large population of *red* dwarf galaxies (e.g. Weinmann et al. 2006, but see Henriques et al. 2013).

By default, the amount of energy released by SNe is assumed to be proportional to the total mass of stars formed  $\Delta M_*$  at that time (but see Section 4.5.3):

$$E_{\text{SN}} = \epsilon_{\text{h}} \cdot \frac{1}{2} \Delta M_* V_{\text{SN}}^2 \quad , \quad (1.45)$$

where  $\epsilon_{\text{h}}$  is the halo-velocity-dependent SN energy efficiency, and  $V_{\text{SN}}$  is the SN ejecta speed, assumed to be fixed at 630 km/s.

The mass of cold gas in the ISM reheated into the CGM due to this injection of energy is given by

$$\Delta M_{\text{reheat}} = \epsilon_{\text{disc}} \cdot \Delta M_* \quad , \quad (1.46)$$

where  $\epsilon_{\text{disc}}$  is the ejection efficiency with which material is removed from the gas disc (see Table 1.2). The amount of hot gas that is ejected from the DM halo is dependent on the amount of SN energy left-over after reheating, and is given by

$$\Delta M_{\text{ejec}} = \frac{E_{\text{SN}} - \frac{1}{2} \Delta M_{\text{reheat}} V_{\text{vir}}^2}{\frac{1}{2} V_{\text{vir}}^2} , \quad (1.47)$$

The ejected gas is then allowed to return to the DM halo over timescales that are proportional to  $t_{\text{dyn,h}}/V_{\text{vir}}$  (but see Henriques et al. 2013). This constitutes a second component of gas infall that has been pre-enriched by the galaxy.

### Mass recycling and metal enrichment

In the default version of L-GALAXIES, the mass instantaneously returned to the ISM by SNe and stellar winds is given by

$$\Delta M_{\text{recyc}} = R \cdot \Delta M_* , \quad (1.48)$$

where the fraction,  $R$ , of the mass formed into stars at a given timestep is set to be 0.43. The yield of metals,  $y'_Z$  (see Section 1.3), is assumed to constitute 3 per cent of this recycled mass. This material is allowed to fully mix with the surrounding cold gas, and then can either be reheated into the CGM by the associated SN feedback or left available to form new stars. Such an IRA implementation has been common in galaxy formation models in the past. In L-GALAXIES, it is intended to mimic the return of *all* material ejected via SNe and stellar winds as if it were returned immediately after star formation. This is a somewhat reasonable approximation for SNe-II, as their progenitor stars have typical lifetimes of  $\sim 3$  to 30 Myr (Portinari, Chiosi & Bressan, 1998), and the timesteps used in the semi-analytic model range in size from  $\sim 1$  to 19 Myr (see red points in Fig 1.2). However, it is not satisfactory for SNe-Ia and stellar winds from intermediate-mass stars on the asymptotic giant branch (AGB), which release material between  $\sim 35$  Myr and 21 Gyr after the progenitor stars are formed. Therefore, although the IRA provides a reasonable description for the overall oxygen abundance in the gas phase of low-redshift galaxies (as oxygen has a primary contribution from SNe-II), it does not adequately represent the abundance of other heavy elements or their evolution over time. A key part of this thesis work addresses the shortcomings of such simple chemical enrichment modelling, by introducing a delayed enrichment scheme that self-consistently tracks the yield of various elements released over time by stars and SNe of different masses (Chapter 4). The new implementation removes the need for restrictive assumptions

such as a fixed yield, recycle fraction, and the IRA, and reproduces a number of key observables in the nearby Universe (see Chapter 5).

### Merging, starbursts, and black hole growth

The merger histories of galaxies in the semi-analytic model are effectively dictated by the merger histories of their DM subhaloes in the underlying N-body simulation. However, during the final stages of a halo-halo merger, subhaloes are generally ‘lost’ in the simulation, as the density contrast between the gravitationally-bound object and its immediate surroundings becomes very low. Consequently, galaxies are often left without a DM halo for the final stages of their associated galaxy-galaxy merger. Therefore, a ‘merger clock’ is required, which is set by the dynamical friction time  $t_{\text{fric}}$ , derived from the dynamical friction formula of Chandrasekhar (1943a) (see Binney & Tremaine 1987, page 747; and Guo et al. 2011, eqn. 31). A galaxy’s merger clock is started when either a) the galaxy becomes a type 2, whose DM subhalo has fallen below the detection limit of SUBFIND, or b) its DM subhalo mass drops below its stellar mass due to gravitational stripping. These two criteria account for all possible galaxy-galaxy mergers in L-GALAXIES.

The dynamical friction time is calculated when a galaxy first meets one of the above criteria. At each timestep thereafter, the galaxy is assumed to be at a radial distance of  $r_{\text{mbp}} \cdot (1 - \Delta t_{\text{merge}}/t_{\text{fric}})$  away from the central galaxy, where  $r_{\text{mbp}}$  is the radial distance of the most-bound computational particle of the old DM subhalo, and  $\Delta t_{\text{merge}}$  is the time since the merger clock started. Once this distance reaches zero, the two galaxies are said to have merged. The 3D position of the infalling galaxy is also updated, assuming it maintains the same polar and azimuthal coordinates as the most-bound particle of its old subhalo. The orbital evolution of a merging satellite galaxy is illustrated by the schematic in Fig. 1.5.

The re-distribution of baryons in a galaxy-galaxy merger depends on whether the merger is a major or minor event. *Major mergers* are those with a total-baryonic-mass ratio for the two merging systems of less than 1:3. *Minor mergers* comprise all the more disproportionate events. In major mergers, the stellar discs of both systems are disrupted into the bulge component of the descendant. The cold gas of the minor progenitor is added to the ISM of the descendant, and any remaining hot gas is transferred to the descendant’s CGM. In minor mergers, the procedure is the same, except that the main progenitor’s disc survives the event (the minor progenitor’s disc is still disrupted into the bulge).

In addition to a redistribution of mass during a merger and the consequential change in morphology of the descendant, the displacement of cold gas in both progen-

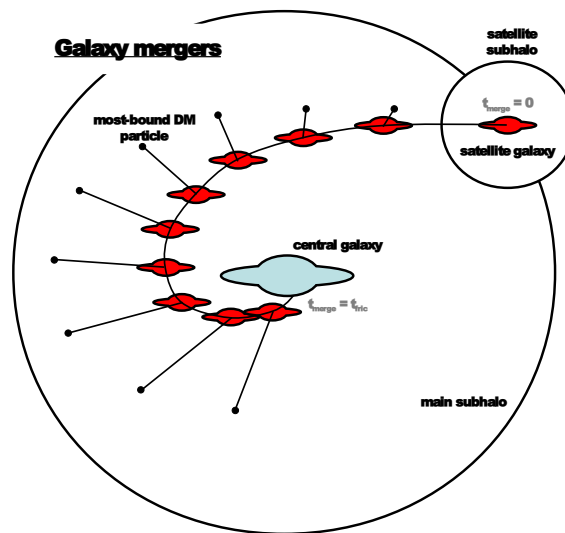


Figure 1.5: An illustration of a merger of a satellite galaxy onto a central galaxy. Once the satellite galaxy's DM subhalo is lost (or stripped below its stellar mass), the merger clock  $t_{\text{merge}}$  is started. Thereafter, the radial distance of the satellite relative to the most-bound DM particle of its old subhalo decreases according to dynamical friction.

itor galaxies can cause a starburst and growth of the central SMBH. In L-GALAXIES, the merger-induced star formation is parameterised using the ‘collisional starburst’ treatment of Somerville, Primack & Faber (2001). A fraction  $e_{\text{burst}}$  of the total cold gas in the two merging galaxies is assumed to form into stars:

$$e_{\text{burst}} = 0.56 \left( \frac{M_{\text{minor}}}{M_{\text{main}}} \right)^{0.7}, \quad (1.49)$$

where  $M_{\text{minor}}$  and  $M_{\text{main}}$  are the total baryonic masses of the minor and main progenitor galaxies, respectively, and the values of the coefficients are consistent with those obtained from SPH simulations of galaxy mergers (see Somerville et al. 2008). In major mergers, these stars form in the stellar bulge. In minor mergers they are assumed to form in the descendant’s stellar disc. The SN feedback from such a starburst can play a significant role in removing any remaining cold gas from the descendant’s ISM.

The central BH of the main progenitor galaxy can grow during a merger by a) swallowing the central black hole from the minor progenitor, and b) ‘quasar-mode’ accretion of cold gas onto an accretion disc and subsequently onto the black hole itself. Following Kauffmann & Haehnelt (2000) and Croton et al. (2006), the mass accreted by the BH in the merger is given by,

$$\Delta M_{\text{BH}} = M_{\text{BH,minor}} + \epsilon_{\text{BH}} \left( \frac{M_{\text{minor}}}{M_{\text{main}}} \right) \left( \frac{M_{\text{cold}}}{1 + (V_{\text{vir}}/280 \text{ km s}^{-1})^{-2}} \right), \quad (1.50)$$

where  $\epsilon_{\text{BH}}$  is the accretion efficiency, which is set to 0.03 in order to match the observed local  $M_{\text{bulge}}-M_{\text{BH}}$  relation (e.g. Häring & Rix 2004). The feedback from such quasar-mode BH accretion is not accounted for separately, but rather assumed to be included in the significant SN feedback that occurs at the same time due to the merger-induced starburst.

### AGN feedback

In early galaxy evolution models within a classical  $\Lambda$ CDM cosmology, it was noted that stars could form too efficiently in high-mass galaxies (e.g. White & Rees 1978), because the hot gas in the CGM could cool too efficiently at low radii, providing excess fuel for star formation. This produces a galaxy luminosity function with an overly-steep slope above  $L^*$  compared to observations (e.g. Benson et al. 2003). Relatedly, the disparity between the cooling rate in some groups and clusters and the mass of stars found in their centres was also seen in observations, and called the

‘cooling-flow problem’ (e.g. Fabian 1994). The need for ‘mass quenching’ of some kind has also been recently highlighted in empirical studies of the observed galaxy population below  $z \sim 1$  (Peng et al., 2010).

This has led to a search for a viable form of high-mass feedback that can suppress most of the secular star formation in model massive galaxies. Active galactic nuclei (AGN) are currently the most promising mechanism for this, despite the incredible difference in spatial scales between the central SMBH of a galaxy and its CGM: For a galaxy with  $M_{\text{BH}} = 5.0 \times 10^8 M_{\odot}$  lying on the  $M_{\text{bulge}}-M_{\text{BH}}$  relation (Häring & Rix, 2004), the central SMBH has a Schwarzschild radius of  $r_s = 2GM_{\text{BH}}/c^2 = \mathcal{O}(10^{-5} \text{ pc})$  and a sphere of influence with a radius of  $r_{\text{BH}} = GM_{\text{BH}}/V_{\text{vir}}^2 = \mathcal{O}(1 \text{ pc})$ . Whereas its surrounding hot gaseous halo is expected to extend out to  $r_{\text{hot}} \sim \mathcal{O}(10^5 \text{ pc})$ .

A straightforward theoretical argument for why AGN can still influence cooling in the surrounding halo is given by Mo, van den Bosch & White (2010, section 14.4): The ratio of the total energy output from an AGN to the gravitational binding energy of a typical massive, elliptical galaxy ( $\sigma \sim 300 \text{ km s}^{-1}$ ) from the virial theorem is  $\sim 10^3 \epsilon_{\text{AGN}}$ , where  $\epsilon_{\text{AGN}}$  is the mean efficiency with which the BH accretion disc can convert mass into energy over its lifetime. Given that the expected value of  $\epsilon_{\text{AGN}}$  for radiatively-efficient accretion is  $\sim 0.1$  (see Mo, van den Bosch & White 2010, section 14.2), it is fair to say that AGN should be powerful enough to play a significant role in shaping the evolution of their host galaxies. Additionally, galaxy-scale signatures of AGN are also seen in observations. Powerful, extended radio jets and lobes are now observed in a large number of massive, ‘active’ galaxies (e.g. de Gasperin et al. 2012). These features are also observed to coincide with heating of the CGM as seen in X-ray emission (e.g. Fabian 2012), and appear to be more than powerful enough to shut-down cooling flows onto galaxies (e.g. Böhringer et al. 2002). Therefore, AGN feedback has justifiably become a common addition to most galaxy formation models.

In L-GALAXIES, the reheating rate due to ‘radio-mode’ AGN feedback is calculated following Croton et al. (2006) as,

$$\dot{M}_{\text{reheat,AGN}} = (2 \epsilon_{\text{AGN}} \dot{M}_{\text{BH}} c^2) / V_{\text{vir}}^2, \quad (1.51)$$

where  $\epsilon_{\text{AGN}}$  is 0.1, and the rate of accretion of hot gas onto the central BH,  $\dot{M}_{\text{BH}}$ , is given by,

$$\dot{M}_{\text{BH}} = \kappa \left( \frac{f_{\text{hot}}}{0.1} \right) \left( \frac{M_{\text{BH}}}{10^8/h M_{\odot}} \right) \left( \frac{V_{\text{vir}}}{200 \text{ km/s}} \right)^3, \quad (1.52)$$

where  $f_{\text{hot}}$  is the ratio of hot gas mass to bound DM mass within the subhalo, and the hot accretion efficiency is set to  $\kappa = 1.5 \times 10^{-3} M_{\odot}/\text{yr}$ .

Although based on physical considerations, this AGN feedback prescription is purely phenomenological, in the sense that the unknown efficiency parameters are tuned to reproduce the massive end of the observed galaxy stellar mass function in the nearby Universe (see e.g. Guo et al. 2011, section 3.9). However, Croton et al. (2006, section 5) have shown that it does provide similar results to simple, ‘first principles’ formalisms in the form of Bondi-Hoyle accretion from a cooling flow Bondi (1952), or the accretion of cold clumps that fragment below the sonic radius as the cooling flow accelerates to the free-fall speed (Berschinger, 1989).

AGN play a particularly important role in the evolution of massive, elliptical galaxies in our model. A consequence of this is discussed in Chapters 2 and 3.

### 1.5.2 A defense of SAMs

In this final introductory section, I will briefly discuss the current *value* of semi-analytic models in the field of galaxy formation modelling. As mentioned at the start of Section 1.5, there are a number of popular criticisms of semi-analytic models, or ‘SAMs’. As this thesis is largely based around such models, it is important to address these concerns, before continuing to a discussion of the results obtained using L-GALAXIES.

One common criticism is that SAMs are too simplistic. This is often the opinion of those who consider the role of free parameters in SAMs as allowing the model to fit any conceivable constraint without teaching us about the physics involved. In response to this, it is important to note that the parameters in galaxy formation models should always represent aspects of a *physical* process, such as the *efficiency* of black hole accretion, or the *fraction* of mass reheated due to SNe. Such parameters should be far from idle normalisation coefficients, and actually highlight the poorly constrained areas of galaxy evolution that require further study. Recent works using statistical methods such as Monte Carlo Markov Chains (MCMC) to help constrain these parameters are therefore a clear step in the right direction (e.g. Kampakoglou, Trotta & Silk 2008; Henriques et al. 2009), as they reveal where models break down and new ideas are needed. It should also be noted that hydrodynamical simulations also contain a large number of such parameters for the same reasons, from sub-grid models and feedback approximations, to gravitational softening lengths and particle mass resolutions. Over-simplicity is therefore a problem to be confronted by all theoretical astrophysicists.

Ironically, another common criticism is that SAMs are too complicated. This appears to be the opinion of some observational astronomers, who instead resort to purely empirical, ‘toy models’ to explain particular observed phenomena in isolation

from their cosmological context. These models certainly have their place (see Section 1.3), however one should be cautious when extending their formalism beyond their original scope, to form comprehensive models of galaxy formation. These are in danger of lacking the physical motivation that is a key part of the semi-analytic formalism.

Finally, another common indictment against SAMs is that they offer no predictive power. They are sometimes believed to simply reproduce known relations, but offer little insight into any potentially undiscovered phenomena shaping the Universe. However, due to their efficiency at modelling the statistical properties of the galaxy population as a whole, SAMs were one of the first methods used to uncover the need for feedback in massive galaxies (White & Rees, 1978). This led to an increase in interest in the large-scale influence of black holes and development of AGN feedback models (see above). SAMs were also the first to point-out the discrepancy between the number of cold-DM substructures in Milky-Way-sized haloes and the number of observed satellite galaxies in the Local Group (Kauffmann, White & Guideroni, 1993). This ‘missing satellite problem’ has since prompted deeper surveys of the Local Group (Bullock, 2010) and revisions to the canonical  $\Lambda$ CDM paradigm, including phenomena such as cosmic-web stripping (Benítez-Llambay et al., 2013) and warm dark matter (e.g. Menci, Fiore & Lamastra 2012). It is also hoped that the results discussed in this thesis can be tentatively seen as predictions. The positive correlation between SFR and  $Z_g$  in massive galaxies presented in Chapter 2 could be explained by the gradual dilution of elliptical galaxies that has not yet been directly observed (see Chapter 3). Also, the new GCE implementation described in Chapter 4 suggests a certain form of SN-Ia delay-time distribution (DTD), at a time when neither the preferred DTD nor progenitor system of SNe-Ia is fully constrained by observations (see Chapter 5).

In conclusion, it is my opinion that SAMs still have a valid place in modern galaxy formation research. This is not to say that they don’t have significant limitations. For example, SAMs only work insofar as physical processes can be approximated on galaxy scales; if there were no global Kennicutt-Schmidt relation, it would be considerably harder to accurately model the star formation histories of galaxies. Also, SAMs lack the capability to accurately model the *dynamical* processes involved in galaxy evolution, due to their zonal modelling of the key baryonic components. Clearly, hydrodynamical simulations are needed in order to study gas kinematics in detail, although this comes at a much higher computational cost. Therefore, it is a *synergy* of different types of theoretical methods, and observations, that is needed in order to tackle the many pressing problems confronting galaxy astrophysics today.



# Chapter 2

## The relation between metallicity, stellar mass, and star formation rate in galaxies

*“Everything should be made as simple as possible, but not simpler.”*

Albert Einstein

### 2.1 Introduction

The metallicity of stars and gas in galaxies is known to correlate strongly with their luminosities, circular velocities and stellar masses (e.g. Lequeux et al. 1979; Garnett 2002; Tremonti et al. 2004; Gallazzi et al. 2005). However, the physical processes that drive these correlations are not yet fully understood.

Mathews & Baker (1971) and Larson (1974) first suggested that interstellar gas can be driven out of galaxies by supernova explosions as *galactic outflows*. They predicted that galaxies of smaller mass have lower metal abundances because their lower escape velocities allow freshly enriched gas to be more efficiently removed.

The input of energy from supernova explosions is now routinely incorporated into hydrodynamical simulations of galaxy formation, either in the form of thermal

heating or ‘kinetic feedback’, whereby radial momentum kicks are imparted to particles surrounding sites of star formation in the galaxy. Although these simulations are now able to demonstrate that galactic outflows can yield a good match to the observed mass-metallicity relation (e.g. Kobayashi et al. 2007; Scannapieco et al. 2008), this does not mean that outflows are the only process at work in regulating the metallicities of real galaxies.

Another possibility is the presence of a *mass-dependent star formation efficiency* (SFE). In this scenario, less-massive galaxies convert their gas reservoirs into stars over longer timescales than more-massive galaxies. Therefore, less-massive galaxies have higher gas-to-stellar mass ratios and are consequently less metal-rich. This mechanism has been studied by Brooks et al. (2007) and Finlator & Davé (2008) using smoothed particle hydrodynamics (SPH) simulations. They have suggested that both metal-rich outflows and a variable SFE must play roles in shaping the mass-metallicity relation. Calura et al. (2009) instead claim that an imposed mass-dependent SFE is enough to reproduce the evolution of the mass-metallicity relation without the need for outflows. However, studies of the effective yield (see Section 1.3.1) in local galaxies strongly suggest that metal-rich outflows are also present, particularly at low masses (Tremonti et al., 2004).

Alternatively, Dalcanton et al. (2004) claim that *metal-poor infall* can regulate metallicity in disc galaxies. Given that lower mass galaxies tend to have lower star formation rates, a net dilution would take place when the time-scale for star formation falls below the time-scale for accretion of metal-poor gas. This would drive down the low mass end of the mass-metallicity relation.

Finally, *variations in the initial mass function* (IMF) have also been cited as another factor that might influence the mass-metallicity relation. Köppen, Weidner & Kroupa (2007) propose that a SFR-dependent (and therefore stellar mass-dependent) IMF causes different galaxies to produce different effective oxygen yields. This hypothesis is based on the premise that most stars form in stellar clusters and that smaller, less actively star-forming galaxies are dominated by clusters with lower masses, containing a smaller fraction of massive, oxygen-producing stars. Calura & Menci (2009) also claim that a SFR-dependent IMF is necessary to reproduce the observed relation between velocity dispersion and the stellar alpha enhancement  $[\alpha/\text{Fe}]$  in local early-type galaxies (but see Chapter 5). However, there are currently conflicting conclusions in the literature as to whether such a variable IMF is present in the real Universe (e.g. Weidner & Kroupa 2006; Elmegreen 2006; Bastian, Covey & Meyer 2010; van Dokkum & Conroy 2010; Gunawardhana et al. 2011; Fumagalli, Da Silva & Krumholz 2011; Conroy & van Dokkum 2012b; Spiniello et al. 2013).

The fact that the interpretation of the mass-metallicity relation is subject to

considerable ambiguity (see also Section 1.2.4) has prompted a number of authors to consider alternative ways of quantifying metallicity in galaxies. For example, higher dimensional relations that include additional physical properties could provide better constraints on the processes that regulate metallicity. A study of such relations was first made by Ellison et al. (2008), who found a weak anti-correlation between gas-phase metallicity and specific star formation rate (sSFR) (as well as half-light radius  $r_h$ ) at low stellar masses. This dependence was inferred to be due to variations in the star formation efficiency: at a given stellar mass, more compact galaxies should have formed stars more rapidly in the past, lowering their present-day sSFR and raising their present-day metallicity.

More recently, Mannucci et al. (2010) have proposed a fundamental metallicity relation (FMR), based on similar findings. In that work, it was shown that the gas-phase metallicities ( $Z_g$ ) of both local and high-redshift galaxies were dependent on both stellar mass ( $M_*$ ) and star formation rate (SFR). The FMR provides a prediction of the metallicity of local galaxies with a  $1\sigma$  scatter of only  $\sim 0.05$  dex. This is a substantial improvement on the mean scatter of  $\sim 0.1$  dex reported by Tremonti et al. (2004) for the  $M_*$ - $Z_g$  relation. Mannucci et al. (2010) found  $Z_g$  to be strongly dependent on SFR at low stellar masses, but only very weakly dependent on SFR at high stellar masses. A simple model, invoking only mass-dependent outflows and pristine infall, was able to reproduce these trends. Mannucci et al. (2010) also claim that the FMR describes galaxies out to  $z \sim 2.5$ , although, more recent studies indicate that this is not the case (Cullen et al., 2013; Zahid et al., 2013c).

Finally, Lara-López et al. (2010b) have also carried out an independent study of the relation between  $M_*$ , SFR and  $Z_g$ . They found a flat fundamental plane which provides a prediction of the stellar mass with a  $1\sigma$  scatter of 0.32 dex, given the SFR and metallicity. They claim that this plane extends unchanged out to  $z \sim 3.5$ , aligning well with high redshift data from Maiolino et al. (2008).

Prompted by these findings, in this work we study higher dimensional relations between metallicity and a variety of physical galactic properties. We examine whether the  $M_*$ - $Z_g$  relation exhibits additional dependences on SFR, specific SFR and  $M_{\text{gas}}/M_*$ . Comparisons are made between the results from observational data and the predictions from semi-analytic models of galaxy formation implemented within a high resolution simulation of the evolution of dark matter in a ‘concordance’  $\Lambda$ CDM cosmology.

In Section 2.2, we present our observational sample, extracted from Sloan Digital Sky Survey (SDSS) spectroscopic data. In Section 2.3, we explain how we obtain estimates of  $M_*$ , SFR and  $Z_g$ . In Section 2.4, we study the dependence of the  $M_*$ - $Z_g$  relation on SFR, and the dependence of the SFR- $Z_g$  and sSFR- $Z_g$  relations on  $M_*$ .

Sample cut	Remaining objects
Removing duplicates	898,302
Redshift cut	761,215
Fibre-to-total light cut	727,012
SNR cut	354,574
$\sigma(m_z, H\delta_A, D_n4000)$ cut	338,547
AGN cut	239,912
$M_*, Z_g$ confidence cut	177,071

Table 2.1: The number of objects remaining after each sample cut is applied (in the order they were applied).

In Section 2.5, we briefly discuss the merits of the different  $Z_g$  diagnostics considered. In Section 2.6, we describe how model galaxies are selected for comparison with the observational data. In Section 2.7, we present these comparisons and show how trends in the relations between stellar mass, star formation rate and metallicity can be understood in terms of the prescriptions used for gas accretion, star formation, and SN and AGN feedback. In Section 2.8, we discuss the viability of different physical mechanisms in regulating the metallicity of galaxies. Finally, in Section 2.9, we summarise our results.

## 2.2 The Observational Sample

The sample of galaxies analysed in this paper is drawn from the Sloan Digital Sky Survey MPA-JHU Data Release 7 catalogue (hereafter, SDSS-DR7, Abazajian et al. 2009)<sup>1</sup>. This catalogue contains  $\sim 900,000$  galaxies with available spectra. The sample cuts used here are the same as those adopted by Tremonti et al. (2004), who investigated the  $M_*$ - $Z_g$  relation using galaxies from the SDSS Data Release 2.

First, we remove all duplicate spectra from the catalogue, reducing it by  $\sim 3.2$  per cent and leaving 898,302 galaxies. Then, we take only galaxies with reliable spectroscopic redshifts within the range  $0.005 < z < 0.25$ . We then remove all galaxies whose fibre-to-total light ratio is less than 0.1. This is defined as the ratio of the flux given by the SDSS fibre magnitude to that given by the SDSS model magnitude, in the r-band. The 3" SDSS fibre only probes the inner 1-9 kpc of the galaxies in our samples, and so this cut is needed to eliminate galaxies with metallicity measurements that are heavily biased towards the inner regions. Removing these

<sup>1</sup>available at; <http://www.mpa-garching.mpg.de/SDSS/DR7>

galaxies raises the median redshift by  $\sim 0.008$ . We have checked that increasing the minimum fibre covering fraction to 0.35 (following the recommendations of Kewley & Ellison 2008), or raising the minimum redshift, does not affect any of the main results presented in this paper (see 2.4.2).

We also make cuts to the signal-to-noise ratio (SNR) of some of the key emission lines required to estimate metallicity, ensuring that  $\text{SNR}(\text{H}\alpha, \text{H}\beta, [\text{NII}]\lambda 6584) > 5$ . Again, we have checked that raising this threshold to  $\text{SNR} > 10$  does not change our main results. Following Tremonti et al. (2004), we also make cuts on the accuracy of some additional parameters that were used to estimate stellar masses in their original analysis. All galaxies for which  $\sigma(m_z) > 0.15 \sinh^{-1}(\text{mag})$ ,  $\sigma(\text{H}\delta_{\text{A}}) > 2.5\text{\AA}$ , and  $\sigma(\text{D}_n 4000) < 0.1$  are removed. This is done purely to achieve consistency with their original sample selection criteria. The stellar masses that we use for our current DR7 analysis are derived using  $u, g, r, i, z$  SDSS photometry.

Of those galaxies for which  $\text{SNR}([\text{OIII}]\lambda 5007) > 3$ , AGN hosts were removed following the prescription given by Kauffmann et al. (2003c) for defining AGN in the BPT diagram (Baldwin, Phillips & Terlevich, 1981). For galaxies with  $\text{SNR}([\text{OIII}]\lambda 5007) < 3$ , only those with  $\log([\text{NII}]\lambda 6584/\text{H}\alpha) < -0.4$  were retained, thus removing low-ionization AGN from the sample.

Finally, a cut to the derived values of  $M_*$  and  $Z_g$  was made, based on the ‘confidence’ with which they were estimated from fits to synthetic spectra or HII region models using CLOUDY (Ferland et al., 1998) (see Section 2.3). The  $1\sigma$  spread in the likelihood distribution of the best-fitting model must be less than 0.2 dex in both quantities for the galaxy to remain in the sample (but see 2.5.1).

The application of these cuts leaves a base sample of 177,071 emission line galaxies. The number of objects removed by each of these cuts can be derived from Table 2.1.

## 2.3 Estimation of Stellar Mass, Star Formation Rate and Metallicity

After creating our base sample, two different data sets were obtained, differing only by the gas-phase metallicity estimation method used. A comparison between these two samples provides an insight into how sensitive the derived relations between  $M_*$ , SFR and  $Z_g$  are to the way metallicity is estimated.

For both data sets, total stellar masses and total star formation rates are provided by the SDSS-DR7 online catalogue. Values have been nominally corrected from a Kroupa (2001) to a Chabrier (2003) IMF. The stellar masses are based on fits to

<b>Sample T1</b>	Minimum	Median	Maximum
$\log(M_*)$	8.775	10.125	11.175
$\log(\text{SFR})$	-0.975	0.075	1.575
$12 + \log(\text{O}/\text{H})$	8.72	9.06	9.13
Redshift	0.030	0.077	0.177
No. of galaxies	120,491		
<b>Sample T2</b>	Minimum	Median	Maximum
$\log(M_*)$	8.625	9.975	11.175
$\log(\text{SFR})$	-1.125	0.075	1.575
$12 + \log(\text{O}/\text{H})$	8.48	8.88	9.13
Redshift	0.019	0.068	0.174
No. of galaxies	112,797		

Table 2.2: Details of the parameter space coverage of our two observational samples. These values are given for data binned by  $M_*$  and SFR, considering only bins containing  $\geq 50$  galaxies. The final number of objects in Sample T1 and T2 is 120,491 and 112,797, respectively. The difference in final size between the two samples is due to the different requirements for estimating  $Z_g$  (see text). 93,971 galaxies are common to both samples.

photometric data, rather than to Lick indices as in Kauffmann et al. (2003a). Dust corrected total-SFRs are calculated using the technique described by Brinchmann et al. (2004), with improvements to the aperture corrections as detailed by Salim et al. (2007). This method for estimating star formation rates is based on fitting to a grid of photoionisation models, as described in Section 1.2.3.

A more traditional way of estimating the SFR in galaxies using optical spectra is via the  $\text{H}\alpha$  emission line flux. The dust-corrected  $\text{H}\alpha$  flux,  $F_c(\text{H}\alpha)$ , is converted to a luminosity using  $L(\text{H}\alpha) = F_c(\text{H}\alpha) \cdot 4\pi D^2 \cdot 10^{-17}$ , where the distance  $D$  to the source was derived from the galaxy's redshift, and  $10^{-17}$  is the factor used to normalise SDSS fluxes to units of  $\text{erg s}^{-1}\text{cm}^{-2}$ . Star formation rate is then determined using the fixed conversion factor from Kennicutt (1998a),

$$\text{SFR} = 7.9 \times 10^{-42} L(\text{H}\alpha) [\text{erg s}^{-1}] , \quad (2.1)$$

which assumes a case B recombination, an electron temperature of  $10^4$  K and a Salpeter IMF. This value can be corrected to a Chabrier IMF by dividing by 1.7. The observed  $\text{H}\alpha$  flux is corrected for external dust extinction using

$$F_c(\text{H}\alpha) = F_{\text{obs}}(\text{H}\alpha) e^{+\tau_{\text{H}\alpha}} \quad , \quad (2.2)$$

where the H $\alpha$  optical depth  $\tau_{\text{H}\alpha}$  can be determined using the wavelength-independent relation  $A_\lambda = 1.086\tau_\lambda$  (Calzetti, 1994). As described for dust corrections in Section 1.2.2, an estimate of  $A_{\text{H}\alpha}$  can be obtained from the Balmer decrement  $B = F_{\text{obs}}(\text{H}\alpha)/F_{\text{obs}}(\text{H}\beta)$  and the following equation;

$$A_{\text{H}\alpha} = -2.5 \log \left( \frac{B}{2.86} \right) \cdot \frac{k_{\text{H}\alpha}}{k_{\text{H}\alpha} - k_{\text{H}\beta}} \quad , \quad (2.3)$$

where 2.86 is the intrinsic Balmer decrement for a case B recombination with electron density  $n_e = 100\text{cm}^{-3}$  and electron temperature  $T_e = 10^4\text{K}$  (Osterbrock, 1989). These values are roughly appropriate for local star forming galaxies (Kewley et al., 2001; Izotov et al., 2006; Liu et al., 2008; Pilyugin & Mattsson, 2011).

It should be noted that such fibre-based SFRs pertain to the region of the galaxy falling within the 3" diameter SDSS fibre aperture, which probes the inner  $\sim 1\text{-}9$  kpc of the galaxies in our sample. The total SFRs utilised in this work use SDSS photometry to correct for missing star formation in the outer regions of the galaxy. The Bayesian method used to obtain these total SFRs also accounts for the fact that the H $\alpha$ -to-SFR conversion factor depends on metallicity, and allows the dust-free value of the Balmer decrement to differ from the ‘standard’ Case B value (see 2.4.2, and Brinchmann et al. 2004).

The use of total- rather than fibre-SFRs shifts the median star formation rate up by  $\sim 0.6$  dex. The size of this shift for each galaxy depends on the redshift and stellar mass. For example, when switching from H $\alpha$ -based, fibre-SFRs to Bayesian, total-SFRs, the star formation rate shifts upwards most dramatically at the lowest redshifts and masses. This is because these galaxies have larger *apparent* sizes, and are therefore more extended with respect to the fibre aperture than more distant, massive galaxies.

As mentioned above, fibre-based metallicities are calculated using two different procedures to produce two different data sets. The first procedure uses two of the strong line diagnostics calibrated by Maiolino et al. (2008), producing our Sample T1. These diagnostics were derived using a combination of empirical and theoretical methods (see Section 1.2). 259 local galaxies of  $Z_g < 8.35$ , with  $T_e$  derived metallicities compiled by Nagao et al. (2006) were used, combined with 22,482 SDSS-DR4 galaxies of  $Z_g > 8.4$ , with metallicities derived using the photoionisation model outlined in Kewley & Dopita (2002). The resulting combined calibrations are given by eqn. 1 and table 4 in the Maiolino et al. (2008) paper.

We then follow Mannucci et al. (2010) by taking the average of the metallicities given by the  $[\text{NII}]\lambda 6584/\text{H}\alpha$  diagnostic and the  $R_{23}$  diagnostic as the final metallicity estimate for each galaxy. We also corrected all line fluxes for dust, following Cardelli et al. (1989). This lowers the metallicities estimated via  $R_{23}$  by  $\sim 0.03$  dex at the highest masses, but makes very little difference to those estimated via  $[\text{NII}]/\text{H}\alpha$  because the two lines involved are of very similar wavelengths.

Once removing those galaxies with a) uncertain estimates of  $M_*$  or SFR from the SDSS-DR7 catalogue, b) emission lines that have too low signal-to-noise for accurate  $Z_g$  estimates, and c) estimates of  $Z_g$  from the two diagnostics used that differ by more than 0.25 dex, Sample T1 is left with 120,491 galaxies.

The second procedure uses the values of  $Z_g$  provided by the SDSS-DR7 catalogue to produce our Sample T2. These metallicities are calculated using the same grid of photoionisation models used to obtain the SFRs, by finding the model that best matches the observed fluxes of all the most prominent optical emission lines ( $[\text{OII}]$ ,  $\text{H}\beta$ ,  $[\text{OIII}]$ ,  $\text{H}\alpha$ ,  $[\text{NII}]$  and  $[\text{SII}]$ ). In Section 2.5, we give a brief discussion on the merits of using this Bayesian technique over simpler emission line ratios when studying local, high- $Z_g$ , star-forming samples.

Removing galaxies without robust estimates for  $M_*$ , SFR or  $Z_g$  from the catalogue reduces Sample T2 to 112,797 galaxies.

Details of Samples T1 and T2, when binned by  $M_*$  and SFR, are provided in Table 2.2. We note that oxygen abundance  $[\log(\epsilon_{\text{O}}) = 12 + \log(\text{O}/\text{H})]$ , as defined in Section 1.1.2] is used as a proxy for total gas-phase metallicity throughout this chapter. The most recent determination of the solar oxygen abundance in these units is  $Z_{\odot} = 8.69$  (Allende Prieto et al., 2001; Asplund et al., 2009).

## 2.4 Observational Results

In this section, we examine whether the  $M_*$ - $Z_g$  relation exhibits additional dependences on other physical properties. The region of the parameter space of interest for our analysis is  $8.6 < \log(M_*) < 11.2$ ,  $-2.0 < \log(\text{SFR}) < 1.6$  and  $8.5 < Z_g < 9.2$ , as this covers 98 per cent of the galaxies in both our observational samples.

### 2.4.1 The $M_*$ - $Z_g$ relation

Firstly, we introduce the basic  $M_*$ - $Z_g$  relation for Sample T2, before analysing any SFR-dependence. In this form, the relation can be seen as an ‘update’ to that of Tremonti et al. (2004), who analysed an SDSS-DR2 sample containing half as many galaxies. The  $M_*$ - $Z_g$  relation for Sample T2 is shown in Fig. 2.1. Individual galaxies

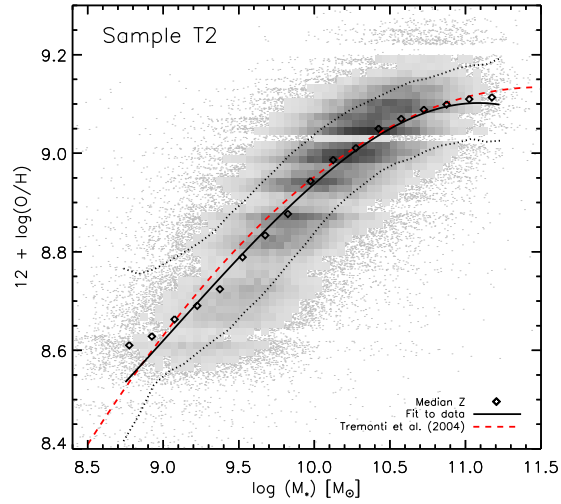


Figure 2.1: The  $M_*$ - $Z_g$  relation for Sample T2. The galaxy distribution is shown in grey, and a fit to this data is given (black solid line). The median metallicity in bins of 0.15 dex in stellar mass is plotted as black diamonds. The  $1\sigma$  dispersion in  $Z_g$  about the mean is shown as dotted lines. Also shown is the Tremonti et al. (2004) fit to data drawn from the SDSS-DR2 (dashed red line).

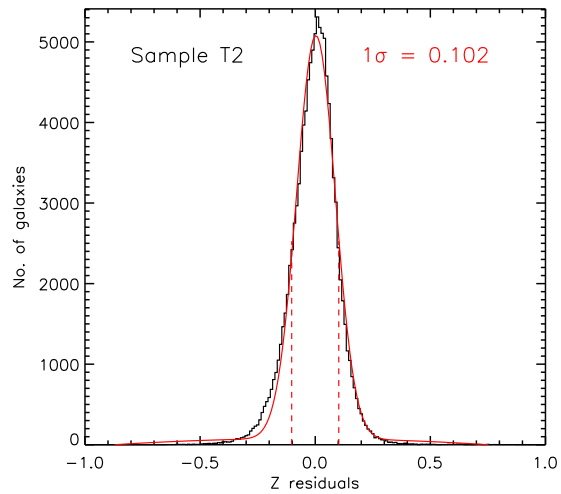


Figure 2.2: The distribution of residuals about  $Z_g$  for the  $M_*$ - $Z_g$  relation shown in Fig. 2.1. The mean dispersion of  $\sim 0.10$  dex is the same as that reported by Tremonti et al. (2004) for their SDSS-DR2 sample.

are shown in grey, with a 3rd order polynomial fit to the whole population shown as a solid black line, and given by the following equation:

$$Z_g = 26.6864 - 6.63995x + 0.768653x^2 - 0.0282147x^3 \quad , \quad (2.4)$$

where  $Z_g = 12 + \log(\text{O}/\text{H})$  and  $x = \log(M_*/M_\odot)$ . A fit to the Tremonti et al. (2004) mass-metallicity relation (red dashed line) is plotted for comparison. The standard deviation about the best fit from residuals is 0.102 dex, as shown by Fig. 2.2. This is the same as the dispersion calculated for the original Tremonti et al. (2004) sample.

There is little quantitative difference between our fit and that of Tremonti et al. (2004). However, our new fit indicates a somewhat more linear relation between mass and metallicity below  $\sim 10^{10}M_\odot$ . Above this mass, the relation flattens and there is a hint of a turnover at the very highest masses. Turnovers in the  $M_*$ - $Z_g$  relation at high mass are not uncommon in the literature (Zaritsky et al., 1994; Kewley & Dopita, 2002; Kobulnicky & Kewley, 2004; McGaugh, 1991; Pettini & Pagel, 2004), and can simply be due to the use of polynomials to fit the data. However, the physical significance of a turnover, and the influence of SFR, have not been widely discussed until now.

### 2.4.2 The $M_*$ - $Z_g$ relation, as a function of SFR

In order to study the dependence of the  $M_*$ - $Z_g$  relation on SFR, we follow the same approach as Mannucci et al. (2010), binning galaxies by  $M_*$  and SFR, and calculating the median metallicity in each bin. Bins are of width 0.15 dex in both dimensions, and only those which contain  $\geq 50$  galaxies are plotted. Fig. 2.3 shows this  $M_*$ - $Z_g$  relation for Sample T1 (left panel) and Sample T2 (right panel). The data are coloured by star formation rate, as are fits to the relation at a series of fixed SFRs (solid lines).

The left panel of Fig. 2.3 shows, qualitatively, the result previously described by Mannucci et al. (2010): there is an increase in metallicity with increasing mass, but also a clear and ordered dependence of metallicity on SFR at fixed mass. Metallicity depends strongly on SFR at low masses, but is virtually independent of SFR at high masses in this sample. A similar result is found when using metallicities based only on the  $[\text{NII}]/[\text{OII}]$  diagnostic calibrated by Kewley & Dopita (2002), although, the dependence of  $Z_g$  on SFR at high masses becomes a little stronger.  $[\text{NII}]/[\text{OII}]$  is considered to be more accurate than  $[\text{NII}]/\text{H}\alpha$ , due to its lack of sensitivity to the ionisation parameter (see Section 1.2.2, and Kewley & Dopita 2002). In order to more directly compare with previous works, we choose to use the average value from the  $R_{23}$  and  $[\text{NII}]/\text{H}\alpha$  diagnostics for Sample T1. The  $1\sigma$  spread about the median

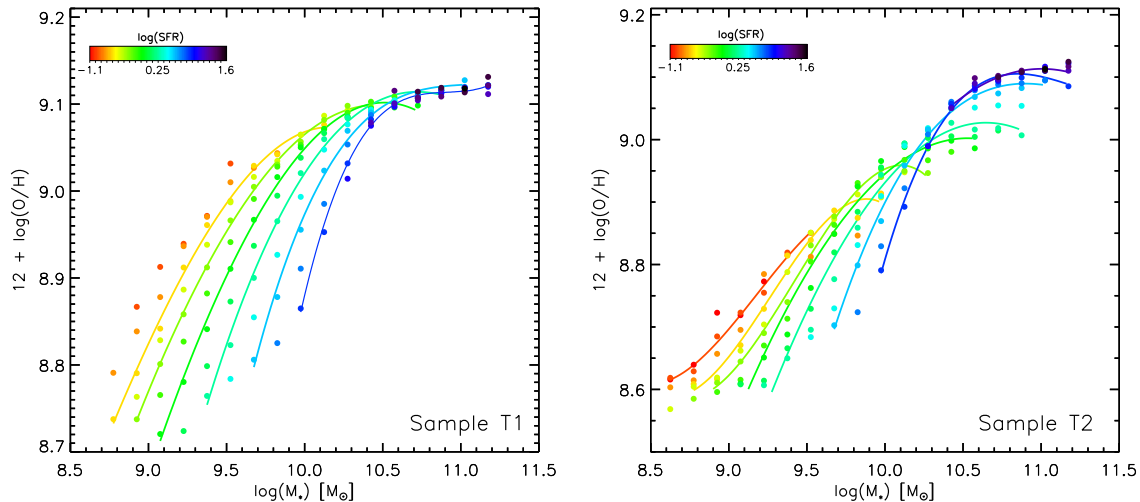


Figure 2.3: The  $M_*$ - $Z_g$  relation for Sample T1 (left panel) and Sample T2 (right panel). Filled circles show the median metallicities of galaxies binned by  $M_*$  and SFR, for bins containing  $\geq 50$  galaxies. Binned data is coloured by SFR, as are the fits at fixed SFRs (solid lines), plotted for  $\log(\text{SFR}) = (-0.975$  Sample T2 only),  $-0.675, -0.375, -0.075, 0.225, 0.525, 0.825, (1.125$  Sample T2 only). The dependence of  $Z_g$  on SFR for the two samples is clearly different. For example, Sample T2 exhibits a clear dependence at high-mass.

$Z_g$  for Sample T1 is 0.07 dex, compared to 0.08 dex reported by Mannucci et al. (2010).

The similarity between our Sample T1 and the Mannucci et al. (2010) sample holds despite the different methods used to obtain SFRs, with Mannucci et al. (2010) adopting  $\text{H}\alpha$ -based, fibre SFRs, rather than the Bayesian, total-SFRs preferred here. This suggests that the particular SFR estimation method chosen is not critical for the *shape* of the relation between  $M_*$ , SFR and  $Z_g$  observed.

The key difference between the Mannucci et al. (2010) sample and our Sample T1 is the *range* of SFRs sampled. The higher range of SFRs seen in Sample T1 (and Sample T2) is explained by a combination of factors. First, total- rather than fibre-SFRs are used, allowing for a more comprehensive estimate of the star formation across a whole galaxy (see Section 2.2). Second, the simpler  $\text{H}\alpha$ -based method yields lower SFR estimates for high- $M_*$  galaxies of given  $\text{H}\alpha$  luminosity, as shown in Fig. 2.4. This is because the fixed conversion factor used in the  $L(\text{H}\alpha)$ -to-SFR equation, provided by Kennicutt (1998a), is dependent on metallicity, and hence stellar mass. Brinchmann et al. (2004) report that the Kennicutt value is most accurate for galaxies

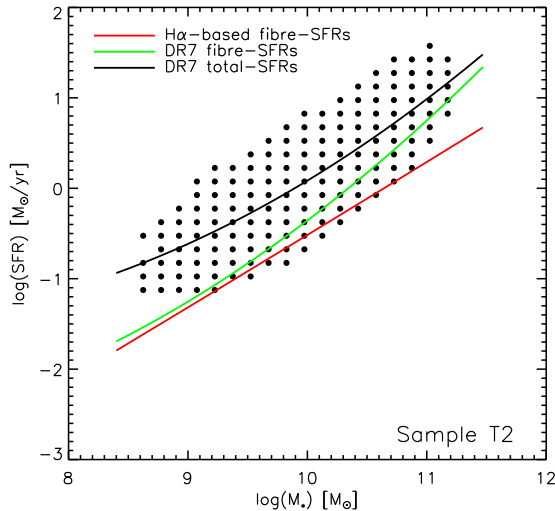


Figure 2.4: The  $M_*$ -SFR relation for our Sample T2, when using three different methods for estimating SFR. Black points indicate the binned sample when using Bayesian, total SFRs, with a fit given by the black line. The green line indicates a fit when using Bayesian, fibre SFRs. The red line indicates a fit when using  $H\alpha$ -based, fibre SFRs. The green line is higher than the red line at high  $M_*$  due to a variable  $L(H\alpha)$ -to-SFR conversion factor (see Section 2.4.2). The black line is higher than the green line at low  $M_*$  due to the larger angular size of low- $M_*$  (low- $z$ ) galaxies in the SDSS (see Section 2.2).

with stellar masses of  $\sim 10^{9.5}M_\odot$ , and will underestimate the SFR in objects of greater mass. Note, however, that the intrinsic Balmer decrement for Case B recombination is also metallicity- and mass-dependent. A fixed Case B ratio can over-estimate the attenuation due to dust by up to  $\sim 0.5$  mag for the most massive, metal-rich galaxies (Brinchmann et al., 2004). This will counteract somewhat the underestimate in SFR from a fixed conversion factor for higher mass galaxies. None the less, the use of total-SFRs and a variable conversion factor combine to shift the median value of SFR up by  $\sim 0.6$  dex for Samples T1 and T2.

The  $M_*$ - $Z_g$  relation for Sample T2 is somewhat different to that of Sample T1. It extends down to lower stellar masses and metallicities, and exhibits a different SFR dependence. At low stellar masses, both samples show a similar dependence on SFR: low-SFR galaxies are more metal-rich. However, at high stellar masses, *high*-SFR galaxies are more metal-rich in Sample T2, whereas there is no dependence on SFR seen in Sample T1. Sample T2, therefore, exhibits a SFR-dependence at both low and high mass, with a ‘twist’ in the  $M_*$ - $Z_g$  relation around  $M_* \sim 10^{10.2}M_\odot$ . We

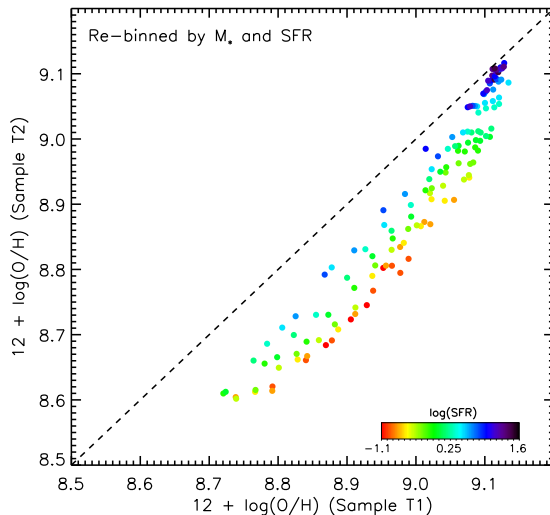


Figure 2.5: A comparison of the oxygen abundances obtained from the two metallicity diagnostics used in this work. Data is binned by  $M_*$  and the estimation of SFR described in Section 2.2. Points are coloured by SFR. The x-axis represents the technique outlined by Mannucci et al. (2010), using strong line ratio calibrations from Maiolino et al. (2008). The y-axis represents the Bayesian technique outlined by Tremonti et al. (2004). There is a clear and systematic over-estimation of  $Z_g$  from the former method relative to the latter. This discrepancy is also more significant for low-SFR galaxies.

note that such a twist is also obtained when using the sample selection criteria of Mannucci et al. (2010), rather than those outlined in Section 2.2. This indicates that the choice of sample cuts does not significantly affect our findings.

The extension to lower stellar masses seen for Sample T2 is mainly due to the removal of galaxies from Sample T1 during ‘cleansing’. Low-redshift galaxies ( $z < 0.03$ ) are excluded from Sample T1 because the  $[\text{OII}]\lambda 3727$  line (required for estimating metallicity using the  $R_{23}$  ratio) is not measurable. These galaxies can remain in Sample T2, extending the  $M_*$ - $Z_g$  relation down a further  $\sim 0.3$  dex in stellar mass.

The difference in the dependence of metallicity on SFR at high stellar masses is mainly attributable to the metallicity derivation method chosen. Fig. 2.5 shows a comparison of the values of  $Z_g$  obtained from the two methods used. Only the 93,971 galaxies present in both samples are included, and these are re-binned by  $M_*$  and SFR. We can see that the strong line ratio method used for Sample T1 yields systematically higher values of  $Z_g$  compared to the Bayesian method used for Sample T2, and that this difference is larger for galaxies with lower SFRs. A similar effect

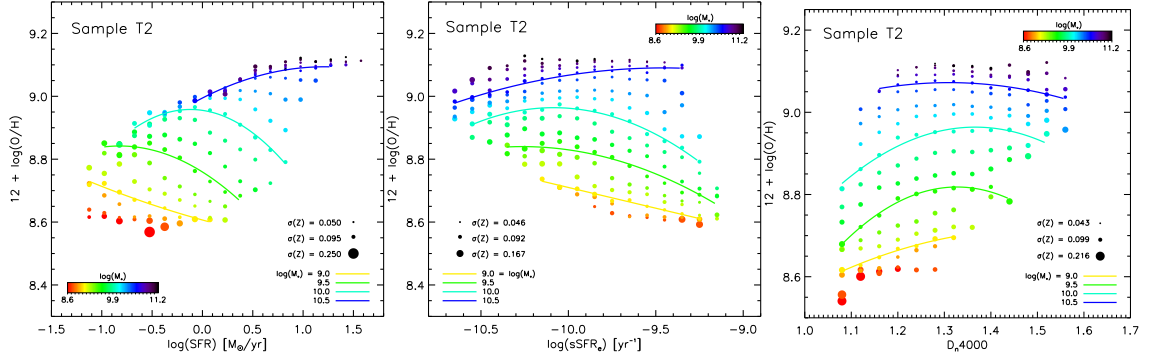


Figure 2.6: The SFR- $Z_g$  relation (left panel),  $(\text{SFR}/M_*)$ - $Z_g$  relation (middle panel) and  $D_n4000$ - $Z_g$  relation (right panel) for Sample T2. Fits to the data for four fixed masses are shown (solid lines). The drop in  $Z_g$  with increasing star formation rate (decreasing  $D_n4000$ ) is seen in all three relations. A drop in  $Z_g$  with decreasing star formation rate (increasing  $D_n4000$ ) is also seen for high-mass galaxies, representing the same effect seen at high masses in Fig. 2.3. The sizes of the points are scaled to the  $1\sigma$  spread in the values of  $Z_g$  in each bin.

is seen when binning galaxies by  $M_*$  and H $\alpha$ -based, fibre-SFRs.

It is not straightforward to determine which of the two methods considered here is most accurate at estimating oxygen abundance (see Section 1.2). However, we discuss the problems of each for this specific case in Section 2.5. Noting that the qualitative properties of Sample T1 are already well described by Mannucci et al. (2010) using their data, we choose to drop further analysis of Sample T1 and focus on Sample T2 in the rest of this work.

We note here that variation in the SDSS fibre aperture covering fraction with SFR is unlikely to account for the positive correlation seen between SFR and fibre-based  $Z_g$  at high mass in Sample T2. Kewley & Ellison (2008) have found that fibre-based metallicity estimates tend to predict higher  $Z_g$  for massive galaxies in the SDSS than *global* metallicity measurements of massive galaxies in the Nearby Field Galaxy Survey (NFGS, Jansen et al. 2000a,b). Given that Ellison et al. (2008) also find high-SFR systems tend to have larger  $r_h$  at fixed mass, it could be that they have larger over-estimates of  $Z_g$  than low-SFR galaxies in our sample, due to their lower covering fractions at fixed redshift. However, Tremonti et al. (2004) have shown that, for the brightest (i.e. most massive) objects in their SDSS sample, those with the smallest covering fractions tend to have  $Z_g$  estimates only  $\sim 0.05$  dex higher than those with the highest covering fractions. This is less than the  $\sim 0.1$  dex spread in metallicity seen in our binned SDSS sample (and much less than the

full spread of the full high-mass population). In addition, the fact that a positive SFR- $Z_g$  remains even when increasing the minimum covering fraction to 0.35 in our sample also suggests that aperture bias is not driving our findings at high mass.

### 2.4.3 The SFR- $Z_g$ and sSFR- $Z_g$ relations, as a function of $M_*$

The SFR- $Z_g$  relation for Sample T2 is shown in the left panel of Fig. 2.6. Points are coloured by stellar mass, and fits to the relation at four fixed stellar masses are also shown (solid lines).

This plot shows the same SFR-dependences seen in the  $M_*$ - $Z_g$  relation, but from another projection onto the  $M_*$ -SFR- $Z_g$  space. Again, in addition to the drop in  $Z_g$  with increasing SFR seen for low-mass galaxies, Sample T2 also clearly exhibits a downturn in metallicity with *decreasing* SFR at higher stellar masses.

When instead considering the dependence of SFR on  $Z_g$ , by re-binning Sample T2 by  $M_*$  and  $Z_g$ , we find that SFR slowly increases with metallicity, and that galaxies at the higher-redshift end of our sample have higher star formation rates. This is complimentary to the findings of previous works, such as Lara-López et al. (2010a), although in that work, H $\alpha$ -based, fibre-SFRs and  $R_{23}$ -based metallicities were used. At fixed mass, we find again that SFR decreases with increasing  $Z_g$  at low mass, and increases with increasing  $Z_g$  at high mass.

Finally, we note that it is actually more sensible to study the dependence of the  $M_*$ - $Z_g$  relation on the *specific* star formation rate (SFR/ $M_*$ , hereafter sSFR $_e$ ), rather than the star formation rate. A dwarf galaxy with a star formation rate of 1  $M_\odot \text{ yr}^{-1}$  is a much more ‘active’ system than a giant elliptical galaxy forming stars at the same rate. The specific star formation rate, on the other hand, is a *normalised* quantity, and provides a measure of the present-to-past-averaged star formation rate of the galaxy. Another related quantity is the 4000-Ångstrom break strength. This is characterised by the  $D_n4000$  index, the average flux from two narrow bands on either side of the break (3850-3950Å and 4000-4100Å). sSFR estimates using H $\alpha$  flux are a good measure of the instantaneous star formation rate in a galaxy, whereas  $D_n4000$  is more sensitive to stars that have formed over timescales of a few hundred million years to a gigayear.

The sSFR $_e$ - $Z_g$  and  $D_n4000$ - $Z_g$  relations for Sample T2 are presented in the middle and right panels of Fig. 2.6. The data has been binned by  $M_*$  and the sSFR indicator in question. The reader should note that small values of  $D_n4000$  correspond to high values of sSFR.

It is encouraging that both these relations exhibit similar trends. Metallicity decreases as a function of sSFR for low-mass galaxies and increases as a function

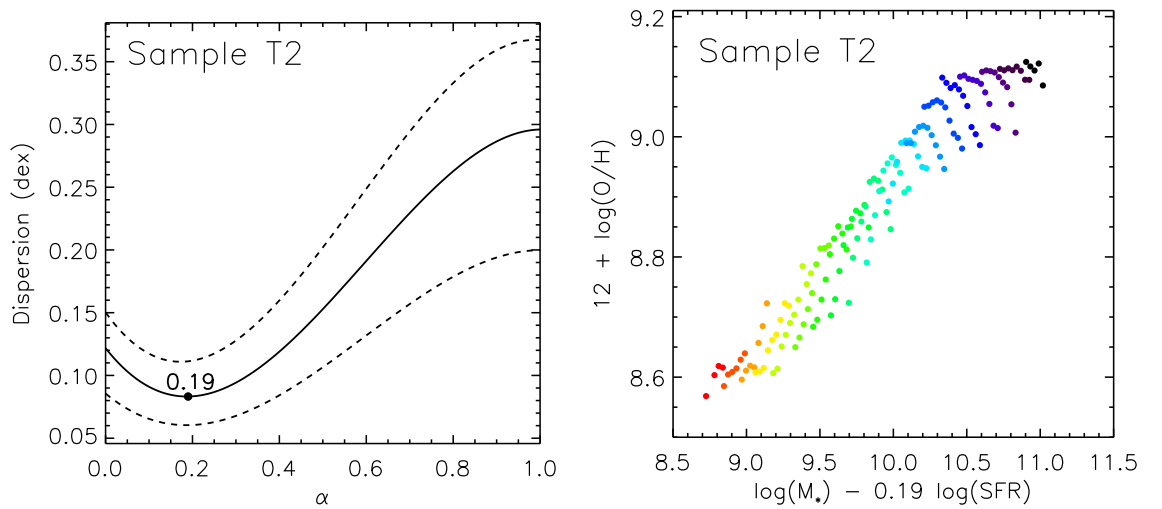


Figure 2.7: **Left panel:** The mean dispersion (solid line) in  $Z_g$  for different projections onto the  $M_*$ -SFR- $Z_g$  space for Sample T2. The  $1\sigma$  scatter in the mean dispersion is also shown (dotted lines). Projections onto the plane are defined by  $\alpha$ , given in Eqn. 2.5. The projection of least scatter for Sample T2 is  $\alpha = 0.19$ , giving a dispersion of  $\sim 0.08$  dex (for Sample T1, this is  $\alpha = 0.36$  and  $\sim 0.06$  dex, respectively). **Right panel:** The projection corresponding to the optimum value of  $\alpha$ . Only a slight improvement in the dispersion is obtained from this projection compared to the  $M_*$ - $Z_g$  relation. Points are coloured by SFR, as in Fig. 2.3.

of sSFR for high-mass galaxies. When noting that  $D_n4000$  (an absorption feature) and  $\text{sSFR}_e$  (computed from emission line fluxes) are independent quantities, the fact that the same trends with metallicity are seen for both indicates that our results are likely to be robust.

#### 2.4.4 Projection of least scatter

If both  $M_*$  and SFR are correlated with metallicity, then a linear combination of the two may provide a tighter relation with metallicity than the traditional  $M_*$ - $Z_g$  relation. This was explored by Mannucci et al. (2010), who calculated the scatter in median metallicity around their FMR for a series of projections onto the  $M_*$ -SFR- $Z_g$  space, fixing  $Z_g$  as a principle axis. We modify this method slightly to find the mean dispersion in  $Z_g$  of our binned data for the same 2D projections. Following Mannucci et al. (2010), the linear combination of  $M_*$  and SFR used is denoted by  $\mu_\alpha$ , where

$$\mu_\alpha = \log(M_*) - \alpha \log(\text{SFR}) \quad . \quad (2.5)$$

The free parameter  $\alpha$  defines the projection, and can be varied to shift from the  $M_*$ - $Z_g$  relation ( $\alpha = 0$ ) to  $\text{sSFR}^{-1}$ - $Z_g$  ( $\alpha = 1$ ). The corresponding dispersion function for the binned data of Sample T2 can be seen in the left panel of Fig. 2.7. To obtain this function, the spread in  $Z_g$  was calculated in 0.1 dex bins in  $\mu_\alpha$ , and the mean spread for each projection found. These mean dispersions from  $\alpha = 0$  to 1 were then fit by a third order polynomial to provide the solid line shown. The  $1\sigma$  spread in the dispersions calculated for each projection was also found and fit in the same way (dotted lines).

It is clear that the  $M_*$ - $Z_g$  relation ( $\alpha = 0$ ) is not the optimum projection for Sample T2. However, the decrease in scatter obtained when using the optimum projection ( $\alpha = 0.19$ ) is only slight ( $\sim 0.04$  dex). The right panel of Fig. 2.7 shows this optimum projection, which can be fit by the following polynomial:

$$Z_g = 43.4476 - 12.1927x + 1.37284x^2 - 0.0498564x^3 \quad (2.6)$$

within the range  $8.5 \leq \mu_{0.19} \leq 11.0$ , where  $Z_g = 12 + \log(\text{O}/\text{H})$  and  $x = \mu_{0.19} = \log(M_*) - 0.19 \log(\text{SFR})$ .

The improvement obtained for our Sample T1 is slightly better. A projection of  $\alpha = 0.36$  reduces the dispersion in  $Z_g$  by  $\sim 0.06$  dex compared to the  $M_*$ - $Z_g$  relation. For comparison, Mannucci et al. (2010) report an optimum projection of  $\alpha = 0.32$  for their sample.

The reason for the less significant improvement seen for Sample T2 is the inverse dependence of  $Z_g$  on SFR seen at low and high masses. The ‘u-shape’ that the

relation therefore forms in the 3D space makes it difficult to find a projection which reduces the overall scatter in  $Z_g$  as much as in Sample T1.

It is also interesting to note that when using fibre-SFRs, the projection of least scatter for Sample T2 drops to  $\alpha = 0.03$ , very close to the  $M_*$ - $Z_g$  relation. This is because the spread in star formation rates at low- $M_*$  is reduced due to the underestimation of SFR for nearby galaxies. For the same reason, when using fibre-SFRs for Sample T1, the value of  $\alpha$  shifts down to 0.26. Therefore, although some improvement to the scatter can be obtained by combining stellar mass and star formation rate in this way, the value of  $\alpha$  seems quite sensitive to the quantity derivation methods chosen. As the dispersion around the  $M_*$ - $Z_g$  relation for Sample T2 is already relatively tight, we suggest that it is still suitable for most purposes.

When fixing stellar mass as the principle axis, and using the optimum projection determined by Lara-López et al. (2010b), we find a mean dispersion of 0.74 dex and a  $1\sigma$  scatter of 0.24 dex around  $M_*$  from residuals. This equates to a  $1\sigma$  scatter of 0.17 dex around the composite axis from residuals, which can be compared to the value of 0.16 dex quoted by Lara-López et al. (2010b). The correspondence between the two values is good, despite differences in the sample selection. This is probably because both samples take values of  $M_*$ , SFR and  $Z_g$  from the SDSS-DR7 catalogue.

## 2.5 Gas-phase metallicity diagnostics

Obtaining accurate estimates of the gas-phase metallicity is not an easy process, as different diagnostics can provide very different results (see Section 1.2, and Kewley & Ellison 2008). However, it should be emphasised that the difference seen between our two observational samples (see Fig. 2.5) is not simply due to the inherent discrepancies between  $T_e$ , empirical and theoretical metallicity derivation methods. For the range of metallicities covered by our samples, both take their metallicities via theoretical methods. The difference is instead likely due to the use of either emission line ratios or a Bayesian approach with emission line fluxes in the analysis.

On this point, it should be remembered that theoretically derived strong line ratios are known to suffer from a number of problems, including degeneracies (Kewley & Dopita, 2002; Kewley & Ellison, 2008), sensitivity to the ionisation parameter (Kewley & Dopita, 2002; Erb et al., 2006a), saturation at high metallicities (Kewley & Dopita, 2002; Liang et al., 2006; Erb et al., 2006a; Kewley & Ellison, 2008) and inconsistency with  $T_e$  derived metallicities (Kennicutt et al., 2003; Bresolin et al., 2004; Garnett et al., 2004; Stasińska, 2005). It is not clear to what extent the technique used for Sample T2 suffers from these effects. There have been some concerns over the treatment of secondary nitrogen in the population synthesis models

used to produce the Sample T2 metallicity estimates (Liang et al., 2006; Yin et al., 2007). Accounting for this by excluding the [NII] (and [SII]) lines from the Bayesian analysis does not change the high-mass SFR-dependence seen. Removing these lines only seems to have a significant effect at low-masses, strengthening the dependence of  $Z_g$  on SFR seen there.<sup>2</sup>

Although the Bayesian estimates seem robust to the form of nitrogen emission modelling, such issues may still affect simpler strong line ratio diagnostics. For example, the twist in the  $M_*$ - $Z_g$  relation for Sample T2 is reproduced when using the diagnostics calibrated by McGaugh (1991) and Koblunicky & Kewley (2004), which do not rely on nitrogen. However, this is not the case for the Denicoló et al. (2002) diagnostic, which utilises the [NII] $\lambda$ 6584/H $\alpha$  ratio (S. Ellison, private communication). This could be an indication of further uncertainty in strong line ratio diagnostics that include nitrogen.

Additionally, there are three particular issues affecting the calibrations used for Sample T1 at high metallicity. First, there is the binning of data by Maiolino et al. (2008) when calibrating the diagnostics used for our Sample T1. A fit to unbinned data would have heavily biased their diagnostics against the lower metallicities crucial for high redshift studies such as theirs, due to the paucity of low- $Z_g$  galaxies available in their present-day calibration sample. However, this does mean that their fits are less precise at high metallicities, which is important for their application to local samples such as ours. Their  $R_{23}$  diagnostic over-predicts the average metallicity slightly compared to the average values obtained from the Kewley & Dopita (2002) model for  $Z_g \gtrsim 9.0$  (see fig. 5 in the Maiolino et al. (2008) paper). This raises the metallicity estimated in this regime somewhat, despite the use of the [NII]/H $\alpha$  diagnostic to bring down the final value.

Second, Nagao et al. (2006) have already pointed out that their metallicity derivation method – which uses the same calibration sample as Maiolino et al. (2008) – may over estimate the gas metallicity at  $Z_g > 9.0$  by a factor of  $\sim 0.1$  dex compared to the Tremonti et al. (2004) method. This is partly due to the bias towards selecting strongly [OII] and [OIII] emitting galaxies in the sample causing the fit to be steeper at high metallicities. When considering the  $R_{23}$  diagnostic, the fact that H $\beta$  emission is also weaker in low star formation environments could explain why the discrepancy we see is more significant at low-SFR (see Fig. 2.5).

Third, the practice of removing galaxies with estimates of  $Z_g$  from the [NII]/H $\alpha$

---

<sup>2</sup>It should be noted that a larger number of double-peaked likelihood distributions are produced when removing emission lines from the analysis. This can make it more difficult to determine the true metallicity. Further analysis of this new set of metallicity estimates is needed before more concrete statements can be made.

and  $R_{23}$  diagnostics that differ by more than 0.25 dex could artificially decrease the range of metallicities seen at high mass. This is because, a) the  $[\text{NII}]/\text{H}\alpha$  diagnostic is prone to *under*-estimating the metallicity in this regime, due to saturation as the electron temperature drops below that required to easily excite the  $[\text{NII}]\lambda 6584$  line. And b) the  $R_{23}$  diagnostic, as calibrated by Maiolino et al. (2008), seems to *over*-estimate the metallicity in this regime compared to the Bayesian technique by up to  $\sim 0.2$  dex, especially for lower-SFR galaxies, as discussed above. Therefore, only those galaxies with  $Z_g$  estimates in the overlapping region between these two discrepant measurements will remain in the sample.

Taking all this into account, it is perhaps prudent to suggest that such ratios are not ideal for estimating metallicities for high- $Z_g$ , local samples, where the availability of good spectroscopic data, including all optical emission lines, allows alternative techniques to be utilised.

### 2.5.1 An additional set of massive galaxies

Finally, we consider an adapted sample which includes an additional 9,275 high-mass ( $\geq 10^{10.5}M_\odot$ ) galaxies. These are the galaxies removed from the default Sample T2 due to having  $1\sigma$  uncertainties in their stellar mass estimates greater than 0.2 dex. The reason for this larger error seems to be due to large errors in the u-band magnitude measured, which is included in the estimation of stellar mass. This error has therefore likely propagated through to the confidence in the best fitting model during SED fitting, causing these galaxies to have a larger uncertainty in their  $M_*$  estimate.

Fig. 2.8 shows that, for masses greater than  $\sim 10^{10.5}M_\odot$ , these additional galaxies have only slightly greater  $1\sigma$  errors on their mass estimates than the default Sample T2 galaxies, and that their metallicity estimates are actually more than good enough for them to remain in the sample. We therefore choose to include these high-mass galaxies to strengthen our analysis of black hole mass in Section 2.7.3, and massive, elliptical galaxies in Chapter 3.

It is interesting to note that when plotting the  $M_*$ - $Z_g$  relation for Sample T2 including these additional galaxies, a range of SFR-dependent turnovers can be even more clearly seen at high mass. This is shown in Fig. 2.9.

## 2.6 Model Sample

In this section, we investigate the relationship between  $M_*$ , SFR and  $Z_{\text{cold}}$  in the Munich semi-analytic model of galaxy formation, L-GALAXIES (see Section 1.5.1).

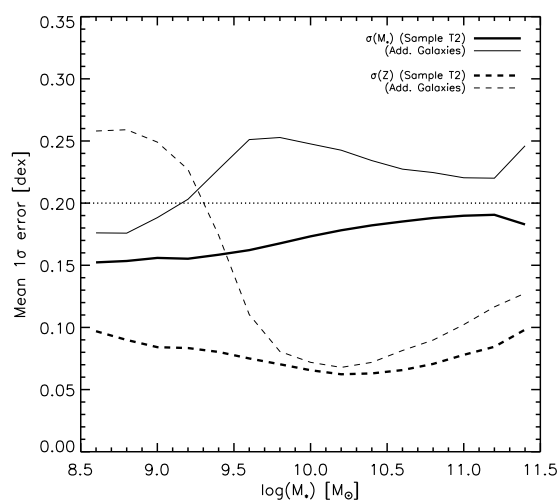


Figure 2.8: The mean  $1\sigma$  errors on the values of  $M_*$  (solid lines) and  $Z$  (dashed lines) provided by the best fitting models for the default Sample T2 (thick lines), and for the additional galaxies described in Appendix C (thin lines). At high masses, the error in  $M_*$  for the additional galaxies is only slightly greater than for the Sample T2 galaxies. The metallicity errors in the high-mass regime are well below the maximum acceptable error of  $\sigma = 0.2$  dex (indicated by the horizontal dotted line).

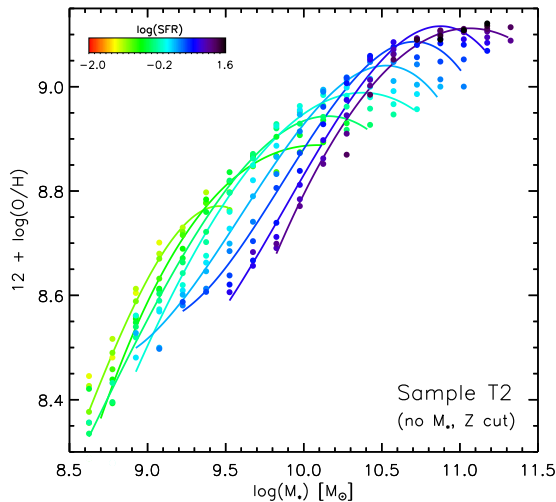


Figure 2.9: The  $M_*$ - $Z$  relation for Sample T2, when including the additional galaxies described in Appendix C. The shape of the overall relation is unchanged, but turnovers in the relation at fixed-SFR are now evident for wide a range of SFRs. This lends favour to the conclusion from our model sample, that processes other than outflows are regulating metallicity at high mass.

This allows us to analyse the detailed evolution of individual galaxies as well as global relations, and to compare the models to observations. Analytic descriptions of physical processes can be self-consistently incorporated into semi-analytic models and then easily adapted, making them more flexible than current SPH simulations. The models also provide large samples of galaxies with predicted stellar masses, metallicities and star formation rates, enabling detailed statistical comparisons with the observations to be made. We note here that the model assumes that the stellar IMF is the same everywhere, and at all epochs.

Our  $z = 0$  model sample comprises 43,767 central galaxies extracted from the Millennium Database (Lemson and the Virgo Consortium, 2006) provided by the German Astrophysical Virtual Observatory (GAVO)<sup>3</sup>. We use the catalogues generated by running the L-GALAXIES code on dark matter halo merger trees formed from the MILLENNIUM-II simulation, which is able to resolve DM halos down to a halo resolution limit of  $1.89 \times 10^8 M_\odot$ . Galaxies were selected by stellar mass ( $8.6 \leq \log(M_*) \leq 11.2$ ) and star formation rate ( $-2.0 \leq \log(\text{SFR}) \leq 1.6$ ) to span the same region of parameter space as our observational samples. Both type 0 and type 1 central galaxies are included in the model sample (see 1.5.1).

<sup>3</sup>available at; <http://www.g-vo.org/Millennium>

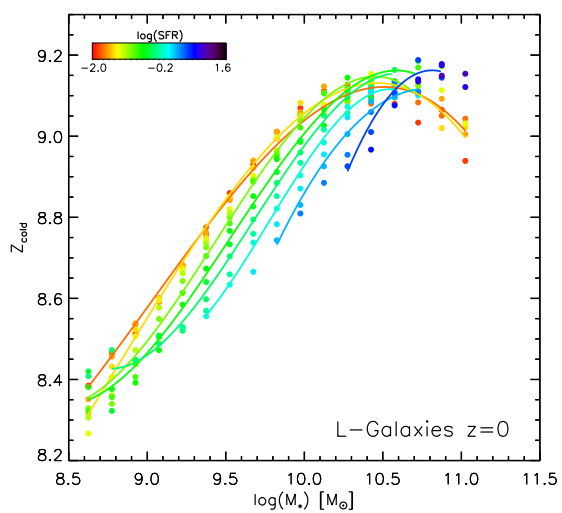


Figure 2.10: The  $M_*$ - $Z_{\text{cold}}$  relation for type 0 and type 1 model galaxies at  $z = 0$ . Binned data (filled circles) are coloured by their SFR, as are the fixed-SFR fits at  $\log(\text{SFR}) = -1.725, -1.425, -0.975, -0.675, -0.375, -0.075, 0.225, 0.525$ . The distinctive feature here is the high-mass turnover for low-SFR galaxies. This turnover causes the reversal of SFR-dependence from low- to high-mass in the model sample, which is also seen in our observational Sample T2.

We note here that, when comparing observations and our model, we are comparing the oxygen abundance of the HII regions surrounding hot, young stars in real galaxies with the average total metallicity of the whole ISM in model galaxies (see Section 2.7). Although these two quantities are similar (see Section 1.1), we have labelled them as  $Z_g$  and  $Z_{\text{cold}}$ , respectively, for clarity.

## 2.7 Model Results

### 2.7.1 The relation between $M_*$ , SFR and $Z_{\text{cold}}$ at $z = 0$

We bin the galaxies in our sample by  $M_*$  and SFR in the same way as was done for our observations. Only bins containing  $\geq 25$  galaxies are included in the model plots – half the number required in the observational samples. This is done in order to expand the dynamic range in the plots, but none of our results depends on this choice.

The *total cold gas-phase metallicity* for each bin is calculated. This is given by the ratio of mass in metals to total cold gas mass, normalised to the solar metal abundances previously assumed by Guo et al. (2011)<sup>4</sup>:  $Z_{\text{cold}} = 9.0 + \log(M_{\text{cold,Z}}/M_{\text{cold}}/0.02)$ .

The  $M_*$ - $Z$  relation for our  $z = 0$  model sample is shown in Fig. 2.10. We see a positive correlation between stellar mass and metallicity, as well as a segregation of this relation by SFR. Interestingly, this segregation is similar to that seen in Sample T2 (Fig. 2.3), with a reversal in the SFR-dependence from low to high masses. Another way of stating this result is that there is a ‘turnover’ at high stellar masses in the  $M_*$ - $Z_{\text{cold}}$  relation for low-SFR galaxies. Such a feature is hinted at in Sample T2, but we note that the number of real massive galaxies with emission lines that are strong enough to measure metallicity and that are not dominated by AGN emission is quite small. This may explain the relative weakness of the feature in the observations compared to the model. The stellar mass at which the turnover occurs is  $\sim 10^{10.4}M_{\odot}$ , again in quite good agreement with what is seen in Sample T2. It should be noted that the same turnover is seen when only type 0 galaxies are included in the model sample, and so is not a consequence of environmental effects.

The SFR- $Z_{\text{cold}}$  and the sSFR- $Z_{\text{cold}}$  relations are shown in the left and middle panels of Fig. 2.11. The  $D_n4000$  index is not available for our model galaxies, so only sSFR = SFR/ $M_*$  is used. As in our observations,  $Z_{\text{cold}}$  depends on star

---

<sup>4</sup>A change in the value of  $Z_{\odot}$  down to that preferred by Asplund et al. (2009) ( $Z_{\odot} = 8.69$ ) does not effect the slope of the relation or the distribution as a function of SFR (see also, Bertone, De Lucia & Thomas 2007). We therefore choose to stick with the value of  $Z_{\odot} = 9.0$  used by Guo et al. (2011) for consistency.

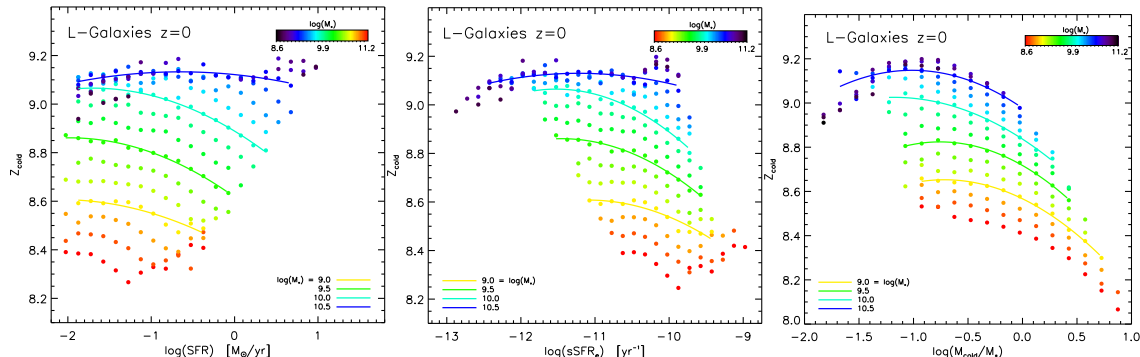


Figure 2.11: The SFR- $Z_{\text{cold}}$  relation (left panel),  $(\text{SFR}/M_*)$ - $Z_{\text{cold}}$  relation (middle panel) and  $(M_{\text{cold}}/M_*)$ - $Z_{\text{cold}}$  relation for the  $z = 0$  model sample. Fits to the data at four fixed stellar masses are shown (solid lines). The change in SFR-dependence from low- to high-masses evident in Fig. 2.10 is again seen. At fixed stellar mass,  $Z_{\text{cold}}$  is seen to decrease with increasing SFR (sSFR) at low masses, but decrease with *decreasing* SFR (sSFR) at high masses. Similarly, there is also a clear anti-correlation between gas-to-stellar mass ratio and metallicity at fixed- $M_*$  above  $\log(M_{\text{cold}}/M_*) \sim -1.0$ , but a direct correlation at lower gas-to-stellar mass ratios. These results are complimentary to those seen for our observational Sample T2 in Fig. 2.6.

formation at fixed stellar mass. As in Sample T2, there are a significant number of high-mass galaxies that show the opposite trend to that seen at low masses. Although the range of SFRs at  $z = 0$  in our model sample is shifted downwards compared to that of Sample T2, the overall trend is still that the metallicities of galaxies of mass  $\gtrsim 10^{10.5}M_{\odot}$  decrease with decreasing SFR and sSFR.

In the right panel of Fig. 2.11 we plot a new relation, that between the gas-to-stellar mass ratio ( $M_{\text{cold}}/M_*$ ) and gas-phase metallicity for the same model galaxies. Because cold gas is the fuel for ongoing star formation in a galaxy, the gas-to-stellar mass ratio should relate to the enrichment of the interstellar medium. We find that the average  $M_{\text{cold}}/M_*$  decreases with stellar mass and with  $Z_{\text{cold}}$  for galaxies with stellar masses less than  $\sim 10^{10.5}M_{\odot}$ . At higher stellar masses, we again see a turnover towards low metallicities at low  $M_{\text{cold}}/M_*$ . We conclude that the low-sSFR galaxies that contribute to the high-mass turnover in the  $M_*$ - $Z_{\text{cold}}$  relation also tend to have lower  $M_{\text{cold}}/M_*$  than other galaxies of a similar mass. This is also seen in the sSFR- $(M_{\text{cold}}/M_*)$  relation, shown in Fig. 2.12, where these galaxies are indicated by red circles.

Currently, there is only limited data available on the gas fractions of high-mass galaxies with low star formation rates. However, with the development of the GASS

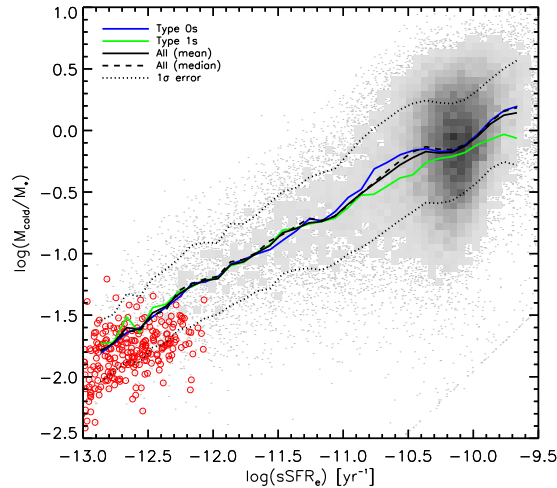


Figure 2.12: The sSFR- $(M_{\text{cold}}/M_*)$  relation for our  $z = 0$  model sample. The relation for type 0 galaxies (blue line) and type 1 galaxies (green line) is shown, as well as the mean (solid black line) and median (dashed black line) relation for the full sample (shown in grey). The  $1\sigma$  spread around the mean is shown as dotted lines. The low-sSFR galaxies that form the high-mass turnover in the model  $M_*$ - $Z_{\text{cold}}$  relation are indicated by red circles. These galaxies tend to have lower-than-average gas-to-stellar mass ratios for their sSFR.

(GALEX Arcicibo SDSS Survey, Catinella et al. 2010) and COLDGASS (CO Legacy Database for GASS, Saintonge et al. 2011) programmes, as well as the maturity of the ALMA survey, we will soon have a significant number of gas-to-stellar mass ratios for high-mass SDSS galaxies with which to compare. Comparisons with the ALFALFA and GASS data sets are made in Chapter 3.

### 2.7.2 Metallicity evolution in model galaxies

In this section, we study the origin of the turnover in the model  $M_*$ - $Z_{\text{cold}}$  relation seen in Fig. 2.10. We do this by splitting the high-mass end of the sample into low-metallicity and high-metallicity sub-populations and studying differences in their evolutionary histories. We extracted two high-mass ( $M_* > 10^{10.8} M_{\odot}$ ) sub-samples: a high- $Z_{\text{cold}}$  ( $Z_{\text{cold}} \geq 9.2$ ) sub-sample containing 134 galaxies, and a low- $Z_{\text{cold}}$  ( $Z_{\text{cold}} \leq 9.0$ ) sub-sample containing 136 galaxies. The mass, metallicity and SFR evolution of these two sub-samples was then compared.

The L-GALAXIES model tracks seven distinct mass components of galaxies: the stellar bulge, stellar disc, black hole mass, cold gas mass (ISM), hot gas mass (ICM),

ejected gas mass (IGM) and halo stars (producing the intra-cluster light). Mass (including metals) can pass between these components along pre-defined routes, depending on the processes taking place (see Fig. 1.4). The top three panels of Fig. 2.13 show the time evolution of some of these mass components for three representative galaxies from the model with high stellar masses and high metallicities. In the middle panels, we show the time evolution of the stellar and gas-phase metallicities of the same galaxies. The bottom panels show the time evolution of their global star formation rates.

The left panels display a type 0 galaxy in which the total stellar mass (solid orange line) has been steadily increasing since redshift two. In this galaxy, the mass of cold gas (solid blue line) is always higher than the critical value required for star formation,  $M_{\text{crit}}$  (dashed blue line). There is a steady, gradual increase in the metallicity of the stellar, cold gas and hot gas components. This is because stars are formed continuously, synthesising and distributing metals throughout the galaxy at a higher rate than the dilution due to the accretion of metal-poor gas. Around 64 per cent of the galaxies in our high- $Z_{\text{cold}}$  sub-sample have formation histories similar to this.

The middle panels show a galaxy that first evolves in a similar way to the galaxy shown in the left panels. It is then accreted onto a more massive DM halo at  $z \sim 1.0$ , becoming a type 1 object, at which point gas and dark matter begin to be tidally stripped. Some of these type 1 galaxies, like the example shown in the middle panel, then exhibit a sharp increase in gas-phase metallicity. This is because gas accretion onto the galaxy is reduced, but star formation continues, and as a result, metals continue to be dispersed into ever decreasing volumes of hot and cold gas. In other type 1 galaxies in the high- $Z_{\text{cold}}$  sub-sample, the cold gas mass drops below  $M_{\text{crit}}$  after being accreted, causing the cold gas metallicity to remain constant thereafter, due to a shut-down in both star formation and galactic gas accretion. Type 1 galaxies with star formation histories of these forms constitute  $\sim 30$  per cent of the high- $Z_{\text{cold}}$  sub-sample.

The right panels of Fig. 2.13 show a class of central galaxy that formed a bulge and a SMBH at redshifts greater than two. The black hole (solid black line) then grew steadily through radio-mode accretion of hot gas from the surrounding halo (see Section 1.5.1). Such galaxies are not representative of the high- $Z_{\text{cold}}$  sub-sample as a whole (they comprise only 6 per cent of the sub-sample) and are almost certainly classified as AGN and so missing from our observational samples. Nevertheless, we think they are rather interesting. The galaxy makes it into our high- $Z_{\text{cold}}$  model sub-sample due to the fact that it accretes many, many satellites over time (4,141 since redshift two, compared to only 21 and 71 for the galaxies in the left and middle

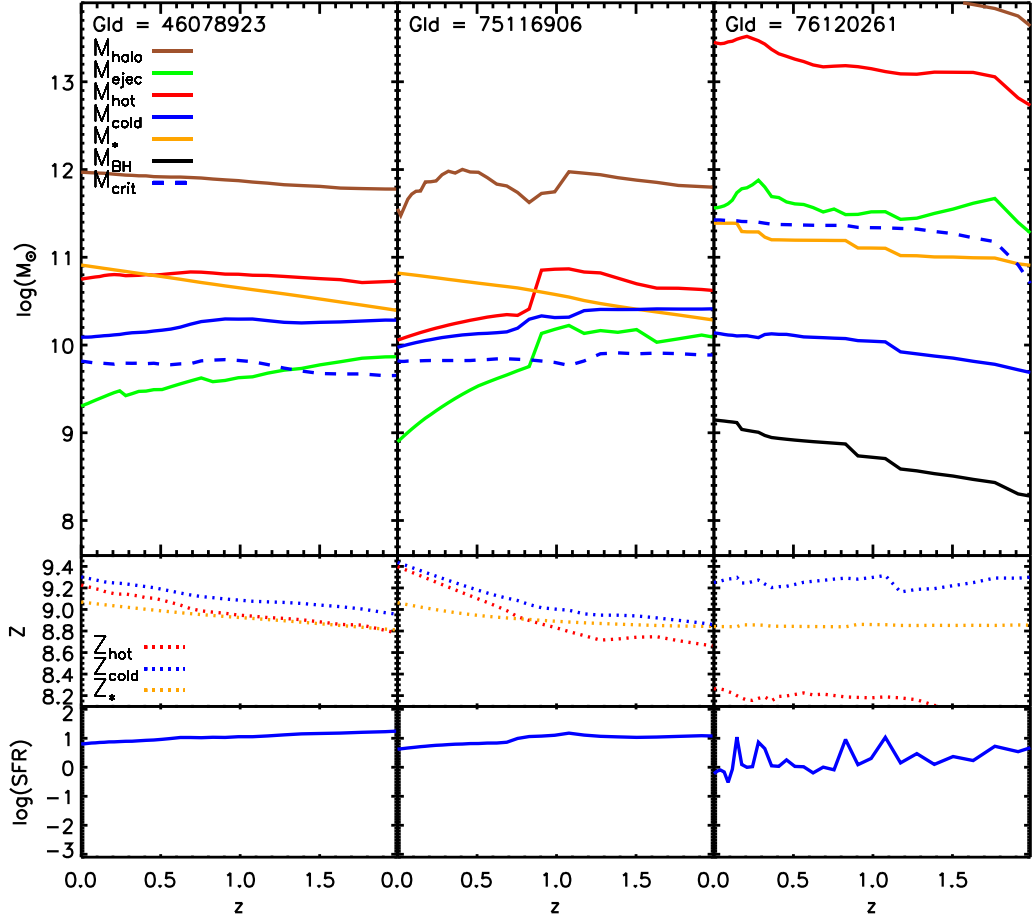


Figure 2.13: The evolution from  $z = 2$  to 0 in mass (top panels), metallicity (middle panels) and SFR (bottom panels) for three typical galaxies from the high-mass, high- $Z_{\text{cold}}$  sub-sample. Galaxies in this sub-sample tend to undergo gradual enrichment of their cold gas phase over time. The galaxy IDs for these galaxies from the Millennium Database are provided at the top of each panel.

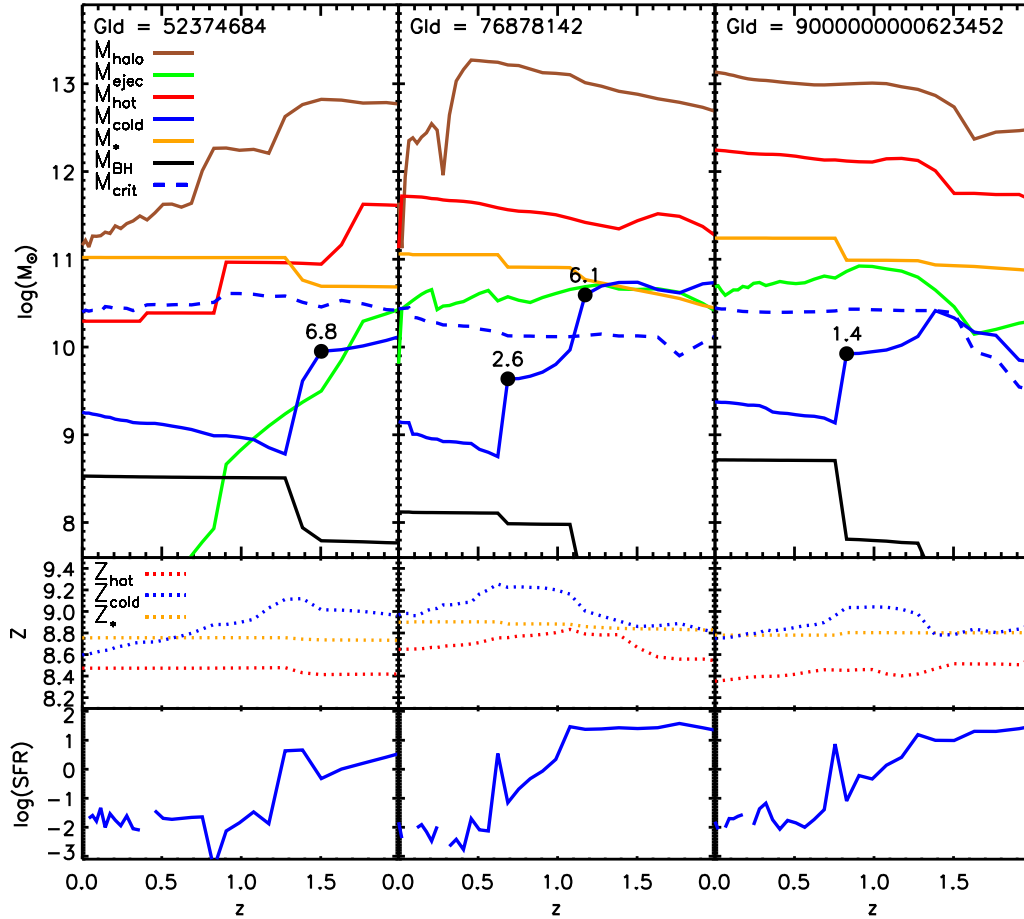


Figure 2.14: The evolution from  $z = 2$  to 0 in mass (top panels), metallicity (middle panels) and SFR (bottom panels) for three typical galaxies from the high-mass, low- $Z_{\text{cold}}$  sub-sample. These galaxies show the gradual dilution of the cold gas phase that is characteristic of the low- $Z_{\text{cold}}$  sub-sample. The Galaxy IDs for these galaxies from the Millennium Database are provided at the top of each panel.

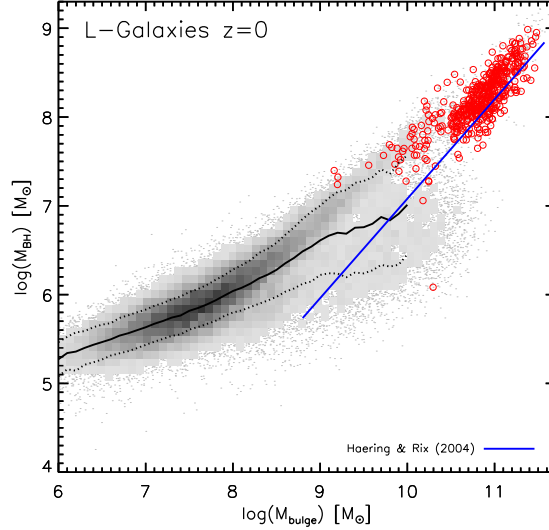


Figure 2.15: The  $M_{\text{bulge}}-M_{\text{BH}}$  relation for our  $z = 0$  model sample. The full sample is shown in grey, with the mean relation plotted as a solid black line. The  $1\sigma$  spread around the mean is shown as dotted lines. Galaxies in the low- $Z_{\text{cold}}$  sub-sample are highlighted by red circles. These galaxies have higher black hole masses than expected from an extrapolation of mean model relation, but lie nicely along the observational relation derived by Häring & Rix (2004).

panels, respectively). The satellites bring in fresh gas, leading to the very ‘bursty’ star formation history seen in the bottom-right panel of Fig. 2.13. We note that this galaxy resides in the center of the 9th most massive DM halo in the whole MILLENNIUM-II simulation at  $z = 0$ , and so such a high rate of satellite accretion is perhaps unsurprising.

In conclusion, for the majority of galaxies in the high- $Z_{\text{cold}}$  sub-sample, the dominant process driving metallicity evolution is clearly a *gradual enrichment* of the gas phase due to continuous star formation. At these high masses, outflows are inefficient at removing cold gas and metals from the galaxy. At these high SFRs, galactic infall rates are too low to dilute the ISM. Consequently, these galaxies become increasingly metal-rich with time.

Fig. 2.14 paints a rather different picture for the evolution of galaxies in the low- $Z_{\text{cold}}$  sub-sample. All three galaxies have undergone dramatic drops in their cold gas masses, coinciding with a merger event at some stage during the past ten gigayears. Mergers with mass ratio less than 10:1 are marked by black dots on the  $M_{\text{cold}}$  evolution line. Note that no such mergers occur for the three high- $Z_{\text{cold}}$

examples in Fig. 2.13 – only 7.5 per cent of galaxies in the high- $Z_{\text{cold}}$  sub-sample have undergone such a significant merger over the last ten gigayears. A merger with mass ratio 3:1 or less is considered a major merger in the model, causing the destruction of the stellar and gas discs and the transfer of this material to the bulge of the descendant. We see from Fig. 2.14 that not only major mergers cause the sudden drop in  $M_{\text{cold}}$ . Gas-rich minor mergers are also effective at inducing starbursts and the rapid growth of the central SMBH through ‘quasar mode’ (cold) accretion. During such events, a black hole can grow by swallowing both cold gas and the smaller black hole of its companion. 92 per cent of the galaxies in the low- $Z_{\text{cold}}$  sub-sample have present-day black holes with masses greater than  $10^{8.0}M_{\odot}$ , that were formed through this process. The remaining 8 per cent have either grown their black holes gradually through ‘radio-mode’ (hot) accretion, or do not contain a central SMBH.

We note that although large black holes are a feature of almost all the galaxies in the low- $Z_{\text{cold}}$  sub-sample, they do not *cause* the low metallicities seen in these galaxies at  $z = 0$ . These are instead caused by a cessation in star formation due to the sudden drop in cold gas mass below  $M_{\text{crit}}$ , followed by accretion of metal-poor gas onto the galaxy. This galactic accretion is limited to a low rate, as secular cooling from the CGM is suppressed by radio-mode AGN feedback (see Section 3.3.2). The three galaxies in Fig. 2.14 therefore show that *gradual dilution* of the gas phase due to metal-poor infall of gas in the absence of star formation is the main process producing the low- $Z_{\text{cold}}$  sub-sample.

Such a dilution effect is not seen in hydrodynamic simulations of galaxy evolution such as those carried out by Finlator & Davé (2008) and Davé, Oppenheimer & Finlator (2011). In those models, galaxies quickly fall back into an equilibrium between their infall, outflow and star formation rates after a perturbative event, whereby  $\dot{M}_{\text{infall}} = \dot{M}_{*} + \dot{M}_{\text{outflow}}$ . Instead, the inclusion of AGN feedback in our model allows  $\dot{M}_{\text{infall}} > \dot{M}_{*} + \dot{M}_{\text{outflow}}$ , enabling galaxies to slowly accrete metal-poor gas for a number of gigayears without forming stars.

We note that it remains to be seen whether the fraction of massive galaxies in the models with very little ongoing star formation and low metallicity reservoirs of cold gas is matched in observations. The low gas fractions of massive galaxies means that the gas is difficult to detect. Until HI maps of a large sample of such objects are made, only indirect indicators of such metal-poor accretion can be studied in observations. This is discussed further in Chapter 3.

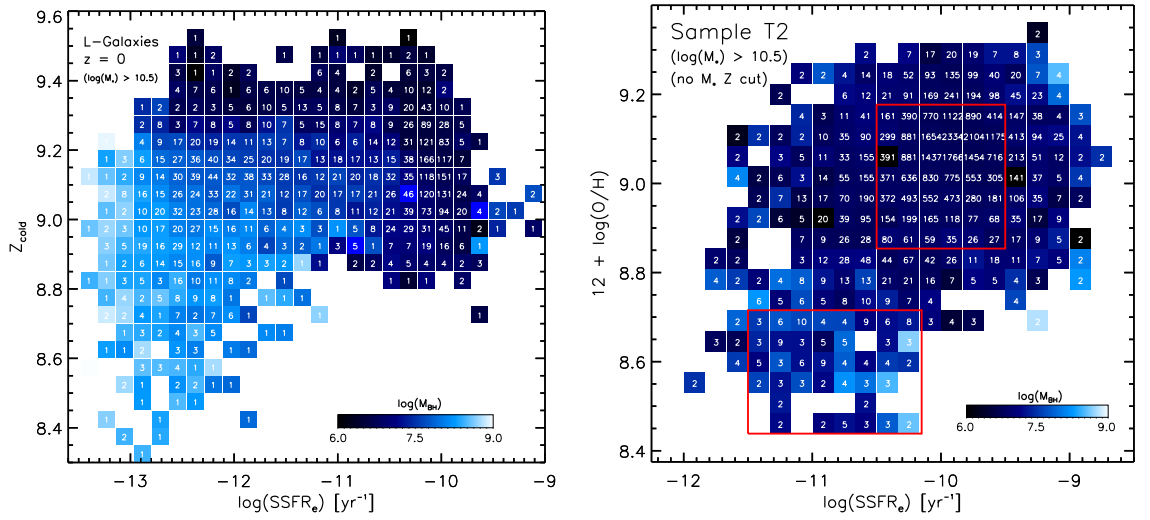


Figure 2.16: The  $(\text{SFR}/M_*)$ - $Z_{\text{cold}}$  relation for our model sample (left panel) and observational Sample T2 (right panel) for galaxies of stellar mass  $> 10^{10.5}M_{\odot}$ . Galaxies had been binned by  $\text{sSFR}_e$  and  $Z_{\text{cold}}$ , and bins are coloured by the mean black hole mass of the constituent galaxies. The number of galaxies in each bin is also given by white text. The low  $\text{sSFR}$ , low- $Z_{\text{cold}}$  population clearly have larger central SMBHs in the model sample. A similar dichotomy can be seen in Sample T2, though the distinction is not as clearly defined. The red boxes in the right panel mark the low- $Z_{\text{cold}}$  and high- $Z_{\text{cold}}$  regions shown in Fig. 2.17.

### 2.7.3 Bulge and black hole masses

As discussed in the previous section, one distinguishing feature of massive, low- $Z_{\text{cold}}$  galaxies in the model is the presence of a massive bulge and massive central black hole formed during a merging event. This is illustrated by the  $M_{\text{bulge}}-M_{\text{BH}}$  relation in Fig. 2.15, where the galaxies in the low- $Z_{\text{cold}}$  sub-sample are highlighted by red circles. Interestingly, it is these galaxies that lie closest to the observational relation found by Häring & Rix (2004). It is unclear whether this relation extends down to lower bulge masses with the same slope, or levels-off as seen in the model. A significant fraction of intermediate to massive galaxies with smaller central black holes have likely had their bulges grown through secular processes (Shankar et al. 2012, 2013). Although massive central black holes are not the cause of the low metallicities in the low- $Z_{\text{cold}}$  sub-sample, they are an associated feature that we can look for in the currently available observational data.

In the left panel of Fig. 2.16, specific star formation rate is plotted against gas phase metallicity for all our high mass model galaxies. Galaxies are binned by  $\text{sSFR}_e$  and  $Z_{\text{cold}}$ , and the bins are coloured by the mean black hole mass of the galaxies in each bin. The number of galaxies in each bin is also indicated on the plot in white text. It is clear that low-sSFR, low- $Z_{\text{cold}}$  galaxies have the largest central black holes in the model.

The right panel of Fig. 2.16 shows the same plot for an adapted version of our observational Sample T2 (see Section 2.5.1). Black hole masses were estimated via the measured stellar velocity dispersion,  $\sigma$ , using the  $M_{\text{BH}}-\sigma$  relation provided by Tremaine et al. (2002):

$$\log(M_{\text{BH}}) = \alpha + \beta \log(\sigma/\sigma_0) \quad , \quad (2.7)$$

where  $\alpha = 8.13$ ,  $\beta = 4.02$ ,  $\sigma_0 = 200\text{km/s}$  and  $M_{\text{BH}}$  is in units of  $M_{\odot}$ . We can see that the observational data also contains a low- $Z_{\text{cold}}$ , high- $M_{\text{BH}}$  population, though the distinction between this population and the majority of the sample is less clear than in the model.

The dichotomy in the observations is more clearly seen in Fig. 2.17, where the distribution of black hole masses is shown for galaxies contained within the two red boxes<sup>5</sup> marked in Fig. 2.16. The black hole population is clearly shifted to higher masses in the low- $Z_g$  region (blue histogram), compared to the high- $Z_g$  region (red histogram). 24 per cent of galaxies within the low- $Z_g$  region have black holes of mass

<sup>5</sup>The boundaries chosen for these boxes are somewhat arbitrary. They are designed to cover the two regimes of interest, namely, high- $Z_g$ , low  $M_{\text{BH}}$  galaxies and low- $Z_g$ , high- $M_{\text{BH}}$  galaxies. Shifting the boundaries of the two regions does not affect the results found.

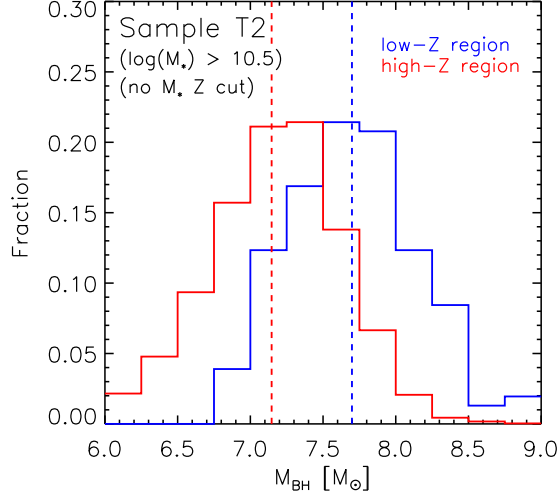


Figure 2.17: The distribution of black hole masses in Sample T2 for low- $Z_g$  (blue histogram) and high- $Z_g$  (red histogram) galaxies. These are the galaxies marked by the red boxes in Fig. 2.16. The mean  $M_{\text{BH}}$  of each region is also shown by vertical dashed lines. Low- $Z_g$ , low-sSFR galaxies have more massive central black holes in Sample T2, as seen in the model sample.

$\geq 10^{8.0} M_{\odot}$ . This is only true for 2.7 per cent of galaxies in the high- $Z_g$  region. A correlation between low metallicities, low-sSFRs and high black hole masses therefore seems present in both our model and observational sample.

#### 2.7.4 Evolution of the $M_*$ - $Z_{\text{cold}}$ relation out to $z \sim 3$

In this section, we analyse the evolution of the  $M_*$ - $Z_{\text{cold}}$  relation out to  $z \sim 3$ . Observations have shown a clear evolution in this relation (e.g. Maiolino et al. 2008; Zahid, Kewley & Bresolin 2011; Moustakas et al. 2011) and the  $M_*$ -SFR relation (e.g. Noeske et al. 2007a,b; Elbaz et al. 2007; Kajisawa et al. 2010) with look-back time, and a certain kind of evolution is required for the Mannucci FMR to remain fixed out to  $z \sim 2.5$ .

In order to investigate this in L-GALAXIES, three supplementary, identically selected samples of type 0 and 1 galaxies were extracted from the database at redshifts  $z = 1.0$ , 2.0 and 3.1. These samples contain 63,745, 63,017 and 50,558 galaxies, respectively, within the parameter space of interest.

The evolution of the model  $M_*$ -SFR relation from  $z = 3.1$  to 0 is plotted in Fig. 2.18. Although there is a strong evolution seen in the mean  $\log(\text{SFR})$  over cosmic

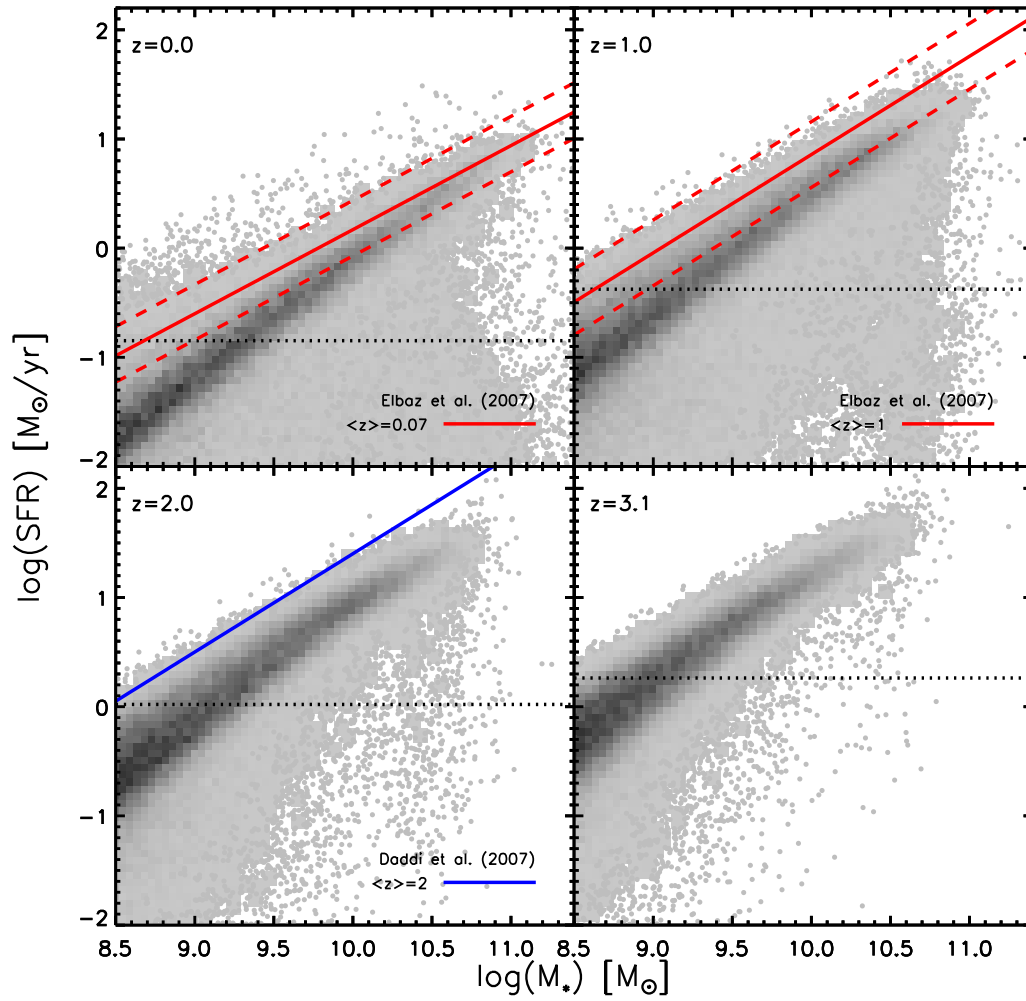


Figure 2.18: The evolution of the model  $M_{*}$ -SFR relation in L-GALAXIES from  $z = 3.1$  to 0. The average  $\log(\text{SFR})$  at each redshift is plotted (horizontal dotted lines). Fits to observational data from the SDSS at  $z \sim 0.07$  and GOODS at  $z \sim 1.0$  by Elbaz et al. (2007), and from GOODS at  $z \sim 2.0$  by Dodd et al. (2007), are also shown for comparison.

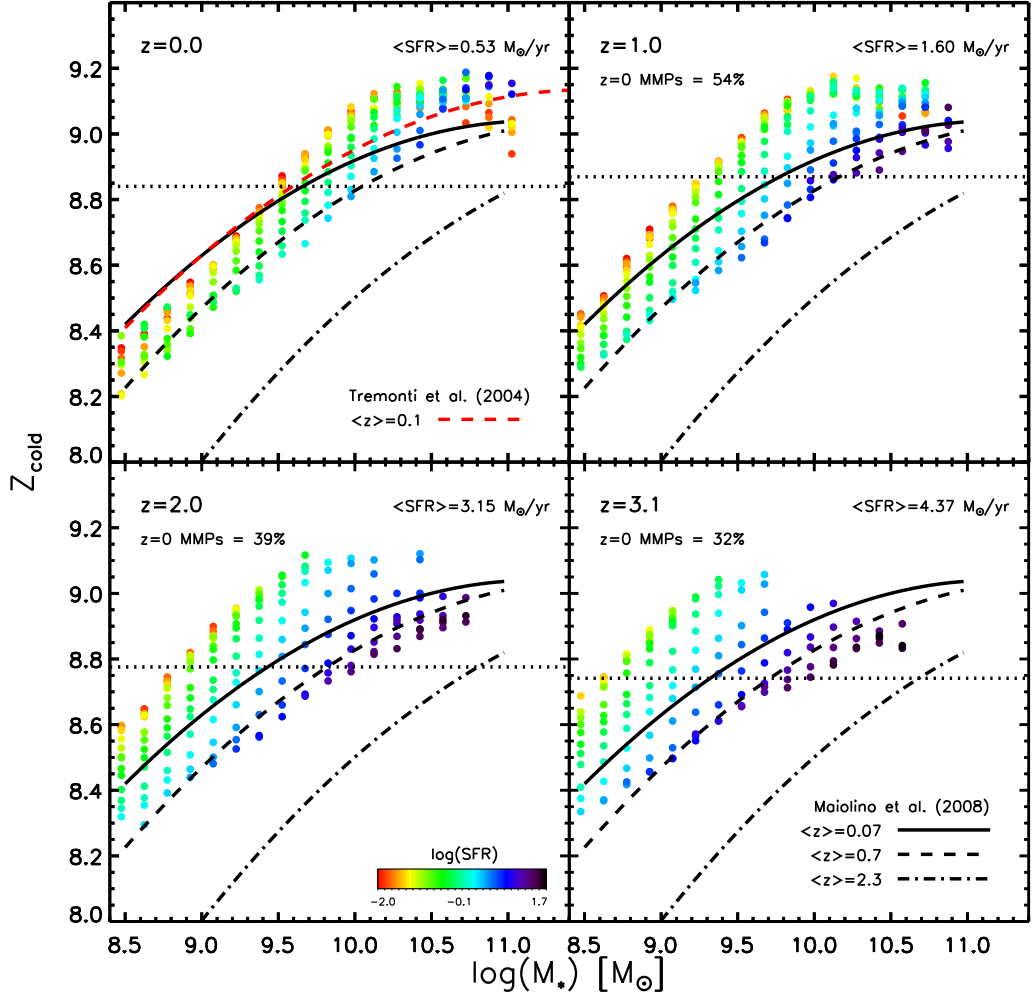


Figure 2.19: The evolution of the model  $M_*$ - $Z_{\text{cold}}$  relation in L-GALAXIES from  $z = 3.1$  to 0. The average metallicity at each redshift is plotted (horizontal dotted lines), and the mean SFR at each redshift is given in the top right of each panel. The percentage of galaxies in each higher redshift sample that have direct descendants in the  $z = 0$  sample is shown in the top left of each higher redshift panel. Fits to observational data at three different redshifts compiled by Maiolino et al. (2008) are also shown. These are taken from Kewley & Ellison (2008) for  $\langle z \rangle = 0.07$ , Savaglio et al. (2005) for  $\langle z \rangle = 0.7$  and Erb et al. (2006a) for  $\langle z \rangle = 2.3$ . A fit to the Tremonti et al. (2004)  $\langle z \rangle = 0.1$  relation (red dashed line) is also shown in the  $z = 0$  panel.

time, dropping by  $\sim 1.0$  dex from  $z = 3.1$  to 0.0, the SFRs of model galaxies are already too low by  $z \sim 3$  compared to observations. For example, at  $z = 2.0$ , the main sequence of star formation in the model is  $\sim 0.5$  dex lower in SFR than is seen in the Great Observatories Origins Deep Survey (GOODS) by Daddi et al. (2007). Additionally, even at low- $z$ , low-mass galaxies tend to have SFRs below that observed in the GOODS and SDSS by Elbaz et al. (2007) (but see Henriques et al. 2013).

The evolution of the model  $M_*$ - $Z_{\text{cold}}$  relation, binned by  $M_*$  and SFR, from  $z = 3.1$  to 0 is plotted in Fig. 2.19. We can see the strengthening of the SFR- $Z_{\text{cold}}$  correlation at high mass from  $z = 1$  to 0, as low-SFR galaxies begin to gradually dilute their ISM and decrease in  $Z_{\text{cold}}$  over time. However, there appears to be no clear evolution in average metallicity at fixed stellar mass at all in the model, contrary to observations. The present day  $M_*$ - $Z_{\text{cold}}$  relation agrees well with those of Tremonti et al. (2004) and Kewley & Ellison (2008) at  $z \sim 0$ , but the discrepancy with observations becomes increasingly pronounced towards higher redshifts.

The discrepancies in the evolution of model  $M_*$ -SFR and  $M_*$ - $Z_{\text{cold}}$  relations suggest that both the star formation and chemical enrichment in the model galaxies proceeds too rapidly at early times.

In order to diagnose whether this hypothesis is correct, we plot the enrichment history from  $z = 2$  to the present day of four representative galaxies from the  $z = 0$  model sample in Fig. 2.20. The  $M_*$ - $Z_{\text{cold}}$  relation for the entire  $z = 0$  sample is also plotted in grey. This is a reasonable test, as a large number of galaxies in the  $z = 0$  sample have main progenitors present in the higher redshift samples; the percentage of galaxies that lie on the most massive progenitor (MMP) branch of a  $z = 0$  galaxy is indicated in the top left corner of each higher redshift panel in Fig. 2.19.

In Fig. 2.20, we can again see the two types of behaviour at high stellar masses described in Section 2.7.2, with both  $Z_{\text{cold}}$  and stellar mass gradually increasing with time for the high-SFR galaxy (blue track), and metallicity decreasing with time without any associated increase in stellar mass for the low-SFR galaxy (red track). At intermediate masses, stellar mass and metallicity increase together, punctuated by periods when  $Z_{\text{cold}}$  drops suddenly, due to an episode of enhanced gas accretion, such as a gas rich merger with a metal-poor satellite.

At low masses, the metallicity evolution appears much more erratic. Drastic fluctuations in  $Z_{\text{cold}}$  may occur when outflows become extreme enough to drive most of the gas out of the galaxy. This is the case for the lowest mass galaxies in the model, as a result of the SN feedback scheme described in Section 1.5.1.

We can see from the grey points in Fig. 2.20 that the scatter in the  $M_*$ - $Z_{\text{cold}}$  relation at  $z = 0$  increases towards lower masses as a consequence of this stochastic

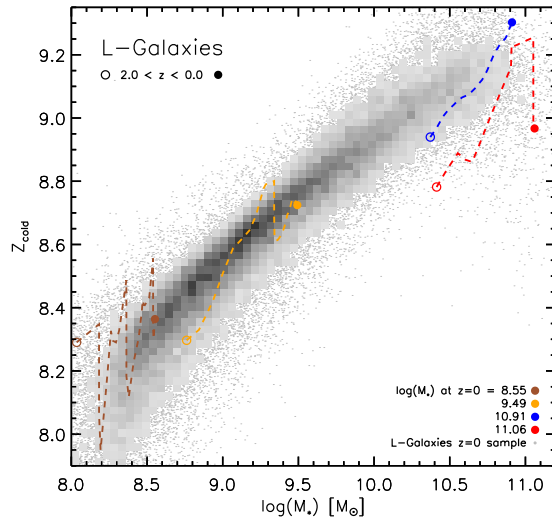


Figure 2.20: The evolution of four model galaxies from our  $z = 0$  sample from redshift 2 to 0. Galaxies of final stellar mass  $\log(M_*) = 8.55, 9.49, 10.91$  and  $11.06$  are shown in brown, orange, blue and red, respectively. The two higher mass examples are GID46078923 (blue) and GID76878142 (red) from the high-mass sub-samples shown in Figs. 2.13 and 2.14. The full present day population is also shown in grey for comparison. We can see that galaxies tend to evolve along the  $z = 0$  relation at all masses, but that the nature of this evolution is different for different mass intervals.

mode of evolution. Lee et al. (2006) have used a sample of 27 nearby dwarf galaxies to argue that the scatter in the observed local  $M_*$ - $Z_{\text{cold}}$  relation remains roughly constant down to stellar masses of  $\sim 10^{6.5}M_{\odot}$ . This might suggest that, unlike metals, cold gas is not driven very effectively out of low mass galaxies by supernovae (Mac Low & Ferrara, 1999). However, more recent observational studies have revealed a much larger scatter in the  $M_*$ - $Z_{\text{cold}}$  relation at low mass (Peeples, Pogge & Stanek, 2008; Zahid et al., 2012a), in closer correspondance with that seen in our model.

The main point to take away from Fig. 2.20 is that galaxies evolve along the present-day  $M_*$ - $Z_{\text{cold}}$  relation in the model, rather than from much lower metallicities, as suggested by observations. This suggests that it is indeed an overly rapid enrichment of the cold gas phase of galaxies before redshift three that is causing the lack of evolution thereafter in the model.

One possible solution to the problem is that accreted gas is ‘hung-up’ in the atomic phase of the ISM for some time, before it is able to reach high enough densities to form the molecular clouds in which stars are formed (Gnedin, Tassis & Kravtsov, 2009; Gnedin & Kravtsov, 2010). Recently, Fu et al. (2010) implemented simplified prescriptions for the formation of molecular gas in galaxies in the L-GALAXIES code, to study scaling relations between gas and stars in local galaxies. Fu et al. (2013) have further shown that such prescriptions allow a greater evolution in the model  $M_*$ - $Z_{\text{cold}}$  relation with time. However this implementation is not part of the Guo et al. (2011) model discussed here. Lagos et al. (2011b) have also implemented star formation laws dependent on the surface density of molecular gas into the GALFORM semi-analytic model. Their results also suggest that such prescriptions lower the typical star formation rate of central galaxies at higher redshifts.

## 2.8 Discussion

In Section 2.4, we have shown that our preferred observational sample, Sample T2, exhibits a reversal in the dependence of metallicity on star formation rate from low to high stellar mass. At low stellar masses, SFR and  $Z_g$  anti-correlate, whereas at high stellar masses, SFR and  $Z_g$  positively correlate.

There remains a multiplicity of explanations for the dependence seen at low mass. When considering galactic outflows, it can be argued that low-SFR galaxies produce relatively fewer SNe, disrupting the ISM less and blowing away metals less efficiently than in high-SFR galaxies (e.g. Mac Low & Ferrara 1999). When considering a closed-box model, lower star formation rates at fixed mass imply lower cold gas masses, which in turn imply a higher rate star formation in the past. The ISM of these galaxies would therefore be more metal-rich today (Ellison et al., 2008).

Alternatively, Dib et al. (2011) have suggested that the inter-dependence between SFR and  $Z_{\text{cold}}$  is due to a more fundamental dependence of the pre-stellar core formation efficiency (CFE) on metallicity. In their analytical model, star forming regions of higher metallicity form more OB stars, whose stellar winds remove the surrounding gas and so truncate star formation more quickly.

The dependence seen at high stellar mass is, however, more difficult to explain. In the absence of effective galactic outflows at high mass, low-SFR galaxies could simply under-enrich the ISM relative to more actively star forming galaxies, by producing fewer metals. However, the high-mass dependence seen in our model sample is caused by a *turnover* in the  $M_*$ - $Z_{\text{cold}}$  relation. Such a feature *cannot* be explained by mass-dependent processes alone. If the turnover seen in the model  $M_*$ - $Z_{\text{cold}}$  relation is indeed real, then additional physical mechanisms must be at play.

Our model points to metal-poor galactic infall at high mass as an explanation. Those high- $M_*$  galaxies with low gas-phase metallicities are known to have undergone gradual dilution of their gas phases after a merger event which shut-down further star formation. The prevention of diffuse cooling by AGN feedback allowed these galaxies to *slowly* dilute their ISM, without accreting enough gas for star formation to quickly resume. The turnover that this causes in the model is not as clearly seen in our observations (although, see Section 2.5.1). However, correlations between these galaxies and the high- $M_*$ , low- $Z_g$  galaxies in our observational sample (namely, their large black hole masses) imply that a dilution process could also be involved in shaping the  $M_*$ - $Z_g$  relation in the real Universe. This is discussed further in Chapter 3.

There are, however, two factors hampering this interpretation. First, the dependence of  $Z_g$  on SFR is itself strongly dependent on how these properties are measured (see Section 2.4). Although a high-mass dependence is undeniable in our Sample T2, it is not present in Sample T1 within the range of masses studied.

Second, the recipes used to model physical processes in this version of L-GALAXIES are still rather crude, and this could be affecting the galaxy evolution seen in our model galaxies. For example, metals are assumed to be ejected by stars instantaneously, and to fully mix with the ISM *before* galactic outflows are allowed to drive gas out of the galaxy. This means that it is the subsequent cessation of star formation in low-mass galaxies that is causing the relation between  $M_*$  and  $Z_{\text{cold}}$  in the model, rather than explicitly metal-rich outflows. Clearly an improved treatment of chemical enrichment is required. Such a treatment is discussed in detail in Yates et al. (2013) and Chapter 4.

Despite these two caveats, we believe our interpretation to be viable. On the observational side, the use of many emission line fluxes and SED fitting (as is done

for many trusted stellar mass estimations) is likely to be a more robust way of estimating metallicities than using individual emission line ratios (see Section 2.5). On the modelling side, the problems outlined above are currently common to models in general. For example, the SPH simulation described by Davé, Finlator & Oppenheimer (2011), which exhibits the same evolution of galaxies along the present-day  $M_*$ - $Z_{\text{cold}}$  relation, also has difficulties reproducing the observed metallicity evolution. Their favoured  $vzw$  model (which invokes momentum-driven winds and metal-rich outflows at all masses) shows an increase in  $Z_{\text{cold}}$  of  $\sim 0.15$  dex from  $z = 2$  to 0 for galaxies of stellar mass  $\sim 10^{9.5}M_{\odot}$ . Their fixed, low wind velocity  $sw$  model shows an evolution of  $\sim 0.1$  dex (an amount similar to that seen in L-GALAXIES). In comparison, observations suggest an evolution of  $\sim 0.5$  dex at the same mass from  $z = 2.3$  to 0.07 (Maiolino et al., 2008). Further improvements to the observational determination of gas-phase metallicities, and the ongoing improvements in accurate modelling of galactic evolution, are necessary before significant progress can be made in this area.

## 2.9 Conclusions

We have shown that the gas-phase metallicities of galaxies are dependent on their star formation rate. This is also true at high masses, where highly star forming galaxies are seen to have *higher* metallicities – the opposite trend to that seen at low masses. Because this dependence is not as straightforward as first assumed, a projection onto the  $M_*$ -SFR- $Z_g$  space that combines  $M_*$  and SFR does little to reduce the scatter in  $Z_g$  compared to the  $M_*$ - $Z_g$  relation, decreasing the mean dispersion by only  $\sim 0.04$  dex.

We also demonstrate the significance of the metallicity diagnostic chosen when assessing the relation between  $M_*$ , SFR and  $Z_g$ . Strong line ratio diagnostics provide significantly different metallicity estimates to Bayesian techniques which utilise emission line fluxes. These differences appear to be greater for low-SFR galaxies. Although we believe that the Bayesian technique used for our Sample T2 provides a more robust measurement of the global gas-phase metallicity in local, high-metallicity, star forming galaxies, it remains unclear to what extent this is so.

In Section 2.7, we show that a high-mass SFR-dependence is also present in our model sample. This is due to a turnover in the model mass-metallicity relation, caused by a gradual dilution of the gas phase in some galaxies. We have proposed that similarities between these low-sSFR model galaxies and those observed at  $z = 0$ , such as their larger-than-average black hole masses, leave open the possibility that such a process is also driving the SFR-dependence seen at high masses in real galaxies.

If this is the case, then physical processes other than mass-dependent outflows must also be playing a part in regulating metallicity. This will be the focus of the following chapter.

# Chapter 3

## Dilution in elliptical galaxies: Implications for the relation between metallicity, stellar mass, and star formation rate

*“I must confess, that a man is guilty of unpardonable arrogance, who concludes, because an argument has escaped his own investigation, that therefore it does not really exist.”*

David Hume

### 3.1 Introduction

As discussed in the previous chapter, a considerable amount of attention in the recent literature has been devoted to studying the relation between stellar mass ( $M_*$ ), star formation rate (SFR) and gas-phase metallicity ( $Z_g$ ) in galaxies. The  $M_*$ -SFR- $Z_g$  relation is believed to be a stronger diagnostic of galactic chemical evolution than the simpler  $M_*$ - $Z_g$  relation, as it provides constraints on the recent star formation, as well as the integrated star formation (i.e.  $M_*$ ) and current  $Z_g$ . However, despite this,

there remain a number of possible explanations for the trends seen in this relation in the local Universe.

For example, Mannucci et al. (2010) found a 3D relation between  $M_*$ , SFR and  $Z_g$ , known as the fundamental metallicity relation (FMR), which corrects for the observed anti-correlation between SFR and  $Z_g$  at low  $M_*$  to provide a prediction of the metallicity of local galaxies with an expected  $1\sigma$  scatter of only  $\sim 0.05$  dex. The SFR- $Z_g$  dependence at low mass was assumed to be due to highly star-forming galaxies driving stronger galactic winds, which can efficiently remove metals from their small gravitational potential wells. No significant dependence of  $Z_g$  on SFR was found at high mass.

Some theoretical studies have been able to replicate this relation between  $M_*$ , SFR and  $Z_g$  (e.g. Davé, Finlator & Oppenheimer 2012; Dayal, Ferrara & Dunlop 2013; Lilly et al. 2013). These studies utilise analytical, ‘bathtub’ models, which assume a rapid restoration of a system to an equilibrium between the gas accretion rate and SFR after a perturbative event (e.g. Bouché et al. 2010). Consequently, these models do not take account of physical processes which could force galaxies out of such an equilibrium for an extended period of time (see Section 3.3).

In Chapter 2, we discussed the study of SDSS-DR7 galaxies by Yates, Kauffmann & Guo (2012, hereafter YKG12), in which we found an anti-correlation between SFR and  $Z_g$  at low mass, but additionally a clear, *positive* correlation between these two properties at high mass. We have argued that our choice of metallicity diagnostic is likely to be more robust for local, high- $Z_g$  galaxies than that used by Mannucci et al. (2010) (see Section 2.5).

Some more recent observational studies support the findings of YKG12. For example, Lara-López et al. (2012, in prep.) found a positive correlation between SFR and  $Z_g$  at high mass when using either a  $[\text{NII}]/[\text{OII}]$  or  $([\text{OIII}]/\text{H}\beta)/([\text{NII}]/\text{H}\alpha)$  diagnostic, demonstrating that it is not just Bayesian metallicities that produce such a trend. Similarly, Andrews & Martini (2012) have found a slight positive correlation at high mass when using a  $R_{23}$  or  $[\text{NII}]/\text{H}\alpha$  diagnostic (separately). However, such a correlation is less clear when using the  $T_e$  method, as their sample has only very few galaxies above  $\log(M_*) = 10.5M_\odot$  (see their figure 11). Additionally, metallicities derived using the  $T_e$  method can be unreliable above  $Z_g \gtrsim 8.6$  due to local and global temperature gradients across galaxies (Stasińska 1978a, 2005, but see Croxall et al. 2013). Zahid et al. (2013a) have found a correlation between SFR and dust extinction very similar to that found between SFR and  $Z_g$  by YKG12. As dust and metals are known to be produced and distributed in similar ways throughout galaxies (e.g. Dwek 1998), these two correlations could share a common cause. Most recently, Kurk et al. (in prep.) have found a strong positive correlation between SFR and  $Z_g$

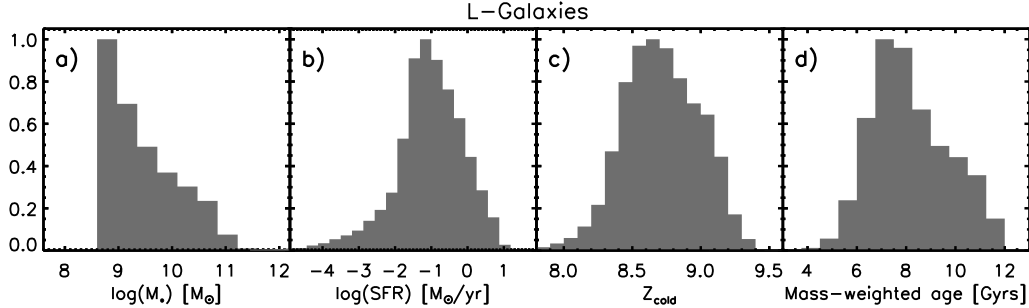


Figure 3.1: The distribution in stellar mass (panel A), star formation rate (panel B), cold gas metallicity (panel C), and mass-weighted age (panel D) for our full model sample.

at high mass in a sample of LUCI/SINS galaxies at  $z \sim 2$ .

As shown in Section 2.7, in the L-GALAXIES semi-analytic model, such a correlation is the consequence of gradual dilution of the interstellar medium (ISM) in low-SFR, massive galaxies by the accretion of metal-poor gas over several gigayears. Secular star formation is shut-down in these systems after a gas-rich merger, which produces a starburst, growth of the central BH, and ejection of gas via supernova feedback. Thereafter, the remaining gas is of too low density to continue forming stars, and the presence of radio-mode AGN feedback suppresses cooling of hot gas from the circumgalactic medium (CGM). However, the accretion of metal-poor, cold gas clumps and low-mass satellites can still proceed (see Section 3.3.2).

There should be a number of signatures at  $z = 0$  of this specific evolution. For example, in Section 2.7.3 we noted that they have larger-than-average central black holes for their mass. In this chapter, we identify a much wider range of properties at  $z = 0$  in the model which are indicative of post-merger, gradual dilution. We then utilise a wide array of publicly-available observational data to see if these signatures are also present in real low-SFR, low- $Z_g$  galaxies at low redshift. If so, this would provide strong, indirect evidence that gradual dilution is also taking place in the real Universe.

In Section 3.2, we describe our model sample. In Section 3.3, we present our model results, including a description of how dilution occurs in some massive, model galaxies. In Section 3.4, we describe our observational sample and the methods used to obtain various galactic properties. In Section 3.5, we present our observational results, and compare them to those from our model. In Section 3.6 we discuss our results in the context of other studies. Finally, in Section 3.7, we provide our conclusions.

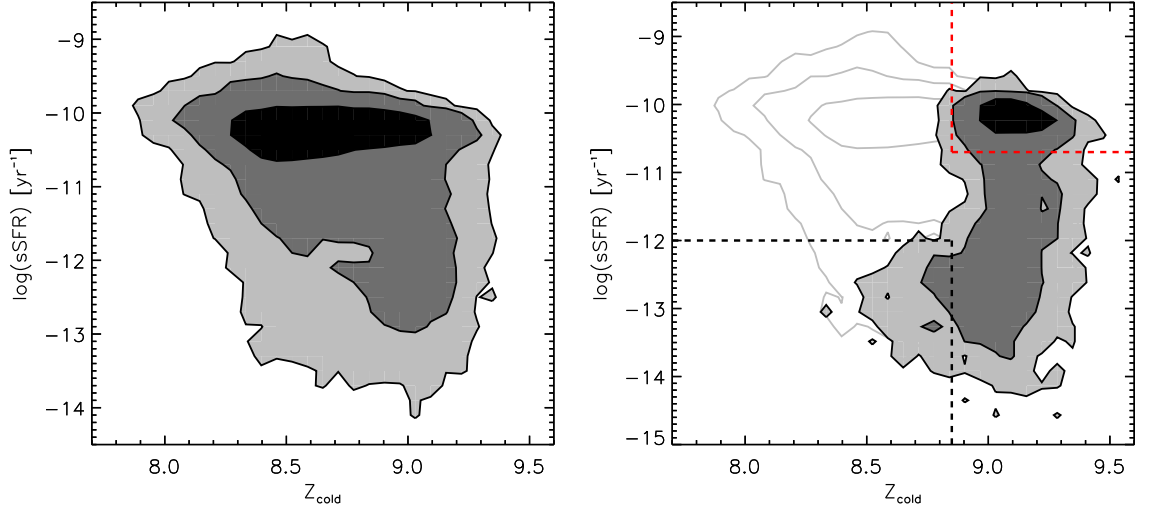


Figure 3.2: *Left panel:* The number density distribution for the whole model sample, in the sSFR- $Z_{\text{cold}}$  plane. *Right panel:* The number density distribution for galaxies with  $\log(M_*) \geq 10.5M_{\odot}$  in the same plane. The regions enclosed by the dashed red lines and dashed black lines define our high-mass enriching and diluting sub-samples, respectively. The contours of the distribution for the whole model sample are shown again in grey for reference.

### 3.2 The model sample

A sample of  $z = 0$  model galaxies similar to that described in Section 2.2 is selected from the Guo et al. (2011) version of L-GALAXIES, made publicly available on the Millennium Database<sup>1</sup> (Lemson and the Virgo Consortium, 2006), provided by the German Astrophysical Virtual Observatory (GAVO). In this case, galaxies were selected only by stellar mass ( $8.6 \leq \log(M_*/M_{\odot}) \leq 11.5$ ), so that the full range of SFRs could be studied and compared to observations. This provides 64,523 type 0 and type 1 galaxies at  $z = 0$ .

Fig. 3.1 shows the normalised  $M_*$ , SFR,  $Z_{\text{cold}}$  and mass-weighted age distributions of our model sample. The parameter  $Z_{\text{cold}}$  represents the mean metallicity of the cold, ISM gas in model galaxies. This is defined in this chapter as  $9.0 + \log(M_{Z,\text{cold}}/M_{\text{cold}}/0.02)$ . A more precise estimate of  $Z_{\text{cold}}$  in model galaxies, using the true ratio of oxygen atoms to hydrogen atoms in the gas, is introduced in Chapter 5. The truncation at  $\log(M_*) = 8.6M_{\odot}$  is done to remove the large number of poorly resolved, very-low-mass galaxies in the model that are not present in our

<sup>1</sup>available at <http://www.g-vo.org/Millennium>

observational sample (Section 3.4). We note that the focus of this chapter is on galaxies with  $\log(M_*) \geq 10.5M_\odot$ .

### 3.3 Model Results

The left panel of Fig. 3.2 shows the number density distribution for our model sample in the sSFR- $Z_{\text{cold}}$  plane. Lara-López et al. (2013) have also used the sSFR- $Z_{\text{cold}}$  plane to study the relation between  $M_*$ , sSFR and  $M_{\text{HI}}$  in local galaxies. In our case, this plane is useful because it clearly separates the two classes of massive galaxy in which we are most interested. The right panel of Fig. 3.2 shows the number density for only galaxies with  $\log(M_*) \geq 10.5M_\odot$  (see Section 3.3.1).

Fig. 3.3 shows ‘maps’ of the full model sample in the same plane, with the colouring in each panel denoting a different physical property. Galaxies are binned by sSFR and  $Z_{\text{cold}}$ , and only bins containing 10 or more galaxies are shown. There are clear trends in a number of properties for the sample as a whole. For example,  $M_*$  and  $M_{\text{BH}}$  (panels A and H) increase with gas-phase metallicity, age decreases with sSFR (panel G), and both the SFR and  $M_{\text{cold}}$  (panels B and C) follow the net cooling rate (panel I). All of these trends are as we would expect from galaxy evolution in a hierarchically-merging,  $\Lambda$ CDM universe, where galaxies are typically expected to grow in mass and metallicity with time.

#### 3.3.1 Two classes of massive galaxy

In order to study the SFR- $Z_{\text{cold}}$  correlation at high mass, we have selected two sub-samples of galaxies with  $M_* \geq 10^{10.5}M_\odot$ . The first contains 2,160 galaxies with  $\log(\text{sSFR}) \geq -10.7 \text{ yr}^{-1}$  and  $Z_{\text{cold}} \geq 8.85$ . The second contains 318 galaxies with  $\log(\text{sSFR}) \leq -12.0 \text{ yr}^{-1}$  and  $Z_{\text{cold}} \leq 8.85$ . For simplicity, we refer to these two sub-samples as *enriching galaxies* and *diluting galaxies*, respectively. The former population are typically undergoing an increase in  $Z_{\text{cold}}$  with time, whereas the latter population are typically undergoing a decrease in  $Z_{\text{cold}}$  with time (see Section 2.7.2). As we will see, they could equally be referred to as disc-dominated and bulge-dominated galaxies, young and old galaxies, or metal-rich and metal-poor galaxies. However, for the purposes of this work, we will label them by their typical net change in  $Z_{\text{cold}}$  at  $z = 0$ .

We note here that the exact limits of the selection criteria are somewhat arbitrary. We have attempted to select massive galaxies with ‘typical’ or enhanced star formation for our enriching sub-sample, and the low-SFR, low- $Z_{\text{cold}}$  tail of the distribution for our diluting sub-sample (see dashed red and black lines in the bottom

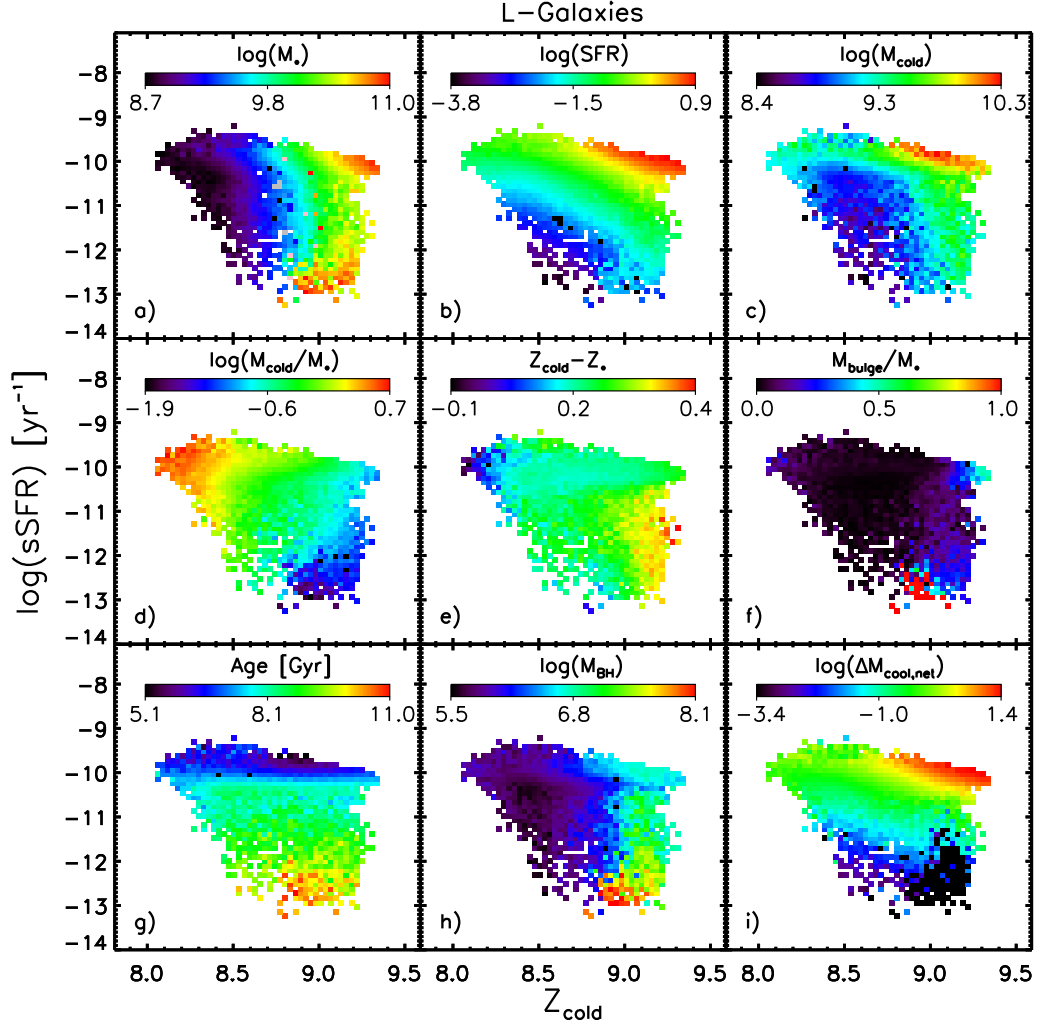


Figure 3.3: Maps of the distribution of a number of properties in the  $\text{sSFR}-Z_{\text{cold}}$  plane for our full model sample. The property shown is stated at the top of each panel.

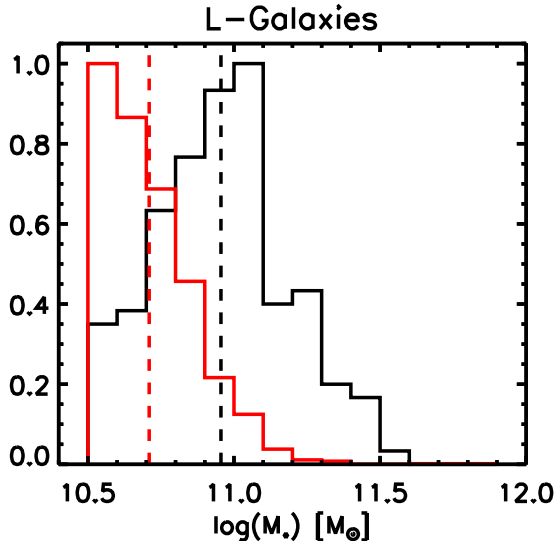


Figure 3.4: The distribution of stellar mass for diluting galaxies (black) and enriching galaxies (red) from the model sample. Mean values are given by the dashed lines for each distribution.

panel of Fig. 3.2). Small changes in these selection criteria do not affect any of our results. For example, increasing the upper  $Z_{\text{cold}}$  limit for the diluting sub-sample to 9.0 more than doubles the number of galaxies, but does not significantly alter their average properties.

A cleaner sample of diluting galaxies could be selected by only choosing those systems with a negative change in  $Z_{\text{cold}}$  over the last few gigayears. 6.6 per cent of the ‘diluting’ sample have undergone a slight net increase in  $Z_{\text{cold}}$  since  $z = 0.28$ , and so can be considered contaminants, or at least early starters in an extended dilution process. Nonetheless, we only select galaxies by their  $z = 0$  properties, to provide a fairer comparison with our observational sample. A cleaner selection simply strengthens the dichotomy seen between the enriching and diluting sub-samples in the model.

Fig. 3.4 shows the stellar mass distribution for the model enriching (red) and diluting (black) galaxies. The mean  $M_*$  is  $\sim 0.25$  dex higher for the diluting sub-sample than the enriching sub-sample. This is because these galaxies tend to live in denser environments and have many more minor mergers (see §3.3.2). However, we note that the local  $M_*-Z_g$  relation flattens-off above  $\log(M_*) \sim 10.5 M_\odot$  in both observations and our model, so this difference in mean stellar mass does not imply enhanced  $Z_{\text{cold}}$  in diluting galaxies. In fact, these galaxies have been specifically

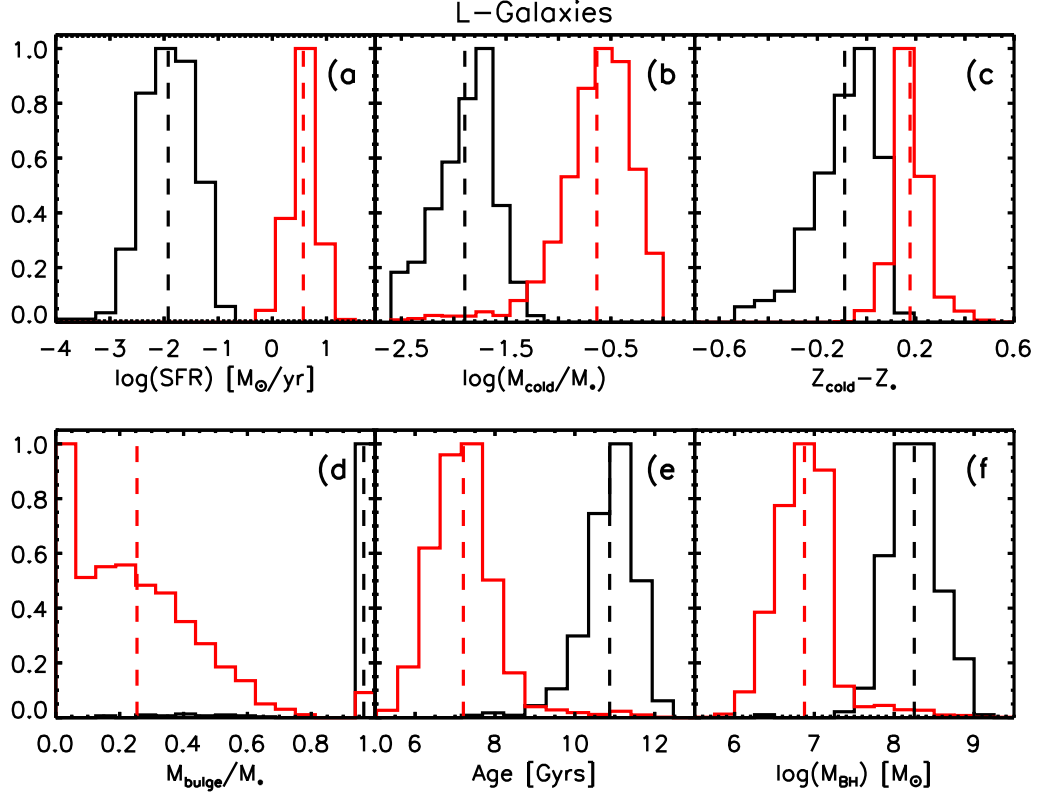


Figure 3.5: The distribution of SFR (panel A), gas-to-stellar mass ratio (panel B), metallicity difference (panel C), bulge-to-total stellar mass ratio (panel D), mass-weighted age (panel E), and central black hole mass (panel F) for diluting galaxies (black) and enriching galaxies (red) from the model sample. Mean values are given by the dashed lines for each distribution.

selected to have low sSFR and low  $Z_{\text{cold}}$ .

In Fig. 3.5, we show histograms of the key physical properties of the enriching (red) and diluting (black) galaxies at  $z = 0$ . We can clearly see that diluting galaxies have lower SFR (panel A),  $M_{\text{cold}}/M_*$  (panel B) and  $Z_{\text{cold}} - Z_*$  (panel C) than enriching galaxies, as well as higher  $M_{\text{bulge}}/M_*$  (panel D), older ages (panel E), and larger  $M_{\text{BH}}$  (panel F). All of these properties reflect the specific evolution that these galaxies have undergone (see Chapter 2).

In the case of  $Z_{\text{cold}} - Z_*$  (panel C), it is more precise to say that enriching galaxies form a tight distribution around  $(Z_{\text{cold}} - Z_*) \sim 0.17$ , whereas diluting galaxies exhibit a wider distribution, down to low (even negative) values. This parameter is a useful

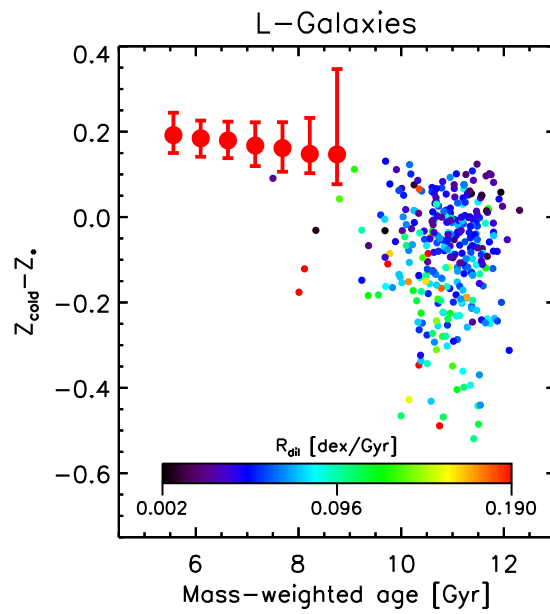


Figure 3.6: The relation between mass-weighted age and  $Z_{\text{cold}} - Z_*$  for our model massive galaxies. Large, red points show the median  $Z_{\text{cold}} - Z_*$  in bins of age for enriching galaxies. Error bars indicate the 16th and 84th percentiles in each bin. Small points show individual, diluting galaxies, coloured by their dilution rate,  $R_{\text{dil}}$  (see text).

diagnostic for dilution of the ISM *after* the last bout of star formation, as low values of  $Z_{\text{cold}} - Z_*$  indicate a decrease in the gas-phase metallicity without a corresponding decrease in the stellar metallicity (Köppen & Edmunds, 1999). Enriching galaxies are undergoing smooth, continuous star formation, and so have reached an equilibrium between their gas and stellar metallicities, whereas diluting galaxies are experiencing dilution of the ISM, at a greater rate than any star formation, for an extended period of time.

We should therefore expect that the value of  $Z_{\text{cold}} - Z_*$  in diluting galaxies anti-correlates with the amount of dilution that has taken place. As no secular star formation occurs during dilution in these model galaxies, we can use the mass-weighted age as a weak proxy for the amount of dilution. Fig. 3.6 demonstrates that older, diluting galaxies have lower  $Z_{\text{cold}} - Z_*$  than younger, enriching galaxies, and that those with the lowest  $Z_{\text{cold}} - Z_*$  are indeed the oldest. The large spread in  $Z_{\text{cold}} - Z_*$  for the oldest ages is due to the majority of the star formation occurring at higher redshifts for *all* diluting, elliptical galaxies. The mass-weighted age is therefore less sensitive to the amount of low-redshift dilution than  $Z_{\text{cold}} - Z_*$ . The colour scheme in Fig. 3.6 shows that, at fixed age, those galaxies with the largest ‘dilution rate’,  $R_{\text{dil}}$ , tend to have the lowest  $Z_{\text{cold}} - Z_*$ . We define  $R_{\text{dil}}$  as  $[Z_{\text{cold}}(t_{\text{dil}}) - Z_{\text{cold}}(0)]/t_{\text{dil}}$ , where  $t_{\text{dil}}$  is the lookback time from  $z = 0$  to when the galaxy first started steadily increasing in  $M_{\text{cold}}$ .<sup>2</sup>

### 3.3.2 Dilution in elliptical galaxies

We will now discuss the *type* of dilution that is occurring in our model diluting galaxies. The final panel in Fig. 3.3 (panel I) shows the net cooling rate of gas, taking into account the suppression from AGN feedback. As described in Section 1.5.1 and Guo et al. (2011, section 3.9), the *gross* cooling rate of hot gas from the circumgalactic medium (CGM) is calculated following White & Frenk (1991) as,

$$\dot{M}_{\text{cool,gross}} = \begin{cases} (r_{\text{cool}}/r_{\text{vir}}) (M_{\text{hot}}/t_{\text{dyn}}) & \text{if } r_{\text{cool}} \leq r_{\text{vir}} \\ M_{\text{hot}}/t_{\text{dyn}} & \text{if } r_{\text{cool}} > r_{\text{vir}} \end{cases}, \quad (3.1)$$

where  $r_{\text{cool}}$  is the radius within which the cooling timescale is shorter than the dynamical time, given by  $t_{\text{dyn}} = r_{\text{hot}}/V_{\text{vir}}$ , and  $r_{\text{hot}}$  is the radius out to which hot CGM gas extends in the system (this is the virial radius for central galaxies).

<sup>2</sup>A similar result is achieved when defining  $t_{\text{dil}}$  as the lookback time to when a galaxy first started steadily decreasing in  $Z_{\text{cold}}$ .

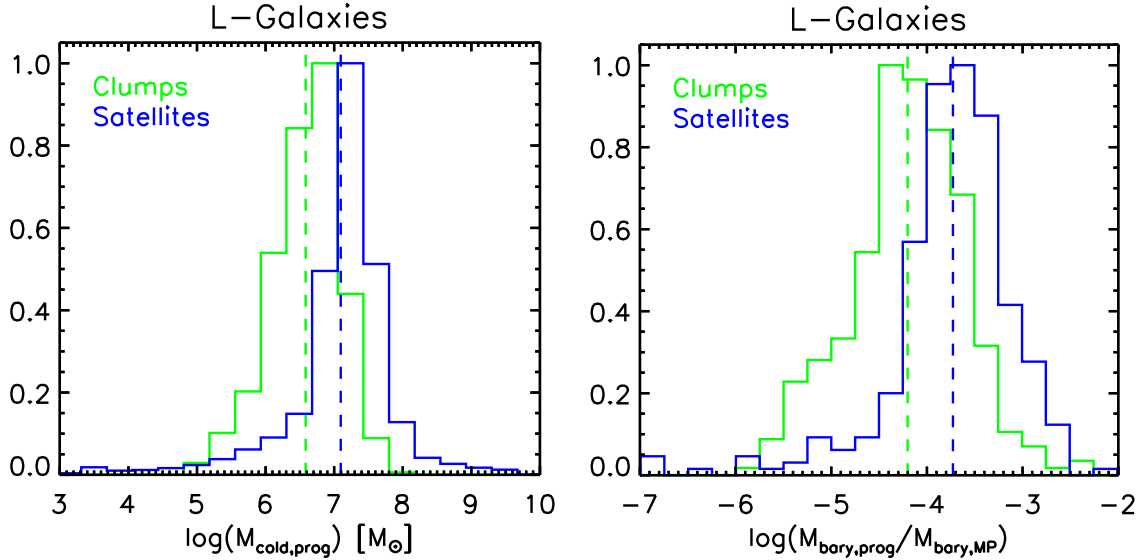


Figure 3.7: *Left panel:* The  $M_{\text{cold}}$  distribution for gas clumps (green) and satellites (blue) accreted onto model, diluting galaxies since  $z \sim 0.28$ . Dashed lines indicate the mean of each distribution. *Right panel:* The  $M_{\text{bary,prog}}/M_{\text{bary,MP}}$  (i.e. merger ratio) distribution for the same accreted gas clumps (green) and satellites (blue).

Because of the heating of some gas due to AGN feedback, as given by Eqn. 1.51, the *net* cooling rate is therefore,

$$\dot{M}_{\text{cool,net}} = \dot{M}_{\text{cool,gross}} - \dot{M}_{\text{reheat,AGN}} \quad (3.2)$$

Panel I of Fig. 3.3 shows us that such ‘diffuse’ cooling is completely shut-down in diluting galaxies, due to strong AGN feedback, whereas it is still occurring in enriching galaxies.<sup>3</sup> This indicates that the gradual dilution of diluting galaxies is *not* due to diffuse cooling of CGM gas, contrary to the conclusion made by YKG12. Instead, we have found that this gradual dilution is due to the accretion of low-mass satellites ( $\sim 87$  per cent by mass) and cold-gas clumps ( $\sim 13$  per cent by mass), carried-in by merging DM subhaloes. This merger-based accretion is not affected by the radio jets emitting from the central BH, and so can occur despite the presence of AGN feedback.

Cold-gas clumps are loosely defined as the cold gas inside DM subhaloes that do *not* contain stars. These have a mean cold gas mass of  $6.8 \times 10^6 M_{\odot}$  for the

<sup>3</sup>Net cooling rates of zero have been set to the minimum positive cooling rate in the sample of  $\log(\dot{M}_{\text{cool,net}}) = -3.4$  when plotting logarithmic values in this figure.

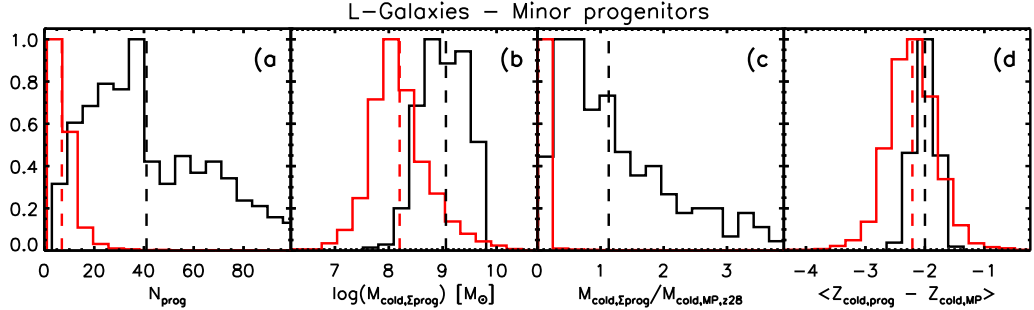


Figure 3.8: Histograms illustrating the accretion of cold gas via minor mergers for model, enriching galaxies (red) and diluting galaxies (black) from  $z = 0.28$  to 0.0. *Panel A*: The total number of minor progenitors (i.e. merging satellites). *Panel B*: The total cold gas accreted via merging satellites. *Panel C*: The ratio of total cold gas accreted to cold gas mass in the central galaxy at  $z = 0.28$ . This parameter tells us how much a central galaxy’s gas mass grew via cold accretion, with a value of 1.0 signifying that it doubled. *Panel D*: The difference between the cold gas metallicity of merging satellites and that of the central galaxy at the time of merging. Dashed lines indicate the median values for panels A and C, and mean values for panels B and D.

environments around our diluting galaxies. All other infalling objects containing gas *and* stars are called merging satellites, which have a mean cold gas mass of  $5.4 \times 10^7 M_\odot$ . Fig. 3.7 shows the  $M_{\text{cold}}$  distributions (left panel), and the merger-ratio distributions (right panel) for gas clumps and satellites accreted onto diluting galaxies over the last  $\sim 3.1$  Gyr. We note that, although 94 per cent of all the accreted cold gas onto diluting galaxies since  $z \sim 0.28$  comes from objects with baryonic masses (i.e. cold gas plus stars) above  $1.0 \times 10^7 M_\odot$ , only 57 per cent comes from objects with stellar masses of that size. Additionally, the median merger ratio for accretion events onto diluting galaxies is only 0.0001. This implies that any significant modifications to the abundance of low-mass structures in the Universe, due to, for example, the presence of warm dark matter (e.g. Markovič & Viel 2013) or cosmic-web stripping (Benítez-Llambay et al., 2013), could reduce the amount of dilution that takes place in these systems.

In Fig. 3.8, we illustrate the significance of this mode of accretion for diluting galaxies in our model. Panel A shows that diluting galaxies tend to have a larger number of minor progenitors (i.e. mergers) since  $z \sim 0.28$  (i.e. over the last  $\sim 3.1$  Gyr) than enriching galaxies. This means that, although the *average* cold gas mass of a merging satellite is similar for both classes ( $2.4 \times 10^7 M_\odot$  for diluting galaxies,

and  $2.0 \times 10^7 M_\odot$  for enriching galaxies), the *total* mass of cold gas accreted is greater for diluting galaxies (panel B). Considering that diluting galaxies also have *low* cold gas masses themselves (Fig. 3.3, panel B), such merger-based accretion can have a significant impact on their cold gas content by  $z = 0$ . Panel C of Fig. 3.8 illustrates this by showing the ratio of the total mass in cold gas accreted to the cold gas mass of the main progenitor at  $z = 0.28$  (i.e. the gross increase in  $M_{\text{cold}}$  due to mergers). For enriching galaxies, the median ratio is  $\sim 1.0$  per cent, whereas for diluting galaxies, satellites add an additional 113 per cent in cold gas on average. This leads to enriching galaxies undergoing a net *decrease* in  $M_{\text{cold}}$  of 11 per cent on average, whereas diluting galaxies undergo a net *increase* in  $M_{\text{cold}}$  of 18 per cent on average, over the last 3.1 Gyr.

This accreted gas is more metal-poor than the cold gas in the central galaxy (panel D), and therefore causes the significant dilution of the gas phase over time in diluting galaxies. The fact that this gas comes in during many minor merger events means that the dilution is gradual rather than sudden, with a median drop in  $Z_{\text{cold}}$  of  $\sim 0.045$  dex per Gyr since  $z = 0.28$  ( $\sim 0.052$  dex per Gyr for those galaxies that show a consistent decrease in  $Z_{\text{cold}}$  since  $z = 0.28$ ). This drop in  $Z_{\text{cold}}$  in low-SFR galaxies over time is the cause of the positive correlation between SFR and  $Z_{\text{cold}}$  at high mass in the model FMR at  $z = 0$ .

Another way to illustrate this evolution is to track the change in key galaxy parameters over time (e.g. Figs. 2.13 and 2.14). Fig. 3.9 shows the median  $Z_{\text{cold}}$  as a function of lookback time (filled circles), for enriching galaxies (red) and diluting galaxies (black). We can see  $Z_{\text{cold}}$  increases with cosmic time for enriching galaxies, and decreases with cosmic time for diluting galaxies. Fig. 3.9 also shows the evolution of the cold gas accretion rate minus SFR. This is a measure of the relative dilution/enrichment of the ISM; positive values indicate a net dilution (from infalling, metal-poor gas) and negative values indicate a net enrichment (from stars). We can see that enriching galaxies always have negative  $\Delta M_{\text{cold}, \Sigma_{\text{prog}}} - \text{SFR}_{\text{MP}}$ . This is true even when including gas cooled from the CGM in the calculation. Diluting galaxies always have positive  $\Delta M_{\text{cold}, \Sigma_{\text{prog}}} - \text{SFR}_{\text{MP}}$ . This shows again how these systems are gradually diluting their ISM over time. We note that the increase in  $\Delta M_{\text{cold}, \Sigma_{\text{prog}}} - \text{SFR}_{\text{MP}}$  for enriching galaxies is due to their average decline in SFR over time, reflecting the evolution of the cosmic SFR density (Madau et al., 1996). The low SFRs and fairly constant merger rates of diluting galaxies ensure that their  $\Delta M_{\text{cold}, \Sigma_{\text{prog}}} - \text{SFR}_{\text{MP}}$  remains fairly constant over time.

It may be surprising that massive, bulge-dominant galaxies are undergoing minor mergers containing cold gas in the model, when the current understanding is that such systems grow in mass and size predominantly through dissipationless, minor

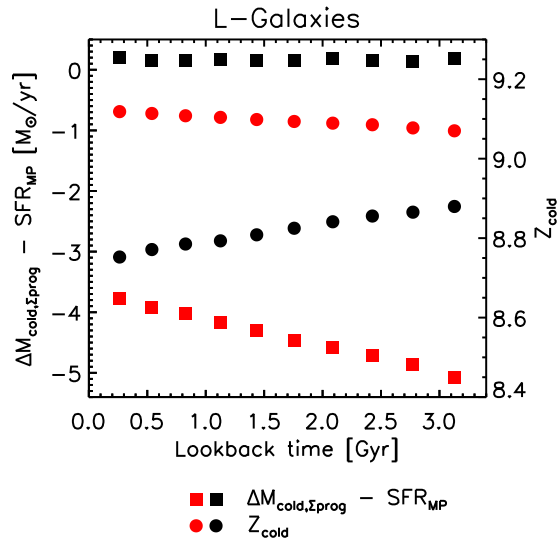


Figure 3.9: The evolution of the *median* accretion rate minus SFR (squares) and  $Z_{\text{cold}}$  (filled circles) with time, for model, enriching (red) and diluting (black) galaxies. The accretion rate,  $\Delta M_{\text{cold},\Sigma\text{prog}}$ , is calculated as the mass of cold gas obtained through mergers per year. Enriching galaxies have negative  $\Delta M_{\text{cold},\Sigma\text{prog}} - \text{SFR}_{\text{MP}}$ , due to low merger rates. Diluting galaxies have positive  $\Delta M_{\text{cold},\Sigma\text{prog}} - \text{SFR}_{\text{MP}}$ , due to low SFRs.

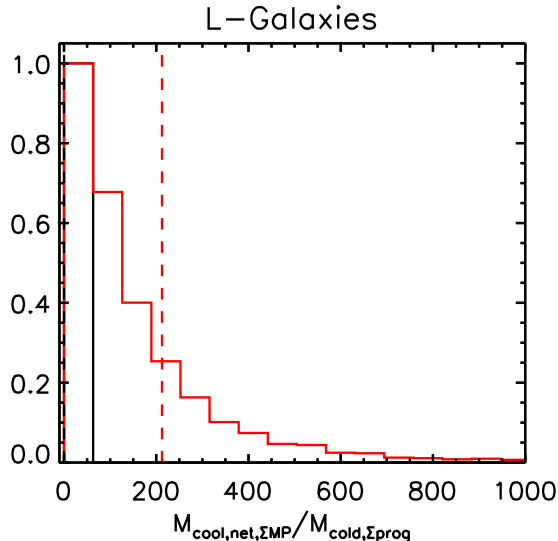


Figure 3.10: The ratio of total gas mass cooled from the CGM to total cold gas accreted for model, enriching galaxies (red) and diluting galaxies (black) from  $z = 0.28$  to 0.0. Dashed lines indicate the mean values. Cooling can be the dominant mechanism for obtaining cold gas in enriching galaxies, whereas accretion of satellites and gas clumps dominates for diluting galaxies.

mergers (e.g. White 1976; Naab, Johansson & Ostriker 2009). However, both these pictures are consistent with each other, as the median SFR of these diluting galaxies is only  $\sim 0.04 M_{\odot}/\text{yr}$  since  $z \sim 0.28$ , with only 0.6 per cent of their present day stellar mass grown from forming new stars since then, on average. The accretion of stars via mergers over the same time is much more significant, contributing an average 13.6 per cent of the total stellar mass at  $z = 0$ .

Finally, in Fig. 3.10 we show the ratio between ‘total gas mass cooled’ and ‘total cold gas mass accreted’ from  $z \sim 0.28$  to the present day. Cooling of CGM gas can clearly be a significant mode of obtaining cold gas in enriching galaxies, whereas it is negligible in diluting galaxies due to the presence of AGN feedback. This reflects the fact that accretion of cold gas via satellites and infalling gas clumps is the dominant mechanism for diluting such galaxies in the model.

In conclusion, we can say that there are a number of clear signatures of dilution in some massive galaxies in the semi-analytic model that can be seen at  $z = 0$ . These include: lower gas-to-stellar mass ratios, older ages, higher bulge-to-total stellar mass ratios, higher central BH masses, and lower  $Z_{\text{cold}} - Z_{*}$ . We have also shown that

metal-poor gas is accreted via minor merger events, rather than via diffuse cooling of hot gas from the CGM. In the next section, we turn to the SDSS, to see if such features are also found in massive, low-sSFR, low- $Z_g$  galaxies in the real Universe.

## 3.4 The observational samples

### 3.4.1 Main sample

A main sample of local galaxies was selected from the SDSS-DR7<sup>4</sup>. 109,678 of these were obtained following the selection criteria of Tremonti et al. (2004), as described in Section 2.2 for Sample T2. An additional 40,254 galaxies were included for which  $\sigma(M_*)$  or  $\sigma(Z_g) > 0.2$ , but that meet all the other requirements described above. The motivation for this is outlined in Section 2.5.1. At  $\log(M_*) \geq 10.5$ , these galaxies actually have estimates of  $Z_g$  well within the  $\sigma(Z_g) < 0.2$  requirement (see Fig. 2.8), and 98 per cent also have  $\sigma(M_*) < 0.3$ . We therefore choose to include these galaxies in order to better probe the high- $M_*$ , low- $Z_g$  region of parameter space that we are interested in for this work. This brings our main sample to a total of 149,932 galaxies.

Stellar masses, total star formation rates and fibre-based, gas-phase metallicities are provided by the SDSS-DR7 catalogue. Their determination is described in Section 2.3, and in more detail in Brinchmann et al. (2004) and Tremonti et al. (2004). We note here that all our conclusions also hold when using a simpler, strong-line-ratio-based metallicity diagnostic (see Section 3.5).

Fig. 3.11 shows the normalised  $M_*$ , SFR,  $Z_g$  and  $z$  distributions of our Main observational sample (grey). There are fewer low- $M_*$  and low-SFR galaxies than in our model sample (Fig. 3.1). This is because such galaxies can be ‘lost’ due to low luminosity or low SNR on the optical emission lines used for selection. This is not a significant issue in this work, as we focus on galaxies with  $\log(M_*) \geq 10.5M_\odot$ .

The number density distribution of the whole Main sample is shown in the left panel of Fig. 3.12. In the right panel, the distribution for galaxies with  $\log(M_*) \geq 10.5$  is shown (see Section 3.5.1).

### 3.4.2 HI-detected sample

In order to assess the significance of gas fraction on the  $M_*$ -SFR- $Z$  relation, we formed a sub-sample containing those galaxies with direct detections of HI gas. There

<sup>4</sup>available at <http://www.mpa-garching.mpg.de/SDSS/DR7>

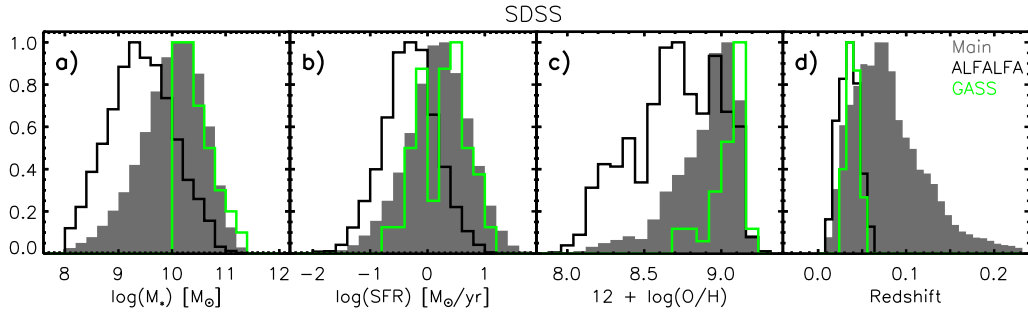


Figure 3.11: The distribution in stellar mass (panel A), star formation rate (panel B), gas-phase metallicity (panel C), and redshift (panel D) for the Main observational sample (grey), only ALFALFA galaxies (black), and only GASS galaxies (green).

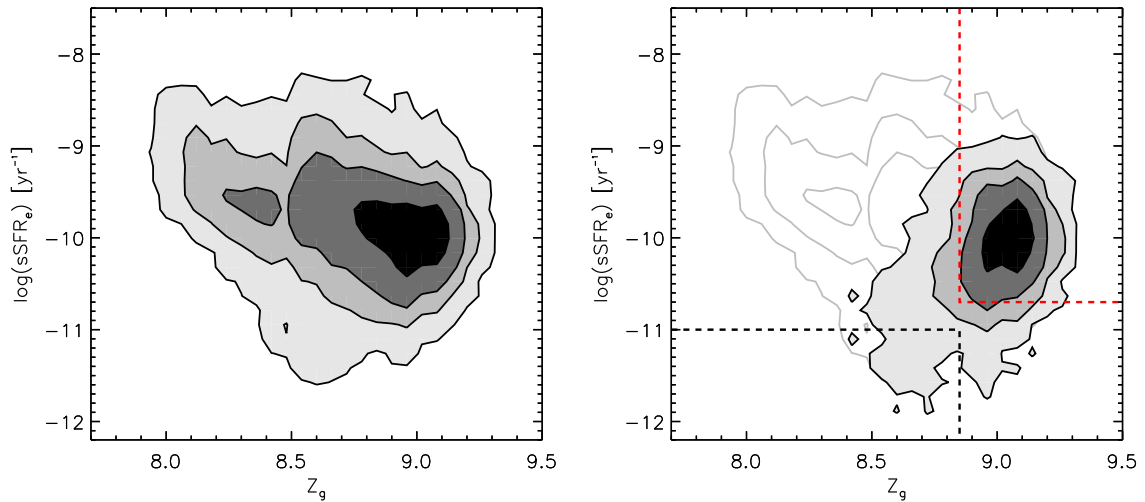


Figure 3.12: *Left panel:* The number density distribution for the main observational sample, in the  $\text{sSFR}_* - Z_g$  plane. *Right panel:* The number density distribution for galaxies with  $\log(M_*) \geq 10.5 M_\odot$  in the same plane. The regions enclosed by the dashed red lines and dashed black lines define our enriching and diluting sub-samples, respectively. The contours of the distribution for the whole main sample are shown again in grey for reference.

is an increasing amount of data available on the HI and H<sub>2</sub> contents of nearby massive galaxies, thanks to surveys such as ALFALFA (Giovanelli et al., 2005), GASS (Catinella et al., 2010) and COLD GASS (Saintonge et al., 2011). Also, scaling relations that provide an estimate of the gas fraction from other observable properties (e.g. Zhang et al. 2009; Catinella et al. 2012b; Li et al. 2012) allow an analysis of the expected HI content for a much larger sample of galaxies (see Section 3.4.5).

3,123 galaxies were found by cross-matching our main sample with the ALFALFA- $\alpha$ .40 sample (Haynes et al., 2011).<sup>5</sup> ALFALFA is a blind survey, detecting HI via the 21cm line within the footprint of the SDSS. In order to match to our main sample, we a) removed all ALFALFA objects with a heliocentric velocity ( $v_{\text{helio}}$ ) < 3000km/s. These are either high-velocity clouds within the Milky Way or galaxies for which redshifts cannot be accurately determined.<sup>6</sup> b) removed all other ALFALFA objects which do not have the `OCCode = I` flag. These are HI regions not associated with galaxies. c) cross-matched the right ascension ( $ra$ ), declination ( $dec$ ) and redshift ( $z$ ) of our main sample with the remaining ALFALFA objects, allowing for maximum errors of  $\sigma(ra, dec) = 10$  arcsecs and  $\sigma(z) = 0.0003$ .

The same maximum errors on  $ra$ ,  $dec$  and  $z$  were used to obtain 38 cross-matched galaxies from the GASS-DR1/DR2 samples (Catinella et al. 2012b, hereafter C12).<sup>7</sup> GASS is a targeted survey of  $\sim 1,000$  known SDSS galaxies (232 of which have direct HI detections) of  $M_* > 10^{10}M_{\odot}$ , so no removal of intragalactic objects is required. Only galaxies with quality `Q = 1` were retained. Right ascensions and declinations were obtained from the GASS data by decomposing the associated SDSS IDs. Of these 38 galaxies, 9 are also found in our ALFALFA sub-sample. For these galaxies, we take the  $M_{\text{HI}}$  measurements obtained by GASS.

An SDSS ID is simply a concatenation of the right ascension ( $ra$ ) and declination ( $dec$ ) of a given object in hexadecimal format, such that, SDSS ID = Jhh-mmss.ss+ddxxyy.y. In these IDs, J indicates the use of the J2000 standard equinox,  $ra = \text{hhmmss.ss}$  in hours, minutes and seconds, and  $dec = \text{ddxxyy.y}$  in days, arcminutes (xx) and arcseconds (yy.y). The + sign before the declination indicates that the object lies in the northern hemisphere (there are no southern hemisphere objects in GASS). Once decomposed from the SDSS ID,  $ra$  and  $dec$  from GASS can be compared to those from any SDSS data release following the straightforward conversion to degrees;  $ra_{\text{deg}} = (360/24) \cdot [\text{hh} + (\text{mm}/60) + (\text{ss.ss}/3600)]$  and  $dec_{\text{deg}} = \text{dd} + (\text{xx}/60) + (\text{yy.y}/3600)$ .

After cross-matching with these surveys, a total of 3,161 unique galaxies (2.11

<sup>5</sup>available at <http://egg.astro.cornell.edu/alfalfa>

<sup>6</sup>ALFALFA redshifts are determined by  $v_{\text{helio}}/c$ , where  $c$  is the speed of light in a vacuum.

<sup>7</sup>available at <http://www.mpa-garching.mpg.de/GASS>

per cent of our main sample) with direct  $M_{\text{HI}}$  measurements were obtained. The normalised  $M_*$ , SFR,  $Z_g$  and  $z$  distributions for the ALFALFA sub-sample (black) and GASS sub-sample (green) are shown in Fig. 3.11, alongside the Main observational sample (grey).

### 3.4.3 $Z_*$ sample

We also draw a sub-sample of galaxies for which stellar metallicities ( $Z_*$ ) have been measured for the SDSS-DR4 (Gallazzi et al., 2005).<sup>8</sup> These galaxies were obtained using the same cross-matching requirements described in Section 3.4.2. We use this sub-sample to obtain values of  $Z_g - Z_*$ . As mentioned in Section 3.3, low  $Z_g$  relative to  $Z_*$  is indicative of dilution of the ISM by metal-poor infall after the last star-formation event.

We convert  $Z_*$  from the SDSS-DR4 catalogue into units of  $12 + \log(\text{O}/\text{H})$  using  $Z_{*,\text{cat}} - \log(0.0134) + 8.69$ , where 0.0134 and 8.69 are the solar metallicity and oxygen abundance as determined by Asplund et al. (2009), respectively. We note that alternative conversions using different solar values would only shift the amplitude of  $Z_g - Z_*$ , and would not affect the relative values of this parameter for the two classes of massive galaxy considered in this work (see Section 3.5.1).

Gallazzi et al. (2005) point out that their stellar metallicity estimates are only reliably constrained for galaxies with a SNR per pixel of  $\sim 20.0$  or higher. Introducing such a cut reduces our  $Z_*$  sample by 84 per cent (although it also *strengthens* slightly the dichotomy in  $Z_g - Z_*$  for our two high-mass sub-samples, see Section 3.5). Therefore, we instead choose a slightly weaker cut, selecting only those galaxies with a SNR per pixel of 14.8 (the mean value for the whole SDSS-DR4). Doing so reduces the  $Z_*$  sample by only 59 per cent, to 24,275 galaxies, and produces very similar results to a sample using SNR per pixel  $\geq 20.0$ .

### 3.4.4 NUV-r sample

In order to obtain  $M_{\text{HI}}/M_*$  estimates via the HI scaling relation derived by C12 (see Section 3.4.5), we select 1,529 brightest cluster galaxies (BCGs) for which NUV-r colours have been measured by Wang et al. (2010) (kindly provided by Jing Wang, priv. comm.). An additional 1,662 galaxies were obtained by cross-matching our Main sample with the Galaxy Evolution Explorer (GALEX) GR6 catalogue<sup>9</sup>, matching objects by position and allowing for  $\sigma(\text{ra}, \text{dec}) \leq 1$  arcsecond. A further 418

<sup>8</sup>available at <http://www.mpa-garching.mpg.de/SDSS/DR4>

<sup>9</sup>available at <http://galex.stsci.edu/GR6/>

galaxies were obtained in the same way, by cross-matching our Main sample with the GALEX photometric data for objects in the Lockman Hole and Spitzer First Look Survey (FLS). This data was compiled for the Galaxy Multi-wavelength Atlas from Combined Surveys (GMACS) catalogue by Johnson et al. (2007a,b).<sup>10</sup> The total number of galaxies in our NUV-r sample comes to 3,609.

### 3.4.5 HI scaling relations

As our HI-detected sample is only a small fraction (2.1 per cent) of our Main sample, we also utilise the HI scaling relation formulated by Zhang et al. (2009, hereafter Z09) to get  $M_{\text{HI}}$  estimates for all our galaxies. Z09 derived a mean relation between  $M_{\text{HI}}/M_*$ , sSFR, and stellar surface brightness ( $\mu_*$ ) for 800 SDSS-DR4 galaxies cross-matched with the HyperLeda HI catalogue (Paturel et al., 2003). Their relation is given by,

$$\log(M_{\text{HI}}/M_*) = -0.77 \log(\mu_*) + 0.26 \log(\text{sSFR}) + 8.53 \quad , \quad (3.3)$$

where  $\log(\mu_*) = \log(M_*/2\pi R_{50,i}^2)$  and  $R_{50,i}$  is the Petrosian i-band half-light radius (in arcsecs). All the properties required to estimate the gas-to-stellar-mass ratio from Eqn. 3.3 are drawn from the SDSS-DR7 catalogue. Z09 also discuss the significance of gas fraction on the  $M_*$ - $Z_g$  relation, and we compare our results to theirs in Section 3.6.3.

We first check that the Z09 scaling relation provides reasonable  $M_{\text{HI}}/M_*$  estimates for galaxies with direct HI detections from ALFALFA or GASS. This comparison is shown in the left panel of Fig. 3.13. We can see that, in general, the agreement is good, although the scatter is large. However, in detail, the Z09 scaling relation seems to predict larger  $M_{\text{HI}}/M_*$  than is measured by GASS (squares).

The GASS survey was specifically designed to observe galaxies until either an HI detection is made or a gas fraction limit of 0.015 is determined (see C12). This allows detections down to much lower HI masses than is possible by ALFALFA, which has an exposure time per galaxy of around a factor of ten smaller than GASS.

We check if the disparity at low  $M_{\text{HI}}/M_*$  is specific to the Z09 scaling relation by also comparing direct HI measurements to the  $M_{\text{HI}}/M_*$  estimates obtained from the C12 scaling relation. This relation is calibrated using GASS galaxies and uses NUV-r colour, rather than sSFR derived from optical emission lines. Catinella et al. (2010) and C12 found that massive, HI-detected galaxies form a flat, 2-dimensional plane in the  $(M_{\text{HI}}/M_*)$ - $\mu_*$ -(NUV-r) parameter space, which can be well described by,

<sup>10</sup>available at <http://www.astro.columbia.edu/~bjohnson/GMACS/catalogs.html>

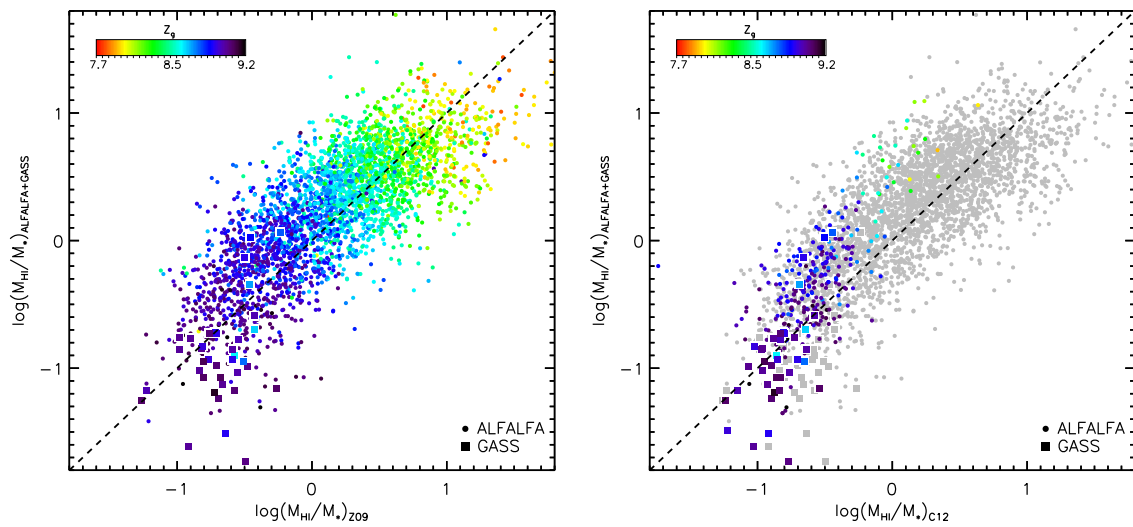


Figure 3.13: *Left panel:* A comparison between the HI-to-stellar-mass ratios obtained from the Zhang et al. (2009) scaling relation and directly from ALFALFA (circles) and GASS (squares), for all 3,182 galaxies from our HI-detected sample. Data points are coloured by the gas-phase metallicity of each galaxy. *Right panel:* The same comparison, but between the C12 scaling relation and ALFALFA (circles) and GASS (squares), for 228 galaxies from our NUV-r sample. For reference, the points from the top panel are shown again in grey.

$$\log(M_{\text{HI}}/M_*) = -0.338 \log(\mu_*) - 0.235 (\text{NUV-r}) + 2.908 . \quad (3.4)$$

This comparison is shown in the right panel of Fig. 3.13 for 228 galaxies from our NUV-r sample that also have direct HI measurements. The C12 relation seems to provide a similar range of  $M_{\text{HI}}/M_*$  estimates as the Z09 relation (grey points) for high- $Z_g$  galaxies. This suggests that the larger scatter found at low  $M_{\text{HI}}/M_*$  is intrinsic to the difficulty in obtaining good 21 cm measurements for galaxies of such low gas fraction. We will show in Section 3.5 that both the direct  $M_{\text{HI}}/M_*$  estimates and the two scaling relations described here indicate larger gas fractions in enriching galaxies than indicated by scaling relations in diluting galaxies.

We also note that the C12 relation seems to under-estimate the gas-to-stellar-mass ratio for low- $Z_g$ , high- $M_{\text{HI}}/M_*$  galaxies, compared to direct measurements (green and yellow points in the bottom panel of Fig. 3.13). Li et al. (2012) have shown that estimators which do not take account of colour gradients in galaxies can underestimate  $M_{\text{HI}}/M_*$  in such gas-rich systems. They propose a new estimator, which includes the  $g - i$  colour gradient ( $\Delta_{g-i}$ ) to account for this effect. However, such a correction is not required in this work, as we choose to focus on galaxies with relatively high- $Z_g$  and low- $M_{\text{HI}}/M_*$ .

### 3.5 Observational Results

Fig. 3.14 shows ‘maps’ of the observational samples in the sSFR- $Z_g$  plane, in the same way as done for the model sample in Fig. 3.3. Galaxies are again binned by sSFR and  $Z_g$ , and only bins containing 10 or more galaxies are plotted. For this figure, each galaxy is weighted by  $1/V_{\text{max}}$ , the inverse of the maximum volume within which a galaxy of that r-band magnitude could be observed by the SDSS. This gives a greater weighting to faint, low-mass galaxies, to account for Malmquist bias.

The first thing we note when comparing Figs. 3.3 and 3.14 is the different regions of parameter space covered. For example, the median sSFR for the model sample (sSFR =  $10^{-10.2}$ ) is lower than that of the observational sample (sSFR =  $10^{-9.82}$ ). This is because galaxies, particularly those with low  $M_*$ , tend to form stars too efficiently at high  $z$  in the semi-analytic model. This means that lower SFRs are required at low  $z$  in order to fit the  $z = 0$  stellar mass function (e.g. Guo et al. 2011). Henriques et al. (2013) have since addressed this problem, by allowing material ejected from model galaxies to return to the ISM over longer periods of time, increasing their SFRs at low  $z$  (see their fig. 9).

Also, there is a greater fraction of low-sSFR galaxies in the model sample than

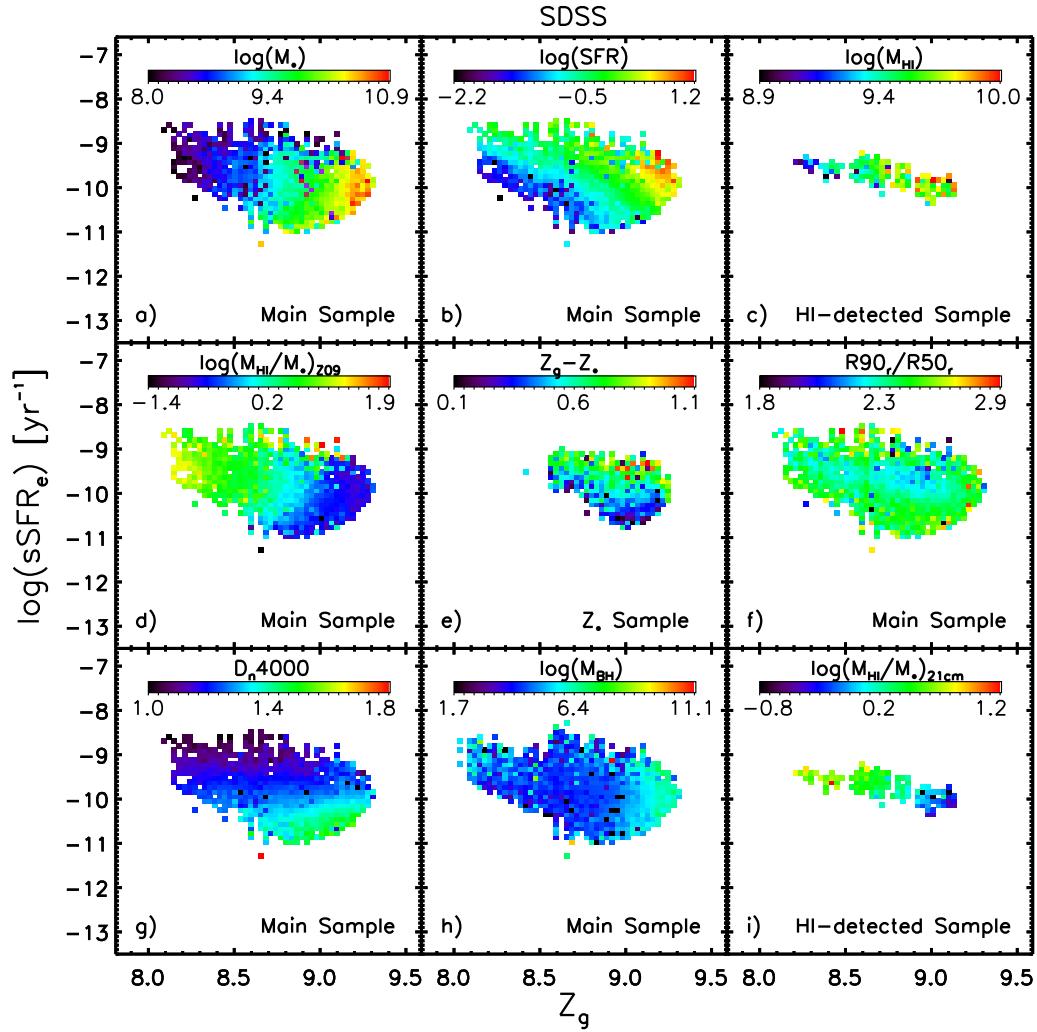


Figure 3.14: Maps of the distribution of a number of properties in the  $\text{sSFR}-Z_g$  plane for the observational samples. The property shown is stated at the top of each panel.

in the observational sample. This is likely due to the difficulty in obtaining SFR, metallicity and gas mass estimates for such galaxies in the real Universe, which will have intrinsically weaker emission line strengths, with lower SNR. Galaxies in this region of parameter space may also host AGN, as we believe them to be post-merger systems with large black holes (according to their model analogues), and so may have been removed via the AGN cut.

Nonetheless, clear similarities can still be seen between the model and observational samples. Fig. 3.14 shows that low-mass galaxies have lower SFRs (panel B), lower HI masses (estimated via the 21cm line measurements of ALFALFA and GASS, panel C), higher gas-to-stellar mass ratios (using both the Z09 scaling relation, panel D, and direct estimates, panel I), lower metallicity differences (panel E), larger concentration indices (measured as the ratio of radius containing 90 per cent of the Petrosian r-band light to the half-light radius, panel F), younger ages (inferred from the time since the last starburst via  $D_n4000$ , panel G), and lower-mass central black holes (inferred from velocity dispersions via the Graham et al. 2011 combined  $M_{\text{BH}}-\sigma$  relation, panel H). All of these trends are also found in our semi-analytic model, L-GALAXIES (see Fig. 3.3).

We have also checked the stability of our results to changes in the selection criteria. When increasing the minimum SNR( $\text{H}\alpha$ ,  $\text{H}\beta$ ,  $[\text{NII}]$ ) to 10, the low-sSFR edge of the galaxy population is ‘trimmed’ slightly, increasing the median SFR of the whole Main sample by  $\sim 0.02$  dex. Conversely, decreasing the maximum redshift to 0.1 removes some high-sSFR galaxies, decreasing the median SFR of the whole Main sample by  $\sim 0.18$  dex. Finally, increasing the minimum fibre-to-total light ratio to 0.35 mainly removes low-redshift galaxies, as these tend to have larger apparent sizes, and reduces the Main sample to 32,550 objects. Despite these changes to the size and extremities of the galaxy population, the general trends described above are all unaffected. The main conclusions for our high- $M_*$  sub-samples are also robust to these changes (see Section 3.5.1).

### 3.5.1 Two classes of massive galaxy in the SDSS

When focusing on massive galaxies, we have again selected two sub-samples with  $M_* \geq 10^{10.5} M_\odot$ . The first contains 28681 galaxies with  $\log(\text{sSFR}) \geq -10.7 \text{ yr}^{-1}$  and  $Z_{\text{cold}} \geq 8.85$ . The second contains 136 galaxies with  $\log(\text{sSFR}) \leq -11.0 \text{ yr}^{-1}$  and  $Z_{\text{cold}} \leq 8.85$ . These two regions are marked-out by the red and black dashed lines in the bottom panel of Fig. 3.12, respectively. To mimic the terminology used for the model sample, we also refer to these as *enriching* and *diluting* galaxies. However, we emphasise that it is *not* a foregone conclusion that these galaxies are the direct

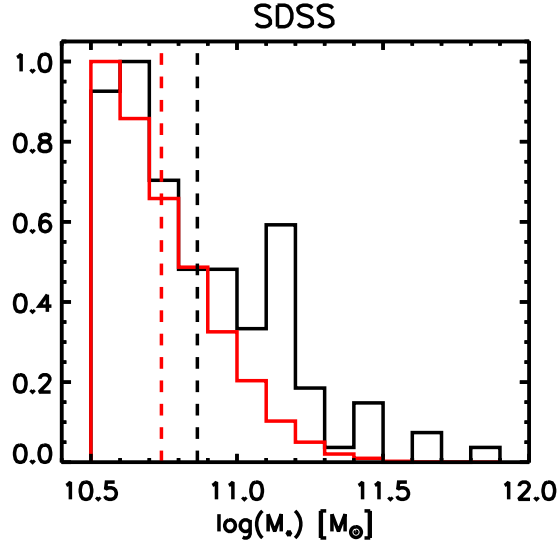


Figure 3.15: The distribution of stellar mass for diluting galaxies (black) and enriching galaxies (red) from the Main sample. Mean values are given by the dashed lines for each distribution.

analogues of those in our model, and that it is the purpose of this paper to determine whether this could be the case.

As with the model sub-samples, we have attempted to select massive galaxies with ‘typical’ or enhanced star formation for our enriching sub-sample (i.e. systems on or above the main sequence of star-forming galaxies, e.g. Elbaz et al. 2011), and the low-SFR, low-metallicity tail of the distribution for our diluting sub-sample. In the case of the observational sample, this low-SFR, low- $Z_g$  tail is less extended due to removal of galaxies with low SNR or which host AGN. Therefore, we have chosen a higher upper limit on sSFR for observed diluting galaxies than in the model sample, in order to recover a statistically significant number of galaxies. All the other limits chosen are the same as used in our model. Again, small changes to the selection criteria do not affect our results. For example, increasing the upper sSFR limit for the diluting sub-sample to  $10^{-10.7} \text{ yr}^{-1}$  roughly doubles the number of galaxies, but does not significantly change our results.

Fig. 3.15 shows the stellar mass distribution for the observational enriching (red) and diluting (black) sub-samples. There is little difference between the distributions for these two sub-samples, meaning that there is no intrinsic mass dependence affecting the results. We have also checked that the diluting galaxies do not exhibit excess star formation in their central regions relative to enriching galaxies from light

reprocessed by dust, by comparing their magnitudes around 12 and 22  $\mu\text{m}$  from the Wide-field Infrared Survey Explorer (WISE, Wright et al. 2010).

The key finding in this chapter is that *all* the signatures of post-merger dilution seen in the semi-analytic model at  $z = 0$  are also found in our SDSS sample. Fig. 3.16 shows that real, ‘diluting’ galaxies have lower SFR (panel A),  $M_{\text{HI}}/M_*$  (panel B), and  $Z_g - Z_*$  (panel C), than enriching galaxies, as well as larger  $R_{90,r}/R_{50,r}$  (panel D), older ages (panel E), and larger  $M_{\text{BH}}$  (panel F). A comparison of the statistical properties of diluting and enriching galaxies between the model and observations is also provided in Table 3.1.

It should be noted here that considering the *absolute* values of  $Z_g - Z_*$  in the semi-analytic model and observations should be treated with caution, as they are sensitive to the set of solar abundances assumed and  $Z_g$  diagnostic chosen (see Sections 1.1 and 1.2). However, the fact that diluting galaxies typically have lower  $Z_g - Z_*$  *relative* to enriching galaxies in both the model and observations is a significant result. Also, the fact that both enriching and diluting galaxies in the SDSS have similar median  $M_*$  and  $Z_*$  (see Table 3.1) supports the dilution scenario interpretation.

The red, purple and maroon histograms in panel B of Fig. 3.16 represent the  $M_{\text{HI}}/M_*$  distribution for massive, enriching galaxies from the main sample (using the Z09 scaling relation), the NUV-r sample (using the C12 scaling relation) and HI-detected sample (using ALFALFA and GASS measurements), respectively. It is encouraging that all three methods for estimating  $M_{\text{HI}}$  show that enriching galaxies have higher gas fractions than diluting galaxies.

We emphasise here that, although it is not surprising to see low-SFR, massive galaxies with low gas fractions, high concentrations, and older ages, it *is* surprising that such galaxies also have low  $Z_g$  and low ( $Z_g - Z_*$ ). This suggests that these galaxies could be undergoing dilution similar to that seen in some massive galaxies in our semi-analytic model.

Changes to the selection criteria for the whole Main sample do not affect the conclusions drawn for these two classes of massive galaxy. More stringent cuts simply decrease the sample sizes. For example, increasing the minimum SNR for the  $\text{H}\alpha$ ,  $\text{H}\beta$  and  $[\text{NII}]$  lines to 10 removes low-sSFR galaxies, and therefore decreases the size of the diluting sub-sample by  $\sim 65$  per cent. Lowering the maximum redshift to 0.1 removes some high-SFR galaxies, therefore reducing the enriching sub-sample size by  $\sim 66$  per cent. Increasing the minimum fibre-to-total light ratio to 0.35 also reduces the diluting sub-sample by  $\sim 69$  per cent. However, the dichotomy seen between the two sub-samples remains strong despite such changes.

Importantly, all the trends described above also hold when using the strong-line-ratio-based metallicities of Mannucci et al. (2010), even though this method predicts

	Diluting galaxies						Enriching galaxies					
	Model			Observations			Model			Observations		
	<i>318 galaxies</i>			<i>136 galaxies</i>			<i>2160 galaxies</i>			<i>28681 galaxies</i>		
	Min	Median	Max	Min	Median	Max	Min	Median	Max	Min	Median	Max
$\log(\text{sSFR}) [\text{yr}^{-1}]$	-15.4	-12.9	-12.0	-12.8	-11.3	-11.0	-10.7	-10.1	-9.1	-10.7	-9.3	-8.4
$Z_g$	8.10	8.74	8.85	8.28	8.69	8.84	8.85	9.13	9.68	8.85	9.08	9.40
<sup>a</sup> $Z_*$	8.66	8.79	8.98	7.77	8.94	9.24	8.66	8.96	9.29	7.22	8.83	9.26
$\log(M_*) [M_\odot]$	10.5	10.9	11.6	10.5	10.8	12.1	10.5	10.7	11.8	10.5	10.7	12.0
SFR [ $M_\odot/\text{yr}$ ]	0.0	0.012	0.17	0.03	0.33	6.22	0.65	3.8	52.9	0.66	6.1	276.0
$z$	-	-	-	0.022	0.087	0.195	-	-	-	0.017	0.119	0.250
$\log(M_{\text{cold}}) [M_\odot]$	7.7	9.1	9.9	-	-	-	8.4	10.1	11.2	-	-	-
<sup>b</sup> $M_{\text{HI}}/M_*$	0.001	0.015	0.063	0.001	0.021	0.245	0.003	0.26	3.2	0.002	0.067	1.1
<sup>a</sup> $Z_g - Z_*$	-0.84	-0.07	0.13	-0.79	-0.27	0.87	-0.12	0.17	0.54	-0.37	0.26	1.94
$M_{\text{bulge}}/M_*$	0.16	1.0	1.0	-	-	-	0.0	0.22	1.0	-	-	-
$R_{90,r}/R_{50,r}$	-	-	-	1.07	2.98	3.51	-	-	-	1.0	2.38	6.25
Age <sub>mw</sub> [Gyr]	7.5	11.0	12.3	-	-	-	3.6	7.2	12.0	-	-	-
$D_n4000$	-	-	-	1.1	1.71	2.10	-	-	-	0.0	1.32	1.89
$\log(M_{\text{BH}}) [M_\odot]$	6.5	8.2	9.1	1.0	7.8	11.9	5.7	6.9	8.9	1.0	6.8	11.9
$\dot{M}_{\text{cool,net}} [M_\odot/\text{yr}]$	0.0	0.0	1.7	-	-	-	0.0	15.0	73.0	-	-	-

Table 3.1: The minimum, median and maximum values of the properties analysed for diluting and enriching galaxies from our model sample and Main/ $Z_*$  observational samples.

<sup>a</sup> For the observational data, only the 43 diluting galaxies and 7,475 enriching galaxies present in the  $Z_*$  sample are considered.  $Z_*$  is converted into units of  $12 + \log(\text{O}/\text{H})$  using solar metallicity and oxygen abundance values from Asplund et al. (2009) accordingly:  $Z_* - \log(0.0134) + 8.69$ .

<sup>b</sup> Using the HI-to-stellar mass fractions obtained via the Z09 scaling relation (Eqn. 3.3) for the observational sample, and using  $M_{\text{cold}}/M_*$  for the model sample.

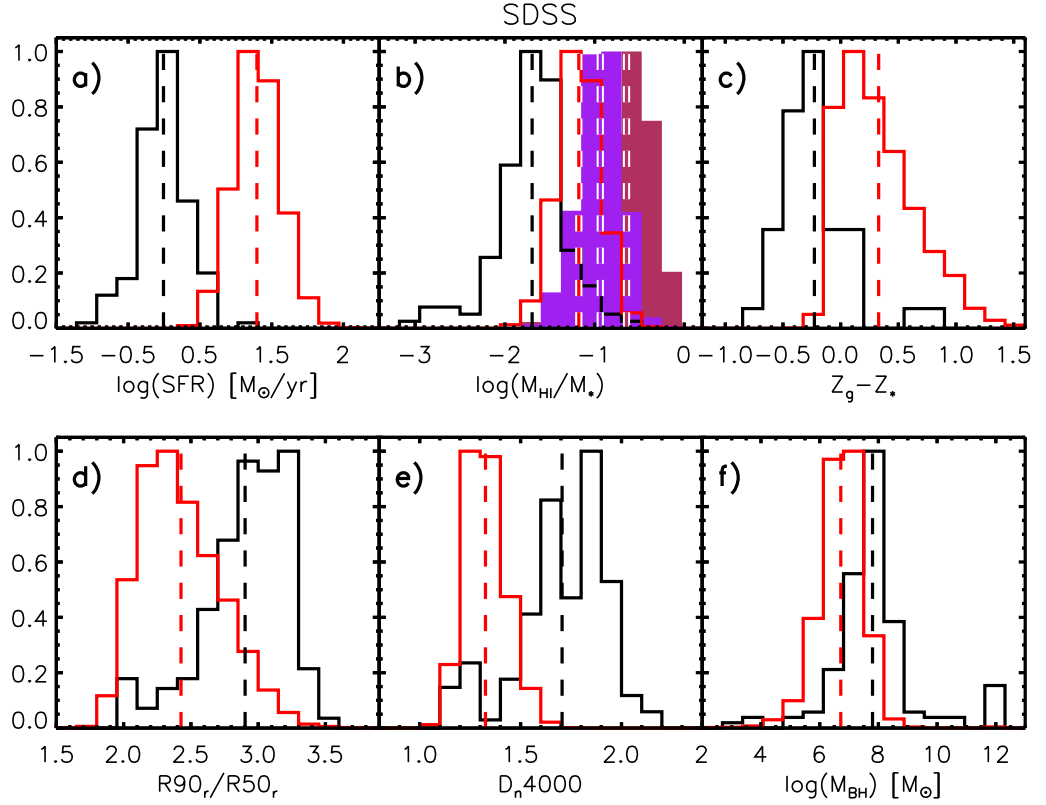


Figure 3.16: The distribution of SFR (panel A), gas-to-stellar mass ratio (from the Z09 scaling relation, panel B), metallicity difference (panel C), concentration index (panel D),  $D_n4000$  (panel E), and central black hole mass (panel F) for diluting galaxies (black) and enriching galaxies (red) from the observational samples. The purple and maroon distributions in panel B show the HI-to-stellar mass ratios from the C12 scaling relation and ALFALFA/GASS direct detections, respectively. Mean values are given by the dashed lines for each distribution.

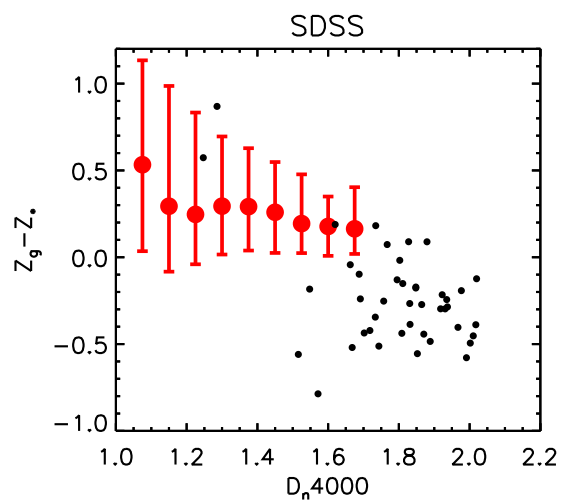


Figure 3.17: The relation between  $D_n4000$  (a proxy for time since the last starburst) and  $Z_g - Z_*$  for our observational  $Z_*$  sample. Red points represent the median  $Z_g - Z_*$  in bins of  $D_n4000$  for the enriching galaxies. Error bars indicate the 16th and 84th percentiles. Black points represent individual diluting galaxies. The oldest diluting galaxies have lower values of  $Z_g - Z_*$  than the youngest diluting galaxies, indicating dilution of the gas phase *after* a bout of star formation.

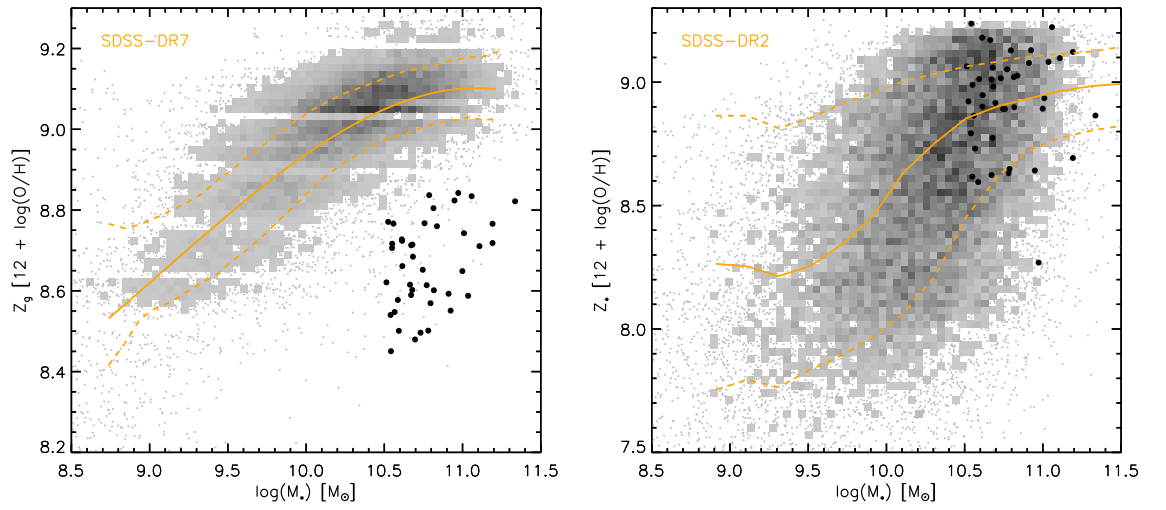


Figure 3.18: *Left panel:* The  $M_*$ - $Z_g$  relation for our Main sample (grey region), diluting galaxies from our  $Z_*$  sample (black points), and star-forming galaxies from the SDSS-DR7 (orange lines, YKG12). *Right panel:* The  $M_*$ - $Z_*$  relation for our Main sample (grey region), diluting galaxies from our  $Z_*$  sample (black points), and star-forming galaxies from the SDSS-DR2 (orange lines, Gallazzi et al. 2005). Stellar metallicities have been converted to units of  $12+\log(\text{O}/\text{H})$  using the solar metallicity and oxygen abundance values from Asplund et al. (2009) of 0.0134 and 8.69, respectively.

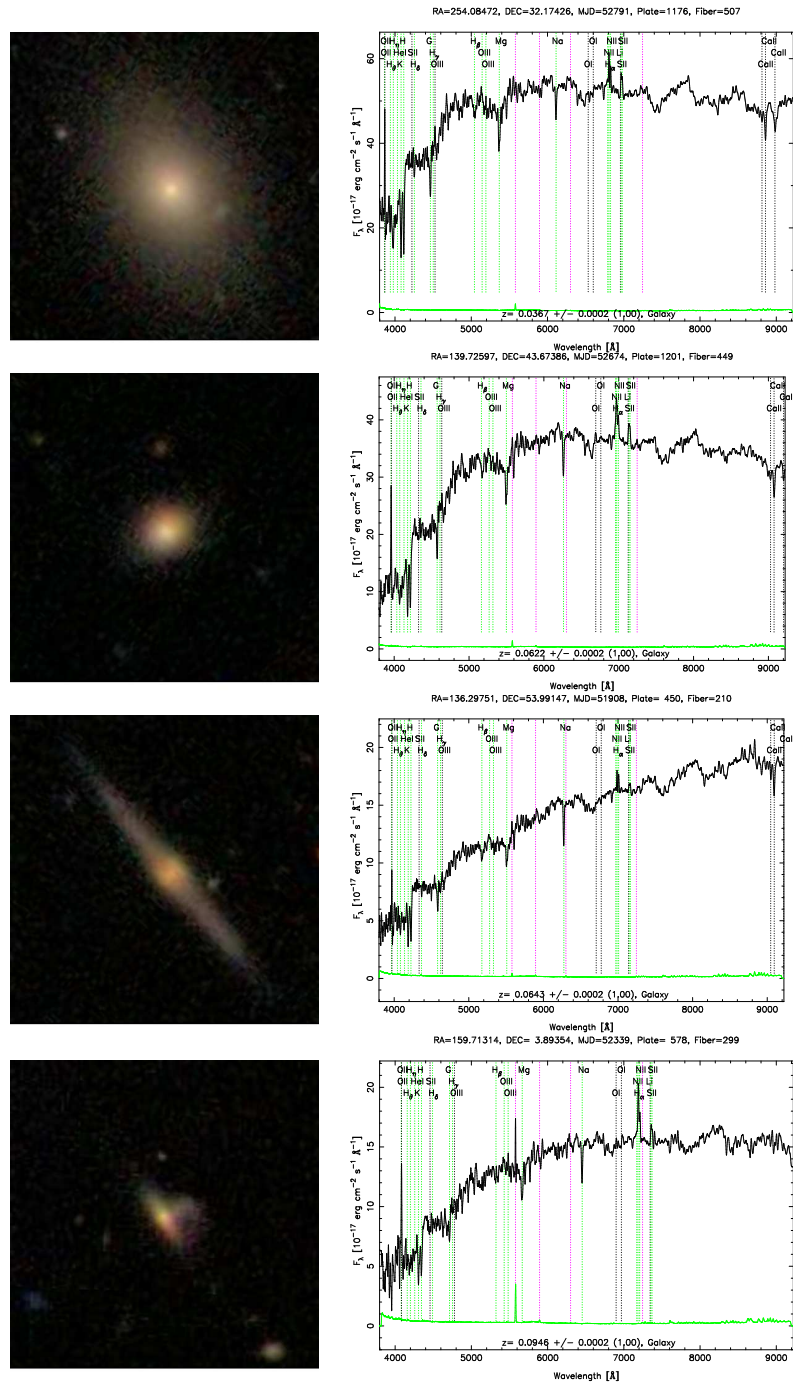


Figure 3.19: Four example objects from our SDSS-DR7 sub-sample of diluting galaxies. Thumbnail images and optical spectra are shown for two elliptical galaxies, an edge-on disc and an interacting system.

higher metallicities for galaxies below  $Z_g \sim 9.1$  than the Bayesian method (see Fig. 2.5). For example, the mean value of the HI-to-stellar mass ratio for diluting galaxies when selecting by this strong-line-ratio-based metallicity is  $\log(M_{\text{HI}}/M_*)_{Z09} = -1.7$ . This is still 0.51 dex lower than the mean value for enriching galaxies using the same selection criteria. Also, the difference in mean  $Z_g - Z_*$  between diluting and enriching galaxies when using the strong-line diagnostic to obtain  $Z_g$  is still 0.45 dex. We therefore consider the *relative* properties of enriching and diluting galaxies to be robust to the metallicity diagnostic chosen.

Fig. 3.17 shows the relation between  $D_n4000$  and  $Z_g - Z_*$  for massive galaxies in our observational  $Z_*$  sample, noting that  $D_n4000$  measures the time since the last bout of star formation (see e.g. Kauffmann et al. 2003a). This relation can be compared to Fig. 3.6 for the model. Although the number of observed diluting galaxies (black points) with reliable stellar metallicities is relatively small (43 galaxies), there is still a clear trend present – diluting galaxies are typically older and have lower  $Z_g - Z_*$  than enriching galaxies, and the maximum  $Z_g - Z_*$  decreases with  $D_n4000$ . Fig. 3.18 illustrates how these low  $Z_g - Z_*$  values are truly due to lower-than-average  $Z_g$ , and *not* simply high  $Z_*$ . Diluting galaxies from our  $Z_*$  sample have, by construction,  $Z_g$  values  $\sim 2.5 - 6.5$  dex *lower* than expected from the mean SDSS-DR7  $M_*$ - $Z_g$  relation (left panel). However, their  $Z_*$  values are typical for objects of their mass (right panel).

It is also interesting to note that many of the diluting galaxies in our observational sample have early-type morphologies. From visual inspection of the SDSS-DR7 optical thumbnail images alone,  $\sim 62$  per cent appear to be elliptical in shape and lack significant blue emission. This is supported by the higher average concentration index in the diluting sub-sample (Fig. 3.16, panel D), and reflects the large bulge-to-total stellar mass ratios seen for diluting galaxies in our model (Fig. 3.3, panel E). Around 18 per cent of the observational sub-sample appears to be edge-on disc galaxies. These are likely assigned low SFRs and low gas-phase metallicities due to their greater optical thickness, which reduces the amount of emission observed from their galactic centres. A further  $\sim 18$  per cent of the diluting galaxies are either currently interacting or of uncertain morphology. Only the final  $\sim 2$  per cent is made up of objects that appear to be nearly face-on disc galaxies with some blue emission. We note, of course, that by-eye classification using only low-resolution optical images can only give a rough indication of the typical morphologies for a sample of nearby galaxies.

Fig. 3.19 shows optical images of four representative galaxies in the diluting sub-sample, along with their SDSS spectra.<sup>11</sup> Although most emission lines are not

<sup>11</sup>Images and spectra obtained from <http://cas.sdss.org/astrodr7/en/tools/chart/list.asp>

particularly strong, [NII] and H $\alpha$  are well detected in all four spectra and could be dominating the metallicity estimates. To test the significance of the [NII] $\lambda$ 6584 line, our analysis was re-run using Bayesian metallicity estimates that do not require [NII] (or [SII]) in the fit. Although this does lower the  $Z_g$  estimate for some massive galaxies, it doesn't affect the relative median  $Z_g - Z_*$  values between the diluting and enriching sub-samples. In Section 2.5, we also describe that removing [NII] from the estimation doesn't affect the positive correlation between SFR and  $Z_g$  at high  $M_*$ . We also note that the majority of galaxies exhibiting low ionisation nuclear emission line regions (LINERs) have already been removed from our sample via the AGN cut described in Section 3.4.1. The [NII]/H $\alpha$  ratio would not provide an accurate estimate of the host galaxy's  $Z_g$  in such systems.

When removing all galaxies with disc-like morphologies from the diluting sub-sample, a slight decrease in the average SFR,  $M_{\text{HI}}/M_*$ , and  $Z_g - Z_*$ , along with a slight increase in  $R_{90,r}/R_{50,r}$ ,  $D_n4000$ , and  $M_{\text{BH}}$  is seen, as would be expected. For example, the median  $Z_g - Z_*$  drops by 0.006 dex, the median  $D_n4000$  rises by 0.02, and the median  $M_{\text{BH}}$  rises by 0.27 dex.

To conclude this section, we can say that all the signatures of post-merger dilution seen in our model sample are also found in low-SFR, low- $Z_g$ , massive galaxies in the SDSS. This is strong, indirect evidence for claiming that real galaxies have also undergone a gradual dilution of their gas phase, after the truncation of continuous star formation following a merger-induced starburst. However direct measurements of metal-poor gas infall onto these galaxies have not yet been made, and so further observational studies are required to confirm or deny the conclusions drawn from this work.

## 3.6 Comparisons to other works

### 3.6.1 Accretion onto elliptical galaxies

There is already a class of spheroidal galaxy identified as possibly undergoing accretion of metal-poor gas, known as polar ring galaxies (PRGs) (Schweizer, Whitmore & Rubin, 1983). PRGs tend to exhibit extended rings or discs of HI gas, dust and sometimes young stars, lying perpendicularly to the equatorial plane of the central spheroid, with the kinematics of the two components decoupled (Whitmore et al., 1990). One explanation for the formation of the rings is the later accretion of cold gas, which is either stripped from nearby or merged satellites (e.g. Reshetnikov & Sotnikova 1997; Bournaud & Combes 2003; Hancock et al. 2009), or accreted from

cosmic filaments (e.g. Macciò, Moore & Stadel 2006; Spavone et al. 2010; Spavone & Iodice 2013). However, a scenario where a major, gas-rich merger forms both the central spheroid and the outer polar ring together is also possible (e.g. Bekki 1998; Iodice et al. 2002a).

Moiseev et al. (2011) have recently compiled the Sloan-based Polar Ring Catalogue (SPRC) of 275 nearby PRGs also observed by the SDSS. We find that 61 of these PRGs are also present in our Main observational sample, 20 of which have  $\log(M_*) \geq 10.5$ . Of these 20 massive PRGs, only 2 are present in our diluting sub-sample: SPRC-37 and SPRC-183. The first has  $\log(\text{sSFR}) = -11.17 \text{ yr}^{-1}$  and  $Z_g = 8.5$ , and the second has  $\log(\text{sSFR}) = -11.57 \text{ yr}^{-1}$  and  $Z_g = 8.5$ .

Interestingly, these two systems have the first and third oldest ages of all the PRGs in our Main sample, with  $D_n4000 = 1.79$  and  $1.67$ , respectively (the median value for the diluting sub-sample is  $1.64$ ). In addition, they also have the first and third lowest metallicity differences, with  $Z_g - Z_* = -0.13$  and  $-0.52$ , respectively (the median value for the diluting sub-sample is  $-0.19$ ). This could be an indication that metal-poor gas is *gradually* accreted onto such systems over time, again supporting the dilution scenario described in this work.

We note that, for the 20 massive PRGs in our Main Sample, the median r-band covering fraction is  $0.24$  (where the median for all galaxies with  $\log M_* \geq 10.5$  is  $0.25$ ). This means that some of the metal-poor gas in the outer polar rings may not fall within the 3-arcsecond SDSS fibre. Therefore, these objects may have even lower overall  $Z_g$  than is observed.

The fact that only two of our observed diluting galaxies are confirmed as PRGs in the SPRC suggests that this is not the main mechanism by which elliptical galaxies accrete metal-poor gas. Indeed, the presence of an AGN, which is often the case for our model diluting sub-sample, would likely preclude the accretion and cooling of gas from filaments (although not necessarily from satellite stripping or mergers).

Russell et al. (2013) have recently suggested that the BCG of Abell 1664, which hosts an AGN, could be undergoing inflow of two molecular gas clumps, which could settle into a disc over several hundreds of megayears (although, they also point out that this material could be part of an outflow, driven by AGN feedback). Such a mode of accretion is much more common for diluting galaxies in our semi-analytic model than smooth infall and cooling from the intergalactic medium (see Fig. 3.10). The advent of the Atacama Large Millimeter Array (ALMA) survey should hopefully facilitate many more observations of infalling molecular gas onto massive ellipticals in the future.

Similarly, Husemann et al. (2011) have found a massive ( $M_{\text{bulge}} \lesssim 3.4 \times 10^{10} M_\odot$ ) QSO-host galaxy at  $z \sim 0.2$  with a large black hole ( $M_{\text{BH}} \sim 3 \times 10^8 M_\odot$ ) and very

low gas-phase metallicity ( $Z_g \lesssim 8.4$ ). The low metallicity in this system is believed to be due to dilution, via accretion of some kind. Husemann et al. (2012) have further found that bulge-dominated, QSO-host galaxies typically have lower  $Z_g$  than their disc-dominated counterparts, and that both have lower  $Z_g$  than ‘non-active’ star-forming galaxies of the same mass (although Stern & Laor 2013 suggest that  $Z_g$  can be under-estimated in active galaxies). These low- $Z_g$  objects are quite distinct from the majority of massive AGN hosts which have super-solar  $Z_g$  (e.g. Hamann & Ferland 1993; Groves, Heckman & Kauffmann 2006), but they do exhibit properties seen in diluting galaxies in our semi-analytic model.

### 3.6.2 Interacting galaxies

Around  $\sim 8$  per cent of the massive, ‘diluting’ galaxies in our observational sample appear, from their SDSS images, to be interacting. Kewley et al. (2010) have shown that four close pairs of galaxies in the local Universe have lower-than-expected central  $Z_g$ , likely due to rapid migration of metal-poor gas from larger radii into the centres of each galaxy during the interaction (see also Kewley, Geller & Barton 2006; Rupke, Veilleux & Baker 2008). Such a process is most effective when the interacting galaxies are of similar mass (Woods et al., 2006; Ellison et al., 2008b; Michel-Dansac et al., 2008). Montouri et al. (2010) and Torrey et al. (2012) have also shown that such a process occurs in their SPH simulations of equal-mass, interacting, disc galaxies.

One of the close pairs investigated by Kewley et al. (2010) is also present in our main observational sample, comprising NGC 3994 and NGC 3995. We find that, although these two galaxies have relatively low central  $Z_g$  (9.01 and 8.67, respectively), they also have high  $\log(\text{sSFR})$  ( $-8.28 \text{ yr}^{-1}$  and  $-8.41 \text{ yr}^{-1}$ ), high  $M_{\text{HI}}/M_*$  (2.55 and 1.40), and young ages ( $D_n4000 = 1.16$  and 1.01). High SFRs were also found for the majority of the 42 low- $Z_g$ , interacting SDSS galaxies studied by Peeples, Pogge & Stanek (2009). These properties are to be expected for galaxies with metal-poor gas flooding into the central regions inducing a nuclear starburst. However, they are not found in any of the small number of interacting systems in our diluting sub-sample. Such a sudden dilution of the ISM is therefore unlikely to be the sole cause of low  $Z_g$  in massive galaxies with disturbed morphologies.

It could be that the interacting galaxies studied by Kewley et al. (2010) are in an initial phase of the evolution seen in our model, and will undergo a gradual dilution in the future. However, the simulations of Montouri et al. (2010) and Torrey et al. (2012), as well as L-GALAXIES, show that  $Z_{\text{cold}}$  increases again shortly after a merger event, due to metal enrichment from the first supernovæ following the starburst. Therefore, any dilution after this time would not be due to the initial

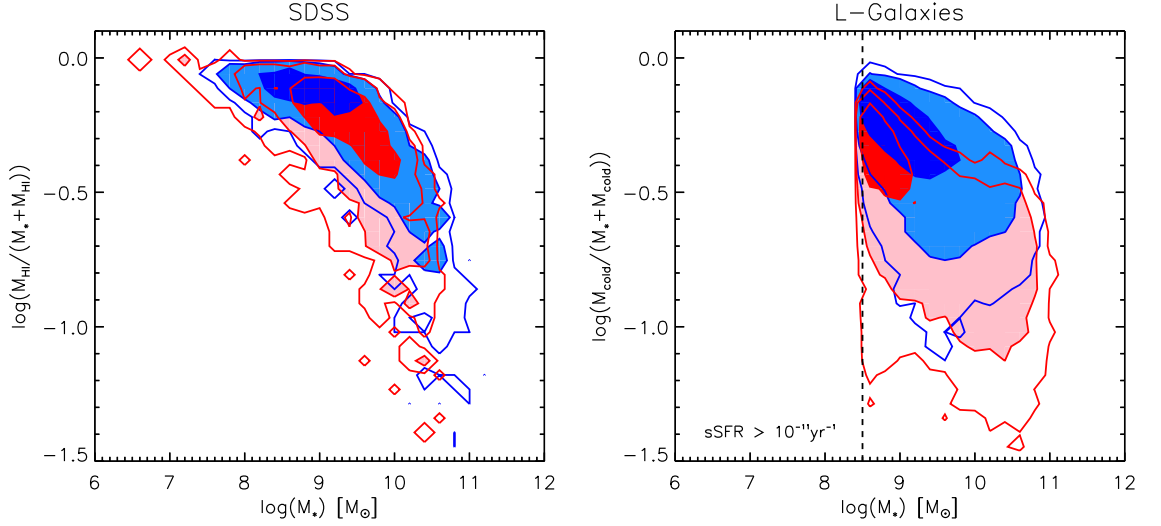


Figure 3.20: *Left panel:* The relation between  $M_*$  and gas fraction for our HI-detected sample, selecting only galaxies with  $\log(\text{sSFR}) > -11.0 \text{ yr}^{-1}$ . Blue contours represent metal-poor galaxies and red contours represent metal-rich galaxies, as defined in the text. *Right panel:* The same relation for our model sample, again selecting only galaxies with  $\log(\text{sSFR}) > -11.0 \text{ yr}^{-1}$ . The vertical dashed line marks the stellar mass limit applied to our model sample.

interaction, and would have to occur through a second process (such as accretion), in the absence of strong star formation.

### 3.6.3 The relation between $M_*$ , $Z_g$ , and $M_{\text{HI}}$

As mentioned in Section 3.4.5, Z09 also studied the dependence of the  $M_*$ - $Z_g$  relation on HI gas mass fraction. They found that, at fixed  $M_*$ , metal-rich galaxies have lower gas fractions than metal-poor galaxies. This may seem to contradict the findings in this work at high mass. However, these two results are compatible with each other due to the difference in the sample selection. Z09 selected galaxies with  $\log(\text{sSFR}) > -11.0 \text{ yr}^{-1}$ , meaning that none of the diluting galaxies in either our observational or model analysis meet the same criterion.

When we also select a sample of massive galaxies with  $\log(\text{sSFR}) > -11.0 \text{ yr}^{-1}$ , we recover similar trends to those found by Z09, for both our observational and model samples. Fig. 3.20 shows the relation between  $M_*$  and gas fraction for our HI-detected sample (left panel) and our model sample (right panel), for massive galaxies with  $\log(\text{sSFR}) > -11.0 \text{ yr}^{-1}$ . Galaxies are split into metal-rich (red contours) and

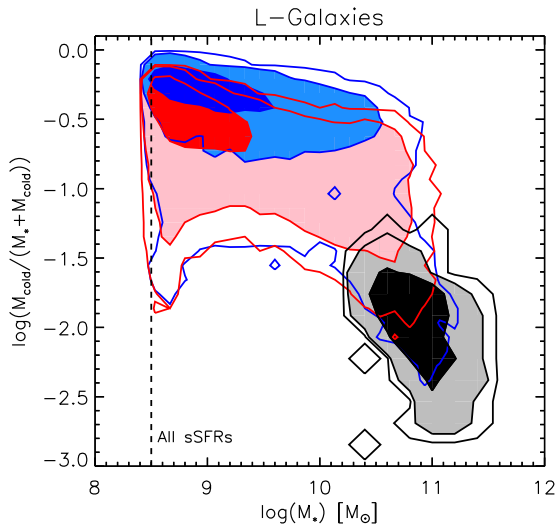


Figure 3.21: The relation between  $M_*$  and gas fraction our whole model sample. Blue and red contours represent the same galaxies as in Fig. 3.20. Black contours represent our diluting-galaxy sub-sample.

metal-poor (blue contours) sub-samples in the same way as done by Z09, by fitting a second order polynomial to the  $M_*$ - $Z_g$  relation of each sample, and selecting galaxies above and below this fit, respectively. When comparing these relations to those obtained for the SDSS and semi-analytic model by Z09 (their figs. 8 and 9), we can see a good qualitative match, with metal-rich galaxies having lower gas fractions at fixed mass, on average. Instead, it is the particular class of low-sSFR galaxies – that are *not* present in the Z09 sample – which deviate from these trends by having low  $Z_g$  and low gas fractions at  $z = 0$ . These diluting galaxies, for our model sample, are highlighted by the black contours in Fig. 3.21.

The case is similar when comparing our results to those of Hughes et al. (2013) and Bothwell et al. (2013), who have also observed an anti-correlation between gas fraction and gas-phase metallicity. Hughes et al. (2013) only selected galaxies with  $\log(\text{sSFR}) \geq -10.9 \text{ yr}^{-1}$ , which also excludes all the diluting galaxies analysed in this work. Likewise, Bothwell et al. (2013) only selected galaxies from the ALFALFA survey, of which we find only two in our diluting sub-sample.

The hydrodynamical simulations of Duffy et al. (2012) and Davé et al. (2013) also report an anti-correlation at high mass. In both cases, AGN feedback is modelled, although for Davé et al. (2013) this is not directly tied to black hole growth. Again, only a comparison with galaxies from the ALFALFA and GASS surveys is made,

so the low-SFR, gas-poor ellipticals in our diluting sub-sample are not considered. These results, together with those discussed in this work, point to the fact that such massive, elliptical galaxies *do not* behave like ‘typical’, secularly-evolving disc galaxies on the main sequence, because their infall and star formation rates have not been in equilibrium for a number of gigayears.

Pleasingly, our findings *do* support the cartoon model described by Lara-López et al. (2013). In that work, it was postulated that massive, low-sSFR, low- $Z_g$  galaxies should have low gas fractions. Our results, using a wide range of observational data and our galaxy formation model, show that this is indeed the case. We further argue that the cause of this trend is a gradual dilution of the gas phase after a merger-induced starburst.

### 3.6.4 The FMR at $z=0$

As discussed previously, there are conflicting conclusions in the literature as to the true nature of this  $M_*$ -SFR- $Z_g$  relation at high mass (Mannucci et al., 2010; Lara-López et al., 2010b; Yates, Kauffmann & Guo, 2012; Andrews & Martini, 2012; Lara-López et al., 2013; Zahid et al., 2013a; Bothwell et al., 2013). It is therefore important to find viable physical processes that can *explain* a given correlation between  $M_*$ , SFR and  $Z_g$ . There now appears to be three observationally-motivated explanations for why some massive galaxies can fall-off the  $M_*$ - $Z_g$  relation to lower metallicities: a) rapid dilution of the central regions of high-SFR, interacting galaxies (e.g. Kewley, Geller & Barton 2006), b) the removal of dust and metals from low-SFR, secularly-evolving galaxies by radiation pressure (known as the slow-flow, dust-efflux model, Zahid et al. 2013b), and c) gradual dilution of low-SFR, elliptical galaxies in the absence of secular star formation (as proposed in this work). The second of these provides a direct explanation for the relation between  $M_*$  and dust extinction in low- $z$  galaxies (Zahid et al., 2013a). However, it is not certain that the radiation-driven winds would be of higher *metallicity* than that measured in the galaxies’ HII regions. If any (or a combination) of these three mechanisms is happening to a significant number of galaxies at low redshift, then the shape of the FMR would be more complicated than first assumed. Therefore, the full population of galaxies in the local Universe would not be adequately fit by a simple 2D projection of the FMR, and caution should be taken when using such a projection to describe low- $z$  galaxies with  $M_* \gtrsim 10^{10.5} M_\odot$ .

## 3.7 Conclusions

We have compared various physical properties of two classes of massive galaxy in the SDSS-DR7 and Munich semi-analytic model of galaxy formation, L-GALAXIES. These two classes are selected by their specific star formation rates and gas-phase metallicities; high-sSFR, high- $Z_g$  systems are labelled as ‘enriching’ galaxies, and low-sSFR, low- $Z_g$  system are labelled as ‘diluting’ galaxies. The following results were obtained from this comparison:

- Diluting galaxies in the semi-analytic model have higher bulge-to-total mass ratios, mass-weighted ages, and central black hole masses than model enriching galaxies at  $z = 0$ , and lower cold gas masses, gas-to-stellar mass ratios, and differences between their gas-phase and stellar metallicities.
- These properties are all signatures of the specific evolution undergone by such galaxies – a gas-rich merger and subsequent starburst, followed by a cessation in secular star formation. A *gradual* dilution of the gas phase then takes place for up to several gigayears, via the accretion of metal-poor, cold gas in clumps and low-mass merging satellites. This gradual dilution drives the positive correlation between SFR and  $Z_{\text{cold}}$  seen in massive galaxies at  $z = 0$  in the model.
- *All* the signatures of the evolution described above are also seen in low-sSFR, low- $Z_g$ , massive galaxies in the SDSS-DR7. Of particular note are their elliptical morphologies, low gas fractions and low  $Z_g - Z_*$ , which suggest dilution of the gas-phase in the absence of star formation. This is strong, indirect evidence that gradual dilution *after* a gas-rich merger event is taking place in some elliptical galaxies in the local Universe.
- These results suggest an alternative mechanism by which galaxies can fall off the  $M_*$ - $Z_g$  relation to lower metallicities. In this scenario, galaxies remain at low  $Z_g$  for a longer period than possible via rapid dilution (and re-enrichment) *during* mergers and interactions.
- The *positive* correlation found between SFR and  $Z_g$  in the local Universe shows that current formulations of the FMR (which assume a weak *anti*-correlation between SFR and  $Z_g$  at high mass) do not accurately represent the whole galaxy population.

We close by highlighting some important limitations of the observational and model analysis in this work. First, the gas-phase metallicities used are measured

from light falling within the 3-arcsecond aperture of the SDSS fibres. This covers the inner  $\sim 1$  to 9 kpc of galaxies in our Main sample. Gas lying at larger radii will therefore not be included in the metallicity estimates.

Second, a significant amount of high- $M_*$ , low- $Z_g$  galaxies are missing from our observational analysis because of poorly-constrained estimates of their key physical properties. Future observations of such galaxies' gas content from near-IR absorption lines in the CGM (e.g. Péroux et al. 2013), and gas-phase metallicity from temperature-insensitive emission lines in the far-IR (e.g. Croxall et al. 2013) would greatly help us probe this important part of the galaxy population. Likewise, the wealth of information available for (potentially) low- $Z_g$ , AGN-host galaxies remains untapped, due to the contamination of their spectra by emission from the nucleus. Continued measurements of  $Z_g$  from their narrow-line regions (e.g. Husemann et al. 2012), or of the molecular gas in and around these objects (e.g. Russell et al. 2013), would open-up these systems for future analysis.

Third, with regard to the model, the analytic prescriptions used to represent physical mechanisms are still rather crude, and this could be affecting the degree to which dilution is possible in model, as well as the nature of other galactic processes. For example, radio-mode AGN feedback is assumed to be continuous in L-GALAXIES, as long as there is hot gas available to feed a large central black hole. In reality, AGN activity is likely to be a cyclical process, with the associated feedback being turned on and off throughout a massive galaxy's lifetime (e.g. Shabala et al. 2008). There is also no gradual stripping of the cold gas in satellites in the current version of L-GALAXIES. This material is only released into the hot CGM of the central galaxy if the satellite's stellar component is entirely disrupted by tidal forces (see Guo et al. 2011, Section 3.6.2). Finally, the chemical enrichment treatment used in the Guo et al. (2011) version of the model is over-simplified: a fixed fraction (3 per cent) of the mass formed into stars during a star formation event is immediately returned to the ISM of a galaxy as 'metals'. No account is taken of the various lifetimes of stars, or the various species of heavy elements that are released in the stellar winds and supernovæ. This last issue is comprehensively addressed with a new implementation of galactic chemical evolution (GCE) in L-GALAXIES, which is described in detail in the following chapter. The results obtained from this new GCE model are discussed in Chapter 5, with reference to observational data from the local Universe.

# Chapter 4

## Galactic Chemical Evolution modelling

*“The men of experiment are like the ant, they only collect and use; the reasoners resemble spiders, who make cobwebs out of their own substance. But the bee takes the middle course: it gathers its material from the flowers of the garden and field, but transforms and digests it by a power of its own.”*

**Francis Bacon**

### 4.1 Introduction

Significant progress has been made in the field of galactic chemical evolution (GCE) since the first postulation of stellar nucleosynthesis by Arthur Eddington in the 1920s (Eddington, 1920). The first techniques to determine element abundances in both gas (e.g. Aller 1942) and stars (e.g. Chamberlain & Aller 1951) were developed, and the theory of stellar nucleosynthesis was given a more formal footing by Burbidge et al. (1957). Later, more sophisticated studies of GCE were stimulated by the celebrated review by Beatrice Tinsley (Tinsley, 1980). Now, it has been determined that a galaxy’s metallicity is related to its luminosity (e.g. Lequeux et al. 1979), age (e.g. Edvardsson et al. 1993, but see e.g. Friel 1995), and stellar mass (e.g. Tremonti

et al. 2004), and that different types of stars contribute to GCE in different ways (e.g. Salaris & Cassisi 2005).

However, many questions relating to the cosmic abundances of heavy elements still remain. For example, it is still unclear what exact role different types of supernovæ (SNe) and stellar winds play in the chemical enrichment of galaxies (e.g. McWilliam 1997), what the shape and universality of the stellar initial mass function (IMF) is (e.g. Bastian, Covey & Meyer 2010), how best to model the metal yields produced in stars (e.g. Romano et al. 2010), and what the progenitors and delay times of SNe-Ia are (e.g. Maoz & Mannucci 2012). These are important questions for us to address, as the chemical evolution of galaxies plays a key part in the evolution of galaxies in general; the presence of metals affects the cooling of gas (e.g. Sutherland & Dopita 1993), the formation of stars (e.g. Walch et al. 2011), stellar evolution (e.g. Salaris & Cassisi 2005), and the yields of newly synthesised metals (e.g. Woosley & Weaver 1995) which are released into the interstellar medium (ISM), circumgalactic medium (CGM) and even the intergalactic medium (IGM).

Aside from the ongoing observational studies into these questions, galaxy evolution models incorporating sophisticated GCE modelling also provide an opportunity to further constrain the chemical evolution of galaxies (see Section 1.3). Many previous theoretical works have focused on reproducing the chemical signatures found in the solar neighbourhood (e.g. Tinsley 1980; Matteucci & Greggio 1986; Matteucci 1986; Thomas, Greggio & Bender 1998; François et al. 2004; De Rossi et al. 2009; Calura & Menci 2009; Calura et al. 2010; Romano et al. 2010; Tissera, White & Scannapieco 2012; Pilkington et al. 2012; Calura et al. 2012; Micali, Matteucci & Romano 2013; Minchev, Chiappini & Martig 2013), chiefly in order to constrain the contributions from different types of SNe and stellar winds. Many others have focused on the chemical properties of local elliptical galaxies (e.g. Matteucci 1994; Thomas & Kauffmann 1999; Thomas, Greggio & Bender 1999; Pipino & Matteucci 2004; Nagashima et al. 2005b; Pipino et al. 2009a,b; Calura & Menci 2009; Arrigoni et al. 2010a; Calura & Menci 2011; Pipino & Matteucci 2011; Gargiulo et al. 2014), chiefly to try to reconcile the observed positive slope in the relation between  $M_*$  and  $[\alpha/\text{Fe}]$  with our theoretical understanding of metal production and galaxy formation.

The aim of this work is to address both of these issues, using a new implementation of detailed chemical enrichment in the Munich semi-analytic model of galaxy formation. We investigate if the chemical properties of MW disc stars and local elliptical galaxies can be simultaneously obtained with a self-consistent model which assumes a  $\Lambda$ CDM hierarchical merging scenario and varied star formation histories (SFHs). We also compare different SNe-II yield sets and SN-Ia delay-time distributions (DTDs), to see which allow us to best match the observational data considered.

This chapter is structured as follows: in Section 4.2 we give a general outline of the Munich semi-analytic model, L-GALAXIES. In Section 4.3 we describe the stellar yields, lifetimes and IMF used as inputs to our model. In Section 4.4 we describe the basic equations required to model GCE and discuss the SN-Ia DTD. In Section 4.5 we explain how this GCE model is implemented into the larger semi-analytic model and review the key physical processes governing the distribution of metals throughout galaxies. We conclude in Section 4.6.

## 4.2 The semi-analytic model

In this chapter, we develop the Guo et al. (2011) version of L-GALAXIES, running the model on subhalo trees built from the MILLENNIUM simulation (see Section 1.4). The model is discussed in detail in Guo et al. (2011), and the aspects most relevant to the work described in this thesis are discussed in Section 1.5.1.

Prior to this work, L-GALAXIES included a simple GCE implementation. A fixed metal yield of  $0.03 \cdot \Delta M_*$  was assumed to be ejected into the ISM immediately after a star formation event, where  $\Delta M_*$  is the mass of stars formed at that time. A further 40 per cent of  $\Delta M_*$  was assumed to return immediately to the gas phase as H and He. Such an ‘instantaneous recycling approximation’ is often used in galaxy formation models for its simplicity, but does not adequately describe the delayed enrichment of metals, particularly from long-lived low- and intermediate-mass stars and SNe-Ia. Previously, L-GALAXIES also did not consider individual chemical elements, but instead tracked only the total metal mass in each galaxy component. The tracking of individual elements allows us to compare with more detailed observational data on the chemical composition of the Milky Way and other galaxies (see Chapter 5). For example, the ratio of  $\alpha$  elements to iron is believed to be a good indicator of the star formation timescale. A comparison of  $[\alpha/\text{Fe}]$  between real galaxies and model galaxies with known star formation histories will allow us to test this. Also, in future, tracking individual elements will provide a more realistic treatment of gas cooling, which depends not only on the total metallicity, but also on the relative abundance of different heavy elements, as well as the ultraviolet background radiation.

The model parameters we use in this paper are identical to those in Guo et al. (2011), with the exception of the halo-velocity-dependent SN energy efficiency,  $\epsilon_h$ , which we have increased in order to maintain the same total SN feedback energy that was used previously (see Sections 1.5.1 and 4.5.3).

### 4.3 GCE Ingredients

In order to model the chemical evolution of galaxies, we first need to know the total mass of heavy elements liberated from stars at any given time. To do this, we need to know a) how many stars eject metals at that time, and b) how much of each element they eject. The former is given by the assumed stellar lifetimes, the IMF and the SFHs of galaxies. The latter is given by the stellar yields, obtained from stellar evolution models. The yield of element  $i$  from a star,  $y_i$ , is defined here as the mass of that element that is synthesised and ejected (see Section 1.3.1). If an element undergoes a net destruction during stellar nucleosynthesis (e.g. hydrogen), then its yield will be negative, whereas the *mass* of the element ejected will not.

The yields, as well as depending on the initial mass (and metallicity) of the star, also depend on the mode of ejection. We consider three modes in this work; stellar winds from low- and intermediate-mass stars during their thermally-pulsing asymptotic giant branch phase (TP-AGB, or simply AGB phase), SNe-Ia from some intermediate-mass binary systems, and the SN-II explosions of massive stars. Each of these three modes releases a different set of heavy elements at different times. Long-lived stars of mass  $0.85 \lesssim M/M_\odot \lesssim 7$  release mainly He, C and N. SNe-Ia produce and eject mainly Fe and other iron-peak elements, whether they originate from single degenerate binaries (Whelan & Iben, 1973), double degenerate binaries (Webbink, 1984; Iben & Tutukov, 1984), or otherwise (e.g. the binary progenitors of double-detonation, sub-Chandrasekhar-mass explosions, see Ruiter et al. 2011). Finally, short-lived stars of mass  $\gtrsim 7M_\odot$  can explode as core-collapse SNe-II, ejecting chiefly  $\alpha$  elements (e.g. O, Ne, Mg, Si, S and Ca).

We note here that we only consider eleven chemical elements in our GCE model, namely, H, He, C, N, O, Ne, Mg, Si, S, Ca and Fe, as these elements are included in all of the yield sets we consider.

The following sub-sections outline in more detail these key ingredients for galactic chemical enrichment. The SFHs of galaxies are tracked self-consistently in our semi-analytic model and are discussed in Section 4.5.1.

#### 4.3.1 The IMF

The IMF,  $\phi(M)$ , is a probability density function, which tells us the fraction of stars in a  $1M_\odot$  simple stellar population (SSP) that are within a given mass range. It is obtained from the observable present day mass function (PDMF) of field stars in the Milky Way, or from PDMF indicators in extragalactic regions. In this work, we assume that the IMF is the same in all regions of space and does not evolve with

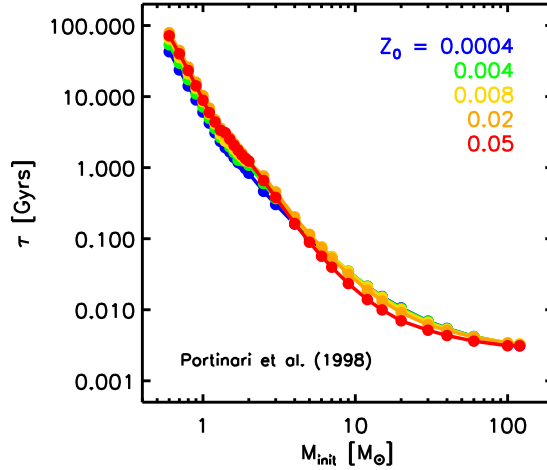


Figure 4.1: The lifetimes of stars as a function of initial mass, for five different initial metallicities, as predicted by Portinari, Chiosi & Bressan (1998).

time. There are, however, currently conflicting conclusions in the literature as to its universality (e.g. Weidner & Kroupa 2006; Elmegreen 2006; Bastian, Covey & Meyer 2010; van Dokkum & Conroy 2010; Gunawardhana et al. 2011; Fumagalli, Da Silva & Krumholz 2011; Conroy & van Dokkum 2012b; Spiniello et al. 2013).

The IMF used in this work is taken from Chabrier (2003). This version is commonly used in chemical enrichment models, and is already utilised in L-GALAXIES via the stellar population synthesis models of Bruzual & Charlot (2003) and Maraston (2005). Its use therefore provides both a good comparison to other works and self-consistency within the code. The Chabrier IMF is given analytically as

$$\phi(M) = \begin{cases} A_\phi M^{-1} e^{-(\log M - \log M_c)^2 / 2\sigma^2} & \text{if } M \leq 1M_\odot \\ B_\phi M^{-2.3} & \text{if } M > 1M_\odot \end{cases}, \quad (4.1)$$

where  $M_c = 0.079M_\odot$  and  $\sigma = 0.69$ . The values of the coefficients  $A_\phi$  and  $B_\phi$  are determined by requiring that a) the overall function is continuous, and b) the IMF *by mass* is normalised to  $1M_\odot$  over the full mass range of stars considered;

$$\int_{M_{\min}}^{M_{\max}} M\phi(M)dM = 1M_\odot, \quad (4.2)$$

where  $M_{\min} = 0.1M_\odot$ . When assuming  $M_{\max} = 120M_\odot$ , as we do in this work, the coefficients in Eqn. 4.1 are  $A_\phi = 0.842984$  and  $B_\phi = 0.235480$ .

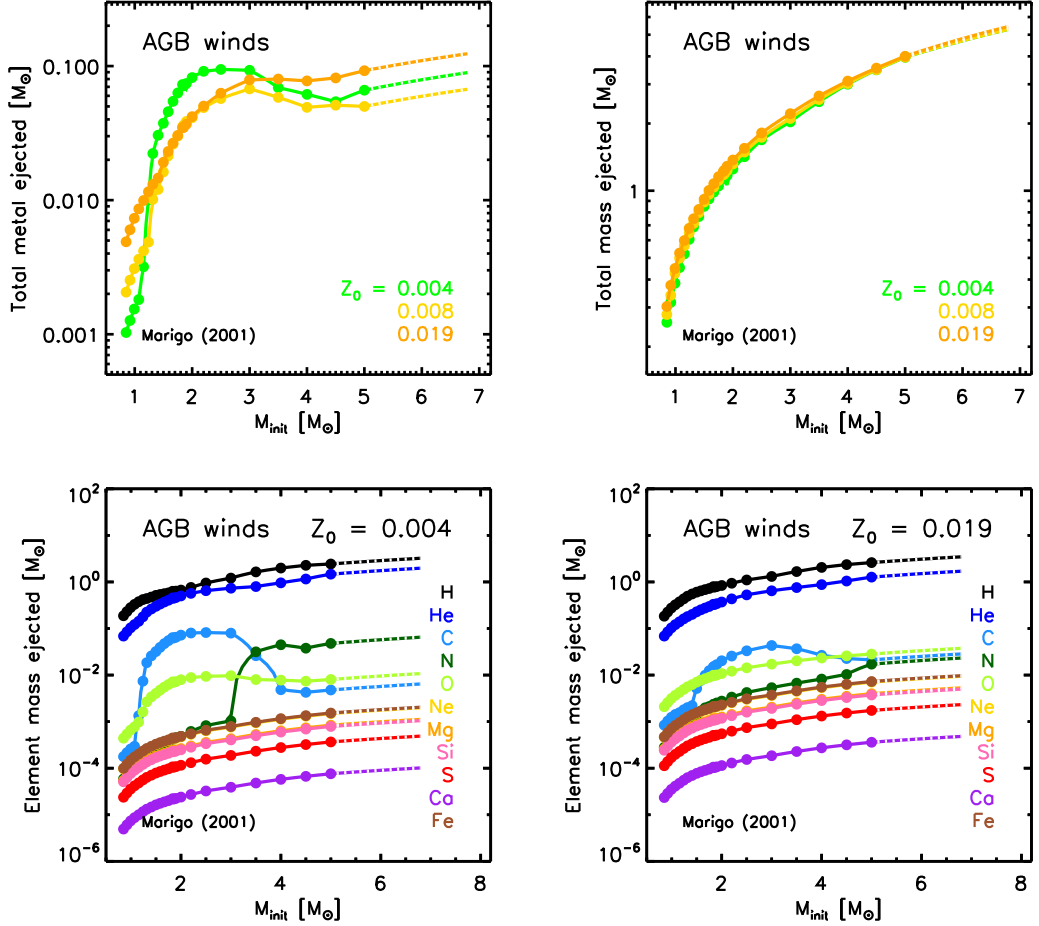


Figure 4.2: Mass released by AGB winds from the Marigo (2001) yield tables. Points indicate values from the yield tables. Solid lines indicate the interpolation used between these points. Dashed lines indicate extrapolations beyond the masses originally modelled. *Top left:* The mass of metals ejected as a function of mass, for three different initial metallicities. *Top right:* The total baryonic mass ejected as a function of mass, for three different initial metallicities. *Bottom left:* The mass of each element ejected as a function of mass, for stars of  $Z_0 = 0.004$ . *Bottom right:* Same as bottom left, for stars of  $Z_0 = 0.019$ .

Once normalised to the total mass of the SSP, Eqn. 4.1 can be integrated over a certain mass range to tell us the number density ( $n = N/V$ ) of stars in that mass range. Assuming that the IMF is the same everywhere, this is equivalent to the *number* of stars in a  $1M_{\odot}$  SSP in a given mass range. This integrated, normalised IMF has units of  $1/M_{\odot}$ .

The Chabrier IMF predicts fewer stars of mass  $< 1M_{\odot}$  than the Salpeter (1955) IMF, and does so with a smoother transition than the multi-segment power-law Kroupa (2001) IMF. At masses above  $1M_{\odot}$ , it has the same slope as the Kroupa IMF (an exponent of -2.3 in linear mass units, rather than the -2.35 used for the Salpeter IMF).

### 4.3.2 Stellar lifetimes

We adopt the metallicity-dependent lifetimes tabulated by Portinari, Chiosi & Bresnan (1998, hereafter P98), kindly provided by R. Wiersma (Wiersma et al., 2009b). These lifetime tables, along with the yields tabulated by P98 for SNe-II and the AGB yields considered here, were also used by the OWLS project for their cosmological, hydrodynamical simulations of galaxy evolution (Wiersma, Schaye & Britton, 2009a; Wiersma et al., 2009b; Schaye et al., 2010). The P98 lifetime tables account for stars in the mass range  $0.6 \leq M/M_{\odot} \leq 120$ , and five different initial metallicities, from 0.0004 to 0.05 (where metallicity is the fraction  $M_Z/M$  here). The same study also provided SN-II yield tables, which we also use (see Section 4.3.5).

The lifetimes for different initial metallicities are plotted as a function of mass in Fig. 4.1. Within the metallicity range shown, the most massive stars ( $\sim 120M_{\odot}$ ) live for up to  $\sim 3.3$  Myrs, depending on their initial metallicity, while the smallest stars that shed material during their lives ( $\sim 0.85M_{\odot}$ ) live for  $\sim 10$  to 21 Gyrs. Stars of  $\sim 1M_{\odot}$  can live from  $\sim 6$  to 10 Gyrs according to these lifetime tables, implying that some G V stars (also known as G dwarfs) would *not* live for more than a Hubble time. The implications of this are briefly discussed in Section 5.3.

### 4.3.3 AGB wind yields

We adopt the metallicity-dependent yield tables of Marigo (2001, hereafter M01) for low- and intermediate mass stars, also kindly provided by R. Wiersma (Wiersma et al. 2009b). These stars eject their metals predominantly through stellar winds during their AGB phase, although total yields from the RGB and AGB phases combined are included in the M01 tables. For simplicity, we refer to these as ‘AGB wind’ yields hereafter. The SN-II yield tables of P98, which we also use, form a complete set with

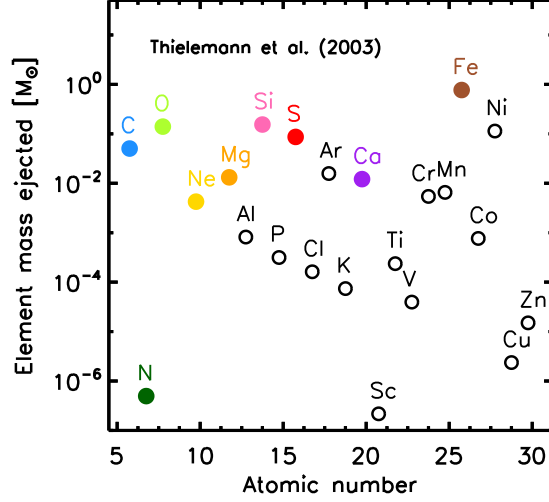


Figure 4.3: The mass of each element ejected from SNe-Ia, according to the tabulation of Thielemann et al. (2003). Coloured circles represent elements that are considered in this work.

those of M01 for AGB winds. They are both based on the same Padova evolutionary tracks and do not require a large interpolation between them, as the AGB yields consider stars up to  $5M_{\odot}$  and the SN-II yields consider down to  $7M_{\odot}$ .<sup>1</sup> In this work, we consider the ejecta from AGB winds to occur at the end of a star’s lifetime.

Fig. 4.2 shows the *ejected mass* of metals (top left panel), total baryons (top right panel), and individual elements (bottom two panels) from AGB stars as a function of initial mass. This is different from the *yield*, as it includes both the mass that passes through the stars unprocessed and any newly synthesised material. The element abundances of the Sun from Asplund et al. (2009) are used to scale the amplitudes of the curves in Fig. 4.2.

We note that no elements heavier than oxygen present in the wind have been synthesised or destroyed in the AGB stars, but have instead been formed in previous generations of stars and pass through the AGB stars unprocessed. We have extrapolated the AGB wind yields from  $5M_{\odot}$  to  $7M_{\odot}$ , so that they meet with the SN-II yields used. The exact position of this interface within the region  $5 < M/M_{\odot} < 8$  does not significantly affect our results.

<sup>1</sup>We note that it is also possible to link the M01 AGB yields to the P98 SN-II yields at  $6M_{\odot}$ , by including the P98 yields for electron-capture SNe (see P98, Section 4.2). Doing this makes a negligible difference to the results discussed in this work.

### 4.3.4 SN-Ia yields

As with many other chemical enrichment models, we adopt the spherically symmetric ‘W7’ model for our SN-Ia explosive yields, originally tabulated by Nomoto et al. (1984). We use a more recent iteration, by Thielemann et al. (2003, hereafter T03). These tables provide the synthesised mass of forty two different element species. Unlike the AGB and SN-II yields, the SN-Ia yields used here are independent of the initial mass and metallicity of the progenitor system. The total mass ejected in a SN-Ia is assumed to be  $1.23M_{\odot}$ , the sum of the ejecta from the eleven elements considered in this work. As no H or He is ejected by SNe-Ia, this sum equals the mass of metals ejected. Fig. 4.3 shows the ejected mass of each element. Iron is the most abundant, while there are also non-negligible amounts of oxygen, silicon and nickel.

SN-Ia yields that depend on the initial mass and metallicity of the progenitors are now also available in the literature (e.g. Seitenzahl et al. 2013). We defer a study of the effect of such yields on our GCE model to future work.

Rather than make assumptions about the type and lifetimes of the progenitor systems involved, we instead use observationally-motivated DTDs to define the lifetimes of SN-Ia progenitors (see Section 4.4.1).

### 4.3.5 SN-II yields

Our preferred set of SN-II yields is tabulated by P98, and also kindly provided by R. Wiersma (Wiersma et al. 2009b). This set contains yields for initial masses ranging from 6 to  $1000 M_{\odot}$ , and five initial metallicities from 0.0004 to 0.05. We only consider the existence of stars up to  $120 M_{\odot}$  here. It is not entirely clear up to what initial mass a star can explode as a SN-II. Early estimates suggested that only stars below  $\sim 40 M_{\odot}$  could explode, rather than directly collapse into black holes (e.g. Freyer 1999). However, the effects of convection, overshooting, rotation and the detail of the stellar structure can all have a significant impact on whether a massive star can explode or not (e.g. Woosley & Janka 2005; Ugliano et al. 2012). Importantly, the P98 yield set takes account of mass loss through stellar winds prior to the SN, which not only directly contributes to the chemical enrichment of the surrounding gas, but also on the composition of the explosive yields, as explained below.

We note here that, unlike the commonly-used tables of Woosley & Weaver (1995), both sets of SN-II yield tables considered in this work account for the decay of nickel into iron shortly after the SN. P98 do so by simply adding the  $^{56}\text{Ni}$  yield to that of  $^{56}\text{Fe}$ , and Chieffi & Limongi (2004) by only tabulating yields  $10^8$ s after the explosion.

Fig. 4.4 shows the *ejected mass* of metals (top left panel), total baryons (top

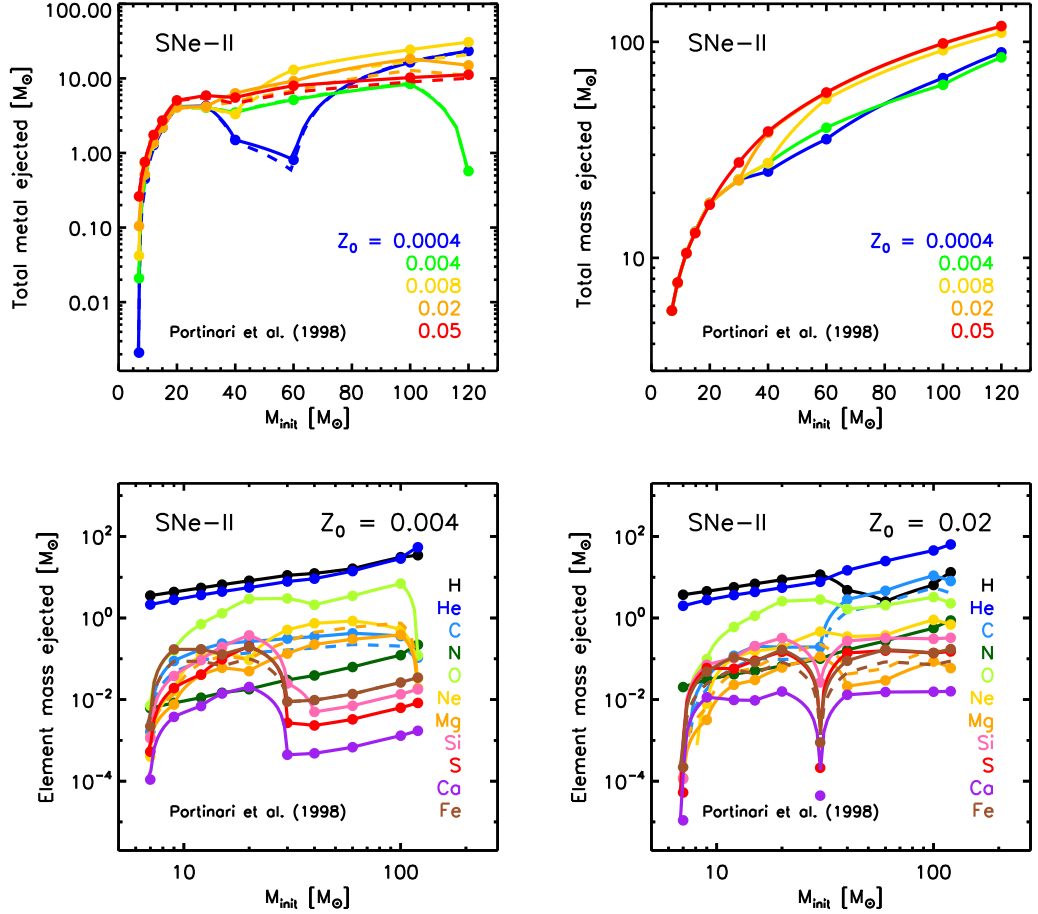


Figure 4.4: Mass released by SNe-II from the Portinari, Chiosi & Bressan (1998) yield tables. Points indicate values from the yield tables. Solid lines indicate the interpolation used between these points. *Top left:* The mass of metals ejected as a function of mass, for five different initial metallicities. *Top right:* The total baryonic mass ejected as a function of mass, for five different initial metallicities. *Bottom left:* The mass of each element ejected as a function of mass, for stars of  $Z_0 = 0.004$ . Dashed lines indicate the corrected C, Mg and Fe yields (see text). *Bottom right:* Same as bottom left, for stars of  $Z_0 = 0.02$ .

right panel), and individual elements (bottom two panels) from SNe-II as a function of initial mass, as is done for AGB winds in Fig. 4.2. The dashed lines in Fig. 4.4 indicate corrections to the C, Mg and Fe yields that we include in our model, following the recommendation of Wiersma et al. (2009, see their Section A3.2). These *ad hoc* corrections can be justified by uncertainties in the explosive yields tabulated by Woosley & Weaver (1995), on which the P98 SN-II yields are based. These corrections halve the yield of C and Fe and double the yield of Mg, relative to the originally tabulated values.

We note that the P98 yields show some sudden drops in the ejecta of certain elements. At low metallicities, the reduction in yield of the heaviest elements above  $\sim 30M_{\odot}$  is due to them being locked in the stellar remnant. Remnant masses increase significantly above  $\sim 30M_{\odot}$  at low metallicities due to low mass-loss efficiency prior to the SN. This effect is less severe for lighter elements, such as oxygen, as ‘pair creation’ SNe are believed to dominate over ‘core collapse’ SNe above  $\sim 60M_{\odot}$ , allowing more of these elements to be ejected. At higher metallicities, more efficient mass loss prior to the SN inhibits large remnant formation below  $\sim 30M_{\odot}$ . Above  $\sim 30M_{\odot}$ , increased mass loss from Wolf-Rayet stars causes the larger He and C yields seen for  $Z_0 \geq 0.02$  in the bottom-right panel of 4.4. The removal of these elements in the wind in turn suppresses the explosive  $\alpha$  element yields. The dip in yield of the heavier elements seen at  $30M_{\odot}$  (between these two regimes of efficient mass loss) is due to these elements being locked in the stellar remnant. For more details, see Section 5 of P98.

These specific features could have a significant impact on our results. We therefore also test our GCE implementation with an alternative set of SN-II yields, that do not take account of prior mass loss, and therefore appear more stable as a function of initial mass and metallicity. This second set is taken from Chieffi & Limongi (2004, hereafter CL04). These account for stars of initial masses from 13 to 35  $M_{\odot}$ , and so require both an extrapolation downwards to the upper mass limit for AGB winds (chosen here to be  $7M_{\odot}$ ), and upwards to a more reasonable maximum mass. We choose  $M_{\max} = 120M_{\odot}$  when using the CL04 SN-II yields in order to match the maximum mass considered for the P98 SN-II yields. However, we caution that this represents a gross extrapolation into a regime well above that constrained by the original yield calculations. For this reason we use the CL04 yields only as a comparison to those of P98, in order to discern what effect prior mass loss might have on our overall results.

## 4.4 The GCE Equation

In this section, we present the GCE equations required to calculate the mass ejection rate from stars. The implementation of these equations into our semi-analytic model is described in Section 4.5.

Following the prescriptions given by Tinsley (1980), the total rate of mass ejected by an SSP at time  $t$  is given by

$$e_M(t) = \int_{M_L}^{M_U} (M - M_r) \psi(t - \tau_M) \phi(M) dM , \quad (4.3)$$

where  $M$  is the initial mass of a star,  $\tau_M$  is its lifetime,  $\psi(t - \tau_M)$  is the star formation rate when the star was born,  $M_r$  is the mass of the stellar remnant, and  $\phi(M)$  is the normalised IMF by number, as given by Eqn. 4.1.

$\psi(t - \tau_M) \cdot \phi(M)$  gives us the birthrate of stars of mass  $M$  at time  $t - \tau_M$ . Multiplying this birthrate by  $(M - M_r)$ , the mass ejected by *one* star of mass  $M$ , then gives us the total mass ejection rate by stars of mass  $M$ , at time  $t$ . We can then integrate this quantity over a suitable range of masses ( $M_L$  to  $M_U$ ) to obtain  $e_M(t)$ .

The same equation can be written when only considering the *metals* ejected by an SSP:

$$e_Z(t) = \int_{M_L}^{M_U} M_Z(M, Z_0) \psi(t - \tau_M) \phi(M) dM , \quad (4.4)$$

where  $M_Z = y_Z(M, Z_0) + Z_0 \cdot (M - M_r)$  is the mass in metals returned to the gas phase by a star of mass  $M$  (as clarified by Maeder 1992, Section 4.1). This is made up of the mass- and metallicity-dependent yield<sup>2</sup>  $y_Z$ , plus those metals present at the formation of the star that are later ejected unprocessed,  $Z_0 \cdot (M - M_r)$ .

The same equation can be written again, when only considering individual chemical elements ejected by an SSP, replacing  $M_Z$  with  $M_i = y_i(M, Z_0) + (M_i/M)(M - M_r)$ , the total mass of element  $i$  returned to the gas phase by a star of mass  $M$ . However, for simplicity, we will proceed by describing the GCE equation in terms of the total metals ejected.

Eqn. 4.4 can be further split-up into four sub-components, representing the three modes of ejection, AGB winds, SNe-Ia and SNe-II:

---

<sup>2</sup>We define the metal yield from a star as a mass, rather than the mass fraction  $p_Z$  proposed by Tinsley (1980).

$$\begin{aligned}
e_Z(t) &= \int_{0.85M_\odot}^{7M_\odot} M_Z^{\text{AGB}}(M, Z_0) \psi(t - \tau_M) \phi(M) \, dM \\
&+ A' k \int_{\tau_{8M_\odot}}^{\tau_{0.85M_\odot}} M_Z^{\text{Ia}} \psi(t - \tau) \text{DTD}(\tau) \, d\tau \\
&+ (1 - A) \int_{7M_\odot}^{16M_\odot} M_Z^{\text{II}}(M, Z_0) \psi(t - \tau_M) \phi(M) \, dM \\
&+ \int_{16M_\odot}^{M_{\text{max}}} M_Z^{\text{II}}(M, Z_0) \psi(t - \tau_M) \phi(M) \, dM . \tag{4.5}
\end{aligned}$$

The first term in Eqn. 4.5 represents the contribution to the ejected metals from AGB winds (approximating that the material is shed at the end of the stars' lives), with the symbols representing the same quantities as in Eqn. 4.4. As can be seen, the integral extends to masses above the minimum mass of SN-Ia-producing binary systems ( $\sim 3M_\odot$ ). Therefore, we are explicitly accounting for the ejection of metals during the AGB phase of such stars, prior to the SN.

The second term represents the contribution from SNe-Ia, parameterised with an analytic DTD motivated by observed SN-Ia rates. The three SN-Ia DTDs that we consider in this work are described in Section 4.4.1. The coefficient  $A'$  in the second term of Eqn. 4.5 gives the fraction of objects from *the whole* IMF that are SN-Ia progenitors. This is subtly different from  $A$  in the third term, which is the fraction of objects only in the mass range  $3\text{--}16M_\odot$  that are SN-Ia progenitors. As clarified by Arrigoni et al. (2010a, Section 3.3), these two coefficients are related by  $A' = A \cdot f_{3-16}$ , where  $f_{3-16}$  is the fraction of all objects in the IMF that have mass between 3 and  $16M_\odot$ . Our chosen value of  $A$  is 0.028 (i.e. 2.8 per cent of the stellar systems in the mass range  $3\text{--}16M_\odot$  are SN-Ia progenitors), as discussed in Section 4.5.4. The coefficient  $k$  is given by

$$k = \int_{M_{\text{min}}}^{M_{\text{max}}} \phi(M) \, dM , \tag{4.6}$$

and gives the number of stars in a  $1M_\odot$  SSP. For the Chabrier IMF used here,  $f_{3-16} = 0.0385$  and  $k = 1.4772$  when assuming  $M_{\text{min}} = 0.1M_\odot$  and  $M_{\text{max}} = 120M_\odot$ .

Using a DTD means we do not have to make additional assumptions about the progenitor type of SNe-Ia, the binary mass function  $\phi(M_b)$ , secondary mass fraction distribution  $f(M_2/M_b)$ , or binary lifetimes in our modelling. These uncertain parameters become problematic when using the theoretical SN-Ia rate formalism of

Greggio & Renzini (1983). In this formalism, the contribution to  $e_Z(t)$  from SNe-Ia is modelled as

$$A \int_{3M_\odot}^{16M_\odot} M_Z \phi(M_b) \times \left[ \int_{\mu_{\min}}^{0.5} f(\mu) \frac{\psi(t - \tau_{M_2})}{M_b} d\mu \right] dM_b , \quad (4.7)$$

which involves an integral over the *binary* mass  $M_b$  within the range  $3 \leq M_b(M_\odot) \leq 16$ . Doing this implicitly assumes that the IMF counts SNe-Ia-producing binaries as single objects, and the distribution of binaries in this mass range is the same as that of single stars, given by Eqn. 4.1. The inner integral in the second term, multiplied by  $A$ , gives the total SNIa rate if all binaries had a fixed mass  $M_b$ . This is done by integrating over the secondary mass fraction  $\mu = M_2/M_b$  from its smallest possible value,  $\mu_{\min} = \max\{0.85/M_b, (M_b - 8)/M_b\}$ , to its largest possible value,  $\mu_{\max} = 0.5$ . Note that this assumes the maximum possible mass of the primary (exploding) C-O white dwarf star is  $8M_\odot$  (Becker & Iben, 1979). Therefore, when  $M_b = 16M_\odot$ , we have  $\mu_{\min} = \mu_{\max} = 0.5$ . Also,  $f(\mu)$  is the distribution function of the secondary mass fraction,

$$f(\mu) = 2^{1+\gamma}(1 + \gamma)\mu^\gamma , \quad (4.8)$$

where  $\gamma = 2$ . This is normalised so that

$$\int_{0.0}^{0.5} f(\mu)d\mu = 1 . \quad (4.9)$$

The normalised function  $f(\mu)$  is plotted in Fig. 4.5. It's form is supported by the observations of Tutukov & Yungelson (1980), who found that the binary mass ratio  $q = M_2/M_1$  in close binaries with two visible spectra (SB2 systems) is preferentially 1. However, assuming that the lifetime of such a binary is the same as that of the secondary star if it were in isolation may not be particularly realistic when moving away from the single-degenerate scenario.

The third term in Eqn. 4.5 represents the ejection of metals, via SNe-II explosions, of all objects within the mass range  $7.0 \leq M/M_\odot \leq 16.0$  that *do not* produce SNe-Ia. Hence, the coefficient is  $(1 - A)$ .<sup>3</sup>

The fourth term in Eqn. 4.5 represents the contribution to the ejection of metals from single, massive stars exploding as SNe-II.

---

<sup>3</sup>Note that, because the distribution of SN-Ia-producing binaries is assumed to follow the distribution of all objects, the value of  $A$  is the same for any mass range within  $3 < M/M_\odot < 16$ .

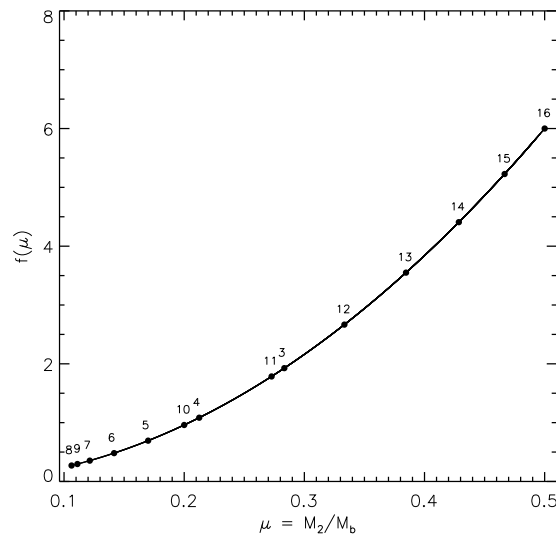


Figure 4.5: The secondary mass fraction distribution function  $f(\mu)$ , when normalised between the limits  $\mu = 0$  and  $0.5$ . In this form, the most likely ratio between the two component masses  $M_2/M_1$  is unity (when  $\mu = 0.5$ ). The points on the function mark the value of  $\mu_{\min}$  for different binary masses  $M_b$ . The value of  $M_b$  is written above each point. The highest possible value of  $\mu_{\min}$  is  $0.5 \equiv \mu_{\max}$ , and occurs when  $M_b = 16$ . In this case, only one value of  $\mu$  is permitted, as neither component star can have a mass  $> 8M_\odot$ . The lowest possible value of  $\mu_{\min}$  is  $0.106$ , and occurs when  $M_b = 8$ . At this binary mass, we have the maximum freedom in choosing values of  $M_1$  and  $M_2$ .

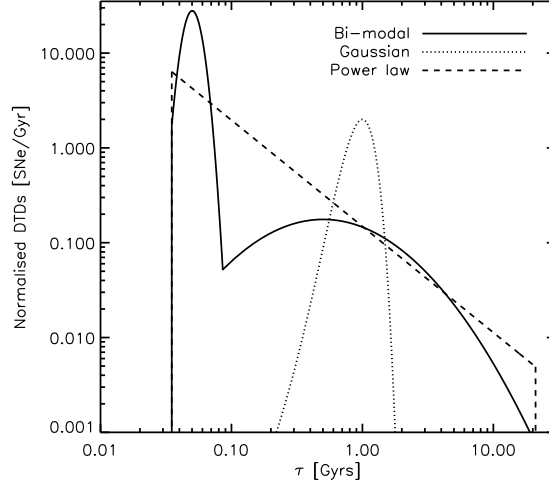


Figure 4.6: The three SN-Ia delay-time distributions considered in this work. The dashed line corresponds to the power-law DTD given by Eqn. 4.10. The dotted line corresponds to the narrow Gaussian DTD given by Eqn. 4.11. The solid line corresponds to the bi-modal DTD given by Eqn. 4.12. All three DTDs are normalised over the time range  $\tau_{8M_{\odot}} = 35$  Myrs to  $\tau_{0.85M_{\odot}} = 21$  Gyrs.

We note here that Eqn. 4.5 can also be rewritten so that all the modes of enrichment are expressed as time integrals, because the stellar lifetimes are a monotonic function of initial mass (e.g. P98, section 8.7).

#### 4.4.1 SN-Ia delay-time distribution

As mentioned in Section 4.4, due to the uncertainties in the true nature of SN-Ia progenitors, we prefer to model the SN-Ia rate using observationally-motivated DTDs, rather than taking a ‘first-principles’ approach. There have been many SN-Ia DTDs formulated in the literature. In this work, we consider three, shown in Fig. 4.6, and compare the results obtained from each.

The first is the power-law DTD with slope  $-1.12$  proposed by Maoz, Mannucci & Brandt (2012), formed from a fit to the SN-Ia rate derived from 66,000 galaxies (comprising 132 detected SNe-Ia) from the Sloan Digital Sky Survey II (SDSS-II):

$$\text{DTD}_{\text{PL}} = a(\tau/\text{Gyr})^{-1.12} , \quad (4.10)$$

where  $\tau$  is the delay time since the birth of the SN-Ia-producing binary systems, and  $a$  is the normalisation constant, taken here to be  $a = 0.15242 \text{ Gyr}^{-1}$  (see Eqn.

4.13). Similar power-law slopes have been suggested by a number of other works (e.g. Totani et al. 2008; Maoz, Sharon & Gal-Yam 2010; Maoz & Mannucci 2012).

The second is the narrow, Gaussian DTD proposed by Strolger et al. (2004), based on observations of 56 SNe-Ia in the range  $0.2 < z < 1.8$  from the GOODS North and South fields. This form is given by

$$\text{DTD}_{\text{NG}} = \frac{1}{\sqrt{2\pi\sigma_\tau^2}} e^{-(\tau-\tau_c)^2/2\sigma_\tau^2} , \quad (4.11)$$

where  $\tau$  is again the delay time,  $\tau_c = 1$  Gyr is the characteristic time (on which the Gaussian distribution is centered), and  $\sigma_\tau = 0.2\tau_c$  Gyrs is the characteristic width of the distribution.

The third is the bi-modal DTD proposed by Mannucci, Della Valle & Panagia (2006), motivated by simultaneously fitting both the observed SN-Ia rate and the distribution of SNe-Ia with galaxy B-K colour and radio flux, for a collection of samples over the redshift range  $0.0 < z < 1.6$ . This DTD includes a ‘prompt’ component of SNe-Ia ( $\sim 54$  per cent of the total) that explode within  $\sim 85$  Myr of the birth of the binary, followed by a broader, delayed distribution. The Mannucci, Della Valle & Panagia (2006) DTD has been expressed by Matteucci et al. (2006) as

$$\log(\text{DTD}_{\text{BM}}) = \begin{cases} 1.4 - 50(\log(\tau/\text{yr}) - 7.7)^2 & \text{if } \tau < \tau_0 \\ -0.8 - 0.9(\log(\tau/\text{yr}) - 8.7)^2 & \text{if } \tau > \tau_0 \end{cases} , \quad (4.12)$$

where  $\tau$  is the delay time, and  $\tau_0 = 0.0851$  Gyr is the characteristic lifetime separating the two components.

For all of these DTDs, the normalisation requirement is,

$$\int_{\tau_{\text{min}}}^{\tau_{\text{max}}} \text{DTD}(\tau) d\tau = 1 , \quad (4.13)$$

where  $\tau_{\text{min}} = \tau_{8M_\odot}$  and  $\tau_{\text{max}} = \tau_{0.85M_\odot}$  are the minimum and maximum assumed lifetimes of a SN-Ia-producing binary in the single-degenerate scenario (i.e. the lifetimes of the largest and smallest possible secondary stars), respectively. Strictly, their values depend on the stellar lifetime tables used, and therefore also on the metallicity of the stars. However, we choose to fix their values for Eqn. 4.13 to those provided by the P98 lifetime tables for stars of  $Z_0 = 0.02$ , namely  $\tau_{\text{min}} = 35$  Myrs and  $\tau_{\text{max}} = 21$  Gyrs. Our chosen value of  $\tau_{\text{min}} = 35$  Myrs is in line with those commonly used in the literature, with assumed values ranging from  $\sim 30$  Myrs (e.g. Matteucci

& Greggio 1986; Padovani & Matteucci 1993; Matteucci & Recchi 2001; Matteucci et al. 2009) to  $\sim 40$  Myrs (e.g. Greggio 2005). This choice also means that  $\sim 48$  per cent of SNe-Ia explode within 400 Myrs when using the power-law DTD, which is close to the  $\sim 50$  per cent predicted from observations of the SN-Ia rate by Brandt et al. (2010), and around the lower limit determined from SN remnants in the Small and Large Magellanic Clouds by Maoz & Badenes (2010).

## 4.5 Implementation

The GCE equation given by Eqn. 4.5 has been implemented into our semi-analytic model so that the mass of chemical elements ejected is calculated at each simulation timestep. The key aspects of this implementation are outlined in the following subsections.

### 4.5.1 SFH, ZH and EH arrays

There are three galaxy-dependent values that are required for us to predict ejection rates from stars: the star formation history (SFH), the total gas-phase metallicity history (ZH) and the gas-phase element abundance history (EH). The SFH is required to identify  $\psi(t - \tau_M)$ , the ZH is required to identify  $Z_0$ , and the EH is required to calculate the unprocessed ejecta of each individual element within the semi-analytic model. We accommodate these histories into arrays in our code.

As described in Sections 1.4.2 and 1.5.1, the L-GALAXIES time structure is made up of 63 snapshots (when run on the MILLENNIUM simulation), each containing 20 timesteps. As there are nearly 26 million galaxies by  $z = 0$  in the semi-analytic model, it would require a significant amount of memory for us to store the full histories of each galaxy at the resolution of one timestep. Therefore, we instead take a more dynamic approach; each galaxy has SFH, ZH and EH arrays of only 20 array-elements (hereafter, time ‘bins’). As time elapses in the simulation, the width of older bins (those storing data from higher redshifts) increases, while new bins are ‘activated’ with a default width of one timestep. Thus, the whole history of each galaxy can be stored with a time resolution that decreases with lookback time. High precision at recent times is especially important when calculating galaxy luminosities as a post-processing step, as young stars from recent star formation episodes tend to dominate the light. We have checked that changing the number of bins in the history arrays does not affect the chemical evolution in the model by testing our model with a range of history bin resolutions including full resolution (i.e.  $63 \times 20$  bins per galaxy).

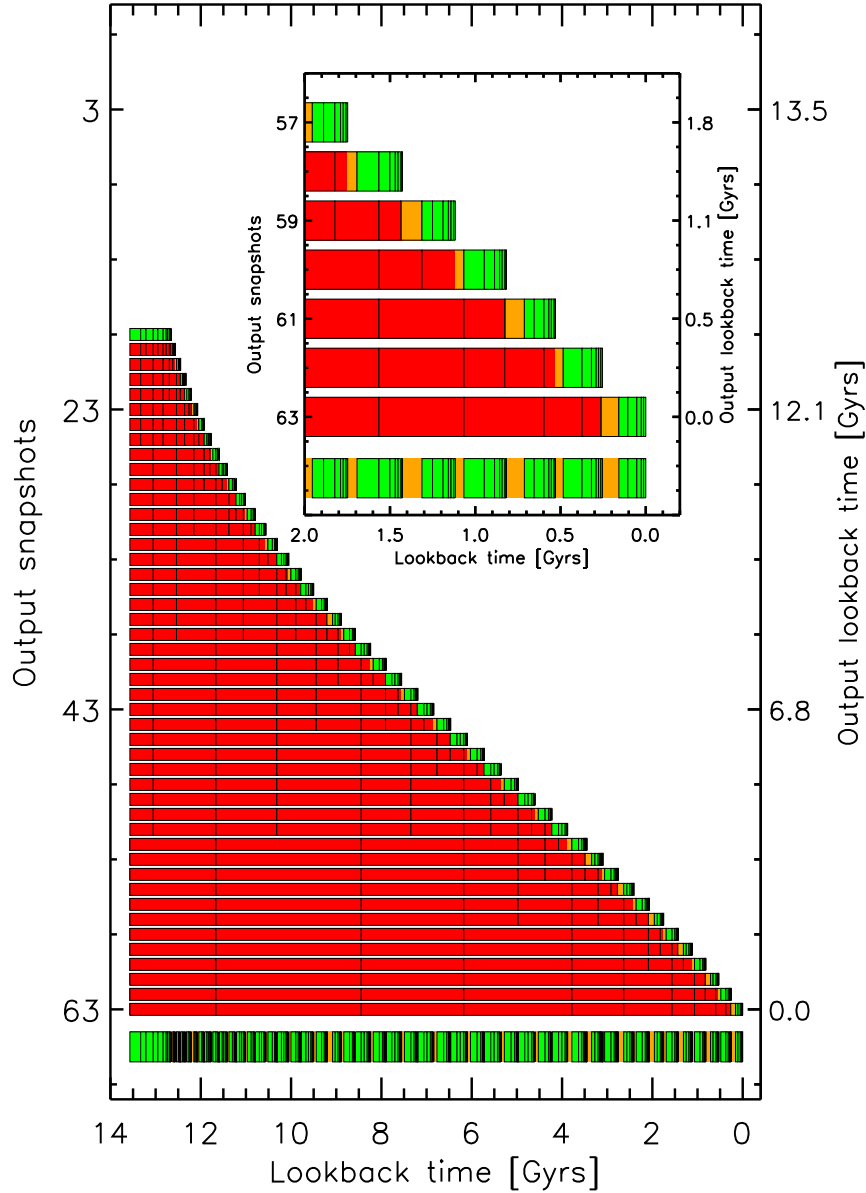


Figure 4.7: Schematic illustrating how history arrays are ‘stitched together’ in post processing to form higher-resolution histories when plotting data. At every output snapshot (y axis), a galaxy has a series of history bins (black boxes). The most recent bins from each output (in green) are extracted and used to form a higher-resolution, non-overlapping history (shown in the bottom row). The other bins (in red) are discarded. So that there are no gaps in the reconstructed histories, a fraction of the mass from partially overlapping bins is also included (in orange). This means that many hundreds of bins (depending on the formation time of the galaxy) can be used to make plots, rather than only 20 from the  $z = 0$  history. The inlay shows a zoom-in of the bottom-right region of the main schematic.

By  $z = 0$ , the older bins in such histories can be up to  $\sim 3$  Gyrs wide. This is acceptable when calculating the chemical enrichment within the code, as the bins are integrated over more finely at each timestep (see Section 4.5.2). However, when *plotting* relations using only the output  $z = 0$  history bins, the lower resolution at high- $z$  does not correctly represent the smooth chemical evolution actually occurring in our model. In these cases (for example, the [Fe/H]-[O/Fe] relation in Fig. 5.4), we construct higher resolution histories as a post-processing step, by ‘stitching together’ the highest-resolution bins from the histories of *all* output snapshots, rather than just those from  $z = 0$ . This procedure is illustrated by the schematic in Fig. 4.7. In this way, a much smoother evolution can be plotted, which more accurately represents the chemical evolution occurring within the code. We note that when doing this for the disc components of galaxies, account needs to be taken of stars that move from the disc to the bulge through disc instabilities, by ensuring that the total mass formed in the stitched-together bins does not exceed the mass formed in the  $z = 0$  history bins over the same time span.

### 4.5.2 Implementing the GCE equation

In order to model GCE, Eqn. 4.4 needs to be implemented into L-GALAXIES as an algorithm, involving numerical integration and interpolation between values in a number of look-up tables. All non-model-dependent terms (i.e. everything except the SFHs, ZHs and EHs) are pre-calculated and stored in look-up tables, in order to speed-up the runtime of the code. This is possible because the time structure of the history arrays is, by construction, the same for all galaxies at any given time. Therefore, we can know *a priori* the range of masses of stars that will explode in any given timestep.

We can re-write Eqn. 4.4 as

$$e_Z(t) = \psi(t - \tau) \left[ \int_{M_L}^{M_U} M_Z(M, Z_0) \cdot \phi(M) \, dM \right], \quad (4.14)$$

where  $\psi(t - \tau)$  can be put outside the integral if we assume, for each thin strip of the SFH integrated, that all the stars of mass  $M_L \leq M \leq M_U$  are born *at the same time* (i.e.  $\tau_{M_L} = \tau_{M_U} = \tau$ ). We can then pre-calculate the integral in Eqn. 4.14 numerically to obtain a value for each initial metallicity, in every history bin of every timestep that the semi-analytic model will run through, and store it in a 3-dimensional look-up table. The true value of  $Z_0$  for a given galaxy is then used within the semi-analytic model to interpolate between these pre-calculated results at each timestep, and  $\psi(t - \tau)$  is multiplied-in. The total mass in metals ejected is then

given by  $e_Z(t) \cdot \Delta t$ , where  $\Delta t$  is the width of the timestep. The same procedure is used to obtain the total mass ejected, and the total amount of each chemical element ejected at each timestep. Once the ejected masses are calculated, we transfer the material to either the galaxy's ISM or CGM, as described below.

### 4.5.3 SN feedback

The chemical enrichment recipe outlined above is only part of the relevant physics needed to accurately model the chemical evolution of galaxies. The distribution of these metals between the various components of galaxies, and out into the IGM, as well as the infall and cooling of gas, are also important considerations when looking beyond a simple closed-box model. Treatments of these physical processes are already incorporated into L-GALAXIES, and are described in Guo et al. (2011) and Section 1.5.1. However, we have now modified the prescription for SN feedback following our improvements to the GCE modelling.

In previous versions of L-GALAXIES, the amount of energy released by SNe was assumed to be proportional to the mass of stars *formed*,  $\Delta M_*$ , at that time. Now that we have discarded the instantaneous recycling approximation, it is more appropriate to relate this energy to the mass of material *released* by stars at that time. The total amount of energy produced by SN feedback is therefore parameterised as

$$E_{\text{SN}} = \epsilon_h \cdot \frac{1}{2} e_M(t) \Delta t V_{\text{SN}}^2, \quad (4.15)$$

where  $\epsilon_h$  is the halo-velocity-dependent SN energy efficiency, and  $V_{\text{SN}}$  is the SN ejecta speed, as before. The new term,  $e_M(t) \cdot \Delta t$ , is the mass released by stars in one timestep (see Eqn. 4.3), which is now used in place of  $\Delta M_*$ . Due to this change, we have doubled the value of  $\epsilon_h$ , in order to have the same total SN feedback energy ( $E_{\text{SN}}$ ) as previously used in the model. A thorough investigation into the precise values of model parameters required following our new GCE implementation is reserved for future work.

In our new, default GCE implementation, all stars dying in the stellar disc release material and energy into the ISM, whereas stars dying in the bulge and stellar halo release material and energy into the hot CGM. The energy dumped into the ISM by disc stars can then be used to reheat and possibly eject some (fully mixed) cold gas. Energy dumped into the CGM can also contribute to ejection. The amount of gas ejected from the DM halo into an external reservoir is now given by

$$\Delta M_{\text{ejec}} = \frac{E_{\text{SN}} - \frac{1}{2} \epsilon_{\text{disc}} e_M(t) \Delta t V_{\text{vir}}^2}{\frac{1}{2} V_{\text{vir}}^2}, \quad (4.16)$$

where  $\epsilon_{\text{disc}} \cdot e_M(t) \cdot \Delta t$  is the amount of gas that is reheated but does not escape the potential well. The ejected gas is then allowed to return to the DM halo over timescales that are proportional to  $t_{\text{dyn,h}}/V_{\text{vir}}$ . This constitutes a second component of gas infall that has been pre-enriched by the galaxy (see Section 1.5.1).

We have also implemented an alternative feedback prescription which includes metal-rich winds. These winds dump some material released by disc SNe-II directly into the hot gas. This scheme is discussed in Section 5.4.3.

#### 4.5.4 Default set-ups

There can be many free parameters involved when developing a chemical enrichment model. We have limited ourselves to only one new free parameter: the fraction,  $A$ , of objects in an SSP in the range  $3 \leq M/M_{\odot} \leq 16$  that are SN-Ia progenitors.<sup>4</sup>  $A$  is specifically ‘tuned’ so that the peak of the [Fe/H] distribution for G dwarfs in our MW-type galaxy sample is around the solar value (see Section 5.3). An increase in  $A$  corresponds to an increase in [Fe/H], and we find that the best value is  $A \sim 0.028$  for all three of the DTDs we consider (see Section 4.4.1). A single value of  $A$  was also found to be suitable for a range of different SN-Ia DTDs by Matteucci et al. (2009). All other results discussed in this work are obtained without further tuning. In the following, we label results using the bi-modal, power-law, and narrow Gaussian DTDs with ‘BM’, ‘PL’ and ‘NG’, respectively.

We note that our preferred value of  $A = 0.028$  is similar to that commonly found in the literature. For example, Greggio (2005) took a value of  $A' = 0.001$  when also using a Chabrier IMF, which equates to a value of  $A = 0.026$ . Similarly, de Plaa et al. (2007) take a preferred value of 0.027 for a Kroupa IMF (assuming a SN-Ia progenitor mass range of  $1.5 - 10M_{\odot}$ ). Arrigoni et al. (2010a) allow for a value between 0.015 and 0.05, preferring 0.03 when using a slightly top-heavy Chabrier IMF (i.e. a slope of 2.15 rather than 2.3 for  $M > 1M_{\odot}$ , see Eqn. 4.1). Other works, which have used IMFs with a smaller fraction of stars above  $1M_{\odot}$ , often take slightly higher values. For example, Matteucci & Recchi (2001) and François et al. (2004) prefer  $A = 0.05$  when using a Scalo (1986) IMF. Calura & Menci (2009) and Matteucci et al. (2006, 2009) take values of  $A' = 0.0020$  and  $0.0025$  for a Scalo IMF, which correspond to  $A \sim 0.05$  and  $0.06$ , respectively. And P98 find  $A = 0.05 - 0.08$  when using a Salpeter IMF (and a SN-Ia progenitor mass range of  $3 - 12M_{\odot}$ ). Most recently, Romano & Starkenburg (2013) and Jiménez, Tissera & Matteucci (2014)

<sup>4</sup>We note again that the SN efficiency parameter  $\epsilon_h$  has also been modified to ensure that the total SN feedback energy is unchanged (see Section 1.5.1). All other model parameters have been kept to the values used by Guo et al. (2011).

have both assumed  $A = 0.03$  when using a Salpeter IMF.

Our chosen value of  $A \sim 0.028$  is also in line with expectations from observations of the SN-Ia rate, with the fraction of SN-Ia-producing stars in the range  $3 - 8M_{\odot}$  believed to be between 0.03 and 0.1 (Maoz & Mannucci, 2012). For the range  $3 - 16M_{\odot}$ , this equates to between  $\sim 0.024$  and 0.081 (for a Chabrier IMF).

## 4.6 Conclusions

In this chapter, we have described the formulation and implementation of a sophisticated GCE scheme into the L-GALAXIES semi-analytic model of galaxy formation. This new model allows us to study, in much greater detail, a large number of chemical properties for a wide range of galaxy types, as discussed in Chapter 5. The key aspects of the new GCE implementation are as follows:

- Delayed chemical enrichment has been implemented into L-GALAXIES by explicitly considering mass- and metallicity-dependent yields from SNe-II and AGB winds, as well as standard, metallicity-independent yields from SNe-Ia.
- A range of key chemical elements are individually tracked throughout the model, namely, H, He, C, N, O, Ne, Mg, Si, S, Ca and Fe.
- Various different SN-Ia DTDs can be included into the model, and we have explicitly considered three common types here, namely, power-law, bi-modal, and narrow Gaussian DTDs.
- Two sets of SN-II yields are also considered, in order to assess the importance of details such as stellar mass loss prior to the supernova.
- The scheme has been implemented to be efficient in terms of computational time, without sacrificing accuracy when outputting the detailed chemical evolution of galaxies.
- Only one new free parameter is tuned to calibrate the GCE scheme: We set  $A$ , the fraction of stellar objects in the mass range  $3-16 M_{\odot}$  that are SN-Ia progenitors, to 0.028, so that the peak of the  $[\text{Fe}/\text{H}]$  distribution for an ensemble of model, MW-type galaxies is at the solar value (see Section 5.3). This value is in accordance with other GCE models and observations of the SN-Ia rate.

- Other uncertain parameters, such as  $\tau_{\min}$ , the minimum lifetime of a SN-Ia progenitor,  $M_{\max}$ , the maximum mass of a SN-II progenitor, or the high-mass-end slope of the IMF, are assumed fixed at their fiducial values.

# Chapter 5

## The chemical properties of star-forming galaxies, the Milky Way disc, and ellipticals in the local Universe

*“There is no need for disappointment at the failure of the model to give perfect agreement with observation; it has served its purpose, for it has distinguished what are the features of the actual phenomena which require new conditions for their explanation.”*

**Arthur Eddington**

### 5.1 Introduction

In the previous chapter, we discussed the implementation of a new GCE model into L-GALAXIES. This implementation includes delayed enrichment from stellar winds, SNe-II and SNe-Ia, as well as metallicity-dependent yields and a reformulation of the associated supernova feedback. Two different sets of SN-II yields and three different SN-Ia delay-time distributions (DTDs) are included, and eleven heavy elements (including O, Mg and Fe) are self-consistently tracked.

We will now make a detailed comparison between this new model and a set of key observables in the local Universe. We will discuss, a) the gas-phase and stellar mass-metallicity relations of local, star-forming galaxies (Section 5.2), b) the G dwarf stars in the Milky Way disc (Section 5.3), and c) the oxygen enhancements measured from the integrated light emitted by local, elliptical galaxies (Section 5.4). In doing so, we are attempting to assess the success of our GCE implementation and to further constrain which of the SN-II yield tables and SN-Ia DTDs described in Section 4.3 and Section 4.4.1 perform best across the range of data considered. This can also be seen as a test of the canonical theory of galaxy formation within a  $\Lambda$ CDM cosmology, which has struggled to reconcile observations of these different chemical properties in the past (e.g. Thomas 1999).

In what follows, ‘element enhancement’ refers to the ratio of element  $x$  to iron,  $[x/\text{Fe}]$ , and ‘element abundance’ refers to the ratio of element  $x$  to hydrogen,  $[x/\text{H}]$ . The element ratios discussed in this work are normalised to solar values as in Section 1.1.3. Note that  $M_x/M_y = (A_x/A_y) \cdot (\epsilon_x/\epsilon_y)$ , where  $A_x$  is the atomic weight of element  $x$ , and  $\log(\epsilon_x) = \log(n_x/n_{\text{H}}) + 12$  is the abundance of element  $x$ . For hydrogen,  $A_{\text{H}} = 1.008$  and  $\log(\epsilon_{\text{H}}) = 12.0$ . In each case, we normalise our model values to the set of solar abundances used for the observations to which we compare. For clarity, we have selected a representative sample of  $\sim 480000$   $z = 0$  galaxies and their progenitors for the plots in this chapter.

We also note here that pristine gas accreted onto DM haloes from the IGM is assumed to be 75 per cent hydrogen and 25 per cent helium.

## 5.2 The mass-metallicity relations

One of the key diagnostics used to analyse the chemical evolution of galaxies is the relation between their stellar mass ( $M_*$ ) and gas-phase metallicity ( $Z_g$ ). The large statistical power of the SDSS allowed Tremonti et al. (2004) to determine the  $M_*$ - $Z_g$  relation for emission-line galaxies in the local Universe. They found a clear positive correlation below  $\sim 10^{10.5} M_{\odot}$  with a  $1\sigma$  scatter of only 0.1 dex. Above this mass, the relation was found to flatten. Here, we compare our  $z = 0$  model mass-metallicity relations for gas and stars with those observed. We also have the opportunity to directly compare L-GALAXIES results before and after the new GCE implementation – something we are not able to do when discussing individual element ratios in later sub-sections.

Fig. 5.1 shows the  $M_*$ - $Z_{\text{cold}}$  relation for L-GALAXIES with the new GCE implementation and using the power-law DTD (points and black lines). 95600 model galaxies were selected such that  $\log(M_*) \geq 8.6$  and  $-2.0 \leq \log(\text{SFR}) \leq 1.6$ , in or-

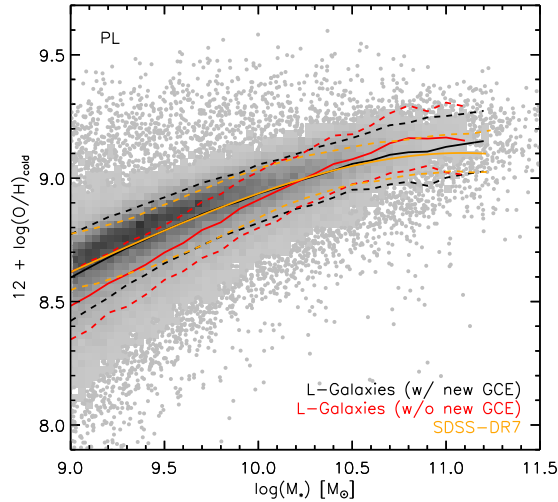


Figure 5.1: The  $M_*$ - $Z_{\text{cold}}$  relation (where  $Z_{\text{cold}} = 12 + \log(N_{\text{O}}/N_{\text{H}})$ ) for L-GALAXIES with the new GCE implementation and using a power-law SN-Ia DTD (points and black lines). This relation is compared to that of L-GALAXIES prior to the new GCE implementation (red lines), and a fit to the observed  $M_*$ - $Z_{\text{g}}$  relation for emission-line galaxies from the SDSS-DR7 (orange lines) by Yates, Kauffmann & Guo (2012).

der to match the dynamic range of the SDSS-DR7 observations. We note here that both the gas-phase and stellar mass-metallicity relations are very similar for all three of the DTDs considered. This is because the SN-Ia DTD has little impact on the abundance of oxygen, which is the most abundant heavy element and is produced predominantly by SNe-II.

In Fig. 5.1 we also plot a fit to the same relation for L-GALAXIES *prior* to the new GCE implementation (red lines), and a fit to the observed  $M_*$ - $Z_{\text{g}}$  relation from the SDSS-DR7 (orange lines, see Eqn. 2.4). We can see that there is very good agreement between the observations and our new model at  $z = 0$ . Both the slope and amplitude of the new model relation are in better agreement with observations than those of the previous model. The increase in amplitude at lower mass is due to a) our new GCE implementation (i.e. the input yields) allowing a different amount of metal into the ISM than the fixed 3 per cent yield assumed before, and b) our new SN feedback scheme allowing more oxygen to stay in the ISM after it is released by stars, rather than being instantly ‘reheated’ into the CGM. This is because the energy input by a population of SNe is now distributed over time, rather than all dumped at once into the ISM straight after star formation, when a lot of oxygen is also released (see Section 4.5.3).

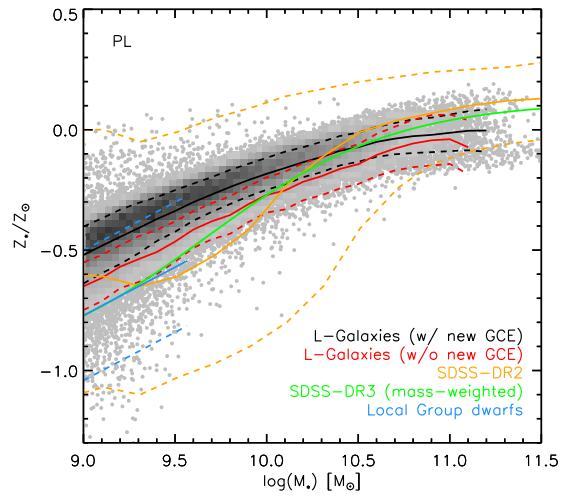


Figure 5.2: The  $M_*$ - $Z_*$  relation (where  $Z_* = \log(M_{*,Z}/M_*/0.02)$ ) for L-GALAXIES with the new GCE implementation and using a power-law SN-Ia DTD (points and black lines). This relation is compared to that of L-GALAXIES prior to the new GCE implementation (red lines), the observed relation from the SDSS-DR2 (orange lines) by Gallazzi et al. (2005), a fit to the mass-weighted relation from the SDSS-DR3 (green line) by Panter et al. (2008), and to a set of Local Group dwarf galaxies (blue lines) by Woo, Courteau & Dekel (2008).

The scatter of our new model  $M_*$ - $Z_g$  relation is slightly larger than that seen in the SDSS. Studying the properties of outliers above and below the  $M_*$ - $Z_g$  relation can tell us a lot about the evolution of galaxies (e.g. Dellenbusch, Gallagher & Knezek 2007; Peeples, Pogge & Stanek 2008; Zahid et al. 2012a). We defer a detailed analysis of such galaxies in our model to later work.

We note here that the gas-phase metallicity is now defined as  $Z_{\text{cold}} = 12 + \log(N_{\text{O}}/N_{\text{H}})$  in our new model, in the same way as in observations, where  $N_{\text{O}}$  and  $N_{\text{H}}$  are the number of atoms of oxygen and hydrogen, respectively. Previously, the approximation  $Z_{\text{cold}} = 9.0 + \log(M_{Z,\text{cold}}/M_{\text{cold}}/0.02)$  was used, where 9.0 was the assumed solar oxygen abundance and 0.02 the assumed solar metallicity. The difference in the value obtained when using these two methods is only small, with the new formulation estimating a metallicity  $\sim 0.04$  dex lower than the old formulation.

Fig. 5.2 shows the  $z = 0$  relation between the stellar mass and stellar metallicity ( $Z_*$ ) of our model galaxies (using a power-law DTD), after our new GCE implementation (points and black lines), and prior to it (red lines). In both cases, solar-normalised metallicities are calculated as  $Z_* = \log(M_{*,Z}/M_*/0.02)$ , using the same solar metallicity of  $Z_{\odot} = 0.02$  assumed in the stellar population synthesis models that obtained stellar metallicities in the SDSS-DR2 (A. Gallazzi, priv. comm.).

Below  $M_* = 10^{10.5}M_{\odot}$ , the new model  $M_*$ - $Z_*$  relation is similar in shape to that of the previous model, but with an amplitude  $\sim 0.1$  dex higher. This is also higher than observed at low mass (although this is a region where observations are not well constrained). The mass-weighted  $M_*$ - $Z_*$  relation of Panter et al. (2008) (green line) from the SDSS-DR3 probably provides the best comparison with our model, as we also consider mass-weighted metallicities. The Panter et al. (2008) relation also shows good correspondance with observations of Local Group dwarfs by Woo, Courteau & Dekel (2008) (blue lines). We can see that the general trend of decreasing  $Z_*$  with  $M_*$  is reproduced in our model, despite low- $M_*$ , star-forming model galaxies being too metal-rich by  $z = 0$ .

Henriques & Thomas (2010) have shown that a more realistic treatment of stellar disruption, whereby satellite galaxies have their stellar component *gradually* stripped, can help steepen the slope of the  $M_*$ - $Z_*$  relation in semi-analytic models. This could bring the low-mass end of our model relation into better agreement with observations.

The model  $M_*$ - $Z_{\text{cold}}$  and  $M_*$ - $Z_*$  relations when using the CL04 SN-II yields have slightly shallower slopes and are  $\sim 0.1$  dex higher than those assuming the P98 yields. They therefore have a higher amplitude than observed. This is because the CL04 yield set allows more oxygen to be produced and ejected from stars when extrapolated to  $120M_{\odot}$ , particularly at low metallicity.

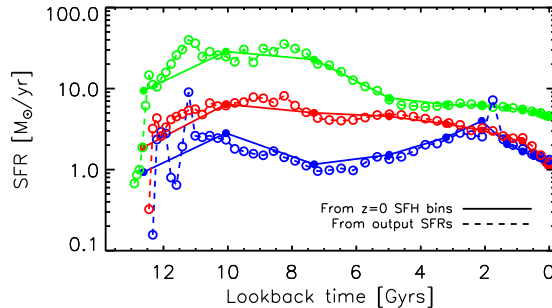


Figure 5.3: Three example SFHs from our MW-type model sample. Filled circles represent the histories as recorded by the 20 SFH bins at  $z = 0$ . Open circles represent the SFRs at every output snapshot of the simulation.

To conclude this section, we can say that our new GCE implementation improves the correspondance between our model and observations of gas-phase metallicities in local, star-forming galaxies. This was by no means a foregone conclusion, considering the significant changes to the chemical evolution modelling we have implemented. However, further improvement to the semi-analytic model is still required in order to better match the observed total *stellar* metallicities of galaxies at  $z = 0$ .

### 5.3 The Milky Way disc

There is now a wealth of recent data available in the literature on the chemical composition of stars in the MW disc (e.g. Holmberg, Nordström & Andersen 2009; Casagrande et al. 2011; Bovy et al. 2012a,b; Adibekyan et al. 2012; Boeche et al. 2013; Bensby, Feltzing & Oey 2013; Anders et al. 2013; Hayden et al. 2013). These data allow us to put firm constraints on the success of our GCE implementation in reproducing realistic MW-type model galaxies. We construct a sample of  $\sim 5200$  central (type 0) galaxies at  $z = 0$  that are disc dominated (i.e.  $M_{\text{bulge}}/(M_{\text{bulge}} + M_{\text{disc}}) < 0.5$ ), with DM halo masses in the range  $11.5 \leq \log(M_{\text{vir}})/M_{\odot} \leq 12.5$ , and recent star formation rates of  $1.0 \leq \text{SFR}/M_{\odot}\text{yr}^{-1} \leq 10.0$  over the redshift range  $0.0 \leq z \leq 0.25$  (i.e. the last  $\sim 3.0$  Gyrs). Our results are not affected by small changes to these criteria. Three example star formation histories (SFHs) from our MW-type model sample are shown in Fig. 5.3. The chemical evolution of the individual galaxy depicted in red is discussed in Section 5.3.2. In this section, the model values are normalised to the solar abundances determined by Anders & Grevesse (1989).

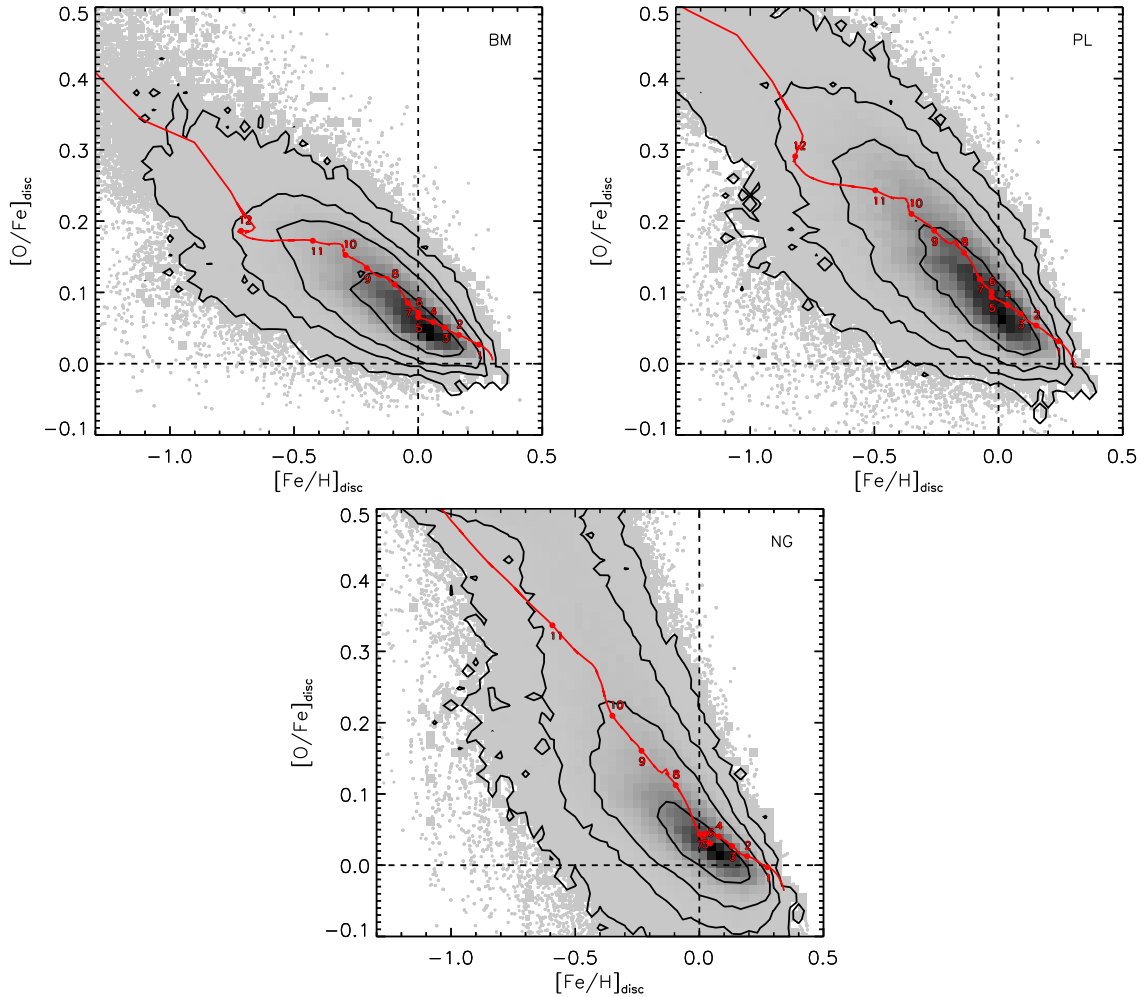


Figure 5.4: The  $[\text{Fe}/\text{H}]-[\text{O}/\text{Fe}]$  relation for G dwarfs in the stellar discs of our MW-type model galaxy sample when using a bi-modal (top-left panel), power-law (top-right panel), and narrow Gaussian (bottom panel) SN-Ia DTD. One galaxy contributes many hundreds of points to this relation (see Section 4.5.1). The greyscale indicates the distribution of SSPs, weighted by the mass formed. Contours show the 68th, 95th, 99th and 99.9th percentiles. The chemical evolution of an individual MW-type model galaxy is over-plotted on each panel (red tracks), and discussed in detail in Section 5.3.2. Points on the track denote the chemical composition at discrete times in the past, labelled by the lookback time in Gyrs. The SFH of the same galaxy is plotted in red in Fig. 5.3.

In order to compare with observations, we only consider G dwarfs ( $0.8 \leq M/M_{\odot} \leq 1.2$ ) still present in the stellar discs of our model MW-type galaxies at  $z = 0$ . When using the P98 stellar lifetimes (Section 4.3.2), *not* all G dwarfs live as long as the age of the MW disc. For example, stars of mass  $1.2M_{\odot}$  (the upper mass limit we assume for G dwarfs) live from 3.1 Gyrs at  $Z_0 = 0.0004$  to a maximum of 4.7 Gyrs at  $Z_0 = 0.02$  (see Fig. 4.1). These timescales are clearly shorter than the typical ages of the oldest SSPs in our MW-type model discs (see Fig. 5.3). Therefore, we re-weight those SSPs for which some of the G dwarfs would no longer be present at  $z = 0$  for the plots in this section. This correction removes a very small contribution from the oldest SSPs, reducing very slightly the number of low-[Fe/H], high-[O/Fe] stars. Although this is a more rigorous treatment, the main conclusions drawn from our MW-type sample also hold when assuming that all G dwarfs survive up to  $z = 0$ .

### 5.3.1 MW-type model galaxies

Fig. 5.4 shows the [Fe/H]-[O/Fe] relation for the G dwarfs in the stellar discs of our model MW-type galaxies, using the stitched-together histories described in Section 4.5.1, for the three DTDs we consider. Care needs to be taken when comparing Fig. 5.4 to observations. In observational studies of the MW disc, the chemical composition of individual stars of various ages are measured and plotted. In the case of our semi-analytic model, individual stars cannot be resolved, and so we must instead rely on the chemical composition of each *population* of stars, formed at each timestep during the evolution of a galaxy. Fig. 5.4 therefore shows the chemical composition of SSPs from  $\sim 5200$  MW-type galaxies, where one MW-type galaxy contributes many hundreds of points (see Section 4.5.1). Considering a whole sample of MW-type galaxies provides a statistically significant indication of the typical variation in the chemical composition of MW-type discs in our model. This method of comparison has been used before in semi-analytic models (e.g. Calura & Menci 2009). Note that we therefore weight the SSPs by the mass of stars formed. The evolution of an example, individual MW-type galaxy is also plotted in each of the panels in Fig. 5.4 (red tracks). This galaxy is discussed in detail in Section 5.3.2.

Each of the panels in Fig. 5.4 shows a clear decrease in [O/Fe] with increasing [Fe/H] towards the solar composition. There are, however, important differences in the distribution of SSPs for each of the three DTDs we consider. These differences can be seen more clearly in Fig. 5.5, where we compare the [Fe/H] and [O/Fe] distributions when using our three DTDs (black histograms) with those of 16,134 F and G dwarfs from the *Geneva-Copenhagen Survey* (*GCS*, orange histograms) (Nordström et al. 2004; Holmberg, Nordström & Andersen 2009) and 293 unique G dwarfs

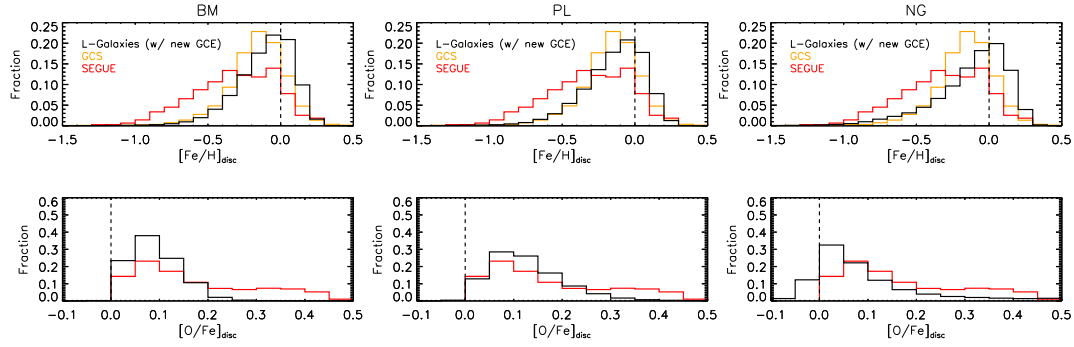


Figure 5.5: *Top row*:  $[\text{Fe}/\text{H}]$  distributions for the stellar discs of our model MW-type galaxies, when using a bi-modal (left), power-law (middle), or narrow Gaussian (right) SN-Ia DTD. Vertical dashed lines indicate the solar iron abundance. *Bottom row*:  $[\text{O}/\text{Fe}]$  distributions for the same model discs and DTDs. Vertical dashed lines indicate the solar oxygen abundance.

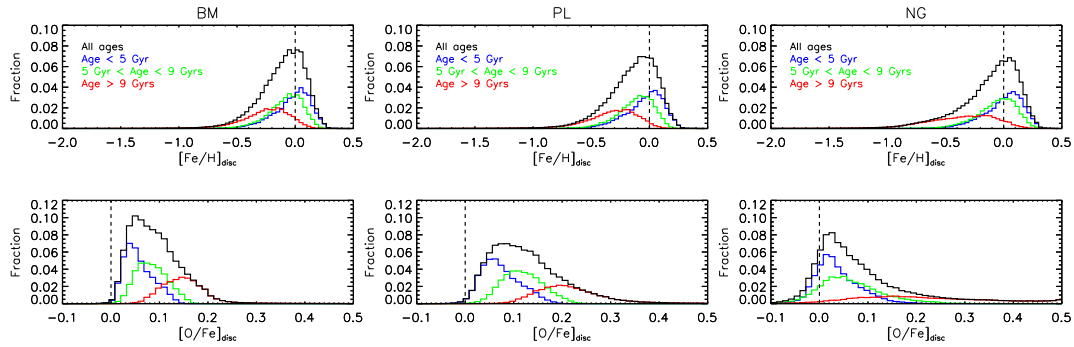


Figure 5.6: *Top row*:  $[\text{Fe}/\text{H}]$  distributions for the stellar discs of our model MW-type galaxies, when using a bi-modal (left), power-law (middle), or narrow Gaussian (right) SN-Ia DTD. Vertical dashed lines indicate the solar iron abundance. *Bottom row*:  $[\text{O}/\text{Fe}]$  distributions for the same model discs and DTDs. Vertical dashed lines indicate the solar oxygen abundance.

from the *Sloan Extension for Galactic Understanding and Exploration* (*SEGUE*, red histograms) survey (Yanny et al. 2009; Bovy et al. 2012a,b).

The difference in [Fe/H] distribution between the two observational samples is likely due to their different depths; the *GCS* probed strictly the solar neighbourhood ( $7.7 \lesssim R_{\text{GC}}/\text{kpc} \leq 8.31$  and  $0.0 \leq |Z_{\text{GC}}|/\text{kpc} \leq 0.359$ ), whereas *SEGUE* covered a wider range of galactic radii but also much higher galactic scale heights ( $5 \lesssim R_{\text{GC}}/\text{kpc} \lesssim 12$  and  $0.3 \leq |Z_{\text{GC}}|/\text{kpc} \leq 3.0$ ).<sup>1</sup> This means that the *SEGUE* sample includes a larger number of metal-poor, ‘thick-disc’ stars, and so has a [Fe/H] distribution spread to lower iron abundances. Our model, in turn, represents the *average* chemical composition of stars born at each timestep in the discs of MW-type galaxies, due to the full mixing of material in the various galactic components.

The model [Fe/H] distributions for all three of our set-ups are in reasonable agreement with the *GCS* data (partly by construction, as we have tuned  $A$  to obtain a peak of the [Fe/H] distribution around 0.0), although the NG set-up is skewed slightly more to higher iron abundances. However, there are significant differences in the model [O/Fe] distributions. For example, the high-[O/Fe] tail in our BM set-up is much less extended than seen in the  $[\alpha/\text{Fe}]$  distribution from the *SEGUE* survey<sup>2</sup>. This suggests that stars are being enriched with iron too quickly when using the bi-modal DTD – a conclusion also reached by Matteucci et al. (2009).

Interestingly, the extent of the high-[O/Fe] tail in the [O/Fe] distribution increases from left to right in Fig. 5.5. This is due to the different number of ‘prompt’ SNe-Ia assumed for each of the three DTDs. The smaller the prompt component, the larger the number of low-[Fe/H], high-[O/Fe] stars that can be formed before a significant amount of Fe gets into the star-forming gas. The bi-modal DTD allows  $\sim 54$  per cent of SNe-Ia to explode within 100 Myrs of star formation ( $\sim 58$  per cent within 400 Myrs), the power-law DTD allows  $\sim 23$  per cent within 100 Myrs of star formation ( $\sim 48$  per cent within 400 Myrs), and the Gaussian has no prompt component at all. Only the Gaussian DTD has a high-[O/Fe] tail as extended as that seen for G dwarfs from *SEGUE*. However, we reiterate that the lack of any prompt component is in contradiction with recent observations (e.g. Maoz & Mannucci 2012). The smaller high-[O/Fe] tail produced when using the power-law DTD, although not as extended as seen in the *SEGUE* data, is still promising, especially when considering

<sup>1</sup>In Fig. 5.5 the stars with  $|Z_{\text{GC}}| < 0.3$  that are missing from the *SEGUE* survey are accounted for via the mass re-weighting of the [Fe/H] distribution described by Bovy et al. (2012a).

<sup>2</sup>Note that Bovy et al. (2012a) and Bovy et al. (2012b) choose  $[\alpha/\text{Fe}]$  to be the average of [Mg/Fe], [Si/Fe], [Ca/Fe] and [Ti/Fe], with no oxygen lines included in the analysis. However, as oxygen is the most abundant  $\alpha$  element in galaxies, a comparison between their  $[\alpha/\text{Fe}]$  and our [O/Fe] is still valid here.

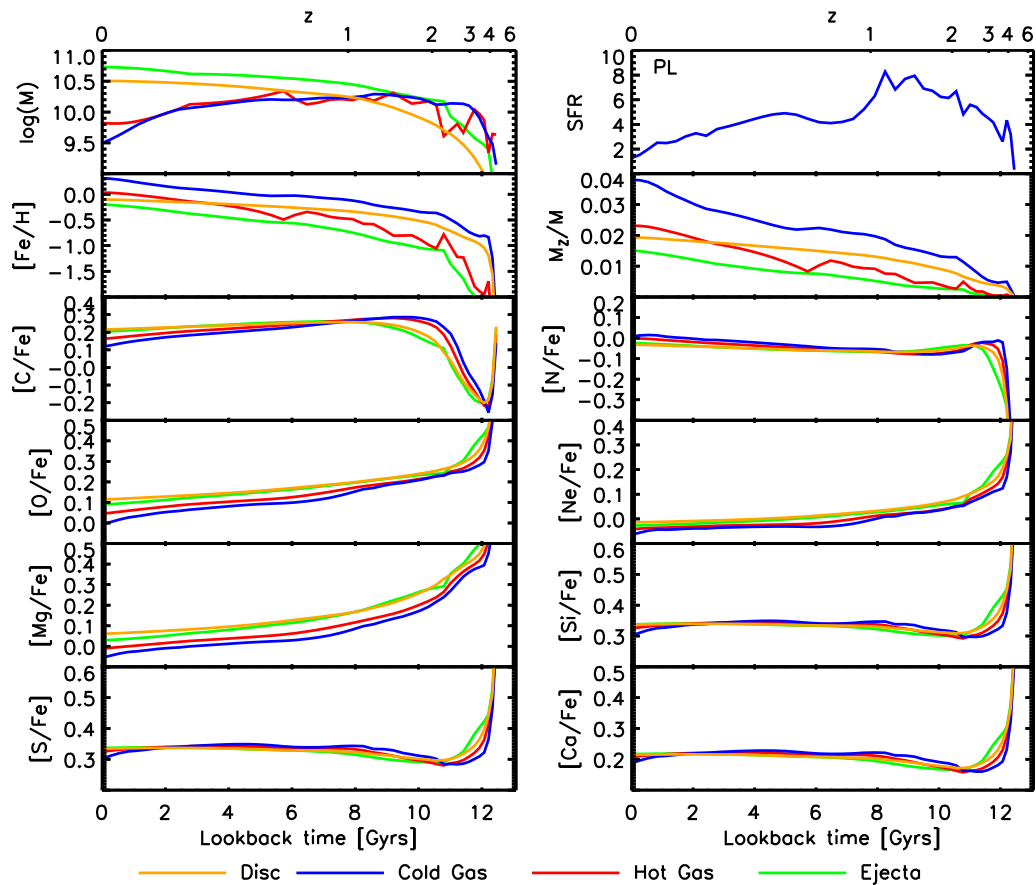


Figure 5.7: The evolution, from redshift 7 to 0, of the mass (in  $M_\odot$ ), SFR (in  $M_\odot/\text{yr}$ ), iron abundance, total metallicity, and heavy element enhancements for four of the eight different galaxy components (see legend) in the example MW-type model galaxy shown in Fig. 5.4, using the power-law DTD.

that a) the *SEGUE* data contain a large number of  $\alpha$ -enhanced, iron-poor stars at high galactic scale heights, and b) our model represents the chemical composition of MW-type stellar discs in a statistical sense, and also assumes full mixing of metals in the stellar disc. Including a treatment of the radial distribution of metals in galaxies, similar to that done by Fu et al. (2013), will be the focus of future work. We will also show in Section 5.4 that the power-law DTD also produces positive slopes in the  $M_{*}$ - $[\alpha/\text{Fe}]$  relations of elliptical galaxies.

In Fig. 5.6 we show a finer binning of the model  $[\text{Fe}/\text{H}]$  and  $[\text{O}/\text{Fe}]$  distributions for the three SN-Ia DTDs considered (black histograms). Sub-distributions for three distinct age ranges (coloured histograms) are also plotted. All panels show nicely that older SSPs have lower  $[\text{Fe}/\text{H}]$  and higher  $[\text{O}/\text{Fe}]$  than younger SSPs, due to the delayed enrichment of the star-forming gas with iron from SNe-Ia. There is also no sign of an extended tail below  $[\text{Fe}/\text{H}] = -1.0$  (the ‘G-dwarf problem’) that is common to closed-box models (Section 1.3.1).

The broader plateau present in the  $[\text{O}/\text{Fe}]$  distribution for the PL set-up is due to the shape of the DTD; the power-law DTD assumes a smoother change in SN-Ia rate with time than the other two DTDs considered (see Fig. 4.6). This means that the ISM in a typical MW-type galaxy undergoes a fairly constant decrease in  $[\text{O}/\text{Fe}]$  of  $\sim 0.025$  dex/Gyr for the power-law DTD. In contrast, the bi-modal DTD causes a more gradual decrease in  $[\text{O}/\text{Fe}]$  of  $\sim 0.016$  dex/Gyr, *after* significantly enriching the ISM with iron shortly after the start of star formation. In turn, the Gaussian DTD produces a steep decrease in  $[\text{O}/\text{Fe}]$  of  $\sim 0.066$  dex/Gyr from very high initial values until  $\sim 1$  Gyr after the peak of star formation, with little change thereafter.

The CL04 SN-II yields produce qualitatively similar results to those discussed above, except that the  $[\text{Fe}/\text{H}]$  distribution is shifted to higher values and the  $[\text{O}/\text{Fe}]$  has a decreased high- $[\text{O}/\text{Fe}]$  tail – in greater contradiction with observations. This is because, when extrapolated to  $120M_{\odot}$ , the CL04 yields predict a higher production of O, Mg and Fe by SNe-II than the P98 yields, particularly at low metallicity.

### 5.3.2 An individual MW-type model galaxy

In this sub-section, we look more closely at the chemical evolution of an individual MW-type galaxy in our model. This galaxy’s SFH is plotted in red in Fig. 5.3, and its evolution in the  $[\text{Fe}/\text{H}]$ - $[\text{O}/\text{Fe}]$  diagram is shown by a red track in each panel of Fig. 5.4. Points on the tracks in Fig. 5.4 denote the chemical composition at discreet times in the past, labelled by the lookback time in Gyrs.

This galaxy nicely demonstrates the fairly smooth evolution that we would expect from a MW-type galaxy. However, it is not necessarily typical of our MW-type

model sample as a whole. Some galaxies (such as that shown in blue in Fig. 5.3) undergo large infall and star formation events that can cause such a track to double-back on itself and otherwise deviate from a ‘smooth’ path (see also Calura & Menci 2009). However, our chosen galaxy provides a good example of the general chemical evolution undergone by MW-type galaxies in our model.

Fig. 5.7 shows the evolution from  $z = 7$  to 0 of the mass, SFR, iron abundance, total metallicity, and complete set of heavy element enhancements for this example MW-type galaxy, when using the power-law DTD. Four of the eight components of the galaxy (stellar disc, cold gas, hot gas, and ejecta reservoir) are coloured according to the legend. Note that Fig. 5.7 shows the *average* chemical composition of a whole galaxy component at any given time.

Fig. 5.7 highlights the dependence of an element’s evolution on the mode of its release, namely SNe-II, SNe-Ia or AGB winds. Those elements that are predominantly produced in massive SNe-II (O, Ne and Mg) show a similar decline in their enhancement with cosmic time, as we would expect for a slowly declining SFR and a delayed enrichment of iron. These light  $\alpha$  elements also show lower enhancements in the cold gas than in the stellar disc for this reason. The heavier  $\alpha$  elements (Si, S and Ca) are ejected mainly by lower-mass SNe-II, and also have a greater contribution from SNe-Ia. They are therefore released into the ISM later than the lighter  $\alpha$  elements, showing a gradual increase in enhancement with time (at a decreasing rate), and higher enhancements in the gas than in the stars while gas fractions are high. Nitrogen, an element with a dominant contribution from (delayed) AGB winds at low metallicity, shows a strong increase in  $[\text{N}/\text{Fe}]$  at the onset of AGB wind enrichment (at  $z \sim 4$  for this galaxy), followed by a more gradual increase thereafter. Finally, the drop in  $[\text{C}/\text{Fe}]$  between  $z \sim 3$  and 4 is due to a decrease in the C/Fe ratio in the ejecta of SNe-II at  $Z_0 \sim 0.004$  compared to other metallicities. The increase in this ratio at higher metallicities, along with a significant contribution to C from AGB winds, causes the sharp rise in  $[\text{C}/\text{Fe}]$  shortly after. This is a specific property of the P98 SN-II yields. When using the CL04 SN-II yields, the  $[\text{C}/\text{Fe}]$  evolution follows that of the light  $\alpha$  elements more closely.

To conclude this section, we can say that our new GCE implementation is able to reproduce the  $[\text{O}/\text{Fe}]$  distribution for G dwarfs in the MW disc *if* there is only a *minor* prompt component of SNe-Ia (i.e.  $\leq 50$  per cent within  $\sim 400$  Myrs). Our NG set-up (narrow Gaussian DTD, delayed SNe-Ia only) and PL set-up (power-law DTD,  $\sim 48$  per cent of SNe-Ia exploding within  $\sim 400$  Myrs) therefore reproduce the observed high- $[\text{O}/\text{Fe}]$  tail best. However, the power-law DTD achieves this whilst assuming a more realistic fraction of prompt SNe-Ia. Our new GCE implementation

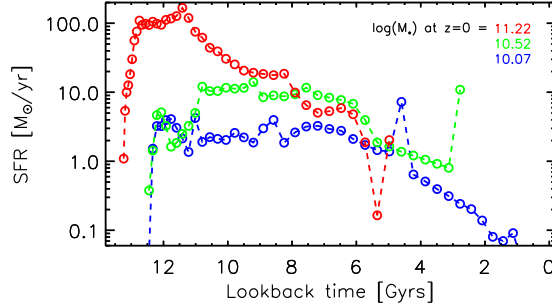


Figure 5.8: Three example SFHs from our model elliptical sample. The different colours correspond to different stellar masses at  $z = 0$  (see legend). The points represent the sum of the SFRs from all progenitors at every output snapshot of the simulation. Low-mass ellipticals tend to have longer star-formation timescales than high-mass ellipticals in our model.

also allows us to examine, in detail, the chemical evolution undergone by individual galaxies, which can help us explain the features seen in the sample as a whole.

## 5.4 Elliptical galaxies

The change in various element ratios as a function of velocity dispersion or  $M_*$  in ellipticals can also provide insight into the chemical evolution of galaxies. It has been observed that  $\alpha$  enhancements increase with  $M_*$  (e.g. Graves, Faber & Schiavon 2009; Thomas et al. 2010; Johansson, Thomas & Maraston 2012; Conroy, Graves & van Dokkum 2013). This has been mainly attributed to massive ellipticals undergoing the majority of their star formation at higher redshifts and over shorter timescales. The stars in these galaxies are therefore likely to be deficient in iron, as they were formed before a significant number of SNe-Ia could enrich the star-forming gas. Less massive ellipticals, on the other hand, are believed to form a larger fraction of their stars later, from gas that has had time to be more enriched with iron. These galaxies should therefore have lower stellar  $\alpha$  enhancements.

Previous GCE models, working within a hierarchical merging scenario, have found it difficult to reproduce this trend between stellar mass and  $\alpha$  enhancement, without invoking either a variable or adapted IMF, morphologically-dependent star formation efficiencies (SFEs), or additional prescriptions to increase star formation at high redshift (e.g. Thomas, Greggio & Bender 1999; Thomas 1999; Nagashima et al. 2005b; Pipino et al. 2009b; Calura & Menci 2009; Arrigoni et al. 2010a,b; Calura &

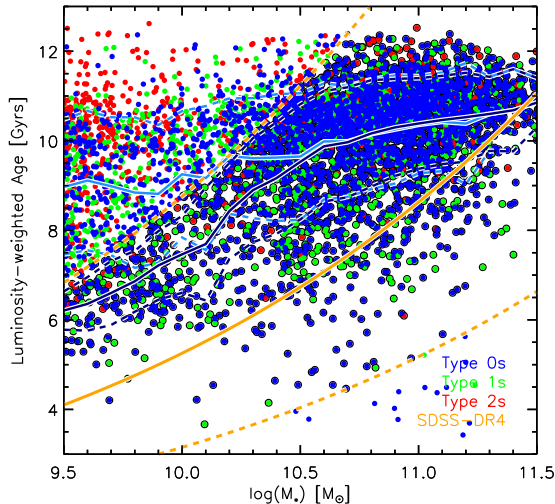


Figure 5.9: The  $M_*$ -age relation for our model elliptical galaxies, coloured by galaxy type (see Section 1.5.1). Model ages are weighted by their r-band luminosity, and the mean relation and  $1\sigma$  spread for the full sample (light blue lines) and the mass-age-selected sub-sample (dark blue lines) are also shown. A linear fit to the same relation for the SDSS-DR4 from JTM12 is given by the solid orange line, with the  $1\sigma$  spread given by the dashed orange lines. Thick-rimmed points indicate model galaxies that lie within one standard deviation ( $\pm 0.222$  dex) of the observed mass-age relation.

Menci 2011; Gargiulo et al. 2014).

We select  $z = 0$  elliptical galaxies by bulge-to-mass ratio and  $(g-r)$  colour, such that  $M_{\text{bulge}}/(M_{\text{bulge}} + M_{\text{disc}}) \geq 0.7$  and  $(g-r) \geq 0.051 \log(M_*) + 0.14$ , to form a sample of  $\sim 8700$  galaxies. These cuts are chosen to match the selection criteria used to obtain the sample of SDSS-DR7 ellipticals shown as green points in Fig. 5.12. The  $(g-r)$  colour cut also nicely separates the red sequence from the blue cloud in our model at  $z = 0$ . Our model sample includes type 0, 1 and 2 galaxies (see Section 1.5).

Fig. 5.8 shows the SFHs of three example galaxies from our model elliptical sample. In this case, the sum of the SFRs from all progenitors at any given snapshot are plotted, rather than the SFRs from only the main progenitors. We can see that the lowest-mass elliptical (blue) has a more extended SFH than the highest-mass elliptical (red). This is the case in general for our model elliptical sample (see also De Lucia et al. 2006). We can also see that the two most massive ellipticals in Fig. 5.8 (red and green) had their star formation shut-down after a merger-induced starburst at  $\sim 5$  and  $\sim 3$  Gyrs lookback time, respectively.

### 5.4.1 The mass-age relation

Before discussing element enhancements, we first show the  $M_*$ -age relation for our model elliptical sample in Fig. 5.9. Also shown is a fit to the luminosity-weighted mass-age relation from the Johansson, Thomas & Maraston (2012, hereafter JTM12) sample (solid orange line) and its  $1\sigma$  scatter (dotted orange lines). The ages of model galaxies are r-band luminosity weighted in this plot, in order to make a fairer comparison with the observations. For the observed relation, we have used the stellar masses taken directly from the SDSS-DR7 catalogue<sup>3</sup>. This is also the case for all subsequent plots showing data from the JTM12 sample.

It is known that semi-analytic models tend to produce too many old, red, dwarf galaxies by  $z = 0$  compared to observations (e.g. Weinmann et al. 2006; Guo et al. 2011). This can be seen by comparing the model and observations in Fig. 5.9, which shows that the majority of ellipticals in the model have luminosity-weighted ages older than 10 Gyrs. This is caused not just by the strong stripping of gas from satellites, but also by the strong SN feedback required to match the observed galaxy stellar mass function. Recent work by Henriques et al. (2013) has improved this problem to some extent, by allowing material ejected from model galaxies at high- $z$  to be reaccreted over longer timescales, allowing them to form more stars at low- $z$ , and therefore be younger and bluer at  $z = 0$ . However, this improvement is not implemented into the L-GALAXIES model presented here. Therefore, in the following sections, we will distinguish between our full elliptical model sample and a ‘mass-age-selected’ sub-sample, which includes only those model galaxies that lie within the  $1\sigma$  scatter of the observed  $M_*$ -age relation, noting that similar results are obtained when instead selecting model galaxies that recover the mean observed relation (see Section 5.4.2). This sub-sample is *not* used in order to evade the evident issues still affecting the galaxy formation model, but rather as a means of testing the relation between mass, age and  $\alpha$  enhancement in our new GCE implementation.

### 5.4.2 $[\alpha/\text{Fe}]$ relations

Fig. 5.10 shows the  $M_*$ - $[\text{O}/\text{Fe}]$  relation for the bulge and disc stars of our model ellipticals at  $z = 0$ , for the three SN-Ia DTDs we consider. Light-blue contours represent our full elliptical sample. Dark-blue, dashed, filled contours represent our mass-age-selected sub-sample. The observed relation from the JTM12 sample is given by the solid orange line. The slopes of the linear fits to these three relations in the range  $10.0 \leq \log(M_*/M_\odot) \leq 12.0$  are given in the top left corner of each panel.

<sup>3</sup>Available at <http://www.mpa-garching.mpg.de/SDSS/DR7>

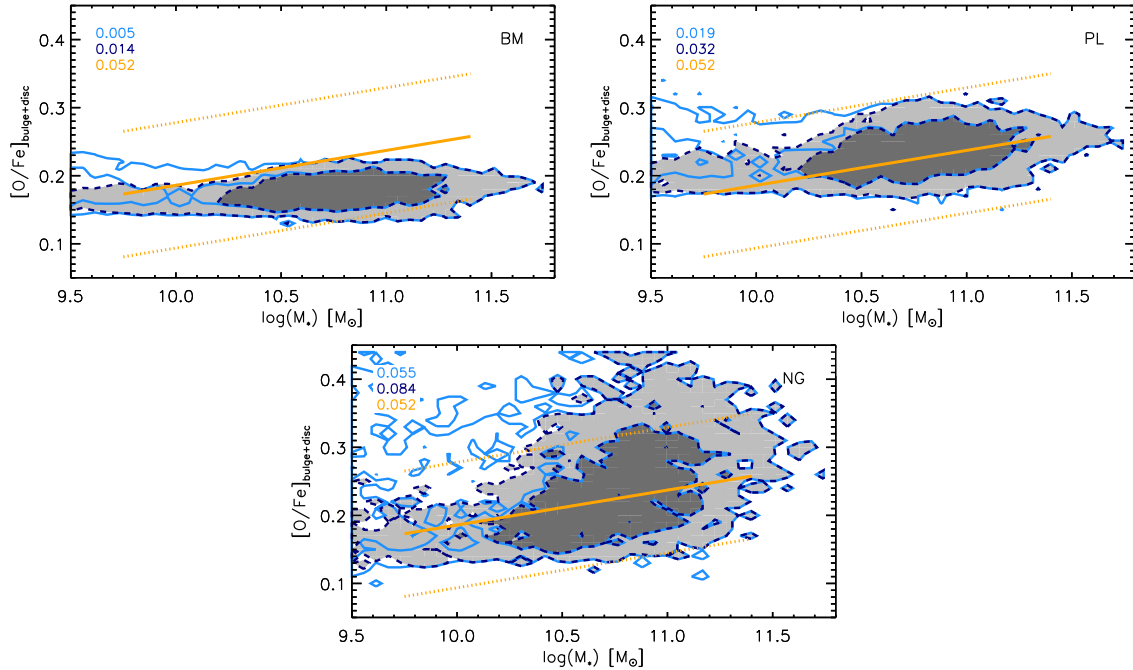


Figure 5.10: The  $M_*$ - $[O/Fe]$  relation for the bulge and disc components of our model elliptical sample, when using a bi-modal (top-left panel), power-law (top-right panel), or narrow Gaussian (bottom panel) SN-Ia DTD. Light-blue contours represent our full elliptical sample. Dark-blue, dashed, filled contours represent our mass-age-selected sub-sample (see text and Fig. 5.9). Contours represent the 68th and 95th percentiles. A linear fit to the observed relation from JTM12 is given by the orange line, with its  $1\sigma$  spread (dotted orange lines). The slopes of these three relations are given in the top left corner of each panel.

Model element ratios in this section have been normalised to the solar abundances measured by Grevesse, Noels & Sauval (1996), in accordance with the observations to which we compare.

We note here that estimates of element enhancements from stellar population synthesis (SPS) models, such as those used by JTM12, are found to be fairly good representations of the true global value, and are not as biased by small younger populations as age estimates can be (Serra & Trager, 2007). It is therefore reasonable for us to compare our model mass-weighted element enhancements with these observations.

As with the extent of the high- $[O/Fe]$  tail in our MW-type sample (see Section 5.3.1), we can see from Fig. 5.10 that the strength of the slope in the model  $M_*$ -

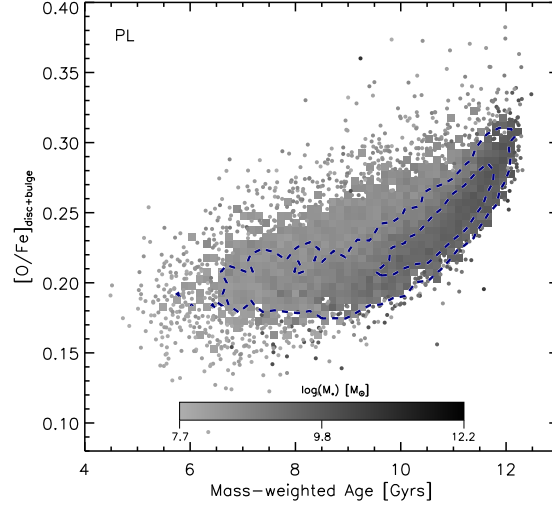


Figure 5.11: The relation between mass-weighted age and oxygen enhancement for our model elliptical galaxies, when using the power-law DTD. Points show the full elliptical sample, with the greyscale indicating the stellar mass. Dark blue, dashed contours show the mass-age-selected sub-sample. There is a clear positive correlation between age and  $[O/Fe]$  in our model ellipticals, both in general and at fixed mass.

$[O/Fe]$  relation is inversely proportional to the fraction of prompt SNe-Ia assumed. For the BM set-up ( $\sim 58$  per cent within 400 Myrs), the model slope is much flatter than observed. For the PL set-up ( $\sim 48$  per cent within 400 Myrs), a positive slope is obtained, although shallower than observed. For the NG set-up (with no prompt component), a strong slope is obtained, with a larger scatter.

The increase in slope is because *massive* ellipticals have shorter star-formation timescales in the model, and so decreasing the fraction of prompt SNe-Ia has a bigger effect on their final iron abundance, increasing their final  $\alpha$  enhancements more than for low-mass ellipticals. The increase in scatter at fixed mass is because *older* galaxies have shorter star-formation timescales in the model, and so undergo a greater increase in their  $\alpha$  enhancements for the same reason. This correlation between mass, age and  $\alpha$  enhancement can also be seen in the increasing difference between the slope for the full elliptical sample and the mass-age-selected sub-sample with increasing prompt SN-Ia component, and also from the age- $[O/Fe]$  relation shown in Fig. 5.11 for the PL set-up. This result supports the canonical thinking that the slopes in  $M_*$ - $[\alpha/Fe]$  relations are driven by differences in the star-formation timescale. If correct, then our model suggests there should only be a minor fraction of prompt SNe-Ia for any given SSP (i.e.  $\leq 50$  per cent within  $\sim 400$  Myrs).

We note here that an even steeper slope is obtained for our mass-age-selected sub-sample when only selecting galaxies that recover the fit to the observed  $M_*$ -age relation (a slope of 0.043, rather than 0.032, for the PL set-up). This is because, at fixed mass, fewer old galaxies are present for such a selection.

Fig. 5.12 shows the enhancements of all the heavy elements that we track as a function of  $M_*$  when using the power-law DTD. As in Fig. 5.10, light-blue contours represent our full elliptical sample. Dark-blue, dashed, filled contours represent our mass-age-selected sub-sample. Fits to observations of ellipticals drawn from the SDSS-DR4 (orange lines, JTM12), the SDSS-DR6 (red line, Graves, Faber & Schiavon 2009), and the SDSS-DR7 (green points, see below) are also shown where possible. The PL set-up is shown here because it provides a positive slope for the  $M_*$ -[O/Fe] relation, while also assuming a more realistic fraction of ‘prompt’ SNe-Ia than the NG set-up.

Pleasingly, Fig. 5.12 shows that positive slopes are obtained for all the  $\alpha$  elements when using our PL set-up (except for Mg, as explained below). This is again because of the correlation between mass, age and  $\alpha$  enhancement in our model. The same is true for our NG set-up, but not for the BM set-up, which has a large fraction of prompt SNe-Ia. This is an important result, as it has been difficult previously for models to obtain positive slopes without invoking additional physics.

The reproduction of positive slopes is a better test for a GCE model than the reproduction of the observed amplitudes of particular element ratios. This is because the latter is mainly dependent on the input yields, whereas the former is also strongly dependent on mass-dependent galaxy evolution and metal distribution in the semi-analytic model.

It should be noted that the slopes (and amplitudes) of the different observational data shown in Fig. 5.12 differ substantially for some element enhancements. This is mainly due to the difference in the SPS modelling techniques used. Therefore, it is more important that our model produces positive slopes at all than reproduces the exact slopes of any particular observational data set.

Regarding the observational data, the methodology of both JTM12 and Graves, Faber & Schiavon (2009) is based on fitting observed and modelled Lick absorption line indices (e.g. Worthey 1994). JTM12 adopt the SPS models of Thomas, Maraston & Johansson (2011b) and 18 Lick indices, whereas Graves, Faber & Schiavon (2009) adopt the models of Schiavon (2007) and use 7 Lick indices. The fits from JTM12 are based on a sample of visually-classified, early-type galaxies in the redshift range  $0.05 < z < 0.06$ . Graves, Faber & Schiavon (2009) selected red-sequence galaxies, classified by the colour-magnitude diagram, in the redshift range  $0.04 < z < 0.08$ . Both samples exclude star-forming galaxies by applying cuts to certain emission line

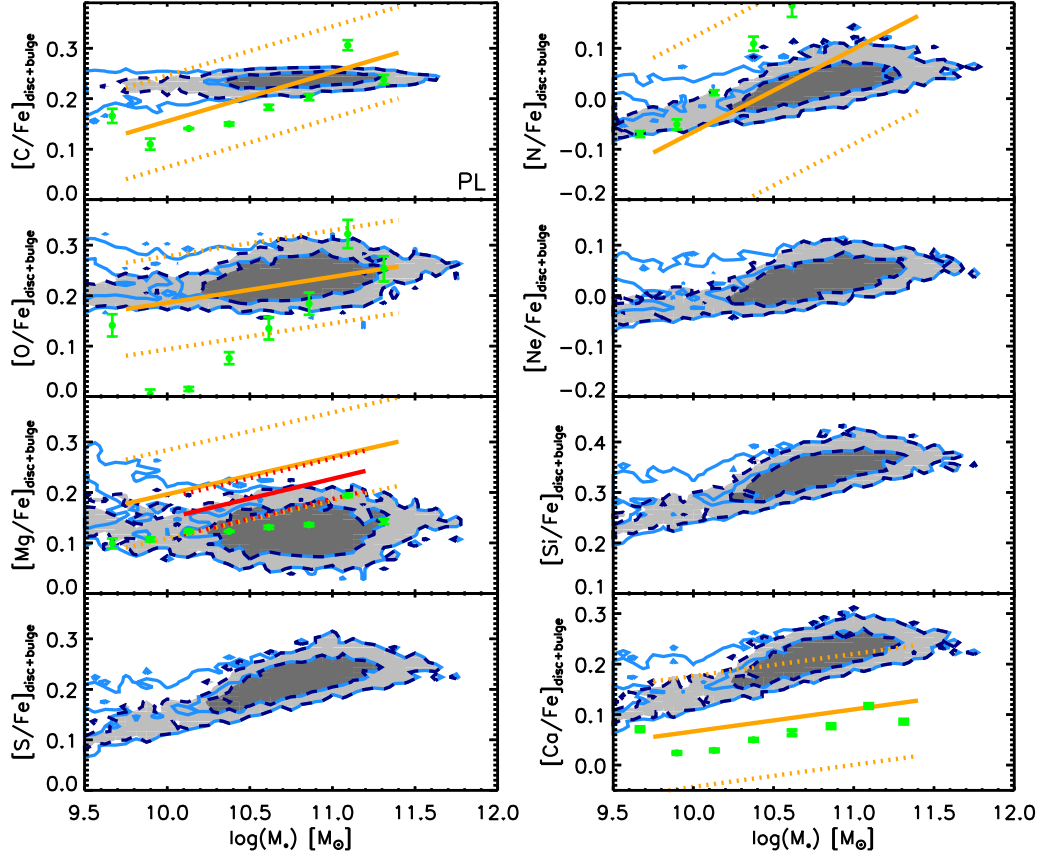


Figure 5.12: Element enhancements as a function of stellar mass for the bulge and disc components of our model elliptical sample for our PL set-up. Light-blue contours represent our full elliptical sample. Dark-blue, dashed, filled contours represent our mass-age-selected sub-sample. For both samples, the contours show the 68th and 95th percentiles. Fits to the observed relations from the JTM12 sample (solid orange lines, with  $1\sigma$  scatter given by dotted orange lines), Graves et al. (2009) (solid red lines, with  $1\sigma$  scatter given by dotted red lines) and a newly-selected SDSS-DR7 sample (C. Conroy & G. Graves, priv. comm.) (green points) are also shown for comparison.

strengths. Stellar masses are obtained from the MPA-JHU catalogue for the JTM12 data, and from mass-to-light ratios obtained using the Bell et al. (2003)  $(g-r)-(M_*/L_g)$  relation for the Graves, Faber & Schiavon (2009) data. The additional observational data (green points), kindly provided by C. Conroy & G. Graves (priv. comm.), are drawn from the SDSS-DR7, selecting galaxies in the redshift range  $0.025 < z < 0.06$  with bulge-to-total light ratios  $\geq 0.7$  and  $(g-r) \geq 0.051 \log(M_*) + 0.14$ . These galaxies are binned by  $M_*$  and their stacked spectra are used to obtain element enhancements using the SPS models of Conroy & van Dokkum (2012a); Conroy, Graves & van Dokkum (2013). For a detailed comparison of these different methods, see Section 6 of Conroy, Graves & van Dokkum (2013).

Looking at the panels in Fig. 5.12 individually, we can see that the slopes of the model relations for  $[C/Fe]$  and  $[N/Fe]$  are shallower than observed. This is discussed further in Section 5.4.4. Although our PL set-up reproduces a slope of the  $M_*-[O/Fe]$  relation for the mass-age-selected sub-sample close to that obtained by JTM12 (as also shown in Fig. 5.10), the newly-selected SDSS-DR7 data suggests a significantly steeper slope. Steeper slopes are obtained in the model when either using the Gaussian (delayed only) DTD, or when allowing direct ejection of light  $\alpha$  elements out of galaxies via galactic winds, as explained in Section 5.4.3. An increase in  $\tau_{\min}$  (the start time for SN-Ia explosions, see Section 4.4.1) also slightly increases the slope. For example, increasing  $\tau_{\min}$  from 35 to 45 Myrs increases the slope of the  $M_*-[O/Fe]$  relation by  $\sim 0.004$  when using the power-law DTD.

Our PL set-up produces a flat  $M_*-[Mg/Fe]$  relation, with a slope slightly shallower than the well-constrained relation obtained from the SDSS-DR7 data. The SDSS-DR7  $M_*-[Mg/Fe]$  relation, in turn, is flatter than the other observational data sets we compare to here. In our model, the slope of the  $M_*-[Mg/Fe]$  relation is flatter than the other light  $\alpha$  elements because Mg is produced in greater amounts by low-metallicity SNe-II than high-metallicity SNe-II when using the P98 yields (compare the bottom two panels in Fig. 4.4). This is not the case for the CL04 SN-II yields, which produce a slope for  $[Mg/Fe]$  very similar to that of  $[O/Fe]$ , due to the negligible difference in their metallicity dependence.

Strong, positive slopes for the heavier  $\alpha$  elements (Si, S and Ca) are obtained for *all* three of the DTDs considered here when using the P98 SN-II yields. This is because these elements are ejected only in small amounts by SSPs at low metallicity, as they are easily locked into the stellar remnants of the most massive, low-metallicity SNe-II (see Section 4.3.5). Low-mass elliptical galaxies, which never obtain high stellar metallicities, therefore never produce enough Si, S or Ca to obtain high enhancements. As the CL04 SN-II yields do not take account of the prior stellar winds' effect on remnant composition, the slopes produced for the heavier  $\alpha$  elements are

very similar to those of the lighter  $\alpha$  elements. This means that *all* slopes are equally sensitive to the choice of DTD when using the CL04 yields, such that positive slopes are *only* obtained if a minor prompt component of SNe-Ia is assumed. We note that the slightly shallower slopes for  $M_*$ -[Ca/Fe] observed in the real Universe may indicate that a larger proportion of heavy  $\alpha$  elements come from SNe-Ia than is the case in our model (see Conroy, Graves & van Dokkum 2013).

### 5.4.3 Galactic winds

The slopes of the  $[\alpha/\text{Fe}]$  relations, for *all* SN-Ia DTDs and SN-II yields considered, are strengthened by introducing metal-rich winds, which suppress the enhancements in low-mass ellipticals. Currently, L-GALAXIES does not invoke direct ejection of material by SNe, instead always fully mixing SN ejecta with the galaxy's ISM before reheating a fraction of this enriched gas into the CGM. However, a simple wind model, which allows a fraction of the material and energy ejected by SN-II explosions in the disc to be deposited directly into the hot gas, increases the slopes of the  $M_*$ - $[\alpha/\text{Fe}]$  relations. This is shown for our PL set-up in Fig. 5.13. This figure can be compared to the middle panel of Fig. 5.10.

A scheme where only SNe-II are expected to form a collimated galactic wind is physically motivated by the fact that metal-rich winds (ubiquitous in local, star-forming galaxies) appear to be oxygen rich,  $\alpha$  enhanced, and occur shortly after bouts of star formation (e.g. Martin, Kobulnicky & Heckman 2002; Tumlinson et al. 2011). This scheme also allows the remainder of the mass and energy returned by disc SNe-II to mix with and reheat cold gas.

We set the fraction of material from disc SN-II that is directly ejected via the wind to be inversely proportional to the cold gas surface density of the ISM through which it must pass;

$$f_{\text{wind}} = \min \left[ 1.0, \left( \frac{\Sigma_{\text{cold}}}{10 \text{ M}_{\odot} \text{pc}^{-2}} \right)^{-1} \right]. \quad (5.1)$$

A similar dependency on the gas surface density has also been used in the smoothed-particle hydrodynamical simulations of Hopkins, Quataert & Murray (2012) and in the GALFORM semi-analytic model by Lagos, Lacey & Baugh (2013) (but see Newman et al. 2012). Interestingly, our preferred characteristic gas surface density of  $\sim 10 \text{ M}_{\odot} \text{pc}^{-2}$ , below which all SN-II ejecta material is put into the wind, is very close to that below which the SFR surface density drops in local, spiral galaxies (e.g. Bigiel et al. 2008; Bigiel, Leroy & Walter 2011).

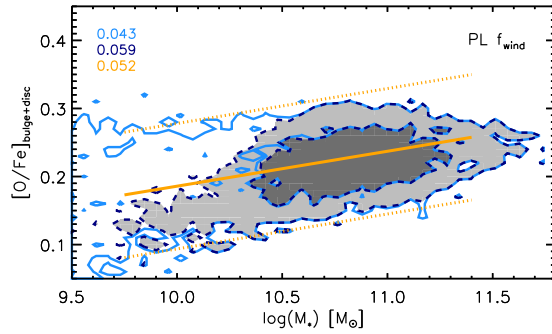


Figure 5.13: The  $M_*$ - $[\text{O}/\text{Fe}]$  relation for our model elliptical sample (when using a power-law SN-Ia DTD), with the SN feedback scheme that allows some direct ejection of light  $\alpha$  elements out of galaxies via galactic winds (see Section 5.4.3). Contours and lines are as in Fig. 5.10.

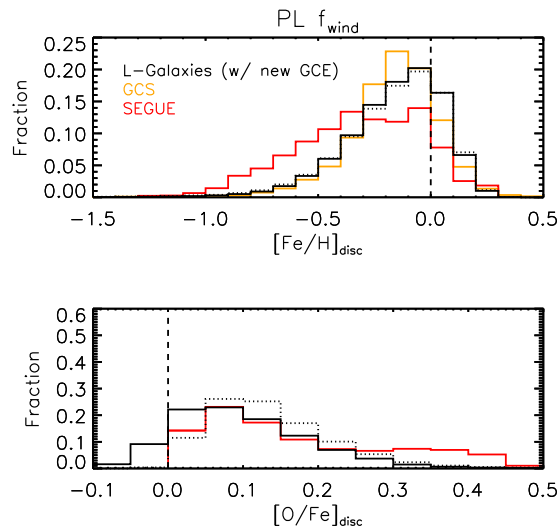


Figure 5.14: The  $[\text{Fe}/\text{H}]$  and  $[\text{O}/\text{Fe}]$  distributions of model MW-type galaxies for the PL set-up, with the alternative wind scheme described in Section 5.4.3 (solid, black histograms). This is compared to the same distributions for the PL set-up without the alternative wind scheme (dotted, black histograms). Although the  $[\text{Fe}/\text{H}]$  distribution is not significantly affected, there is a slight increase in the number of low- $[\text{O}/\text{Fe}]$  SSPs formed when including galactic winds.

This simple wind scheme lowers the stellar  $\alpha$  enhancements of low-mass ellipticals more than high-mass ellipticals, because low-mass ellipticals tend to have lower-density ISM, and so can dump their SN-II ejecta more efficiently into the CGM. This does *not* significantly affect the [Fe/H] distribution in the discs of MW-type model galaxies, although the number of low-[O/Fe] SSPs does increase slightly, as shown in Fig. 5.14. However, this simple wind scheme *does* cause a significant under-enrichment of the ISM in low-mass star-forming galaxies by  $z = 0$ , which steepens the slope of the model  $M_*$ - $Z_{\text{cold}}$  relation away from that seen in observations. Therefore, although we show here that metal-rich winds are a way of strengthening positive slopes in the  $M_*$ -[ $\alpha$ /Fe] relations of ellipticals, we do *not* claim that our simple wind model can solve all the problems of GCE modelling.

#### 5.4.4 Carbon and Nitrogen

The case of C and N is more complicated than that of other heavy elements, not least because N is both a primary and secondary element. Our model produces slopes for C and N that are flatter than for the  $\alpha$  elements (see top two panels in Fig. 5.12). This is to be expected if C and N are predominantly released in AGB winds (as they are at low metallicity in our model), yet observations suggest that these enhancements should also produce positive slopes. To further compound the problem, observations by JTM12 of the  $M_*$ -[C/O] and  $M_*$ -[N/O] relations show that these also have positive slopes.

Fig. 5.15 shows the  $M_*$ -[N/O] relation for our PL model (without additional galactic winds), along with the fit to observations from JTM12. This model relation is also flatter than observed, and its slope *increases* with the amount of prompt SNe-Ia in the DTD. We note that there is a scatter of high-mass model galaxies with [N/O] values more similar to those observed. However, these higher-[N/O] galaxies tend to be young for their mass in the model, whereas the opposite is true in the observational sample.

One way to increase the slopes in both the  $M_*$ -[N/Fe] and  $M_*$ -[N/O] relations is to assume a greater amount of N production in high-metallicity *massive* stars, as suggested by JTM12. Doing so implies a boost in secondary nitrogen production. Given the current uncertainty in the amount of secondary N production in stars, this *could* be a plausible solution, although this is far from certain. The red line in Fig. 5.15 is a fit to the full model elliptical sample when arbitrarily increasing the N released by SNe-II of metallicity  $\geq 0.02$  by a factor of 1.5. A similar increase is also seen in the slope of the  $M_*$ -[N/Fe] relation. Although this is an *ad hoc* adjustment made to the stellar yields, it does indicate that such a change is capable of improving

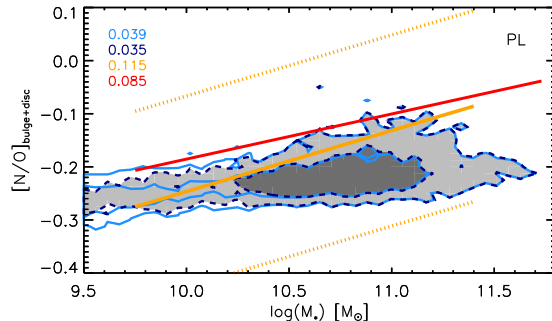


Figure 5.15: The  $M_*$ -[N/O] relation for our model elliptical sample (PL set-up). Contours and lines are as in Fig. 5.10, plus a fit to the model relation when increasing the yield of nitrogen from high-metallicity SNe-II by a factor of 1.5 (see Section 5.4.4) (red line). We find that a simple (although *ad hoc*) increase in the nitrogen yield is enough to obtain a strong, positive slope in this relation.

the values of both [N/Fe] and [N/O] in our model ellipticals.

When using the CL04 yields, the  $M_*$ -[C/Fe] and  $M_*$ -[N/Fe] relations are even flatter and the  $M_*$ -[N/O] relation has a negative slope, due to the lower production of C and N by SNe-II that these yield tables infer. This, again, is in contradiction with the observational data considered, suggesting that the P98 yields, which take account of prior stellar mass loss from massive stars (and so are more dependent on initial mass and metallicity), produce more realistic results in our GCE model.

To conclude this section, we reiterate that positive slopes in the  $M_*$ -[ $\alpha$ /Fe] relations of local elliptical galaxies can be obtained if a SN-Ia DTD with minor prompt component (i.e.  $\leq 50$  per cent within  $\sim 400$  Myrs) is used, and/or galactic winds driven by SNe-II are allowed to directly eject metals out of galaxies.

Below  $\log(M_*) \sim 10.3 M_\odot$ , slopes become shallower for our full elliptical sample. This is because the majority of low-mass ellipticals in the current model are significantly older than is observed. Recent improvements to the model that allow low-mass galaxies to be younger and bluer by  $z = 0$  will likely remedy this problem. This is indicated by the results for our mass-age-selected sub-sample, but a re-analysis of the semi-analytic model results will also be required once these improvements are merged with the GCE model presented here.

## 5.5 Conclusions

We have discussed the results of our new GCE model into the Munich semi-analytic model, L-GALAXIES, which accounts for the delayed enrichment of a series of heavy elements from SNe-II, SNe-Ia and AGB stars. We compare these results to the chemical composition of local, star-forming galaxies, the MW stellar disc, and local, elliptical galaxies. Our conclusions are as follows:

- The gas-phase mass-metallicity relation for local, star-forming galaxies (when using the Bayesian, SDSS metallicities of Tremonti et al. 2004) is very well reproduced by our new model. However, we caution that both the slope and amplitude of the observed  $M_*$ - $Z_g$  relation depend strongly of the metallicity diagnostic chosen (see Section 1.2 and Kewley & Ellison 2008). The stellar components of low-mass, star-forming galaxies tend to be more metal-rich in our model than observed.
- The [Fe/H] distribution of G dwarfs in the MW disc is reasonably reproduced by our model, for all forms of SN-Ia DTD we consider. However, the high-[O/Fe] tail in the MW [O/Fe] distribution is best reproduced when using a SN-Ia DTD with a *minor* prompt component (i.e.  $\leq 50$  per cent within  $\sim 400$  Myrs), such as a Gaussian DTD centered on  $\sim 1$  Gyr, or a power-law DTD with slope  $\sim -1.12$  and  $\tau_{\min} \gtrsim 35$  Myrs.
- Positive slopes in the  $M_*$ -[ $\alpha$ /Fe] relations of local, elliptical galaxies are also obtained when assuming a minor prompt component (i.e.  $\leq 50$  per cent within  $\sim 400$  Myrs). The strength of the slope is inversely proportional to the fraction of prompt SNe-Ia. These results are achieved when using the same implementation which produces our star-forming-galaxy and MW results.
- The inclusion of metal-rich galactic winds, driven by SN-II explosions, strengthens the positive slopes in the  $M_*$ -[ $\alpha$ /Fe] relations of ellipticals for *all* forms of SN-Ia DTD and SN-II yields considered. However, our simple, ISM-density-dependent wind scheme reduces the gas-phase metallicity of low-mass, star-forming galaxies, and so does not fully solve the problem.
- There is a clear correlation between mass, age and  $\alpha$  enhancement in our model. This, along with the above findings, suggests that the chemical compositions of a diverse array of galaxies can be reconciled within a  $\Lambda$ CDM cosmology, without requiring a variable IMF. Although an IMF that varied with SFR would likely produce similar results, it is instructive to see that this is not the only solution, given that the true behaviour of the stellar IMF is still uncertain.

- The metallicity-dependent SN-II yields tabulated by P98, which take account of mass loss from the progenitor star prior to the SN and its affect on the ejected yields, provide the best results for the range of galaxy types considered here. This supports the findings of the OWLS project (Schaye et al., 2010), which showed that the same set of yields also provided the best results in their galaxy formation simulations.
- Overall, our results suggest, given the assumptions and limitations discussed, that the best model for matching the wide range of observational data considered here should include a) a power-law SN-Ia DTD, b) SN-II yields that take account of prior mass loss through stellar winds, and c) some direct ejection of light  $\alpha$  elements into the CGM.

We conclude by highlighting two unavoidable limitations of this work and GCE models in general. First, the stellar yields used as an input have a strong influence on the results, as shown here by comparing the SN-II yields of P98 and CL04, and also in other studies (e.g. François et al. 2004; Romano et al. 2010). Until the true yields ejected by stars of all masses and metallicities are better understood, the accuracy of GCE models will always be uncertain. Second, we only consider one free GCE parameter in this work,  $A$ , the fraction of objects in a stellar SSP in the range  $3 \leq M/M_{\odot} \leq 16$  that are SN-Ia progenitors. However, the values assumed for other GCE parameters (such as  $\tau_{\min}$ ,  $M_{\max}$ , or the high-mass slope of the IMF) could also take on different values in reality. If so, our tuning of  $A$  could also be correcting for these other uncertainties, and would not solely represent the efficiency of SN-Ia-progenitor formation. Further testing against additional observational data from Local Group dwarf galaxies, outliers from the mass-metallicity relation, and the intracluster medium of galaxy clusters, should help better constrain such uncertainties.



# Bibliography

- Adibekyan V. Z., Sousa S. G., Santos N. C., Delgado Mena E., González Hernández J. I., Israelian G., Mayor M., Khachatryan G., 2012, *A&A*, 545, 32
- Allende Prieto C., Lambert D. L., Asplund M., 2001, *ApJ*, 556, 63
- Aller L. H., 1942, *ApJ*, 95, 52
- Aller L. H., 1984, 'Physics of Thermal Gaseous Nebulae', *ASSL*, Vol. 112
- Anders E., Grevesse N., 1989, *Geochim. Cosmochim. Acta*, 53, 197
- Anders F., et al., 2013, arXiv:1311.4549 [astro-ph]
- Andrews B. H., Martini P., 2012, *ApJ*, 765, 140
- Arrigoni M., Trager S. C., Somerville R. S., Gibson B. K., 2010a, *MNRAS*, 402, 173
- Arrigoni M., Trager S. C., Somerville R. S., 2010b, arXiv:1006.1147 [astro-ph]
- Asplund M., Grevesse N., Sauval A. J., Scott P., 2009, *ARA&A*, 47, 481
- Abazajian K. N., et al., 2009, *ApJS*, 182, 543
- Baldwin J. A., Phillips M. M., Terlevich R., 1981, *PASP*, 93, 5
- Bastian N., Covey K. R., Meyer M. R., 2010, *ARA&A*, 48, 339
- Becker S. A., Iben I. Jr., 1979, *ApJ*, 232, 111
- Bekki K., 1998, *ApJ*, 499, 635
- Benítez-Llambay A., Navarro J. F., Abadi M. G., Gottlöber S., Yepes G., Hoffman Y., Steinmetz M., 2013, *ApJ*, 763, 41L

- Bensby T., Feltzing S., Oey M. S., 2013, arXiv:1309.2631 [astro-ph]
- Benson A. J., Bower R. G., Frenk C. S., Lacey C. G., Baugh C. M., Cole S., 2003, ApJ, 599, 38
- Bell E. F., McIntosh D. H., Katz N., Weinberg M. D., 2003, ApJS, 149, 289
- Bertone S., De Lucia G., Thomas P. A., 2007, MNRAS, 379, 1143
- Bertschinger E., 1989, ApJ, 340, 666
- Begiel F., Leroy A., Walter F., Brinks E., de Blok W. J. G., Madore B., Thornley M. D., 2008, AJ, 136, 2846
- Begiel F., Leroy A., Walter F., 2010, IAUS, 270, 327B
- Binney J., Tremaine S., 1987, 'Galactic Dynamics', Princeton Univ. Press, Princeton, NJ
- Boeche C., et al., 2013, A&A, 553, 19
- Böhringer H., Matsushita K., Churazov E., Ikebe Y., Chen Y., 2002, A&A, 382, 804
- Bondi H., 1952, MNRAS, 112, 195
- Bothwell M. S., Maiolino R., Kennicutt R., Cresci G., Mannucci F., Marconi A., Ciccone C., 2013, MNRAS, 433, 1425
- Bouché N., et al., 2010, ApJ, 718, 1001
- Bournaud F., Combes F., 2003, A&A, 401, 817
- Bovy J., Rix H.-W., Hogg D. W., 2012a, ApJ, 751, 131
- Bovy J., Rix H.-W., Liu C., Hogg D. W., Beers T. C., Lee Y. S., 2012b, ApJ, 753, 148
- Boylan-Kolchin M., Springel V., White S. D. M., Jenkins A., Lemson G., 2009, MNRAS, 398, 1150
- Brandt T. D., Tojeiro R., Aubourg É, Heavens A., Jimenez R., Strauss M. A. , 2010, AJ, 140, 804
- Bresolin F., Garnett D. R., Kennicutt R. C., 2004, ApJ, 615, 228

- Bresolin F., 2007, *ApJ*, 656, 186
- Brinchmann J., Charlot S., White S. D. M., Tremonti C. A., Kauffmann G., Heckman T., Brinkmann J., 2004, *MNRAS*, 351, 1151
- Brooks A. M., Governato F., Booth C. M., Willman B., Gardner J. P., Wadsley G., Stinson G., Quinn T., 2007, *ApJ*, 655, L17
- Bruzual A. G., Charlot S., 2003, *MNRAS*, 344, 1000
- Bullock J. S., 2010, arXiv:1009.4505 [astro-ph]
- Burbidge E. M., Burbidge G. R., Fowler W. A., & Hoyle F., 1957, *Reviews of Modern Physics*, 29, 547
- Calura F., Pipino A., Chiappini C., Matteucci F., Maiolino R., 2009, *A&A*, 504, 373
- Calura F., Menci N., 2009, *MNRAS*, 400, 1347
- Calura F., Recchi S., Matteucci F., Kroupa P., 2010, *MNRAS*, 406, 1985
- Calura F., et al., 2012, *MNRAS*, 427, 1401
- Calura F., Menci N., 2011, *MNRAS*, 413, 1
- Calzetti D., Kinney A. L., Storchi-Bergmann T., 1994, *ApJ*, 429, 582
- Calzetti D., 2001, *PASP*, 113, 1449
- Cardelli J. A., Clayton G. C., Mathis J. S., 1989, *ApJ*, 345, 245
- Casagrande L., Schönrich R., Asplund M., Cassisi S., Ramírez I., Meléndez J., Bensby T., Feltzing S., 2011, *A&A*, 530, 138
- Catinella B., et al., 2010, *MNRAS*, 403, 683
- Catinella B., et al., 2012b, *A&A*, 544, 65, (C12)
- Chabrier G., 2003, *PASP*, 115, 763
- Chamberlain J. W., Aller L. H., 1951, *ApJ*, 114, 52
- Chandrasekhar S., 1943a, *ApJ*, 97, 255
- Charlot S., Longhetti M., 2001, *MNRAS*, 323, 887

- Chieffi A., Limongi M., 2004, ApJ, 608, 405, (CL04)
- Conroy C., van Dokkum P. G., 2012a, ApJ, 747, 69
- Conroy C., van Dokkum P. G., 2012b, ApJ, 760, 71
- Conroy C., Graves G. J., van Dokkum P. G., 2013, arXiv:1303.6629 [astro-ph]
- Croton D. J., et al., 2006, MNRAS, 365, 11
- Croxall K. V., et al., 2013, ApJ, 777, 96
- Cullen F., Cirasuolo M., McLure R. J., Dunlop J. S., 2013, arXiv:1310.0816 [astro-ph]
- Daddi E., et al., 2007, ApJ, 670, 156
- Dalcanton J. J., Yoachim P., Bernstein R. A., 2004, ApJ, 608, 189
- Dalla Vecchia C., Schaye J., 2008, MNRAS, 387, 1431
- Davé R., Oppenheimer B. D., Finlator K., 2011, MNRAS, 415, 11
- Davé R., Finlator K., Oppenheimer B. D., 2011, MNRAS, 416, 1354
- Davé R., Finlator K., Oppenheimer B. D., 2012, MNRAS, 421, 98
- Davé R., Katz N., Oppenheimer B. D., Kollmeier J. A., Weinberg D. H., 2013, MNRAS, 434, 2645
- Davis M., Efstathiou G., Frenk C. S., White S. D. M., 1985, ApJ, 292, 371
- Dayal P., Ferrara A., Dunlop J. S., 2013, MNRAS, 430, 2891
- de Gasperin F., et al., 2012, A&A, 547, 56
- Dellenbusch K. E., Gallagher III, J. S., Knezek P. M., 2007, ApJ, 655, L29
- De Lucia G., Kauffmann G., White S. D. M., 2004, MNRAS, 349, 1101
- De Lucia G., Springel V., White S. D. M., Croton D., Kauffmann G., 2006, MNRAS, 366, 499
- De Lucia G., Blaizot J., 2007, MNRAS, 375, 2
- Denicoló G., Terlevich R., Terlevich E., 2002, MNRAS, 330, 69

- de Plaa J., Werner N., Bleeker J. A. M., Vink J., Kaastra J. S., Méndez M., 2007, *A&A*, 465, 345
- De Rossi M. E., Tissera P. B., De Lucia G., Kauffmann G., 2009, *MNRAS*, 395, 210
- Dib S., Piau L., Mohanty S., Braine J., 2011, *MNRAS*, 415, 3439
- Duffy A. R., Kay S. T., Battye R. A., Booth C. M., Dalla Vecchia C., Schaye J., 2012, *MNRAS*, 420, 2799
- Dwek E., 1998, *ApJ*, 501, 643
- Eddington A. S., 1920, *Observatory*, 43, 341
- Edvardsson B., Andersen J., Gustafsson B., Lambert D. L., Nissen P. E., Tomkin J., 1993, *A&A*, 275, 101
- Elbaz D., et al., 2007, *A&A*, 468, 33
- Elbaz D., et al., 2011, *A&A*, 533, 119
- Ellison S. L., Patton D. R., Simard L., McConnachie A. W., 2008, *ApJ*, 672, L107
- Ellison S. L., Patton D. R., Simard L., McConnachie A. W., 2008b, *AJ*, 135, 1877
- Elmegreen B. G., 2006, *ApJ*, 648, 572
- Erb D., Shapley A. E., Pettini M., Steidel C. C., Reddy N. A., Adelberger K. L., 2006, *ApJ*, 644, 813
- Fabian A. C., 1994, *ARA&A*, 32, 277
- Fabian A. C., 2012, *ARA&A*, 50, 455
- Ferland G. J., 1996, 'Hazy, A Brief Introduction to Cloudy 90', Univ. Kentucky Internal Report, Lexington
- Ferland G. J., Korista K. T., Verner D. A., Ferguson J. W., Kingdon J. B., Verner E. M., 1998, *PASP*, 110, 761
- Finlator K., Davé R., 2008, *MNRAS*, 385, 2181
- François P., Matteucci F., Cayrel R., Spite M., Spite F., Chiappini C., 2004, *A&A*, 421, 613

- Freyer C., 1999, *ApJ*, 522, 413
- Friel E. D., 1995, *ARA&A*, 33, 381
- Fu J., Kauffmann G., Krumholz M. R., 2010, *MNRAS*, 409, 515
- Fu J., Kauffmann G., Huang M., Yates R. M., Moran S., Heckman T. M., Davé R., Guo Q., 2013, *MNRAS*, 434, 1531
- Fumagalli M., da Silva R. L., Krumholz M. R., 2011, *ApJ*, 741, 26
- Gallazzi A., Charlot S., Brinchmann J., White S. D. M., Tremonti C. A., 2005, *MNRAS*, 362, 41
- Gargiulo I. D., et al., 2014, arXiv:1402.3296 [astro-ph]
- Garnett D. R., 2002, *ApJ*, 581, 1019
- Garnett D. R., Kennicutt R. C., Bresolin F., 2004, *ApJ*, 607, 21
- Giovanelli R., et al. 2005, *AJ*, 130, 2598
- Gnedin N. Y., 2000, *ApJ*, 542, 535
- Gnedin N. Y., Tassis K., Kravtsov A. V., 2009, *ApJ*, 697, 55
- Gnedin N. Y., Kravtsov A. V., 2010, *ApJ*, 728, 88
- Graham A. W., Onken C. A., Athanassoula E., Combes F., 2011, *MNRAS*, 412, 2211
- Graves G. J., Faber S. M., Schiavon R. P., 2009, *ApJ*, 698, 1590
- Greggio L., Renzini A., 1983, *A&A*, 118, 217
- Greggio L., 2005, *A&A*, 441, 1055
- Grevesse N., Noels A., Sauval A. J., 1996, *ASP Conference Series*, Volume 99, 117
- Groves B. A., Heckman T. M., Kauffmann G., 2006, *MNRAS*, 371, 1559
- Gunawardhana M. L. P., et al., 2011, *MNRAS*, 415, 1647
- Guo Q., White S. D. M., Boylan-Kolchin M., De Lucia G., Kauffmann G., Lemson G., Li C., Springel V., Weinmann S., 2011, *MNRAS*, 413, 101

- Guo Q., White S. D. M., Angulo R. E., Henriques B., Lemson G., Boylan-Kolchin M., Thomas P., Short C., 2013, MNRAS, 428, 1351
- Hamann F., Ferland G., 1993, ApJ, 418, 11
- Hancock M., Smith B. J., Struck C., Giroux M. L., Hurlock S., 2009, AJ, 137, 4643
- Häring N., Rix H-W., 2004, ApJ, 604, L89
- Hayden M. R., et al., 2013, arXiv:1311.4569 [astro-ph]
- Haynes M. P., et al., 2011, AJ, 142, 170
- Henriques B. M. B., Thomas P. A., Oliver S., Roseboom I., 2009, MNRAS, 396, 535
- Henriques B. M. B., Thomas P. A., 2010, MNRAS, 403, 768
- Henriques B., White S. D. M., Thomas P. A., Angulo R. E., Guo Q., Lemson G., Springel V., 2013, MNRAS, 431, 3373
- Holmberg J., Nordström B., Andersen J., 2009, A&A, 501, 941
- Hopkins P. F., Quataert E., Murray N., 2012, MNRAS, 421, 3522
- Hughes T. M., Cortese L., Boselli A., Gavazzi G., Davies J. I., 2013, A&A, 550, 115
- Husemann B., Wisotzki L., Jahnke K., Sánchez S. F., 2011, A&A, 535, 72
- Husemann B., Wisotzki L., Jahnke K., Sánchez S. F., Nugroho D., 2012, IAUS, 295, 269
- Iannuzzi F., Dolag K., 2012, MNRAS, 417, 2846
- Iben I. Jr., Tutukov A. V., 1984, ApJS, 54, 335
- Iodice E., Arnaboldi M., De Lucia G., Gallagher III J. S., Sparke L. S., Freeman K. C., 2002a, AJ, 123, 195
- Izotov Y. I., Stasińska G., Meynet G., Guseva N. G., Thuan T. X., 2006, A&A, 448, 955
- Jansen R. A., Fabricant D., Franx M., Caldwell N., 2000a, ApJS, 126, 331
- Jansen R. A., Franx M., Fabricant D., Caldwell N., 2000b, ApJS, 126, 271

- Jiménez N., Tissera P. B., Matteucci F., 2014, arXiv:1402.4137 [astro-ph]
- Johansson J., Thomas D., Maraston C., 2012, MNRAS, 421, 1908, (JTM12)
- Johnson B. D., et al., 2007, ApJS, 173, 377
- Johnson B. D., et al., 2007, ApJS, 173, 392
- Kajisawa M., Ichikawa T., Yamada T., Uchimoto Y. K., Yoshikawa T., Akiyama M., Onodera M., 2010, ApJ, 723, 129
- Kampakoglou M., Trotta R., Silk J., 2008, MNRAS, 384, 1414
- Kauffmann G., White S. D. M., Guideroni B., 1993, MNRAS, 264, 201
- Kauffmann G., Colberg J. M., Diaferio A., White S. D. M., 1999a, MNRAS, 303, 188
- Kauffmann G., Haehnelt M., 2000, MNRAS, 311, 576
- Kauffmann G., et al., 2003a, MNRAS, 341, 33
- Kauffmann G., et al., 2003c, MNRAS, 346, 1055
- Kennicutt R. C., 1989, ApJ, 344, 685
- Kennicutt R. C., 1998a, ARA&A, 36, 189
- Kennicutt R. C., 1998b, ApJ, 498, 541
- Kennicutt R. C., Bresolin F., Garnett D. R., 2003, ApJ, 591, 801
- Kewley L. J., Heisler C. A., Dopita M. A., Lumsden S., 2001, ApJS, 132, 37
- Kewley L. J., Dopita M. A., 2002, ApJS, 142, 25
- Kewley L. J., Geller M. J., Barton E. J., 2006, AJ, 131, 2004
- Kewley L. J., Ellison S. L., 2008, ApJ, 681, 1183
- Kewley L. J., Rupke D., Zahid H. J., Geller M. J., Barton E. J., 2010, ApJ, 721, L48
- Kobayashi C., Springel V., White S. D. M., 2007, MNRAS, 376, 1465
- Kobulnicky H. A., Kewley L. J., 2004, ApJ, 617, 240

- Köppen J., Weidner C., Kroupa P., 2007, MNRAS, 375, 673
- Köppen J., Edmunds M. G., 1999, MNRAS, 306, 317
- Kroupa P., 2001, MNRAS, 322, 231
- Lagos C. d. P., Lacey C. G., Baugh C. M., Bower R. G., Benson A. J., 2011, MNRAS, 416, 1566
- Lagos C. d. P., Lacey C. G., C. M. Baugh, 2013, MNRAS, 436, 1787
- Lara-López M. A., Bongiovanni A., Cepa J., Pérez Garcia A. M., Sánchez-Portal M., Castañeda H., Fernández Lorenzo M., Pović M., 2010, A&A, 519, 31L
- Lara-López M. A., Cepa J., Bongiovanni A., Pérez Garcia A. M., Ederoclite A., Castañeda H., Fernández Lorenzo M., Pović M., Sánchez-Portal M., 2010, A&A, 521, 53L
- Lara-López M. A., et al., 2013, MNRAS, 433, 35L
- Larson R. B., 1974, MNRAS, 169, 229
- Lee H., Skillman E. D., Cannon J. M., Jackson D. C., Gehrz R. D., Polomski E. F., Woodward C. E., 2006, ApJ, 647, 970
- Lemson G., Virgo Consortium, 2006, preprint (arXiv:astro-ph/0608019)
- Lequeux J., Peimbert M., Rayo J. F., Serrano A., Torres-Peimbert S., 1979, A&A, 80, 155L
- Li C., Kauffmann G., Fu J., Wang J., Catinella B., Fabello S., Schiminovich D., Zhang W., 2012, MNRAS, 424, 1471
- Liang Y. C., Yin S. Y., Hammer F., Deng L. C., Flores H., Zhang B., 2006, ApJ, 652, 257
- Liu X., Shapley A. E., Coil A. L., Brinchmann J., Ma C-P., 2008, ApJ, 678, 758L
- Lilly S. J., Carollo C. M., Pipino A., Renzini A., Peng Y., 2013, ApJ, 772, 119
- Lodders K., 2003, ApJ, 591, 1220
- Macciò A. V., Moore B., Stadel J., 2006, ApJ, 636, L25

- Mac Low M-M., Ferrara A., 1999, *ApJ*, 513, 142
- Madau P., Ferguson H. C., Dickinson M. E., Giavalisco M., Steidel C. C., Fruchter A., 1996, *MNRAS*, 283, 1388
- Maeder A., 1992, *A&A*, 264, 105
- Maiolino R., et al., 2008, *A&A*, 488, 463
- Mannucci F., Della Valle M., Panagia N., 2006, *MNRAS*, 370, 773
- Mannucci F., Cresci G., Maiolino R., Marconi A., Gnerucci A., 2010, *MNRAS*, 408, 2115
- Maoz D., Badenes C., 2010, *MNRAS*, 407, 1314
- Maoz D., Sharon K, Gal-Yam A., 2010, *ApJ*, 722, 1879
- Maoz D., Mannucci F., 2012, *PASA*, 29, 447
- Maoz D., Mannucci F., Brandt T. D., 2012, *MNRAS*, 426, 3282
- Marigo P., 2001, *A&A*, 370, 194, (M01)
- Maraston C., 2005, *MNRAS*, 362, 799
- Markovič K., Viel M., 2013, arXiv:1311.5223 [astro-ph]
- Martin C. L., Kobulnicky H. A., Heckman T. M., 2002, *ApJ*, 574, 663
- Mathews W. G., Baker J. C., 1971, *ApJ*, 170, 241
- Matteucci F., 1986, *MNRAS*, 221, 911
- Matteucci F., Greggio L., 1986, *A&A*, 154, 279
- Matteucci F., 1994, *A&A*, 288, 57
- Matteucci F., Recchi S., 2001, *ApJ*, 558, 351
- Matteucci F., Panagia N., Pipino A., Mannucci F., Recchi S., Della Valle M., 2006, *MNRAS*, 372, 265
- Matteucci F., Spitoni E., Recchi S., Valiante R., 2009, *A&A*, 501, 531

- Matteucci F., 2012, 'Chemical Evolution of Galaxies', Springer, Germany
- McGaugh S. S., 1991, *ApJ*, 380, 140
- McMillan P. J., 2011, *MNRAS*, 414, 2446
- McWilliam, 1997, *ARA&A*, 35, 503
- Menci N., Fiore F., Lamastra A., 2012, *MNRAS*, 421, 2384
- Micali A., Matteucci F., Romano D., 2013, *MNRAS*, 436, 1648
- Michel-Dansac L., Lambas D. G., Alonso M. S., Tissera, P., 2008, *MNRAS*, 386, L82
- Minchev I., Chiappini C., Martig M., 2013, *A&A*, 558, 9
- Mo H., van den Bosch F., White S. D. M., 2010, 'Galaxy Formation & Evolution', Cambridge Univ. Press, New York, NY
- Moiseev A. V., Smirnova K. I., Smirnova A. A., Reshetnikov V. P., 2011, *MNRAS*, 418, 244
- Montuori M., Di Matteo P., Lehnert M. D., Combes F., Semelin B., 2010, *A&A*, 518, 56
- Moustakas J., et al., 2011, arXiv:1112.3300 [astro-ph]
- Naab T., Johansson P. H., Ostriker J. P., 2009, *ApJ*, 699, L178
- Nagao T., Maiolino R., Marconi, A., 2006, *A&A*, 459,85
- Nagashima M., Lacey C. G., Okamoto T., Baugh C. M., Frenk C. S., Cole S., 2005, *MNRAS*, 363, L31
- Newman S. F., et al., 2012, *ApJ*, 761, 43
- Noeske K. G., et al., 2007a, *ApJ*, 660, L43
- Noeske K. G., et al., 2007b, *ApJ*, 660, L47
- Nomoto K., Thielemann F.-K., Yokoi K., 1984, *ApJ*, 286, 644
- Nordström B., et al., 2004, *A&A*, 418, 989
- Okamoto T., Gao L., Theuns T., 2008, *MNRAS*, 390, 920

- Osterbrock D. E., 1989, 'Astrophysics of Gaseous Nebulae and AGN', Univ. Sci. Books, New York
- Padovani P., Matteucci M., 1993, *ApJ*, 416, 26
- Pagel B. E. J., Edmunds M. G., Blackwell D. E., Chun M. S., Smith G., 1979, *MNRAS*, 189, 95P
- Panter B., Jimenez R., Heavens A. F., Charlot S., 2008, *MNRAS*, 391, 1117
- Paturel G., Theureau G., Bottinelli L., Gouguenheim L., Coudreau-Durand N., Hallet N., Petit C., 2003, *A&A*, 412, 57
- Peebles M. S., Pogge R. W., Stanek K. Z., 2008, *ApJ*, 685, 904
- Peebles M. S., Pogge R. W., Stanek K. Z., 2009, *ApJ*, 695, 259
- Peng Y.-J., 2010, *ApJ*, 721, 193
- Péroux C., Bouché N., Kulkarni V. P., York D. G., 2013, *MNRAS*, 436, 2650
- Pettini M., Pagel B. E. J., 2004, *MNRAS*, 348, 59
- Pilkington K., et al., 2012, *MNRAS*, 425, 969
- Pilyugin L. S., Vílchez J. M., Cédres B., Thuan T. X., 2010, *MNRAS*, 403, 896
- Pilyugin L. S., Mattsson L., 2011, *MNRAS*, 412, 1145
- Pipino A., Chiappini C., Graves G., Matteucci F., 2009a, *MNRAS*, 396, 1151
- Pipino A., Devriendt J. E. G., Thomas D., Silk J., Kaviraj S., 2009b, *A&A*, 505, 1075
- Pipino A., Matteucci F., 2004, *MNRAS*, 347, 968
- Pipino A., Matteucci F., 2011, *A&A*, 530, 98
- Planck Collaboration XVI. 2013, submitted to *A&A*
- Portinari L., Chiosi C., Bressan A., 1998, *A&A*, 334, 505, (P98)
- Press W. H., Schechter P., 1974, 187, 425
- Reddy N., Erb D. K., Pettini M., Steidel C. C., Shapley A. E., 2010, *ApJ*, 712, 1070

- Reshetnikov V., Sotnikova N., 1997, *A&A*, 325, 933
- Rich J. A., Kewley L. J., Dopita M. A., 2014, *ApJ*, 781, 12L
- Romano D., Karakas A. I., Tosi M., Matteucci F., 2010, *A&A*, 522, 32
- Romano D., Starkeburg E., 2013, *MNRAS*, 434, 471
- Ruiter A. J., Belczynski K., Sim S. A., Hillebrandt W., Fryer C. L., Fink M., Kromer M., 2011, *MNRAS*, 417, 408
- Rupke D. S. N., Veilleux S., Baker A. J., 2008, *ApJ*, 674, 172
- Russell H. R., et al., 2013, arXiv:1309.0014 [astro-ph]
- Saintonge A. et al., 2011, *MNRAS*, 415, 32
- Salaris M., Cassisi S., 2005, 'Evolution of Stars and Stellar Populations', Wiley, Chichester
- Salpeter E. E., 1955, *ApJ*, 121, 161
- Salim S., et al., 2007, *ApJS*, 173, 267
- Savaglio S., et al., 2005, *ApJ*, 635, 260
- Scalo J. M., 1986, *Fundamentals of Cosmic Physics*, Volume 11, 1
- Scannapieco C., Tissera P. B., White S. D. M., Springel V., 2008, *MNRAS*, 389, 1137
- Schaye J., et al., 2010, *MNRAS*, 402, 1536
- Schiavon R. P., 2007, *ApJS*, 171, 146
- Schmidt M., 1959, *ApJ*, 129, 243
- Schmidt M., 1963, *ApJ*, 137, 758
- Schweizer F., Whitmore B. C., Rubin V. C., 1983, *AJ*, 88, 7
- Seitzzahl I. R., et al., 2013, *MNRAS*, 429, 1156
- Seljak U., Zaldarriaga M., 1996, *ApJ*, 469, 437
- Serra P., Trager S. C., 2007, *MNRAS*, 374, 769

- Shabala S. S., Ash S., Alexander P., Riley J. M., 2008, MNRAS, 388, 625
- Shankar F., Marulli F., Mathur S., Bernardi M., Bournaud F., 2012, A&A, 540, 23
- Shankar F., Marulli F., Bernardi M., Mei S., Meert A., Vikram V., 2013, MNRAS, 428, 109
- Somerville R., Primack J. R., Faber S. M., 2001, MNRAS, 320, 504
- Somerville R., Hopkins P. F., Cox T. J., Robertson B. E., Hernquist L., 2008, MNRAS, 391, 481
- Spavone M., Iodice E., Arnaboldi M., Gerhard O., Saglia R., Longo G., 2010, ApJ, 714, 1081
- Spavone M., Iodice E., 2013, MNRAS, 434, 3310
- Spergel D. N., et al., 2003, ApJS, 148, 175
- Spiniello C., Trager S. C., Koopmans L. V. E., Chen Y. P., 2013, ApJ, 753, 32
- Springel V., White S. D. M., Tormen G., Kauffmann G., 2001a, MNRAS, 328, 726
- Springel V., Yoshia N., White S. D. M., 2001b, New Astronomy, 6, 79
- Springel V., et al., 2005, Nature, 435, 629
- Springel V., 2005, MNRAS, 364, 1105
- Springel V., 2010, MNRAS, 401, 791
- Stasińska G., 1978, A&A, 66, 257
- Stasińska G., 2002, RMxAC, 12, 62
- Stasińska G., Schaerer D., Leitherer C., 2002, Ap&SS, 281, 335
- Stasińska G., 2005, A&A, 434, 507
- Stasińska G., et al., 2012, 'Oxygen in the Universe', EAS Pub. Series, Vol.54
- Stern J., Laor A., 2013, MNRAS, 431, 836
- Strolger L.-G., et al., 2010, ApJ, 613, 200

- Sutherland R. S., Dopita M. A., 1993, *ApJS*, 88, 253
- Talbot R. J. Jr., Arnett W. D., 1971, *ApJ*, 170, 409
- Thielemann F.-K., et al., 2003, ‘From Twilight to Highlight: The Physics of Supernovæ, Supernova Nucleosynthesis and Galactic Evolution.’
- Thomas D., Greggio L., Bender R., 1998, *MNRAS*, 296, 119
- Thomas D., Kauffmann G., 1999, *ASPC*, 192, 261
- Thomas D., Greggio L., Bender R., 1999, *MNRAS*, 302, 537
- Thomas D., 1999, *MNRAS*, 306, 655
- Thomas D., Maraston C., Schawinski K, Sarzi M., Silk J., 2010, *MNRAS*, 404, 1775
- Thomas D., Maraston C., Johansson J., 2011b, *MNRAS*, 412, 2183
- Tinsley B. M., 1980, *Fundamentals of Cosmic Physics*, Volume 5, 287
- Tissera P. B., White S. D. M., Scannapieco C., 2012, *MNRAS*, 420, 255
- Toomre A., 1964, *ApJ*, 139, 1217
- Torrey P., Cox T. J., Kewley L., Hernquist L., 2012, *ApJ*, 746, 108
- Totani T., Morokuma T., Oda T., Doi M., Yasuda N., 2008, *PASJ*, 60, 1327
- Tremonti C. A., et al., 2004, *ApJ*, 613, 898
- Tremaine S., et al., 2002, *ApJ*, 574, 740
- Tumlinson J., et al., 2011, *Science*, 334, 948
- Tutukov A. V., Yungelson L. R., 1980, *IAUS*, 88, 15
- Ugliano M., Janka H.-T., Marek A., Arcones A., 2012, *ApJ*, 757, 69
- van den Bergh S., 1962, *AJ*, 67, 486
- van Dokkum P. G., Conroy C., 2010, *Nature*, 468, 940
- van Dokkum P. G., et al., 2013, *ApJ*, 771, 35

- Vogelsberger M., Genel S., Sijacki D., Torrey P., Springel V., Hernquist L., 2013, MNRAS, 436, 3031
- Walch S., Wunsch R., Burkert A., Glover S., Whitworth A., 2011, ApJ, 733, 47
- Wang J., Overzier R., Kauffmann G., von der Linden A., Kong X., 2010, MNRAS, 401, 433
- Webbink R. F., 1984, ApJ, 277, 355
- Weidner C., Kroupa P., 2006, MNRAS, 365, 1333
- Weinmann S. M., van den Bosch F. C., Yang X., Mo H. J., Croton D. J., Moore B., 2006, MNRAS, 372, 1161
- Whelan J., Iben I. Jr., 1973, ApJ, 186, 1007
- White S. D. M., 1976, MNRAS, 174, 19
- White S. D. M., Rees M. J., 1978, MNRAS, 183, 341
- White S. D. M., Frenk C., 1991, ApJ, 379, 52
- Whitmore B. C., Lucas R. A., McElroy D. B., Steiman-Cameron T. Y., Sackett P. D., Olling R. P., 1990, MNRAS, 100, 5
- Wiersma R. P. C., Schaye J., Britton S. D., 2009a, MNRAS, 393, 99
- Wiersma R. P. C., Schaye J., Theuns T., Dalla Vecchia C., Tornatore L., 2009b, MNRAS, 399, 574
- Wong T., Blitz L., 2002, ApJ, 569, 157
- Woo J., Courteau S., Dekel A., 2008, MNRAS, 390, 1453
- Woods D. F., Geller M. J., Barton, E. J., 2006, AJ, 132, 197
- Woosley S. A., Weaver T. A., 1995, ApJS, 101, 181
- Woosley S. A., Janka H.-T., 2005, Nature Physics, 1, 147
- Worthey G., 1994, ApJS, 95, 107
- Wuyts E., Rigby J. R., Sharon K., Gladders M. D., 2012, ApJ, 755, 73

- Wright E. L., et al., 2010, *AJ*, 140, 1868
- Yanny B., et al., 2009, *AJ*, 137, 4377
- Yates R. M., Kauffmann G., Guo Q., 2012, *MNRAS*, 422, 215, (YKG12)
- Yates R. M., Kauffmann G., 2014, arXiv:1310.5151 [astro-ph]
- Yates R. M., Henriques B., Thomas P. A., Kauffmann G., Johansson J., White S. D. M., 2013, *MNRAS*, 435, 3500
- Yin S. Y., Liang Y. C, Hammer F., Brinchmann J., Zhang B., Deng L. C., Flores H., 2007, *A&A*, 462, 535
- Zahid H. J., Kewley L. J., Bresolin F., 2011, *ApJ*, 730, 137
- Zahid H. J., Bresolin F., Kewley L. J., Coil A. L., Davé R., 2012a, *ApJ*, 750, 120
- Zahid H. J., Yates R. M., Kewley L. J., Kudritzki R. P., 2013, *ApJ*, 763, 92
- Zahid H. J., Torrey P., Kudritzki R. P., Kewley L. J., Davé R., Geller M. J., 2013, *MNRAS*, 436, 1852
- Zahid H. J., et al., 2013, arXiv:1310.4950 [astro-ph]
- Zaritsky D., Kennicutt R. C., Huchra, J. P., 1994, *ApJ*, 420, 87
- Zhang W., Li C., Kauffmann G., Zou H., Catinella B., Shen S., Guo Q., Chang R., 2009, *MNRAS*, 397, 1243, (Z09)



# Acknowledgements

The one person I wish to thank above all others is Kathrin. Her support during the undertaking of my PhD – looking after our daughter while I’ve been away at conferences, allowing me to work on weekends, providing emotional support and motivation whenever she could, and experiencing many happy times together with me – has been indispensable. There is no question that this thesis could not have been completed without her dedication, patience, understanding, and love. My work has had a significant impact on her life over the last few years, and for this I am deeply indebted. She is an immensely strong, intelligent, and caring person, and I will always be grateful for the sacrifices she has made in her life so that ours could be better.

A special thanks should also go to Charlie, for being simply the most quick-thinking, kind, strong, funny, brave, beautiful person I have ever known. Everything I do is in some way with her in mind, and no greater motivation is needed in my life.

I would also like to thank my parents for their seemingly infinite reserves of patience, love, and enthusiasm. It is clear that I would not have come this far had it not been for them. No one could ask for more than they have gladly given.

Eva and Manfred have also been major sources of support during my time in Munich, for which I thank them. They have helped us frequently in many ways, and always made clear that their home is our home whenever we have visited. I will never forget the kindness and hospitality that they have shown me ever since the first time we met. For all this, I am truly grateful.

In addition, there are my teachers and friends during my undergraduate times at Imperial College. Those days formed the foundation of my interest in physics research, and allowed me to consider a PhD as a viable next step.

I also thank the host of friends I have made during my time working in Garching. There have been many over the years, but particular thanks goes to (in roughly chronological order) Silvia Fabello, Francesca Iannuzzi, Francesco De Gasperin, Tomek Rembiaz, Katarina Markovič, Luca Graziani, David Gruber, Sandra Benítez, Zaz

Magic, Thomas Maedler, Victor Silva, Rob Wiersma, Irina Thaler, Ludwig Oser, Iva Karovičová, Marcel van Daalen, Diederik Kruijssen, Jonas Johansson, Margherita Molaro, and Andressa Jendrieck. I have benefited greatly from our chats over lunch, coffee, alcohol, and complicated plots on a wide range of subjects, and have been privileged to know them all. The same extends to my fellow IMPRS student representatives. I have had tremendous fun collaborating with them all on the various events and parties we have organised, and I am certain that I leave the group in significantly better hands than mine. I also wish to thank the Wednesday- and Friday-evening footballers, who have provided a much needed physical outlet at times when work has not been going according to plan. The exercise and companionship has been invaluable.

It is also important to mention the huge debt of thanks I owe to Bruno Henriques, who has been both a wise advisor and great friend to me in and out of the office. His understanding of semi-analytic modelling, and the physics of galaxy evolution in general, has had a significant impact on a lot of the work presented in this thesis. I count him as one of my closest friends, and look forward to many more good times together after my PhD time is finished. Similarly, I especially thank Chervin Laporte for all the moments of laughter and dismay we have spent together as office mates and friends. I also wish to thank Simon White for his support as my official supervisor, and his willingness to hire me in the first place. I have clear memories of his prompts and encouragements during my first group and conference presentations, and also greatly appreciate his important input to key parts of the work presented here.

Further thanks has to go to Peter Thomas, who was an excellent host and collaborator during my brief spell visiting the University of Sussex. I thank him for his patience when progress was slow, and friendly, honest, and encouraging comments throughout. I also thank Lisa Kewley and Jabran Zahid for making the collaborative work we have done together so productive and fun.

Lastly, I would like to particularly thank Guinevere Kauffmann for her support as my project supervisor. This thesis would never have been realised had she not taken the risk of supervising me. Its content would also have been significantly worse, had it not been for her regular responses to emails at all times of day, careful reading of paper drafts, frequent suggestions and improvements, comprehensive knowledge on all aspects of galactic astrophysics, and enthusiasm for the subject and the importance of contributing good-quality work to it. I also thank her for her honest appraisals, which have sometimes provided a much-needed motivation.

I hope that this thesis goes some way to repaying the trust that all of the above have put in me over the years.